

Technische Universität München
Institut für Energietechnik

Lehrstuhl für Thermodynamik

Influence of Water Injection on the Thermoacoustic Stability of a Lean-Premixed Combustor

Nicolai Vasko Stadlmair

Vollständiger Abdruck der von der Fakultät für Maschinenwesen der
Technischen Universität München zur Erlangung des akademischen
Grades eines

DOKTOR – INGENIEURS

genehmigten Dissertation.

Vorsitzender:

Prof. Dr.-Ing. Hans-Jakob Kaltenbach

Prüfer der Dissertation:

1. Prof. Dr.-Ing. Thomas Sattelmayer
2. Prof. Jacqueline O'Connor, Ph.D.
Pennsylvania State University, USA

Die Dissertation wurde am 21.11.2017 bei der Technischen Universität München
eingereicht und durch die Fakultät für Maschinenwesen am 27.02.2018 angenommen.

Vorwort

Die vorliegende Arbeit entstand während meiner Tätigkeit als wissenschaftlicher Mitarbeiter am Lehrstuhl für Thermodynamik der Technischen Universität München. Sie wurde im Rahmen des Forschungsprojektes *TUM.Energy Valley Bavaria* im Teilprojekt *Flexible Kraftwerke* durch die Munich School of Engineering und das Bayerische Staatsministerium für Bildung und Kultus, Wissenschaft und Kunst gefördert.

Mein Dank gilt insbesondere meinem Doktorvater Herrn Professor Dr.-Ing. Thomas Sattelmayer für die fachliche Betreuung der Arbeit und die Übernahme des Hauptreferats. Darüber hinaus möchte ich mich bei ihm für sein außerordentliches Interesse an meiner Arbeit, sein Engagement und die wertvollen Impulse während meiner Zeit am Lehrstuhl bedanken. Ich schätze das Vertrauen und die Freiheit, die er mir bei der Umsetzung der Projektziele ließ, sehr.

Frau Professor Jacqueline O'Connor danke ich für die äußerst zügige Begutachtung meiner Arbeit und für die lange Anreise, die sie für die Übernahme des Koreferats auf sich genommen hat. Weiterhin danke ich Herrn Professor Dr.-Ing. Hans-Jakob Kaltenbach für den Vorsitz bei meiner mündlichen Prüfung.

Für die kollegiale Zusammenarbeit möchte ich mich bei allen aktuellen und ehemaligen Mitarbeitern des Lehrstuhls sowie denen der Werkstätten, des Sekretariats und allen Studenten mit denen ich zusammengearbeitet habe, bedanken. Ausdrücklich danken möchte ich auch meinen Projektkollegen Stephan Lellek und Max vom Stein für die erfolgreiche und freundschaftliche Zusammenarbeit. Ein besonderer Dank gehört außerdem Tobias Hummel für die unzähligen fachlichen Diskussionen, die zu wesentlichen Impulsen geführt haben und letztlich entscheidend zum Erfolg der Arbeit beigetragen haben, sowie für seine kritische Begutachtung des Manuskripts. Weiterhin danke ich Noah Klarmann für seine Unterstützung bei der Umsetzung der CFD-Simulationen, sowie Frederik Berger und Georg Fink für ihren Support bei sämtlichen messtechnischen und konstruktiven Aufgaben und ihre wertvollen Korrekturvorschläge. Weiterhin bin ich sehr dankbar für all die Freundschaften, die sich aus der gemeinsamen Arbeit am Lehrstuhl entwickelt haben.

Abseits des Lehrstuhls gilt mein herzlichster Dank Johannes, meiner Schwester Lara und all meinen Freunden die mich direkt oder indirekt während dieser Zeit unterstützt haben.

Zu guter Letzt wäre all das nicht ohne meine Mutter Ruth und ihre unermüdliche Unterstützung in allen Lebenslagen möglich gewesen. Hierfür danke ich ihr von ganzem Herzen!

München, im Mai 2018

Nicolai Stadlmair

Kurzfassung

Wassereinspritzung bei konstanter Flammentemperatur ist eine vielversprechende Möglichkeit zur kurzfristigen Leistungssteigerung von Gasturbinen, ohne dabei wesentliche Nachteile in Bezug auf den Emissionsausstoß zu verursachen. Dabei wird Wasser in flüssiger Form in die Hauptverbrennungszone eingespritzt, während gleichzeitig die Brennstoffmenge erhöht wird. Brennkammern moderner Gasturbinen werden meist mager-vorgemischt betrieben und sind daher anfällig für thermoakustische Instabilitäten. Die Untersuchung von thermoakustischen Phänomenen in Gasturbinenbrennkammern ist Gegenstand aktueller Forschung, wobei Wasserinjektion bisher nicht berücksichtigt wurde.

Die vorliegende Arbeit untersucht den Einfluss von Wasserinjektion auf thermoakustische Instabilitäten anhand eines Einzelbrennerversuchsstandes unter atmosphärischen Bedingungen. Zu diesem Zweck werden die akustischen Eigenschaften von Brenner und Flamme durch gemessene Streumatrizen und Flammentransferfunktionen über einen weiten Betriebsbereich charakterisiert. Anhand der Ergebnisse wird gezeigt, dass die Flammentransferfunktion von Flammen für Wasser-zu-Brennstoff-Verhältnisse von bis zu 2 bei konstanter Flammentemperatur über einen breiten Frequenzbereich mit der Flammenlänge korreliert. Die akustischen Eigenschaften des Brenners werden zusätzlich numerisch auf Basis der linearisierten Euler-Gleichungen berechnet und erfolgreich mit gemessenen Streumatrizen validiert. Um den Einfluss des Wasser-zu-Brennstoff-Verhältnisses auf die thermoakustische Stabilität zu quantifizieren, werden experimentell bestimmte Eigenfrequenzen und Dämpfungsraten analysiert. Deren Messungen zeigen, dass die thermoakustische Dämpfung einer Helmholtz-Mode mit zunehmendem Wasser-zu-Brennstoff-Verhältnis sinkt und schließlich zu selbst-erregten Schwingungen bei sehr niedrigen Frequenzen führt. Eine quantitativ präzise Vorhersage von Eigenfrequenzen, thermoakustischer Dämpfung, akustischer Dissipation und Flammentreiben wird durch Stabilitätsanalysen auf Basis der Streumatrizen und Flammentransferfunktionen erreicht. Die Genauigkeit der numerischen Simulation wird mit gemessenen Eigenfrequenzen der ersten longitudinalen Mode der Brennkammer und deren Dämpfungsraten erfolgreich über einen weiten Betriebsbereich mit Wassereinspritzung validiert.

Abstract

Water injection at constant flame temperature is a promising option to achieve a short-term load increase of gas turbines without causing major drawbacks in pollutant formation. For this purpose, liquid water droplets are directly injected into the main combustion zone while simultaneously increasing the fuel mass flow rate. Commonly, combustors of modern gas turbines are operated with lean-premixed flames, which provide low emission levels but are often highly susceptible to thermoacoustic instabilities. Thermoacoustic phenomena occurring in gas turbine combustion chambers have been the subject of research for more than two decades, whereas water injection has not been included so far.

This work investigates the influence of water injection on the thermoacoustic stability of a single-burner test-rig under atmospheric conditions for water-to-fuel ratios of up to 2. The acoustic properties of the burner as well as the flame dynamics are characterized by measured scattering matrices and flame transfer functions over a broad range of operating conditions. It is shown that for water injection at constant flame temperature, the flame transfer function scales with the flame length over a wide frequency range. The acoustic properties of the burner are calculated based on linearized Euler equations and are successfully validated with measured scattering matrices. Experimentally determined eigenfrequencies and damping rates are obtained to quantify the influence of the water-to-fuel ratio on the thermoacoustic stability. Measured damping rates show that an increasing water-to-fuel ratio decreases the stability of the Helmholtz mode and finally leads to self-sustained oscillations. Quantitatively accurate prediction of longitudinal eigenfrequencies, thermoacoustic damping, acoustic dissipation and flame driving is achieved using stability analyses on the basis of the scattering matrices and measured flame transfer functions. The accuracy of the numerical predictions are benchmarked quantitatively with measured eigenfrequencies and damping rates associated with the first longitudinal eigenmode of the combustor.

Contents

List of Figures	xiii
List of Tables	xix
Nomenclature	xxi
1. Introduction	1
1.1. Steam- and Water Injection in Gas Turbines	1
1.2. Thermoacoustic Instabilities	3
1.3. Goal and Structure of this Work	5
2. Theoretical Background	9
2.1. Governing Equations	9
2.1.1. Linearized Euler Equations (LEE)	9
2.1.2. Wave Equation	11
2.1.3. Analytical Solution of the Wave Equation	13
2.2. Low-Order Network Modeling	14
2.3. Boundary Conditions	16
2.4. Finite Element Method in Acoustics	17
2.5. Flame Dynamics	19
2.5.1. Flame Transfer Functions	20
2.5.2. Rankine-Hugoniot Relations for Acoustic Perturbations	21
2.6. Combustor Dynamics	24
2.6.1. Modal Expansion of the Wave Equation	25
2.6.2. Harmonic Oscillator	27
2.6.2.1. Linear Systems	28
2.6.2.2. Non-Linear Systems	30
2.7. Solution of Non-Linear Optimization Problems	31
2.7.1. Least-Squares Optimization	32
2.7.2. Bayesian Inference	33
2.7.3. Markov-Chain Monte-Carlo Method (MCMC)	33

2.7.4.	Metropolis-Hastings Algorithm	34
2.7.5.	Gibbs Sampling	35
3.	Measuring Methods and Data Processing	37
3.1.	Determination of Scattering Matrices	37
3.2.	Measurement of Source Terms	40
3.3.	Measurement of Flame Transfer Functions	40
3.4.	Determination of Damping and Growth Rates	42
3.4.1.	Impulse Response Method	43
3.4.2.	Stochastic Forcing Method	46
3.4.3.	Determination of Acoustic Dissipation and Flame Gain	48
3.4.4.	Growth Rate Determination	49
3.5.	Flame Imaging	50
3.5.1.	Stationary Flame Images	51
3.5.2.	Phase-Resolved Flame Images	52
3.6.	Spray Distribution and Droplet Sizes	54
3.6.1.	Mie-Scattering	54
3.6.2.	Particle Sizing	55
4.	Experimental Setup	57
4.1.	Atmospheric Single Burner Test-Rig	57
4.2.	Swirl-Burner with Water Injection	59
5.	Stationary Flame and Flow Properties	63
5.1.	Operating Conditions	63
5.2.	Flame Shape and Flame Length	65
5.3.	Spray Distribution	70
5.4.	Droplet Properties	71
6.	Acoustic Properties and Flame Response	75
6.1.	Scattering Matrices of the Burner	75
6.2.	Noise Emission with Water Injection	77
6.3.	Flame Transfer Functions	78
6.3.1.	Dry Operation	79
6.3.2.	Water Injection at Constant Equivalence Ratio	81
6.3.3.	Water Injection at Constant Adiabatic Flame Tem- perature	83

6.4.	Phase-Resolved Heat Release Oscillations	87
7.	Thermoacoustic Modes with Water Injection	91
7.1.	Aeroacoustic Damping Properties of the Combustor	91
7.2.	Combustor Damping under Dry Operation	94
7.3.	Combustor Damping with Water Injection	97
7.3.1.	Water Injection at Constant Equivalence Ratio	97
7.3.2.	Water Injection at Constant Adiabatic Flame Temperature	100
7.3.3.	Influence of the Downstream Boundary Condition on Thermoacoustic Damping	104
7.3.4.	Acoustic Dissipation and Flame Gain	107
7.4.	Benchmark of Different Methods for Thermal Power Increase	113
8.	Numerical Simulation and Stability Analysis	117
8.1.	Modeling Approach and Numerical Setup	117
8.1.1.	Acoustic Scattering Behavior: CFD/CAA Approach .	117
8.1.2.	Thermoacoustic Stability: Eigenvalue Analysis	120
8.2.	Determination of Stationary Flow- and Temperature Fields .	123
8.2.1.	Stationary Flow Field	123
8.2.2.	Determination of the Local Speed of Sound	124
8.3.	Acoustic Scattering Behavior of the Burner	127
8.4.	Qualitative Analysis of Occurring Modes	130
8.5.	Quantitative Stability Analysis	133
8.5.1.	Acoustic Damping	135
8.5.1.1.	Acoustic Damping under Non-reactive Conditions	135
8.5.1.2.	Acoustic Damping under Reactive Conditions	137
8.5.2.	Thermoacoustic Damping with Water Injection	138
8.5.2.1.	Experimental Scattering Matrices of Burner and Flame	138
8.5.2.2.	Simulated Burner Scattering Matrix and Analytical Flame Transfer Function	140
8.5.2.3.	Simulated Burner Scattering Matrix and Scaled Flame Transfer Function	144
9.	Summary and Conclusion	147

A. Matrix-Vector Notation of the LEEs	151
B. Validation of the Stochastic Forcing Method	153
B.1. Single Mode Case	155
B.2. Multi-Mode Case	156
B.3. Error Analysis	157
C. Operating Parameters of the Test-Rig	159
D. Comparison Between Flame Driving and FTF	163
E. Scattering Matrices of Burner and Flame	167
Supervised Student Theses	171
Previous Publications	173
Bibliography	175

List of Figures

3.1.	Multi-microphone method to determine acoustic scattering matrices.	37
3.2.	Measurement procedure of the impulse response method to determine combustor damping.	44
3.3.	Representative measured and reconstructed decaying pressure time series for two resonant frequencies of a combustor with mean flow.	45
3.4.	Probability densities of the normalized damping rate and frequency and reconstructed autocorrelation function over the number of oscillation cycles for a representative pressure time series.	47
3.5.	Transfer function between integral OH [*] -chemiluminescence as a marker for unsteady heat release and dynamic pressure.	48
3.6.	Representative autocorrelation function of the slowly varying amplitude fluctuations for a limit-cycle oscillation.	50
3.7.	Determination of the flame position from time-averaged OH [*] -chemiluminescence images.	51
3.8.	Triggering scheme for offline phase averaging of OH [*] -chemiluminescence images.	53
4.1.	Schematic of the atmospheric single burner test-rig.	58
4.2.	Downstream siren for acoustic excitation with modulator valve for decay rate measurements using the impulse response method.	59
4.3.	Modular swirl burner with water injector.	61
5.1.	Spatial distribution of the OH [*] -chemiluminescence intensity in the combustor centerplane with water injection at constant adiabatic flame temperature for operating range $\textcircled{A} _{T_{\text{ad}}}$	66

5.2.	Spatial distribution of the OH [*] -chemiluminescence intensity in the combustor centerplane with water injection at constant equivalence ratio for operating range $\textcircled{A} \phi$	67
5.3.	Normalized axial stand-off distance of the vortex breakdown of the flame with water injection.	69
5.4.	Normalized axial position of maximum OH [*] -chemiluminescence intensity in the flame with water injection.	69
5.5.	Superposition of OH [*] -chemiluminescence intensity and Mie scattering intensity in the combustor centerplane for increasing water-to-fuel ratio at constant adiabatic flame temperature for operating range $\textcircled{A} T_{\text{ad}}$	70
5.6.	Measured Sauter mean diameter (SMD) of water droplets for constant atomization air mass flow of 1 g s^{-1}	72
6.1.	Scattering matrices of the burner: Comparison between original burner and burner with water injector.	76
6.2.	Measured source terms for water injection at constant flame temperature of $T_{\text{ad}} = 1923 \text{ K}$ plotted over frequency.	78
6.3.	Flame transfer functions of the four baseline operating conditions depending on frequency and Strouhal number.	79
6.4.	Flame transfer functions with water injection at constant adiabatic flame temperature for varying operating conditions depending on frequency.	81
6.5.	Flame transfer functions with water injection at constant equivalence ratio for varying operating conditions depending on Strouhal number.	83
6.6.	Flame transfer functions for operating points with water injection at constant adiabatic flame temperature depending on frequency.	84
6.7.	Flame transfer functions for operating points with water injection at constant adiabatic flame temperature depending on Strouhal number.	85
6.8.	Fourier amplitude and phase images from phase-resolved OH [*] -chemiluminescence images at excitation frequency f_1	88
6.9.	Fourier amplitude and phase images from phase-resolved OH [*] -chemiluminescence images at excitation frequency f_2	90

7.1.	Reflection coefficients with nozzle and perforated plate for three different temperature levels.	92
7.2.	Experimentally determined acoustic damping rates for two modes without combustion.	93
7.3.	Distribution of the pressure amplitudes, power spectral density and autocorrelation functions with envelope (----) under dry operation.	95
7.4.	Experimentally determined eigenfrequencies and thermoacoustic damping rates under dry operation.	96
7.5.	Distribution of the pressure amplitudes, power spectral density and autocorrelation functions with envelope (----) for water injection at constant equivalence ratio.	98
7.6.	Experimentally determined eigenfrequencies and thermoacoustic damping rates for water injection at constant equivalence ratio.	99
7.7.	Experimentally determined eigenfrequencies for water injection at constant equivalence ratio depending on the adiabatic flame temperature.	100
7.8.	Distribution of the pressure amplitudes, power spectral density and autocorrelation functions with envelope (----) for water injection at constant adiabatic flame temperature for operating range $\textcircled{A} _{T_{ad}}$	102
7.9.	Experimentally determined eigenfrequencies and thermoacoustic damping rates for water injection at constant adiabatic flame temperature.	103
7.10.	Experimentally determined eigenfrequencies and thermoacoustic damping rates for operating range $\textcircled{A} _{T_{ad}}$ using different boundary conditions at the combustor exit.	105
7.11.	Transfer function between integral OH*-chemiluminescence as a marker for unsteady heat release and dynamic pressure for operating point $\textcircled{A} _{T_{ad}}^{\Omega=1.0}$	107
7.12.	Experimentally determined acoustic eigenfrequencies and damping rates for water injection at constant equivalence ratio.	108
7.13.	Experimentally determined acoustic eigenfrequencies and damping rates for water injection at constant equivalence ratio depending on the adiabatic flame temperature.	109

7.14. Experimentally determined acoustic eigenfrequencies and damping rates for water injection at constant adiabatic flame temperature.	110
7.15. Experimentally determined frequency shifts and flame gains for water injection at constant adiabatic flame temperature.	111
7.16. Experimentally determined frequency shifts and flame gains for water injection at constant adiabatic flame temperature depending on the Strouhal number.	112
7.17. Eigenfrequencies and thermoacoustic damping rates for increasing thermal load.	115
8.1. Computational grid used for the CAA simulation: Representation of one quarter of the burner and injector geometry.	118
8.2. FEM-Model with boundary conditions used for the determination of the burner scattering matrix using CAA. . . .	119
8.3. Computational Grid for FEM-Model of the single-burner test-rig with experimentally determined boundary conditions and coupling between plenum and combustor via scattering matrix used for stability analysis.	121
8.4. Normalized root mean square (RMS) values of the flow velocity in the burner centerplane obtained from non-reactive CFD simulations of the flow field.	124
8.5. Normalized temperature field along the combustor centerplane obtained from reactive CFD simulation.	126
8.6. Mean speed of sound obtained from acoustic eigenfrequency for operating range $\textcircled{A} _{T_{ad}}$	127
8.7. Axial gradient of the speed of sound from reactive CFD simulations and scaled to acoustically determined speed of sound at operating point $\textcircled{A} _{T_{ad}}^{\Omega=1.0}$	128
8.8. Scattering matrices of burner with water injector: Comparison between numerical results and experiment.	129
8.9. Calculated mode shapes with water injection at operating point $\textcircled{A} _{T_{ad}}^{\Omega=1.0}$	131

8.10. Amplitude and phase of pressure oscillations in the combustor: Comparison between experiment and numerical simulations based on experimentally determined scattering matrices.	132
8.11. Schematic representation of the simulation cases for eigenvalue studies based on scattering matrices.	134
8.12. Acoustic eigenfrequencies and damping rates under non-reactive conditions: Comparison between experiment and numerical results.	136
8.13. Acoustic eigenfrequencies and damping rates for operating range $\textcircled{A} _{T_{ad}}$: Comparison between experiment and simulation.	137
8.14. Eigenfrequencies and thermoacoustic damping rates for operating range $\textcircled{A} _{T_{ad}}$: Comparison between experiment and numerical results based on experimentally determined scattering matrices.	139
8.15. Experimentally determined flame transfer functions for operating point $\textcircled{A} _{T_{ad}}^{\Omega=1.0}$ and fitted analytical representation.	141
8.16. Eigenfrequencies and thermoacoustic damping rates for operating range $\textcircled{A} _{T_{ad}}$: Comparison between experiment and numerical results based on modeled scattering matrices.	142
8.17. Frequency shifts and flame gains for operating range $\textcircled{A} _{T_{ad}}$: Comparison between experiment and numerical results based on modeled scattering matrices.	143
8.18. Eigenfrequencies and thermoacoustic damping rates for operating range $\textcircled{A} _{T_{ad}}$: Comparison between experiment and numerical results based on modeled and scaled scattering matrices.	145
8.19. Frequency shifts and flame gains for operating range $\textcircled{A} _{T_{ad}}$: Comparison between experiment and numerical results based on modeled and scaled scattering matrices.	146
B.1. Block diagram of the second order oscillator system to generate synthetic time series.	153

B.2.	Numerical validation test cases for a single mode system and multi-mode system: Time series of raw signal, probability density of pressure signal, normalized power spectral density, autocorrelation and envelope of the autocorrelation.	154
B.3.	Numerical validation test case A: Probability densities of the fitting parameters and their corresponding standard deviations and autocorrelation functions.	155
B.4.	Comparison of different numerical validation test cases: Autocorrelation function of the signal, fitted autocorrelation, identified parameters and simulation parameters.	156
B.5.	Evolution of the error for the damping for the identification of one mode and two modes.	158
D.1.	Comparison between frequency shifts, flame gain and flame transfer function for water injection at constant flame temperature.	164
E.1.	Scattering matrices of burner and flame for operating range $\textcircled{A} _{T_{ad}}$, for $\Omega = 0, 1.0$ and 1.2 at constant adiabatic flame temperature.	168
E.2.	Scattering matrices of burner and flame for operating range $\textcircled{A} _{T_{ad}}$, for $\Omega = 1.5, 1.7$ and 2.0 at constant adiabatic flame temperature.	169

List of Tables

5.1. Overview on the operating parameters of the dry baseline operating conditions.	64
6.1. Overview on operating parameters used to record phase-resolved OH*-chemiluminescence images.	87
7.1. Control parameters for three methods to increase the thermal load of the combustor.	114
B.1. Overview of numerical validation cases for the statistical identification of damping rates from the autocorrelation function.	154
C.1. Overview on the operating conditions with water injection on the basis of operating point ④.	159
C.2. Overview on the operating conditions with water injection on the basis of operating point ⑤.	160
C.3. Overview on the operating conditions with water injection on the basis of operating point ⑥.	160
C.4. Overview on the operating conditions with water injection on the basis of operating point ⑦.	161

Nomenclature

Latin Letters

A	[m ³]	Surface area
\mathcal{A}	[Pa]	Amplitude of modal pressure
A_f	[%]	Ratio of free axial cross-sectional area
$\underline{\underline{\mathbf{A}}}_i, \underline{\underline{\mathbf{C}}}$	[–]	Convective matrices
A_n	[–]	Scaled amplitude
b_s	[m]	Slot width
c	[m/s]	Speed of sound
c_p	[J/(kgK)]	Isobaric specific heat capacity
d	[m]	Diameter
d_{32}	[m]	Sauter mean diameter
$\underline{\underline{\mathbf{E}}}$	[–]	Mass matrix
f	[1/s]	Frequency
\hat{f}	[m/s]	Riemann invariant
f_n	[1/s]	Eigenfrequency of the n -th mode
\hat{f}^s	[–]	Source term vector
\overline{f}_s	[m/s]	Noise source term of the flame
\hat{g}	[m/s]	Riemann invariant
g_s	[m/s]	Noise source term of the flame
h	[J/kg]	Specific enthalpy
$\underline{\underline{\mathbf{H}}}$	[–]	Coefficient matrix
h_∞	[W/(m ² K)]	Heat transfer coefficient
h_n	[m]	Grid element height
i	[–]	Imaginary unit
$\underline{\underline{\mathbf{I}}}$	[–]	Identity matrix
I	[–]	Intensity
k	[1/m]	Wave number
$\underline{\underline{\mathbf{K}}}$	[–]	Stiffness matrix
k_{xx}	[–]	Autocorrelation function
l	[m]	Length

Nomenclature

L	[–]	Boundary condition vector
\dot{m}	[kg/s]	Mass flow
n_i	[–]	Surface normal vector
n_T	[–]	Number of oscillation cycles
p	[Pa]	Pressure
P_{th}	[W]	Thermal power
\dot{Q}	[W]	Heat release rate
\dot{q}_V	[W/m ³]	Volumetric heat release rate
R	[–]	Reflection coefficient
$R^{+/-}$	[–]	Reflection coefficients of the scattering matrix
\mathbb{R}	[J/(kg K)]	Specific gas constant
$\underline{\underline{\mathbf{S}}}$	[–]	Scattering matrix
s	[–]	Laplace variable
S_{xx}	[W/s]	Power spectral density
t	[s]	Time
$T^{+/-}$	[–]	Transmission coefficients of the scattering matrix
$\underline{\underline{\mathbf{T}}}$	[–]	Transfer matrix
$\underline{\underline{\mathcal{T}}}$	[–]	Stabilization matrix
T_{ad}	[K]	Adiabatic flame temperature
u	[m/s]	Velocity component in x direction
v	[m/s]	Velocity component in y direction
V	[m ³]	Volume
w	[m/s]	Velocity component in z direction
\underline{w}	[–]	Weighting function
x	[m]	Spatial coordinate
\underline{x}	[–]	Solution vector for least-squares minimization
y	[m]	Spatial coordinate
y_n	[–]	Observation vector
z	[m]	Spatial coordinate
Z	[–]	Impedance

Greek Letters

α	[rad/s]	Acoustic damping rate
α_τ	[–]	Stabilization parameter
β	[rad/s]	Flame gain

χ	[Pa/s]	Stochastic noise source term
ϵ	[–]	Relative error
η	[Pa]	Modal pressure amplitude
γ	[–]	Isentropic exponent
Γ	[Pa ² /s]	Noise intensity
H_{xy}	[–]	Transfer function
κ	[1/(s Pa ²)]	Non-linear saturation coefficient
λ	[m]	Wavelength
μ	[Pa s]	Dynamic viscosity
ν	[rad/s]	Thermoacoustic damping rate
ω	[rad/s]	Angular frequency
$\underline{\underline{\Omega}}$	[–]	Coordinate transformation matrix
$\underline{\Omega}$	[–]	Water-to-fuel ratio
ω_n	[rad/s]	Angular eigenfrequency
Ψ	[–]	Mode shape
φ	[rad]	Phase angle
$\underline{\Phi}$	[–]	Vector containing the acoustic quantities
φ	[–]	Ratio of specific impedances
ϕ	[–]	Equivalence ratio
ρ	[kg/m ³]	Density
τ	[s]	Time lag
θ	[–]	Temperature ratio
τ_{ij}	[Pa]	Reynolds stress tensor
ξ	[Pa/s]	Stochastic noise source term

Superscripts

$(\dots)'$	Perturbation
$(\overline{\dots})$	Mean value
$(\hat{\dots})$	Fourier transformed
$(\dots)^A$	Forcing location upstream
$(\dots)^B$	Forcing location downstream
$(\dots)^{fg}$	<i>fg</i> -Notation of a matrix
$(\dots)^\dagger$	Pseudo-inverse
$(\dots)^{pu}$	<i>pu</i> -Notation of a matrix

$(\dots)^T$ Transposed

Subscripts

$(\dots)_0$ Reference state
 $(\dots)_{11}$ Order of transfer matrix element
 $(\dots)_{12}$ Order of transfer matrix element
 $(\dots)_{21}$ Order of transfer matrix element
 $(\dots)_{22}$ Order of transfer matrix element
 $(\dots)_{ac}$ Acoustic
 $(\dots)_{at}$ Atomization
 $(\dots)_B$ Burner
 $(\dots)_{BF}$ Burner and flame
 $(\dots)_c$ Cold
 $(\dots)_{CC}$ Combustion chamber
 $(\dots)_{cut}$ Cut-on
 $(\dots)_{ds}$ Downstream
 $(\dots)_{exp}$ Experimental
 $(\dots)_F$ Flame
 $(\dots)_f$ Forcing
 $(\dots)_h$ Hot
 $(\dots)_{in}$ Inlet
 $(\dots)_L$ Longitudinal
 $(\dots)_{max}$ Maximum
 $(\dots)_{min}$ Minimum
 $(\dots)_{mod}$ Modeled
 $(\dots)_{MT}$ Mixing tube
 $(\dots)_{OH^*}$ OH*-chemiluminescence
 $(\dots)_{out}$ Outlet
 $(\dots)_P$ Plenum
 $(\dots)_{ph}$ Preheat
 $(\dots)_R$ Recording
 $(\dots)_{sim}$ Simulated
 $(\dots)_T$ Transverse
 $(\dots)_{ta}$ Thermoacoustic
 $(\dots)_{us}$ Upstream

$(\dots)_{VB}$ Vortex-breakdown

Operators

\mathcal{D} Computational domain
 d_{ij} Kronecker delta
 \mathcal{F} Fourier coefficient
 $\underline{\mathcal{L}}$ Differential operator of the LEE
 \mathcal{O} Order of magnitude
 \mathcal{P} Transition kernel
 P Probability distribution
 Π Target distribution
 q^* Proposal distribution
 \mathcal{R} Residual error
 σ Standard deviation

Dimensionless Numbers

Ma Mach number
 Pe Peclet number
 Str Strouhal number

Acronyms

CAA Computational aero-acoustics
 CFD Computational fluid dynamics
 CTA Constant temperature anemometry
 DLN Dry-low-NO_x
 FEM Finite element method
 FFT Fast fourier transform
 FGM Flamelet generated manifold
 FTF Flame transfer function
 FVM Finite volume method
 GLS Galerkin/least-squares

LEE	Linearized Euler equations
MCMC	Markov-chain Monte-Carlo
MMM	Multi-microphone method
MUMPS	Multifrontal massively parallel sparse
NSE	Navier Stokes equations
PDE	Partial differential equation
PDF	Probability density function
PSD	Power spectral density
RANS	Reynolds averaged Navier Stokes
RMS	Root mean square
SMD	Sauter mean diameter
TM	Transfer matrix
TMM	Two-microphone method

1 Introduction

In the western industrialized countries, particularly in Germany, the phasing-out of nuclear power and the abandonment of fossil fuels have been successively promoted over the last few decades [64]. In the long term, this means the gradual transition from conventional energy sources to renewables. As a result, a major part of the stable base load supplies are to be discontinued, which in turn increases the dependency on natural factors such as wind or sun. Therefore, there is an ever-growing demand for expanding the operational windows of existing, conventional power plants both towards part load operation as well as to absorb short-term peak loads. Gas turbine power stations serve as an important bridging technology since they offer short start-up times and a broad operating range. However, with regard to short-term load increase, compliance with emission regulations is compulsory. Options such as increasing the operating temperature are usually unsuitable since they lead to raised formation of nitrogen oxides (NO_x) [87]. That means, one strives especially for retrofittable techniques to increase the overall power output of stationary gas turbines without causing drawbacks in pollutant formation. One promising option fulfilling these requirements is to improve the electrical power output of the overall gas turbine process by adding steam or water to the reactants. The particular technical challenge is the compatibility of water injection with premixed combustion systems.

1.1. Steam- and Water Injection in Gas Turbines

Historically, the use of liquid water or steam has already been proposed in the early 1960s and was a frequently used method for the reduction of NO_x emissions in gas turbines up to the middle of the 1990s. However, the importance of water or steam injection for emission control of gas turbines is decreasing. A comprehensive review on technical applica-

tions of water injection in gas turbine processes is given by Jonsson and Yan [78]. Pioneering work regarding fundamentals of water addition to flames has been carried out by Dryer [40]. Especially for non-premixed kerosene flames, the use of fuel-water emulsions was almost indispensable to reduce the formation of thermal NO_x [89]. Furthermore, water injection is applicable for a (short-term) boost of the thrust of aircraft engines, since the increase of the mass flow raises the overall power output of the turbine [101, 160]. However, since lean premixed combustion has established as a standard technology in stationary gas turbines, water injection is no longer mandatory to comply with emission regulations. In contrast to conventional diffusion combustors, premixed combustors require that the entire compressor air is premixed with fuel before reaching the reaction zone. Using high amounts of excess air with a homogeneous mixture of the reactants allows to operate with significantly reduced peak flame temperatures, leading to a lower formation of thermal NO_x . Combustors achieving the emission targets without water injection are therefore often referred to as Dry-Low NO_x (DLN) combustors.

Nevertheless, steam- and water injection have experienced a recent upsurge in interest by offering a promising technology for power augmentation without causing drawbacks regarding pollutant formation. Although water injection basically lowers the total efficiency of the gas turbine process [87], it offers a high potential for short-term load increase without increasing the turbine inlet temperature significantly. In particular, the energy required for the evaporation of the liquid water droplets serves as a heat sink in the flame which initially causes a drop of the flame temperature. This effect is counteracted by simultaneously increasing the fuel mass flow rate to keep the flame temperature constant. Thus, the thermal power of the flame can be raised while leaving the flame temperature approximately constant. The associated increase of the overall mass flow through the turbine causes a further rise of the electrical power output.

In the past, most of the studies on premixed combustion at high humidity levels have focused on steam diluted combustion [18, 67, 78], whereas fundamental studies were mainly subjected to flame speeds and emission formation [86, 100]. The stable operation of a premixed flame in a gas turbine combustor using excessive amounts of steam was demonstrated for example by Göke [60]. Studies on liquid water being directly injected

into a lean premixed combustor under gas turbine like conditions have recently been presented by Lellek et al. [90–92].

1.2. Thermoacoustic Instabilities

Despite of offering favorable properties with regard to emissions, lean premixed combustors are more prone to thermoacoustic instabilities [87,89,97]. In the context of gas turbine combustion, the term *Thermoacoustics* means the interaction between unsteady heat release of the flame and the acoustic field in the combustor [97]. Depending on the phasing between fluctuating heat release (\dot{q}') and sound pressure (p'), a periodic thermodynamic process establishes which can either produce or consume work. In this regard, work appears in the form of acoustic energy which is fed into the acoustic field when the phase shift is less than 90° . This necessary condition is known as the Rayleigh criterion [129]:

$$\oint p' \dot{q}' dt > 0. \quad (1.1)$$

If the Rayleigh criterion is positive, self-excited oscillations may develop and the combustor operates in a thermoacoustically unstable region. This condition, however, is not sufficient; rather, instability requires that the driving forces of the flame exceed the acoustic losses in the combustion chamber. If both applies, a net gain of acoustic energy occurs and oscillations grow over time. This is manifested by excessive pulsations of the combustor pressure and may lead to flame blowout, increased pollutant formation or in the worst case to severe damage of the hardware [97]. These oscillations appear as thermoacoustic modes at distinct eigenfrequencies of the entire system and may be classified into the following categories which are relevant in gas turbine combustors:

1. **Longitudinal modes:** One of the most frequently studied oscillation types in gas turbine combustors are longitudinal modes. Their characteristic eigenfrequencies are usually of the order of several hundreds of Hertz. Wave propagation is commonly treated as one-dimensional and acoustic compactness¹ of the flame can be assumed. In gas tur-

¹Acoustic compactness: If the geometric dimensions of an acoustic element are much shorter than the acoustic wavelength at a particular frequency, the element can be considered as acoustically compact.

bines, strong acceleration of the flow after the combustor causes reflection of acoustic waves at the combustor outlet. Thus, longitudinal modes often occur as standing waves in the combustion chamber. In addition, so-called Helmholtz modes may occur which are often approximated by the analogy that plenum, burner and combustor function as a Helmholtz resonator resulting in a quasi zero-dimensional pressure field in the combustion chamber. [28, 154, 155].

2. **Azimuthal modes:** In annular combustors, circumferential modes can occur at the azimuthal eigenfrequencies. The frequencies are of a similar order of magnitude as the longitudinal modes. Acoustic wave propagation can be described by a combination of one and two-dimensional approaches (see e.g. [49]), while acoustic compactness of the flame is mostly presumed.
3. **High frequency oscillations:** High frequency modes may occur above the cut-on frequency of the first transverse eigenfrequencies. The resulting pressure field is multi-dimensional with gradients in multiple directions. In this case, acoustic compactness cannot be assumed (see e.g. [113]).

Note that this classification applies to narrow combustion chambers for which the length-to-height ratio is considerably larger than 1, i.e. $l_{cc}/h_{cc} \gg 1$. Furthermore, mixed modes may occur since their characteristic frequency ranges can overlap e.g. due to the occurrence of higher-order modes. In the scope of this work, longitudinal modes will be investigated. The most dominant driving mechanisms for oscillations in this frequency range are fluctuations of the equivalence ratio or the mass flow at the burner outlet. This results in a fluctuating flame volume and therefore causes a periodically oscillating heat release. A comprehensive overview on phenomenology and mechanisms causing combustion instabilities can be found in [27, 41]. The acoustic properties of the burner are often described by using burner transfer matrices (BTM). These may be obtained experimentally [7, 52, 116], from one-dimensional network models [11, 13] or from numerical simulations using a hybrid approach by combining computational fluid dynamics (CFD) and computational aero-acoustics (CAA) [58, 163]. Many common approaches seek to describe the flame dynamics by means of flame transfer functions (FTF)

which relate the unsteady heat release of the flame with fluctuations of the acoustic velocity at the burner outlet. This concept relies on the premise that the dynamic response of premixed natural gas flames can be determined in a much simpler test environment than in a full-scale combustor [140,143,144]. Flame transfer functions may be obtained from experiments [7,14,140,142,144] or from numerical simulations [31,79,153]. With regard to wet premixed combustion, data on thermoacoustic properties is only available with steam injection [61,138,139]. The representation of flame dynamics by means of the FTF allows to predict the thermoacoustic stability of an entire combustion system. For this purpose, the use of network models is widespread [136,137] while also solvers relying on the finite element method (FEM) have recently gained in importance [25,26,56] because of their ability to handle even non-compact high frequency oscillations [73,75,76,146]. In particular, prediction of the eigenfrequencies of a combustor and a quantification of the stability margin is of major interest. Results from stability analyses of technically relevant combustion systems have mostly only been validated qualitatively in the past. Quantitative validations of the predicted damping rates by using measurement data are rare [152,162]. One reason for this is the lack of practicable and robust methods for the experimental determination of damping rates in gas turbine combustors. In the past, there have been isolated studies [103,118] which suggest that water injection promotes higher pressure pulsations in a combustor than steam. However, there were neither studies on the thermoacoustic properties of combustion chambers with water injection, nor did suitable analysis tools exist for predicting the thermoacoustic stability of such combustion systems. The present work is the first to report on the influence of water injection on flame dynamics and the thermoacoustic stability margin in lean-premixed combustors.

1.3. Goal and Structure of this Work

This work is focused on providing a sound basis for understanding and characterizing thermoacoustic phenomena in lean premixed gas turbine combustors with water injection. The aim is to exploit these findings to provide quantitatively validated tools for the prediction of thermoacoustic

instabilities. Particular attention is placed on excessive water injection to increase the thermal load at a constant flame temperature level. This thesis is subdivided into an experimental and a numerical part, while the measurements serve to validate the simulation results. For this purpose, an existing modular burner system is equipped with a water injection system which supplies a finely atomized spray of liquid water directly to the main combustion zone. This set-up allows to conduct experimental work pursuing the following objectives:

1. To provide a phenomenological description of the thermoacoustic effects occurring when premixed flames interact with liquid water droplets.
2. To characterize the flame dynamics over a wide range of operating conditions and water injection rates.
3. To quantify the impact of water injection on the stability margin and thus to validate the results of the numerical predictions.

The strategy pursued is to divide the system into its single components like flame, burner and combustor and determining their frequency dependent acoustic properties from experiments over a wide range of operating conditions. Particular attention is given to the scalability of the flame transfer functions depending on adiabatic flame temperature and flame position. This refers to the first two points mentioned above. Regarding the third point, a widely applicable output-only identification technique is developed within the scope of this work, which allows to quantify the stability margin of the combustor depending on varying operating parameters. This approach allows to identify the impact of water injection on the pure flame driving by separating the acoustic dissipation from the thermoacoustic damping and thus identifying the impact of water injection on these quantities.

The numerical part of this work introduces a unified simulation framework with the following features:

1. To calculate the acoustic scattering behavior of the modified burner geometry without the need for experimental input data.

2. To provide an experimentally validated and extendable tool to predict thermoacoustic oscillations in gas turbine combustors with water injection.

A three-dimensional FEM based approach is chosen to meet the above mentioned requirements. The acoustic scattering behavior of the burner is calculated using a combined CFD/CAA approach by solving the linearized Euler equations (LEE). This refers to the first mentioned point. Thermoacoustic modes and their damping rates are calculated using numerical stability analyses based on a spatial FEM discretized solution of the Helmholtz equations. Burner impedance and flame dynamics are incorporated from measured and simulated scattering matrices. Finally, it is shown that these parameters can be robustly predicted for flames with water injection by taking into account the acoustic properties of the burner and the experimentally determined FTFs. The results of the numerical simulations are validated quantitatively by using the generated experimental database.

This thesis is organized as follows: Chapter 2 starts with the mathematical description of mean flow quantities and wave propagation in gas turbine combustors in general and introduces strategies to solve the governing equations. This chapter also encompasses a brief introduction to Bayesian statistics and highlights its use for solving non-linear optimization problems. The employed measurement techniques and system identification methods are presented in Chapter 3. Besides established measuring methods, particular attention is paid to the newly developed statistical method to determine the damping rates of the combustor. Chapter 4 introduces the atmospheric single-burner test-rig including the modular swirl burner system with water injector. Visualization of the stationary flame- and flow properties by optical measurements is provided in Chapter 5 by placing special emphasis on the differences between dry and water injected operating conditions. Experimental results are presented in Chapters 6 and 7. Chapter 6 presents the dynamic properties of the given combustion system. In this context, dry conditions are compared against water injected operation using scattering matrices, flame transfer functions and source terms. Insight into the spatial distribution of the flame response is given by means of phase-locked OH^* -chemiluminescence imaging. Experimentally determined (thermo-)acoustic damping rates which were obtained

by applying the newly developed identification method are discussed in Chapter 7. Finally, a FEM model of the entire combustion test-rig is introduced in Chapter 8. This chapter is divided into two parts: The first part encompasses the calculation of acoustic scattering matrices of the burner. The second part deals with the prediction of the combustor damping with water injection by means of numerical stability analyses.

2 Theoretical Background

This chapter presents the theoretical framework of this thesis to analyze the thermoacoustic properties of lean premixed flames with water injection in respect of predicting combustion instabilities. First, the governing equations to describe mean flow as well as acoustic wave propagation are derived from the conservation of mass, energy and momentum. Network models as well as methods based on the calculation of three-dimensional acoustic fields using the finite element methods (FEM) are introduced as a way to describe acoustic wave propagation in combustion systems. Furthermore, flame transfer functions (FTF) are introduced which are commonly used to represent the dynamic response of a flame. Acoustic and thermoacoustic damping are derived using an approach to describe the modal dynamics in a combustor as a second order, harmonic oscillator. Against the background of identifying thermoacoustic damping rates from measurement data, an introduction to solution methods for non-linear optimization problems is given with particular emphasis on Bayesian methods for parameter identification.

2.1. Governing Equations

2.1.1. Linearized Euler Equations (LEE)

The macroscopic transport properties of a compressible flow in time and space are generally described by the conservation equations for mass (2.1), momentum (2.2) and energy (2.3) [158]:

$$\frac{\partial \rho}{\partial t} + \frac{\partial \rho u_i}{\partial x_i} = 0 \quad (2.1)$$

$$\frac{\partial u_i}{\partial t} + u_j \frac{\partial u_i}{\partial x_j} + \frac{1}{\rho} \frac{\partial p}{\partial x_i} = \frac{\partial \tau_{ij}}{\partial x_j} \quad (2.2)$$

$$\frac{\partial p}{\partial t} + u_i \frac{\partial p}{\partial x_i} + p \gamma \frac{\partial u_i}{\partial x_i} = (\gamma - 1) \dot{q}_V + (\gamma - 1) \tau_{ij} \frac{\partial u_i}{\partial x_j}. \quad (2.3)$$

This set of equations is often referred to as Navier-Stokes equations (NSE). Herein, p refers to the pressure, ρ is the density, u_i the velocity field defined in the cartesian coordinates x_i , γ is the ratio of specific heats and \dot{q}_V is a source of volumetric heat. Viscous stress is described by the stress tensor τ_{ij} :

$$\tau_{ij} = \mu \left(\frac{\partial u_i}{\partial x_j} + \frac{\partial u_j}{\partial x_i} - \frac{2}{3} \frac{\partial u_k}{\partial x_k} \delta_{ij} \right), \quad (2.4)$$

where δ_{ij} denotes the Kronecker delta and μ is the viscous stress.

It is furthermore assumed that the quantities density, velocity, pressure and heat release rate consist of a spatially varying mean quantity ($\bar{\cdot}$) with a superimposed fluctuating part (\cdot') being significantly smaller than its mean value. With regard to velocity, this refers to the speed of sound c . Due to this smallness assumption, products of the fluctuating parts cancel out and thus the instantaneous values of ρ , p , u_i and \dot{q}_V can be expressed as follows:

$$\rho = \bar{\rho} + \rho' \quad (2.5)$$

$$p = \bar{p} + p' \quad (2.6)$$

$$u = \bar{u} + u' \quad (2.7)$$

$$\dot{q}_V = \bar{\dot{q}}_V + \dot{q}'_V. \quad (2.8)$$

As pointed out by Gikadi et al. [57], dissipation effects described by the NSEs play a subordinate role when considering propagation of longitudinal plane waves in combustors. Therefore, neglecting viscous stress ($\mu = 0$) and inserting the linearization conditions (2.5-2.8) into Equations (2.1-2.3) yields the linearized Euler equations (LEE):

$$\frac{\partial \rho'}{\partial t} + \bar{u}_i \frac{\partial \rho'}{\partial x_i} + u'_i \frac{\partial \bar{\rho}}{\partial x_i} + \bar{\rho} \frac{\partial u'_i}{\partial x_i} + \rho' \frac{\partial \bar{u}_i}{\partial x_i} = 0 \quad (2.9)$$

$$\frac{\partial u'_i}{\partial t} + \bar{u}_j \frac{\partial u'_i}{\partial x_j} + u'_j \frac{\partial \bar{u}_i}{\partial x_j} + \frac{1}{\bar{\rho}} \frac{\partial p'}{\partial x_i} + \frac{\rho'}{\bar{\rho}} \bar{u}_j \frac{\partial \bar{u}_i}{\partial x_j} = 0. \quad (2.10)$$

$$\frac{\partial p'}{\partial t} + u'_i \frac{\partial \bar{p}}{\partial x_i} + \bar{u}_i \frac{\partial p'}{\partial x_i} + \gamma \left(\bar{p} \frac{\partial u'_i}{\partial x_i} + p' \frac{\partial \bar{u}_i}{\partial x_i} \right) = (\gamma - 1) \dot{q}'_V \quad (2.11)$$

The LEEs (2.9-2.11) describe the formation and transport of small disturbances in a moving medium. These can either originate from acoustics waves, from entropy waver or from vorticity fluctuations. While acoustic

perturbations propagate with the speed of sound, vorticity and entropy modes are transported convectively with the velocity of the respective mean flow field. Due to their unsteady nature, time-resolved simulations of Equations (2.9-2.11) may lead to enormous computational effort for systems with a large number of degrees of freedom. Additionally, unwanted growth of unstable waves may encounter, such as Kelvin-Helmholtz instabilities [4]. A suitable approach to circumvent these difficulties is to reformulate the set of equations in the frequency domain by assuming the time-dependent quantities ρ , p , u and \dot{q}_V to be harmonic functions:

$$\rho'(x_i, t) = \hat{\rho}_i(x_i) \exp(i\omega t) \quad (2.12)$$

$$p'(x_i, t) = \hat{p}_i(x_i) \exp(i\omega t) \quad (2.13)$$

$$u'_i(x_i, t) = \hat{u}_i(x_i) \exp(i\omega t) \quad (2.14)$$

$$\dot{q}'_V(x_i, t) = \hat{q}'_V(x_i) \exp(i\omega t). \quad (2.15)$$

Herein, $(\hat{\dots})$ denotes the complex Fourier coefficient of the respective quantity oscillating harmonically at a specific angular frequency $\omega = 2\pi f$. Inserting relationships (2.12-2.15) into the LEEs in time domain (2.9-2.11) leads to the LEEs in frequency space:

$$i\omega \hat{\rho} + \bar{u}_i \frac{\partial \hat{\rho}}{\partial x_i} + \hat{u}_i \frac{\partial \bar{\rho}}{\partial x_i} + \bar{\rho} \frac{\partial \hat{u}_i}{\partial x_i} + \hat{\rho} \frac{\partial \bar{u}_i}{\partial x_i} = 0 \quad (2.16)$$

$$i\omega \hat{u}_i + \bar{u}_j \frac{\partial \hat{u}_i}{\partial x_j} + \hat{u}_j \frac{\partial \bar{u}_i}{\partial x_j} + \frac{1}{\bar{\rho}} \frac{\partial \hat{p}}{\partial x_i} + \frac{\hat{\rho}}{\bar{\rho}} \bar{u}_j \frac{\partial \bar{u}_i}{\partial x_j} = 0 \quad (2.17)$$

$$i\omega \hat{p} + \bar{u}_i \frac{\partial \hat{p}}{\partial x_i} + \hat{u}_i \frac{\partial \bar{p}}{\partial x_i} + \gamma \left(\bar{p} \frac{\partial \hat{u}_i}{\partial x_i} + \hat{p} \frac{\partial \bar{u}_i}{\partial x_i} \right) = (\gamma - 1) \hat{q}'_V \quad (2.18)$$

2.1.2. Wave Equation

A substantially simplified form of the LEEs which finds frequent application in describing acoustic wave propagation in combustors is obtained by neglecting velocity gradients ($\partial \bar{u}_i / \partial x_i = 0$). Furthermore, when assuming isentropicity which gives a linear relationship between acoustic pressure and density, i.e. [130]:

$$\rho' = p' / c^2, \quad (2.19)$$

the LEEs (2.16-2.18) simplify to the following set of equations, formulated in the time domain:

$$\frac{\partial p'}{\partial t} + \bar{u}_i \frac{\partial p'}{\partial x_i} + \bar{\rho} c^2 \frac{\partial u'_i}{\partial x_i} = (\gamma - 1) \dot{q}'_V \quad (2.20)$$

$$\frac{\partial u'_i}{\partial t} + \bar{u}_j \frac{\partial u'_i}{\partial x_j} + \frac{1}{\bar{\rho}} \frac{\partial p'}{\partial x_i} = 0 \quad (2.21)$$

Transformation of Equations (2.20-2.21) into the frequency domain by expressing acoustic pressure and velocity by their Fourier coefficient (Equations 2.12-2.15) yields:

$$i\omega \hat{p} + \bar{u}_i \frac{\partial \hat{p}}{\partial x_i} + \bar{\rho} c^2 \frac{\partial \hat{u}_i}{\partial x_i} = (\gamma - 1) \hat{q}'_V. \quad (2.22)$$

$$i\omega \hat{u}_i + \bar{u}_j \frac{\partial \hat{u}_i}{\partial x_j} + \frac{1}{\bar{\rho}} \frac{\partial \hat{p}}{\partial x_i} = 0. \quad (2.23)$$

Subtraction of the spatial derivative of Equation (2.21) from the temporal derivative of Equation (2.20) results in the convective wave equation which can be expressed either in the time domain:

$$\frac{1}{c^2} \left(\frac{\partial}{\partial t} + \bar{u}_i \frac{\partial}{\partial x_i} \right)^2 p' - \frac{\partial^2 p'}{\partial x_i^2} = \frac{\gamma - 1}{c^2} \frac{\partial \dot{q}'_V}{\partial t}, \quad (2.24)$$

or in the frequency domain:

$$\frac{1}{c^2} \left(i\omega + \bar{u}_i \frac{\partial}{\partial x_i} \right)^2 \hat{p} - \frac{\partial^2 \hat{p}}{\partial x_i^2} = \frac{\gamma - 1}{c^2} i\omega \hat{q}'_V. \quad (2.25)$$

In gas turbine combustors often the mean flow Mach number $Ma = \bar{u}_i / c$ is low with respect to the ratio between the flame thickness l_F and the characteristic wavelength λ of the oscillation frequency [107]. Inserting this assumption by setting the mean flow velocities to zero ($\bar{u}_i = 0$), Equation (2.24) and Equation (2.25) reduce to the inhomogeneous Helmholtz equation, which can either be formulated in the time domain, according to:

$$\frac{1}{c^2} \frac{\partial^2 p'}{\partial t^2} - \frac{\partial^2 p'}{\partial x_i^2} = \frac{\gamma - 1}{c^2} \frac{\partial \dot{q}'_V}{\partial t}, \quad (2.26)$$

or in frequency space:

$$\frac{(i\omega)^2}{c^2}\hat{p} - \frac{\partial^2 \hat{p}}{\partial x_i^2} = \frac{\gamma - 1}{c^2}i\omega\hat{q}_V. \quad (2.27)$$

2.1.3. Analytical Solution of the Wave Equation

To obtain a compact analytical solution for the convective wave equation (2.24), the heat release source term ($\dot{q}_V = 0$) is neglected and a uniform temperature distribution is assumed. Considering wave propagation along the x direction only yields the transport equation for plane waves in a moving medium, according to:

$$\left(\frac{1}{c^2} \left(\frac{\partial}{\partial t} + \bar{u} \frac{\partial}{\partial x} \right)^2 - \frac{\partial^2}{\partial x^2} \right) p' = 0. \quad (2.28)$$

Inserting the harmonic ansatz according to Equation (2.13), the acoustic pressure can be expressed in the frequency space:

$$p' = \hat{p} \exp \left(i\omega \left(t - \frac{x}{c} \right) \right). \quad (2.29)$$

By introducing the convective wave number $k = \omega/c$ and inserting Equation (2.29) into the Equation (2.28) yields the following quadratic equation:

$$((i\omega + \bar{u}k)^2 - c^2k^2) p' = 0, \quad (2.30)$$

for which two solutions for k can be found:

$$k^\pm = \frac{\pm\omega}{c \mp \bar{u}}. \quad (2.31)$$

By inserting Equation (2.31) into Equation (2.30) gives a linear combination of both solutions:

$$p'(x, t) = C_1 \exp(i\omega t + k^+ x) + C_2 \exp(i\omega t + k^- x). \quad (2.32)$$

Herein, C_1 and C_2 are frequency dependent integration constants resulting from initial values and boundary conditions. Inserting the analytical solutions k for Equation (2.30) then leads to:

$$u' = \frac{1}{\rho c} C_2(\omega) \exp(i\omega t + k^- x) - \frac{1}{\bar{\rho} c} C_1(\omega) \exp(i\omega t + k^+ x). \quad (2.33)$$

By introducing the Riemann variants \hat{f} and \hat{g} , acoustic pressure and velocity can be expressed as follows:

$$p'(x, t) = \bar{\rho}c \left(f \exp(i\omega t + k^+ x) + g \exp(i\omega t + k^- x) \right) \quad (2.34)$$

$$u'(x, t) = \left(\underbrace{f \exp(i\omega t + k^+ x)}_{\hat{f}} - \underbrace{g \exp(i\omega t + k^- x)}_{\hat{g}} \right). \quad (2.35)$$

These can be interpreted as two waves traveling in the positive (\hat{f}) and the negative (\hat{g}) flow direction, respectively. Considering a straight duct, and assuming loss-less propagation of plane waves, the relationship of the up- and downstream traveling waves \hat{f} and \hat{g} between two locations x_1 and x_2 can be expressed in a convenient way in the matrix notation:

$$\begin{bmatrix} \hat{f} \\ \hat{g} \end{bmatrix}_{x_2} = \underbrace{\begin{bmatrix} \exp(k^- \Delta x_{12}) & 0 \\ 0 & \exp(k^+ \Delta x_{12}) \end{bmatrix}}_{\underline{\underline{\mathbf{T}^{\text{fg}}}}} \begin{bmatrix} \hat{f} \\ \hat{g} \end{bmatrix}_{x_1}. \quad (2.36)$$

Here, $\underline{\underline{\mathbf{T}^{\text{fg}}}}$ represents the simplest form of a transfer matrix, namely the time lag between two axial positions x_1 and x_2 .

2.2. Low-Order Network Modeling

Originally known from electrical engineering, low-order network models are widely used for describing and analyzing wave propagation in acoustic systems [105, 106]. Their main advantage is that, under certain conditions, complex acoustic systems can be described by a few known elements leading to a low-order representation. The basic principle of this method is to subdivide such a complex system into multiple, separately treatable components with known acoustic properties. The acoustic scattering behavior of each of these components is represented by an acoustic two-port, having each two inputs and two outputs. Low-order network models are a commonly used way to represent the acoustic properties of gas turbines combustors [38, 144] with the aim to predict thermoacoustic instabilities [136, 137].

Acoustic two-ports are often represented by a transfer matrix which links the acoustic state variables between a position upstream (x_u) and downstream (x_d) of the respective element [105]. In principle, the frequency-dependent acoustic properties of any acoustic element can be expressed by an acoustic transfer matrix. Some very simple elements such as straight ducts, area jumps, joints and forks may be represented by analytical descriptions [52, 122]. In principle, an arbitrary acoustic element may be integrated into a network model by its acoustic transfer matrix obtained from measurements or numerical simulations. A general definition of a transfer matrix is given by:

$$\begin{bmatrix} \widehat{f} \\ \widehat{g} \end{bmatrix}_d = \underbrace{\begin{bmatrix} \text{TM}_{11} & \text{TM}_{12} \\ \text{TM}_{21} & \text{TM}_{22} \end{bmatrix}}_{\underline{\underline{\mathbf{T}^{\text{fg}}}}} \begin{bmatrix} \widehat{f} \\ \widehat{g} \end{bmatrix}_u. \quad (2.37)$$

The transfer matrix notation implies that both state vectors appear separately for each reference location. Instead of linking the Riemann variants to each other, the transfer matrix can be rearranged to couple acoustic pressure \widehat{p} and velocity \widehat{u} between two reference planes upstream and downstream:

$$\begin{bmatrix} \frac{\widehat{p}}{\rho c} \\ \widehat{u} \end{bmatrix}_d = \underbrace{\begin{bmatrix} \text{TM}_{11} & \text{TM}_{12} \\ \text{TM}_{21} & \text{TM}_{22} \end{bmatrix}}_{\underline{\underline{\mathbf{T}^{\text{pu}}}}} \begin{bmatrix} \frac{\widehat{p}}{\rho c} \\ \widehat{u} \end{bmatrix}_u. \quad (2.38)$$

The transfer matrices (2.37) and (2.38) can be converted into one another by a linear coordinate transformation [52]:

$$\underline{\underline{\mathbf{T}^{\text{pu}}}} = \underline{\underline{\mathbf{\Omega}}} \cdot \underline{\underline{\mathbf{T}^{\text{fg}}}} \cdot \underline{\underline{\mathbf{\Omega}}}^{-1} \quad (2.39)$$

$$\underline{\underline{\mathbf{T}^{\text{fg}}}} = \underline{\underline{\mathbf{\Omega}}}^{-1} \cdot \underline{\underline{\mathbf{T}^{\text{pu}}}} \cdot \underline{\underline{\mathbf{\Omega}}}, \quad (2.40)$$

$$(2.41)$$

and using the transformation matrix:

$$\underline{\underline{\mathbf{\Omega}}} = \begin{bmatrix} 1 & 1 \\ 1 & -1 \end{bmatrix}. \quad (2.42)$$

Another common representation is given by the scattering matrix, which is defined as follows:

$$\begin{bmatrix} \widehat{f}_d \\ \widehat{g}_u \end{bmatrix} = \underbrace{\begin{bmatrix} T^+ & R^- \\ R^+ & T^- \end{bmatrix}}_{\underline{\underline{\mathbf{S}}}^{\text{fg}}} \begin{bmatrix} \widehat{f}_u \\ \widehat{g}_d \end{bmatrix}. \quad (2.43)$$

Therein, the matrix elements represent the complex reflection (R^+ , R^-) and transmission coefficients (T^+ , T^-). Transformation between $\underline{\underline{\mathbf{S}}}^{\text{fg}}$ and $\underline{\underline{\mathbf{T}}}^{\text{fg}}$ is possible using the relationship:

$$\underline{\underline{\mathbf{S}}}^{\text{fg}} = \frac{1}{\text{TM}_{22}^{\text{fg}}} \begin{bmatrix} \text{TM}_{11}^{\text{fg}} & \text{TM}_{22}^{\text{fg}} - \text{TM}_{12}^{\text{fg}} \text{TM}_{21}^{\text{fg}} & \text{TM}_{12}^{\text{fg}} \\ -\text{TM}_{21}^{\text{fg}} & & 1 \end{bmatrix}. \quad (2.44)$$

The advantage of scattering matrices over transfer matrices is that the causality of the problem is maintained since waves leaving and entering the acoustic element appear separately [1, 52].

2.3. Boundary Conditions

The boundary conditions of acoustic systems can be described by the frequency dependent reflection coefficient R , which is defined as the ratio of the in- and outgoing waves at the respective location. Depending on whether the boundary is located at the inlet (in) or the outlet (out) of a system R is defined differently:

$$R_{\text{in}} = \frac{\widehat{f}_{\text{in}}}{\widehat{g}_{\text{in}}}, \quad R_{\text{out}} = \frac{\widehat{g}_{\text{out}}}{\widehat{f}_{\text{out}}}. \quad (2.45)$$

An acoustically closed end (e.g. a rigid wall), which implies that the acoustic velocity is zero ($\widehat{u} = 0$) is defined by a reflection coefficient of $R = 1$. In turn, for an open end, the fluctuations in acoustic pressure vanish ($\widehat{p} = 0$), thus yielding a reflection coefficient of $R = -1$. An ideally absorbing end

is characterized by $R = 0$. The impedance Z relates acoustic pressure and velocity at the boundary, according to:

$$Z = \frac{1}{\bar{\rho}c} \frac{\hat{p}}{\hat{u}}. \quad (2.46)$$

Conversion between R and Z is possible using the following relationship:

$$Z = \frac{1 + R}{1 - R}. \quad (2.47)$$

Here, an closed end has an infinitively high impedance ($Z = \infty$), an open end provides $Z = 0$ and a fully absorbing end has $Z = 1$.

2.4. Finite Element Method in Acoustics

In order to calculate spatially resolved fields of the acoustic quantities, finite element methods (FEM) are suitable for the discretization of the governing equations. Within the scope of this work, FEM methods are utilized for two purposes: First, to calculate the acoustic scattering behavior of a swirl burner by accounting for acoustic losses associated with a mean flow field. This involves the solution of the LEEs in frequency space (Equations 2.18-2.18). Second, to predict the stability of the combustion system. In this case, the Helmholtz Equation (2.27) is solved in the frequency space while the acoustic properties of the burner and the flame are supplied by their corresponding scattering matrices. For a more compact notation of the governing equations, first the differential operator $\underline{\mathcal{L}}$ is introduced:

$$\underline{\mathcal{L}}(\underline{\hat{\Phi}}) = i\omega\underline{\hat{\Phi}} + \underline{\mathbf{A}}_i \frac{\partial \underline{\hat{\Phi}}}{\partial x_i} + \underline{\mathbf{C}} \underline{\hat{\Phi}} - \underline{\hat{f}}_s = 0, \quad (2.48)$$

wherein $\underline{\hat{\Phi}} = [\hat{\rho}, \hat{p}, \hat{u}, \hat{v}, \hat{w}]^T$ contains the acoustic quantities, $\underline{\mathbf{A}}_i$ is the coefficient matrix containing the respective coordinate directions, $\underline{\mathbf{C}}$ includes the spatial derivatives of the mean flow quantities and $\underline{\hat{f}}_s$ is the vector containing the source terms. The full definition of each of these matrices is given in Appendix A. When considering isentropic wave propagation in a medium at rest, the mean flow quantities \bar{u}_i in Equation (2.48) vanish and

the partial differential equation (PDE) reduces to the Helmholtz Equation (Equation (2.27)). In this case, the PDE can be formulated in its weak form by using a standard Galerkin approach [37]:

$$\int_{\mathcal{D}} \left(\underline{\mathcal{L}}(\underline{\hat{\Phi}}) - \underline{\hat{f}}_s \right) \underline{w} d\mathcal{D} = 0, \quad (2.49)$$

wherein a weighting function $\underline{w} = [w_{\hat{\rho}}, w_{\hat{p}}, w_{\hat{u}}, w_{\hat{v}}, w_{\hat{w}}]^\top$ is introduced for each component of $\underline{\hat{\Phi}}$ in order to formulate the problem integrally over a computational domain \mathcal{D} . Using linear shape functions for $\underline{\hat{\Phi}}$ and \underline{w} allows to transfer Equation (2.49) from its integral to the discretized form in order to solve the equation system numerically.

However, for the discretization of the LEEs in frequency space the standard Galerkin approach is unsuitable. This lies in the nature of the LEEs which describe - in contrast to the Helmholtz equations - a convection dominated problem. Solution of equations describing convection dominated problems using FEM may lead to spurious oscillations of the flow field which causes partly unstable and unphysical solutions [37,125]. One option for obtaining a stable FEM discretization of the LEEs [37,56] is to use a stabilized finite element (SFEM) approach. In this work, a stabilized Galerkin/least-squares (GLS) approach [71] is used for discretization. The basic principle of this approach is to minimize the residual error \mathcal{R} of the FEM solution according to:

$$\int_{\mathcal{D}} \left(\underline{\mathcal{L}}(\underline{\hat{\Phi}}) - \underline{\hat{f}}_s \right) \underline{w} d\mathcal{D} + \int_{\mathcal{D} \setminus \partial\mathcal{D}} \underline{\mathcal{T}} \left(\underline{\mathcal{L}}(\underline{\hat{\Phi}}) - \underline{\hat{f}}_s \right) \underline{\mathcal{L}}(\underline{w}) d\mathcal{D} = 0. \quad (2.50)$$

In Equation (2.50), the first term represents the standard Galerkin discretization known from Equation (2.49) and the second term represents the so-called GLS term. The GLS term introduces a stabilization matrix $\underline{\mathcal{T}}$, which is defined by:

$$\underline{\mathcal{T}} = \max \left(\frac{\alpha_\tau h_n}{|\bar{u}_n| + c} \right) \underline{\mathbf{I}} \quad (2.51)$$

where $\underline{\mathbf{I}}$ denotes the identity matrix and h_n and u_n represent the size and the velocity magnitude of the n -th finite element. In the present work, a constant stabilization coefficient α_τ is used for each element and equation to

be stabilized. More information on the choice of the stability parameter can be obtained from [56, 156]. Note that this stabilization technique by nature introduces artificial damping to the system and, with regard to application for analyzing thermoacoustic stability problems, may have an impact on the results where damping is of particular importance. For a more detailed discussion on the application of FEM stabilization to (thermo-)acoustic problems, the reader is referred to [56, 145]. Combined with an appropriate set of boundary conditions, Equation (2.48) can directly be transferred to a set of algebraic equations, which is expressed as follows:

$$\underline{\underline{\mathbf{E}}}i\omega\hat{\underline{\underline{\Phi}}} + \underline{\underline{\mathbf{K}}}\hat{\underline{\underline{\Phi}}} = \underline{\underline{L}}, \quad (2.52)$$

Here, $\hat{\underline{\underline{\Phi}}}$ represents the nodal values of the solution vector containing the desired acoustic quantities, $\underline{\underline{\mathbf{E}}}$ is the mass matrix and $\underline{\underline{\mathbf{K}}}$ the stiffness matrix, which both result directly from the FEM discretization. Boundary conditions are lumped into $\underline{\underline{L}}$. Spatial solutions representing the respective mode shapes of the acoustic quantities can, for instance, be obtained by prescribing a forcing source term with a fixed angular frequency ω and sweeping over the frequency range of interest. This forcing term is then implemented in the boundary condition vector $\underline{\underline{L}}$. In practice, this is often done to obtain the frequency response of a system over a certain frequency range. Secondly, the eigensolutions of Equation (2.52) deliver both the spatial distribution (mode shape) and the complex valued eigenfrequency (resonance frequency and damping). This method is often employed in the context of thermoacoustics to assess the system stability and implies that the forcing terms contained in Equation (2.52) are set to zero. Details on different solution techniques for solving eigenvalue problems can be found in [56, 145].

2.5. Flame Dynamics

For predicting thermoacoustic oscillations in gas turbine combustors, an appropriate description of the flame's frequency dependent heat-release source term is required. In the context of this work, the dynamic flame response to acoustic perturbations is provided by measured flame transfer functions (FTF). The concept of the flame transfer function will be pre-

sented in the following and the underlying assumptions are explained.

2.5.1. Flame Transfer Functions

The flame transfer function (FTF) describes the amplitude and phase response of the flame's oscillating heat release to acoustic perturbations. For a perfectly premixed flame, the FTF is defined by the relationship

$$\text{FTF} = \frac{\dot{Q}' / \bar{Q}}{u_B' / \bar{u}_B}, \quad (2.53)$$

representing the ratio between oscillating heat release \dot{Q}' and velocity fluctuations at the burner exit u_B' . To yield a dimensionless number, both quantities are normalized by their respective mean values. The velocity fluctuations at the burner outlet are caused by fluctuations of the mass flow, whereas the mass flow is proportional to the velocity at the burner outlet and so are their fluctuating components. These velocity perturbations in turn induce fluctuations of the azimuthal vorticity which influence the amplitude and phase behavior of the FTF and exhibit a strong dependency on both the frequency and the flow properties [68]. Assuming that the fluctuating quantities u_B' and \dot{Q}' oscillate harmonically at a certain angular frequency ω , both can be transformed into the frequency space, expressed by their complex-valued Fourier coefficients:

$$\dot{Q}'(\omega) = \hat{Q}(\omega) \exp(i\omega t + \varphi_{\dot{Q}}) \quad (2.54)$$

$$u_B'(\omega) = \hat{u}_B(\omega) \exp(i\omega t + \varphi_{u_B}). \quad (2.55)$$

Commonly, the FTF is represented by its frequency-dependent amplitude and phase response, defined by:

$$\widehat{\text{FTF}}(\omega) = \frac{\hat{Q} / \bar{Q}}{\hat{u}_B / \bar{u}_B} \quad (2.56)$$

$$\angle \widehat{\text{FTF}}(\omega) = \varphi_{\dot{Q}} - \varphi_{u_B}. \quad (2.57)$$

As a good approximation, the phase of the FTF can also be represented as a function of the global time lag τ [53, 66]:

$$\angle \widehat{\text{FTF}}(\omega) \approx -\omega\tau. \quad (2.58)$$

For very low frequencies, that is $\omega \rightarrow 0$, the FTF results in

$$\lim_{\omega \rightarrow 0} \left| \widehat{\text{FTF}} \right| = 1 \quad (2.59)$$

$$\lim_{\omega \rightarrow 0} \angle \widehat{\text{FTF}} = 0. \quad (2.60)$$

Physically, this corresponds to a quasi-steady flame response which implies that any velocity disturbance is instantaneously converted into a heat release perturbation of the same strength [123]. However, it should be noted that this behavior only applies for perfectly premixed flames. For partially premixed flames, as they are usually found in technical applications, heat release oscillations also occur due to fluctuations in the equivalence ratio [95]. These are superimposed to those mentioned here and originate from an oscillating fuel mass flow at the injector and exhibit different limits towards lower frequencies (see e.g. [12, 53, 141]). On the other hand, for higher frequencies the amplitude tends to zero and the phase becomes undefined, i.e.:

$$\lim_{\omega \rightarrow \infty} \left| \widehat{\text{FTF}} \right| = 0. \quad (2.61)$$

This implies that the flame can no longer respond to velocity disturbances which is a result of the increasing axial dispersion of the flame response towards higher frequencies [53]. Note that this only applies for longitudinal oscillations with frequencies of the order of several hundreds of Hertz. Transversal pressure fluctuations may arise at frequencies of several Kilohertz, where the interaction between the oscillating velocity field and the periodic displacement of the heat release zone governs the flame dynamics. For the description of the flame response to high-frequency oscillations, different approaches are required which can be found, e.g. in [16, 72, 148, 165].

2.5.2. Rankine-Hugoniot Relations for Acoustic Perturbations

In the following, a derivation of the FTF is given based on the Rankine-Hugoniot relations. The aim of this approach is to obtain a coupling condition of the acoustic variables u' and p' between the states up- and downstream of the flame as a function of the FTF. From a measurement point

of view, this allows to extract the FTF from purely acoustic measurements without the oscillating heat release rate being known.

First, it is supposed that the entire heat release of the flame is condensed in an infinitely thin plane [32,80] such that the flame embodies a discontinuity between cold reactants (index c) and hot products (index h). This assumption is justified when the axial expansion of the flame is significantly lower than the wavelength of the investigated frequency range. By doing so, the flame is treated as an acoustically compact element. Integration of the conservation equations for mass, momentum and energy over a control volume across the flame leads to the following relationships [124,144]:

$$\rho_h u_h - \rho_c u_c = 0 \quad (2.62)$$

$$p_h + \rho_h u_h^2 - p_c - \rho_c u_c^2 = 0 \quad (2.63)$$

$$\rho_h u_h^2 \left(h_h + \frac{u_h^2}{2} \right) - \rho_c u_c^2 \left(h_c + \frac{u_c^2}{2} \right) - \dot{Q} = 0. \quad (2.64)$$

Herein, \dot{Q} denotes the heat release rate of the flame over the flame surface and h is the specific enthalpy. Supposing a stationary, isentropic one-dimensional flow field up- and downstream of the flame, the ideal gas law applies, according to:

$$p = \rho \mathbb{R} T, \quad (2.65)$$

where \mathbb{R} is the specific gas constant. The specific enthalpy can therefore be expressed by the following relationship:

$$h = c_p T = \frac{\gamma}{\gamma - 1} \frac{p}{\rho}. \quad (2.66)$$

From this, also the conservation equation for the thermodynamic state can be formulated:

$$\frac{\rho_h \mathbb{R} T_h}{p_h} - \frac{\rho_c \mathbb{R} T_c}{p_c} = 0. \quad (2.67)$$

Through combining and rearranging Equations (2.63-2.67) and using the definition for the Mach number according to $Ma = u/c$, the Rankine-

Hugoniot relations describing the jump conditions across the flame [32,124] are obtained:

$$\frac{u_h}{u_c} = 1 + \frac{\gamma - 1}{\gamma} \frac{\dot{Q}}{p_c u_c} + \mathcal{O}(\text{Ma}^2) \quad (2.68)$$

$$\frac{p_h}{p_c} = 1 - (\gamma - 1) \frac{\dot{Q}}{p_c u_c} \text{Ma}_c^2 + \mathcal{O}(\text{Ma}^4) \quad (2.69)$$

$$\frac{T_h}{T_c} = \left(\frac{c_h}{c_c}\right)^2 = 1 + \frac{\gamma - 1}{\gamma} \frac{\dot{Q}}{p_c u_c} + \mathcal{O}(\text{Ma}^2) \quad (2.70)$$

Assuming low Mach-numbers (which is a valid assumption in practical combustion chambers), higher order terms $\mathcal{O}(\dots)$ are neglected. After rearranging and linearizing the equations across the discontinuity by splitting p , ρ and \dot{Q} and u into their mean and perturbation, two equations representing a correlation between acoustic pressure and velocity fluctuations across the flame can be derived:

$$p'_h = p'_c - \bar{\rho}_c c_c \left(\frac{T_h}{T_c} - 1\right) \text{Ma}_c \bar{u}_c \left(\frac{\dot{Q}'}{\bar{\dot{Q}}} + \frac{u'_c}{\bar{u}_c}\right) \quad (2.71)$$

$$u'_h = u'_c + \left(\frac{T_h}{T_c} - 1\right) \bar{u}_c \left(\frac{\dot{Q}'}{\bar{\dot{Q}}} - \frac{p'_c}{\bar{p}_c}\right). \quad (2.72)$$

By introducing the ratio of specific impedances ϑ and the relative temperature increase across the flame θ :

$$\vartheta = \frac{\bar{\rho}_c c_c}{\bar{\rho}_h c_h}, \quad \theta = \frac{T_h}{T_c} - 1, \quad (2.73)$$

Equations (2.71-2.72) and can be expressed more conveniently:

$$\frac{p'_h}{\bar{\rho}_h c_h} = \vartheta \frac{p'_c}{\bar{\rho}_c c_c} - \vartheta \theta \text{Ma}_c u'_c \left(1 + \frac{\dot{Q}'/\bar{\dot{Q}}}{u'/\bar{u}}\right) \quad (2.74)$$

$$u'_h = -\theta \gamma \text{Ma}_c \frac{p'_h}{\bar{\rho}_c c_c} + \left(1 + \theta \frac{\dot{Q}'/\bar{\dot{Q}}}{u'_c/\bar{u}_c}\right) u'_c. \quad (2.75)$$

Inserting the definition of the FTF according to Equation (2.53) and expressing the set of Equations (2.74-2.75) in the matrix-vector notation yields the flame transfer matrix ($\underline{\mathbf{T}}_F$) in pu -notation:

$$\begin{bmatrix} \frac{p'}{\rho c} \\ u' \end{bmatrix}_h = \underbrace{\begin{bmatrix} \vartheta & -\vartheta\theta\text{Ma}_c (1 + \text{FTF}) \\ -\theta\gamma\text{Ma}_c & 1 + \theta \text{FTF} \end{bmatrix}}_{\underline{\mathbf{T}}_F} \begin{bmatrix} \frac{p'}{\rho c} \\ u' \end{bmatrix}_c \quad (2.76)$$

By using the flame transfer matrix, the dynamic response of a flame can be implemented into an acoustic network or may be prescribed to the boundaries of an FEM model. For bulk flows with negligible Mach numbers, Equation (2.76) simplifies to:

$$\begin{bmatrix} \frac{p'}{\rho c} \\ u' \end{bmatrix}_h = \underbrace{\begin{bmatrix} \vartheta & 0 \\ 0 & 1 + \theta \text{FTF} \end{bmatrix}}_{\underline{\mathbf{T}}_F} \begin{bmatrix} \frac{p'}{\rho c} \\ u' \end{bmatrix}_c. \quad (2.77)$$

The acoustic scattering behavior of the flame by means of waves \hat{f} and \hat{g} is obtained by applying conversion relationship (2.44) to Equation (2.77), leading to the scattering matrix of the flame $\underline{\mathbf{S}}_F$:

$$\begin{bmatrix} \hat{f}_d \\ \hat{g}_u \end{bmatrix} = \frac{1}{\vartheta + 1 + \theta \text{FTF}} \underbrace{\begin{bmatrix} 2\vartheta(1 + \theta \text{FTF}) & \vartheta - (1 + \theta \text{FTF}) \\ (1 + \theta \text{FTF}) - \vartheta & 2 \end{bmatrix}}_{\underline{\mathbf{S}}_F} \begin{bmatrix} \hat{f}_u \\ \hat{g}_d \end{bmatrix}. \quad (2.78)$$

2.6. Combustor Dynamics

In the following, a mathematical description for the modal dynamics in a combustor is derived. The given approach models the thermoacoustic system as a second order harmonic oscillator and allows the flame to be integrated as a source term and to consider damping effects. Determination of the thermoacoustic damping is based on the autocorrelation function of a linearly stable oscillator, which is derived subsequently. Finally, a

description of non-linear thermoacoustic systems will be given which allows to derive its linear growth rate.

2.6.1. Modal Expansion of the Wave Equation

Starting from the inhomogeneous Helmholtz Equation in frequency space (cf. Equation (2.27)) and assuming wave propagation only in the x -direction leads to the following differential equation [109]:

$$\Delta \hat{p}(s, x) - \left(\frac{s}{c}\right)^2 \hat{p} = -s \frac{\gamma - 1}{c^2} \hat{q}_V. \quad (2.79)$$

Therein, s corresponds to the Laplace variable and the spatial derivatives are denoted by $\Delta = \nabla^2 = \partial^2 / \partial x_i^2$. Furthermore, a boundary condition is prescribed to the surface of the burner outlet A_B , represented by the complex valued burner impedance

$$Z(s, x) = \frac{\hat{p}(s, x)}{\hat{u}(s, x) n'}, \quad (2.80)$$

where n is the normal on the burner surface A_B . It is moreover assumed that the thermoacoustic system described by Equations (2.79-2.80) is governed by only one single dominant thermoacoustic mode being similar in its eigenshape to the pure acoustic mode. Equation (2.79) can thus be formulated by separation of variables:

$$\hat{p}(s, x) = \hat{\eta}_n(s) \Psi_n(x). \quad (2.81)$$

Here, $\hat{p}(s, x)$ denotes the Laplace transform of the pressure and $\Psi_n(x)$ is the eigenmode of interest being a solution of the homogeneous Helmholtz equation. Hence, insertion of Equation (2.81) into Equation (2.79) with $\hat{q} = 0$ yields:

$$\Delta \Psi_n = \left(\frac{s}{c}\right)^2 \Psi_n. \quad (2.82)$$

Whereas insertion of Equation (2.81) into Equation (2.79) with $\hat{q} \neq 0$ leads to:

$$\hat{\eta}_n \Delta \Psi_n - \left(\frac{s}{c}\right)^2 \Psi_n \hat{\eta}_n = -s \frac{\gamma - 1}{c^2} \hat{q}_V(s, x). \quad (2.83)$$

Multiplication with the orthogonal mode Ψ_m and integration over the combustor volume V yields to the following integral equation:

$$\hat{\eta}_n c^2 \int_V \Psi_m \Delta \Psi_n \, dV - s^2 \hat{\eta}_n \int_V \Psi_n \Psi_m \, dV = -s \int_V (\gamma - 1) \Psi_n \hat{q}_V(s, x) \, dV. \quad (2.84)$$

In order to obtain a modal solution for the inhomogeneous Helmholtz Equation (2.79), subsequently, the first term on the left hand side of Equation (2.84) is integrated over the combustor volume V by applying Gauss' theorem and inserting $\nabla \Psi_n n = 0$ on the burner surface area A , i.e.:

$$\int_V \Psi_m \Delta \Psi_n \, dV = \int_V \Delta \Psi_m \Psi_n \, dV + \int_A \Psi_m \nabla \Psi_n n \, dA. \quad (2.85)$$

Assuming that the acoustic eigenmodes ($\hat{q} = 0$) coincide with the thermoacoustic eigenmodes ($\hat{q} \neq 0$) justifies inserting the homogeneous solution for Ψ_n according to Equation (2.83). Furthermore, Ψ is an orthogonal function, such that:

$$\frac{1}{V} \int_V \Psi_n \Psi_m \, dV = \begin{cases} \Lambda_n & \text{for } n = m \\ 0 & \text{for } n \neq m, \end{cases} \quad (2.86)$$

where Λ_n denotes the normalization coefficient for the mode given by:

$$\Lambda_n = \frac{1}{V} \int_V |\Psi_n|^2 \, dV. \quad (2.87)$$

Hence, the boundary condition given by the burner impedance (Equation (2.80)) can be expressed as follows:

$$Z(s, x) = \frac{\hat{p}(s, x)}{\hat{u}(s, x) n} = \frac{\Psi_n}{-\nabla \Psi_n n} s \rho, \quad (2.88)$$

which leads after rearranging to:

$$\nabla \Psi_n n = -\frac{s \rho}{Z(s, x)} \Psi_n. \quad (2.89)$$

Finally, an analytical, modal solution for Equation (2.79) is found [109]:

$$\hat{\eta}_n(s) \left(s^2 + s \underbrace{\frac{\rho c^2}{V \Lambda_n} \int_A \frac{|\Psi_n|^2}{Z(s, x)} dA}_{2\alpha_n} + \omega_n^2 \right) = s \underbrace{\frac{(\gamma - 1)}{V \Lambda_n} \int_V \hat{q}_V(s, x) \Psi_n dV}_{\hat{q}}, \quad (2.90)$$

where, ω_n represents the eigenfrequency of the thermoacoustic system. By lumping the acoustic dissipation in a damping constant α and expressing the heat release source term on the right hand side by \hat{q} , Equation (2.90) can be expressed in a simpler form:

$$\hat{\eta}_n(s) (s^2 + 2\alpha_n s + \omega_n^2) = s \hat{q}. \quad (2.91)$$

2.6.2. Harmonic Oscillator

As shown by Culick [34], the contribution of the modal amplitudes η_n in Equation (2.91) are governed by a second order oscillator system [34]. After re-transforming Equation (2.91) into the time domain, the modal dynamics in a combustor can be described by the following differential equation:

$$\sum_{n=1}^N [\ddot{\eta}_n + 2\alpha_n \dot{\eta}_n + \omega_n^2 \eta_n = \dot{q}'_n]. \quad (2.92)$$

Assuming no modal interactions, the summation operator can be dropped to treat each differential equation of the modes η_n individually. Furthermore, the flame is considered as the main acoustic driving force in the system. This allows to express the volumetric heat release on the right hand side by the following relationship [112]:

$$\dot{q}'_n(t) = 2\beta_n \eta_n - \frac{\kappa}{3} \eta_n^3, \quad (2.93)$$

where β_n is the flame gain and κ denotes a non-linearity coefficient which becomes negligible when the system oscillates in a linearly stable state. After taking the time derivative of Equation (2.93), a representation for the fluctuating heat release rate is found:

$$\dot{q}'_n = 2\beta_n \dot{\eta}_n - \kappa \eta_n^2 \dot{\eta}_n. \quad (2.94)$$

Inserting this relationship into Equation (2.92), the combustion system may be modeled by a noise driven Van der Pol oscillator [110–112] where the combustion noise acts as a stochastic driver, represented by the non-correlated stochastic forcing term $\tilde{\zeta}(t)$:

$$\dot{\eta}_n + 2(\alpha_n - \beta_n + \kappa\eta_n^2)\dot{\eta}_n + \omega_n^2\eta_n = \tilde{\zeta}(t). \quad (2.95)$$

This mathematical representation can be used to describe both linear and non-linear combustor dynamics, which will be described in the following sections.

2.6.2.1. Linear Systems

In practical applications, it is often of major interest to obtain information on the net damping rate of a combustor. By definition, this combines both the flame gain and the acoustic dissipation into a single quantity which is designated by ν and is defined as follows:

$$\nu_n = \alpha_n - \beta_n. \quad (2.96)$$

This net damping rate ν is hereinafter referred to as *thermoacoustic damping rate*, because it includes both the flame and the acoustics. In turn, this means that if the dissipation of the acoustic energy exceeds the flame gain ($\alpha_n > \beta_n$) which results in a positive thermoacoustic damping rate ν_n , the system is considered as *linearly stable*. In this case, the non-linearity coefficient κ becomes negligibly small and implies that the heat release oscillations \dot{q}' are proportional to the acoustic pressure. Equation (2.95) then simplifies to:

$$\ddot{\eta}_n + 2\nu_n\dot{\eta}_n + \omega_n^2\eta_n = \tilde{\zeta}(t). \quad (2.97)$$

Under these conditions, the modal dynamics in the combustor is described by a damped, harmonic oscillator which is stochastically driven by broadband noise of the turbulent flame. Equation (2.97) can thus be transformed into the frequency domain in the form of its power spectral density (PSD) [94, 111]:

$$S_{\eta_n\eta_n}(\omega) = \frac{\Gamma}{(\omega_n^2 - \omega^2)^2 + 4\nu_n^2\omega^2}. \quad (2.98)$$

In this expression Γ is the intensity of the broadband noise term $\zeta(t)$ and ω denotes the angular frequency. Using the Wiener-Khinchin-Theorem [54], Equation (2.98) can be linked to the autocorrelation function of the modal amplitude:

$$k_{\eta_n \eta_n}(\tau) = \int_{-\infty}^{\infty} S_{\eta_n \eta_n}(\omega) \exp(i\omega\tau) d\omega, \quad (2.99)$$

where τ is a discrete time delay vector obtained from measurement or simulation data. Assuming that $\nu_n \ll \omega_n$ and applying the residue theorem [5], the integral in Equation (2.99) can be evaluated analytically and finally one finds after normalization:

$$k_{\eta_n \eta_n}(\tau) = \exp(-\nu_n \tau) \cos(\omega_n \tau). \quad (2.100)$$

Recalling Equation (2.92) and noting that all operations carried out so far were linear, the autocorrelation function of the pressure signal can also be decomposed into its modal components η_n :

$$k_{p' p'}(\tau) = \sum_{n=1}^N k_{\eta_n \eta_n}(\tau) \quad (2.101)$$

$$= \sum_{n=1}^N \exp(-\nu_n \tau) \cos(\omega_n \tau). \quad (2.102)$$

Furthermore, it is possible to formulate Equation (2.92) by a transfer function H between unsteady heat release \dot{q}' and pressure fluctuations p' , expressed by its corresponding modal amplitudes by the following relationship [22,73]:

$$H_{\eta q}(\omega) = \frac{\hat{\eta}_n(\omega)}{\hat{q}_n(\omega)} = \frac{-i\omega}{\omega^2 - 2i\omega\alpha_n - \omega_n^2}. \quad (2.103)$$

Proceeding in the same way as for Equations (2.98)-(2.100), the transfer function $H(\omega)$ can be expressed by means of an autocorrelation function [73]:

$$k_{\eta_n q_n}(\tau) = \exp(-\alpha_n \tau) \cos(\omega_n \tau). \quad (2.104)$$

The fundamental difference between Equation (2.100) and Equation (2.104) is that the former makes use of the autocorrelation function of the pressure oscillations only to describe the thermoacoustic damping rate ν_n . System

identification techniques relying on this equation are therefore termed as *output-only* methods. The latter, on the other hand, considers the transfer function between an input (heat release) and an output (pressure oscillations) and implies a *single-input single-output* (SISO) system. This requires instead two sets of data, namely the dynamic pressure and the heat release rate. In return, the pure acoustic damping rate α_n can be extracted from fitting a data set to Equation (2.104). As a logical consequence, this also provides access to the flame gain β_n , according to Equation (2.96). Furthermore, Equation (2.104) is valid not only for linearly stable ($\nu_n > 0$) but also for linearly unstable cases ($\nu_n < 0$) since it only describes to the pure acoustics. The assumption of acoustic linearity still holds in this case, since the fluctuating quantities are small with respect to the mean flow quantities. This implies harmonic heat release oscillations which also allows their transformation into the frequency space [23,73].

2.6.2.2. Non-Linear Systems

If the flame gain β_n exceeds the acoustic dissipation α_n , a net gain of acoustic energy occurs which leads to the growth of the pressure oscillations in the thermoacoustic system. These pressure oscillations then grow with a certain growth rate $\nu < 0$ before being limited by saturation processes. This state is therefore referred to as *limit-cycle* and implies that the non-linearity coefficient κ in Equation (2.95) is no longer negligibly small [93,96,112]. One method to obtain the growth rate of such systems makes use of a linearized description of the limit-cycle oscillations [20,22,73,111,112]. The proposed procedure allows to transform the second order system in Equation (2.92) into a first order system. This yields in a set of stochastic differential equations describing the dynamics of the limit cycle oscillations by their slowly varying amplitudes \mathcal{A} and phases φ . This set of SDEs is given by [111]:

$$\dot{\mathcal{A}} = \mathcal{A} \left(-\nu_n - \frac{\kappa}{8} \mathcal{A}^2 \right) + \frac{1}{A} \frac{\Gamma}{4\omega_n^2} + \xi(t) \quad (2.105)$$

and

$$\dot{\varphi} = \frac{1}{\mathcal{A}} \chi(t). \quad (2.106)$$

Herein, both $\zeta(t)$ and $\chi(t)$ represent sources of uncorrelated white noise with an intensity of $\Gamma/2\omega_0^2$. If the fluctuations of the amplitudes are much smaller than their respective mean value ($\mathcal{A}' \ll \bar{\mathcal{A}}$). Both can be treated separately thus allowing to linearize the limit-cycle oscillations. By presuming that the broadband forcing is small with respect to the overall amplitude level, the mean amplitude $\bar{\mathcal{A}}$ is supposed to coincide with its deterministic value \mathcal{A}_0 given by:

$$A_0 = \sqrt{\frac{-8\nu_n}{\kappa}}, \text{ for } \nu_n < 0. \quad (2.107)$$

Insertion of these conditions into Equation (2.105) and neglecting higher order terms, yields:

$$\dot{\mathcal{A}}' = \left(2\nu_n - \frac{\Gamma}{4\omega_n^2 \mathcal{A}_0^2} \right) \mathcal{A}' + \zeta(t), \text{ for } \nu_n < 0. \quad (2.108)$$

Finally, Equation (2.108) can be transformed into an autocorrelation function to extract the growth rate $\nu_n < 0$ [73]:

$$k_{\mathcal{A}'\mathcal{A}'} = \exp(2\nu_n \tau). \quad (2.109)$$

Contrary to the autocorrelation functions of the second order systems (cf. Equations (2.100) and (2.100)), Equation (2.109) contains no oscillatory part since it originates from a differential equation of first order.

A more rigorous derivation of Equations (2.105-2.106) can be found in [111]. Note that contrary to the notation in the given references here ν is defined as a damping rate, being positive for linearly stable systems and negative for linearly unstable systems. The reason is that this work predominantly considers damped and linearly stable thermoacoustic systems, while unstable systems for which growth rates are analyzed occur only in exceptional cases.

2.7. Solution of Non-Linear Optimization Problems

Several evaluation techniques used in this thesis are based on the solution of non-linear optimization problems which aim to extract unknown pa-

rameters from experimental or numerical data. Depending on the field of application either least-squares regression or Bayesian parameter estimation are used. The former is deployed, for example, for the determination of scattering matrices, the latter serves to determine damping rates.

2.7.1. Least-Squares Optimization

Commonly used approaches to solve non-linear optimization problems rely on least-squares minimization by means of a residual \mathcal{R} (see e.g. [39, 59]) according to:

$$\mathcal{R}(\underline{x}) = \sum_{n=1}^N (y_n - f_n(\underline{x}))^2, \quad (2.110)$$

where \underline{x} is the solution vector, described by an underlying model equation $f_n(x)$ and y_n contains the observations made. Observations can, for example, appear in the form of measurement data, to which the coefficients contained in the solution vector are fitted using an appropriate model. This is done by calculating the covariance matrix using classical statistics which can inherently be used for error estimation. In this context, the problem is often formulated in matrix notation:

$$\mathcal{R}(\underline{x}) = \sum_{m=1}^M \left| y_m - \sum_{n=1}^N H_{mn} x_n \right|^2 \quad (2.111)$$

$$= \left\| \underline{y} - \underline{\mathbf{H}} \underline{x} \right\|^2, \quad (2.112)$$

where $\underline{\mathbf{H}}$ is a $m \times n$ -matrix, with $m < n$ and thus a solution for \underline{x} is obtained [85]:

$$\underline{x} = \underline{\mathbf{H}}^{\dagger} \underline{y}, \quad (2.113)$$

where $\underline{\mathbf{H}}^{\dagger}$ denotes the pseudo-inverse of the matrix $\underline{\mathbf{H}}$, given by:

$$\underline{\mathbf{H}}^{\dagger} = \left(\underline{\mathbf{H}}^{\top} \underline{\mathbf{H}} \right)^{-1} \underline{\mathbf{H}}^{\top}. \quad (2.114)$$

Least-squares optimization is known as an easy-to-implement and computationally cheap way to obtain a posterior distribution for \underline{x} which results directly from one known observation state y_n . However, non-linear

regression relies on linearization and for solutions exhibiting multiple local minima, convergence might be difficult to achieve. Furthermore, this approach presumes that measurement errors or noise are normally distributed. This means in practice, that a sufficient amount of test-states with a high signal-to-noise ratio is required for successfully solving such an optimization problem in a least-square sense [44].

2.7.2. Bayesian Inference

A powerful alternative to least-square optimization is statistical inference wherein Bayes' theorem [15] is applied to formulate a mathematical problem inversely. Basically, it means that probability for a hypothesis to occur is continuously updated as more information is available. This information may be, for example, data that is directly or indirectly related to the original problem. Bayesian inference has become increasingly popular to solve non-linear optimization problems in a variety of applications such as physics, engineering and social sciences [104] as well as in artificial intelligence and machine learning. It relies on the principle that a posterior probability which resembles the "most likely" combination of parameters is derived from prior knowledge, expressed by means of probability distributions. The problem is therefore formulated *probabilistically* and not *deterministically*. Correlations between the prior and posterior distribution are prescribed by an underlying statistical model. In this respect, estimates and uncertainty characteristics for each unknown parameter are supplemented with the posterior. This has the advantage that systematic and random effects contained in the data are treated equally since the method is not inherently based on linearization. This implies that Bayesian methods are clearly superior to a least-square formulation, especially in the case of coarse or sparse data sets or when the signal-to-noise ratio is weak. The latter often applies to measurements taken in combustors, where signals are usually corrupted by noise and the operating conditions often vary over the time. A comprehensive comparison between least-squares optimization and Bayesian regression can be found in [44,98].

2.7.3. Markov-Chain Monte-Carlo Method (MCMC)

In practice, Markov-chain Monte Carlo (MCMC) methods [131,132] are used to solve the necessary integrals numerically. To this end, it is possible

to obtain accurate estimates for a very large number of unknowns, for example for the parameter identification of dynamic systems with multi-modal contents, to which thermoacoustic systems clearly count. The basic principle of the MCMC works as follows: At the beginning, a final parameter distribution $\Pi(x)$, the *target distribution*, which has only one unknown parameter and appears as a multiplication factor, is predefined. Assuming that $\Pi(x)$ is sufficiently complex such that direct sampling from it is not possible, one can implicitly draw samples from $\Pi(x)$ by constructing an aperiodic and irreducible Markov chain. Running this chain long enough, the simulation results can be considered as dependent samples from the target distribution representing the character of the distribution $\Pi(x)$.

2.7.4. Metropolis-Hastings Algorithm

The most generic computational implementation of the MCMC method is the Metropolis-Hastings algorithm [65, 102]. The starting point is here to use a proposal distribution $q^*(\underline{x}, \underline{y})$ which is in general arbitrary and aims at constructing an aperiodic, irreducible chain with the stationary target distribution $\Pi(x)$. Originating from a current state this leads to a new state $y = (x_1, \dots, x_{n-1}, y_n, x_{n+1}, \dots, x_k)$, whereas the criterion to accept the new state is given by the acceptance probability:

$$P(\underline{x}, \underline{y}) = \min \left(1, \frac{\Pi(\underline{y}) q^*(\underline{y}, \underline{x})}{\Pi(\underline{x}) q^*(\underline{x}, \underline{y})} \right). \quad (2.115)$$

This yields the transition kernel $\mathcal{P}(\underline{x}, A)$ which essentially resembles the probability that the next state in the Markov chain lies within the range of some set A when the current state is \underline{x} . In turn, this means that when a possible state is rejected due to Equation (2.115), the chain remains in its current state. In case the proposal distribution is symmetric such that $q^*(\underline{x}, \underline{y}) = q^*(\underline{y}, \underline{x})$, the proposal distribution cancels out and P reduces to

$$P(\underline{x}, \underline{y}) = \min \left(1, \frac{\Pi(\underline{y})}{\Pi(\underline{x})} \right). \quad (2.116)$$

2.7.5. Gibbs Sampling

The procedure which is applied within this work uses Gibbs sampling - a modification of the Metropolis-Hastings algorithm for solving non-linear regression problems. It was introduced by Geman and Geman [55] and presumes a symmetric proposal distribution according to Equation (2.116). The basic principle is to split the state vector \underline{x} into its individual components and to update them consecutively, while keeping all others constant. This is achieved by using the so-called Gibbs transition kernel, which has the advantage that only one single observation is required for each distribution. For example this means that when the i -th element of \underline{x} is updated, the proposal distribution q^* is chosen such that

$$q^*(\underline{x}, \underline{y}) = \begin{cases} \prod(y_n | x_n) & \text{for } y_n = x_n, n = 1, \dots, m, \\ 0 & \end{cases} \quad (2.117)$$

Thus, per definition, the only possible values of P are 0 or 1, which means in turn that the next state of the chain is only accepted when \underline{y} is equal to \underline{x} for all but the n -th component [24].

3 Measuring Methods and Data Processing

In this chapter, measurement techniques and methods for processing the acquired data are introduced. The major part of these techniques rely on dynamic pressure measurements. Methods for the experimental determination of acoustic scattering matrices and flame transfer functions (FTF) operating in the frequency domain are outlined first. Furthermore, procedures used for the experimental determination of the damping rate in combustors are presented. Particular emphasis is placed on a newly developed method for the determination of thermoacoustic damping rates from combustion noise. Finally, optical measurement techniques are introduced which serve to infer either on the heat release distribution of the flame and the distribution and properties of the water spray.

3.1. Determination of Scattering Matrices

The acoustic properties of the swirl burner with and without flame are represented using acoustic scattering matrices. This allows for including the acoustic losses of the burner and provides a frequency-dependent description of the flame dynamics. While the flame is described purely by experimental data, the scattering matrices of the burner are determined experimentally as well as numerically. The subsequently presented method

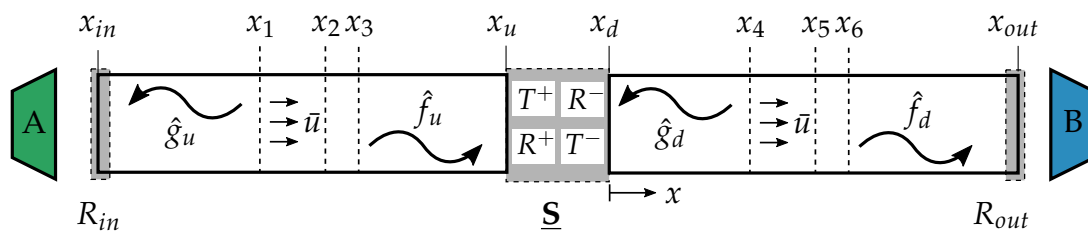


Figure 3.1.: Multi-microphone method to determine acoustic scattering matrices.

is applicable both to pressure signals measured at discrete locations as well as to numerically calculated pressure fields. Independent of whether a combustion system with or without a flame is considered, the same measuring procedure is used for determining the scattering matrices.

The procedure utilized seeks to determine the four, frequency dependent elements of the scattering matrix $\underline{\mathbf{S}}$, according to Equation (2.43), which represent each two reflection and transmission coefficients, respectively [1]. A schematic of a generic test setup to determine acoustic scattering matrix is shown in Figure 3.1. To obtain the scattering matrix coefficients, the Riemann invariants of the waves entering (\hat{f}_u and \hat{g}_d) and leaving (\hat{g}_u and \hat{f}_d) the acoustic element to characterize have to be determined and correlated to an external forcing signal. Furthermore, since Equation (2.43) contains four unknown elements but only two equations, two linearly independent states are necessary. These are achieved by producing two independent forcing conditions using each one forcing location far upstream (A) and downstream (B) of the acoustic element to characterize, known as the two-source location method [106]. The Riemann-invariants are then obtained by exploiting the analytical solution of the convective, homogeneous wave equation, according to Equation (2.34) by providing the dynamic pressures acquired up- and downstream at the frequency of interest. This procedure is called multi-microphone method (MMM) [52, 117, 140] allowing to include acoustic pressures measured (e.g. by microphones) at multiple axial locations x_n up- and downstream. The MMM is an advanced variant of the two-microphone method (TMM) [2, 3] without limitation of the number of measurement locations. In order to solve the optimization problem to calculate the Riemann-invariants from dynamic pressures acquired at fixed locations, Equation (2.34) is reformulated in a least-squares sense (see Section 2.7.1):

$$\begin{bmatrix} \hat{f}_{u/d}^A(\omega) & \hat{f}_{u/d}^B(\omega) \\ \hat{g}_{u/d}^A(\omega) & \hat{g}_{u/d}^B(\omega) \end{bmatrix} = \underline{\underline{\mathbf{H}}}_{u/d}^+ \hat{\underline{\underline{p}}}_{u/d} \quad (3.1)$$

wherein $\hat{p}(x, \omega_n)$ is the Fourier transform of the acoustic pressure signal $p'(x, t)$ acquired at a specific location $x_{u/d,n}$ and evaluated at the discrete forcing frequency $f_n = \omega_n/2\pi$:

$$\underline{\hat{p}}_{u/d} = \begin{bmatrix} \hat{p}^A(x_{u/d,1}, \omega) & \hat{p}^B(x_{u/d,1}, \omega) \\ \vdots & \vdots \\ \hat{p}^A(x_{u/d,N}, \omega) & \hat{p}^B(x_{u/d,N}, \omega) \end{bmatrix}, \quad (3.2)$$

the matrix $\underline{\underline{\mathbf{H}}}_{u/d}$ contains the wave numbers k^\pm and the measurement locations $x_{u/d}$, given by:

$$\underline{\underline{\mathbf{H}}}_{u/d} = \begin{bmatrix} \exp(-ik^+ x_{u/d,1}) & \exp(ik^- x_{u/d,1}) \\ \vdots & \vdots \\ \exp(-ik^+ x_{u/d,N}) & \exp(ik^- x_{u/d,N}) \end{bmatrix}. \quad (3.3)$$

An error measure for the fitted values of $\hat{f}_{u/d}$ and $\hat{g}_{u/d}$ can be formulated as follows [21]:

$$\epsilon_{u/d} = \frac{\|(\underline{\mathbf{I}}^N - \underline{\underline{\mathbf{H}}}_{u/d} \underline{\underline{\mathbf{H}}}_{u/d}^+) - \underline{\hat{p}}_{u/d}\|_2}{\|\underline{\hat{p}}_{u/d}\|_2}, \quad (3.4)$$

wherein $\underline{\mathbf{I}}^N$ denotes the symmetric identity matrix of size $N \times N$ and $\|\underline{\hat{p}}_{u/d}\|_2$ is the l_2 norm of the complex measured pressures. Finally, the following linear equation system to determine the scattering matrix coefficients is obtained:

$$\underbrace{\begin{bmatrix} T^+ & R^- \\ R^+ & T^- \end{bmatrix}}_{\underline{\underline{\mathbf{s}}}^{\text{fg}}} = \begin{bmatrix} \hat{f}_{\text{ds}}^A & \hat{f}_{\text{ds}}^B \\ \hat{g}_u^A & \hat{g}_u^B \end{bmatrix} \begin{bmatrix} \hat{f}_u^A & \hat{f}_u^B \\ \hat{g}_{\text{ds}}^A & \hat{g}_{\text{ds}}^B \end{bmatrix}^{-1}. \quad (3.5)$$

In the used setup, measurements of the sound pressure are conducted using dynamic pressure transducers. Each three of them are located in the upstream- and downstream section. To reduce disturbing noise, the phase trigger signal from the excitation source is used as a reference phase. Pressure transducers are calibrated externally against an independent reference

sensor and calibration is carried out at regular intervals in compliance with guidelines provided in [77]. More details on calibration of pressure sensors are given in [6,52].

3.2. Measurement of Source Terms

In general, scattering matrices can be used to characterize both acoustically passive and active elements. Swirl burners implemented in gas turbine combustors are usually acoustically passive elements, while turbulent flames are among the acoustically active elements. The scattering matrix describes all linearly dependent contributions of an acoustic element which are correlated to an externally provided excitation signal. In a combustor with a turbulent flame, the flame itself acts as an acoustic monopole and also generates acoustic waves with a certain amplitude and phase. These emitted waves are termed *source terms* and are in the following denoted by \hat{f}_s and \hat{g}_s . Source terms appear as coherent noise and are independent of the in- and outbound waves \hat{f}_u and \hat{g}_d [117,140]. However, due to their coherence, they can be determined by an additional measurement without external excitation. The thus measured pressure field upstream and downstream of the flame incorporates the contribution of the source term. The source terms can be obtained by evaluating the Riemann invariants up- and downstream of the flame, analogously to the procedure outlined in Section 3.1 and inserting the measured scattering matrix:

$$\begin{bmatrix} \hat{f}_s \\ \hat{g}_s \end{bmatrix} = \begin{bmatrix} \hat{f}_d^{NF} \\ \hat{g}_u^{NF} \end{bmatrix} - \begin{bmatrix} T^+ & R^- \\ R^+ & T^- \end{bmatrix} \begin{bmatrix} \hat{f}_u^{NF} \\ \hat{g}_d^{NF} \end{bmatrix}. \quad (3.6)$$

Therein, the superscript *NF* refers to the Riemann invariants for the non-forced case. In the context of the present work, the source term is used to determine whether water injection changes the noise generation of the flame and how it depends on the quantity of water injected.

3.3. Measurement of Flame Transfer Functions

Flame transfer functions are a common way to describe the dynamic response of the flame to acoustic perturbations (see Section 2.5). The acoustic

description of the frequency-dependent flame response is required to predict the thermoacoustic stability of an entire combustion system. In order to represent the flame dynamics of the present combustor with water injection, FTFs are determined experimentally in a single burner test-rig. The measuring procedures used to acquire these FTFs are outlined in the following.

For perfectly premixed flames where the equivalence ratio can be locally assumed as constant, the normalized heat release fluctuations \dot{Q}'/\bar{Q} in Equation (2.53) can be obtained indirectly by measuring the integral OH*-chemiluminescence intensity with a photomultiplier, leading to:

$$\text{FTF}_{\text{OH}^*}(\omega) = \frac{I'_{\text{OH}^*}(\omega)/\bar{I}_{\text{OH}^*}}{u'_B(\omega)/\bar{u}_B}, \quad (3.7)$$

where $I'_{\text{OH}^*}/\bar{I}_{\text{OH}^*}$ represents the ratio between the measured fluctuations of the OH*-chemiluminescence intensity, normalized by the mean value without external forcing. The intensities are acquired using a photomultiplier equipped with a narrow-band interference filter which corresponds to the wave length of the light emission in the OH*-radical ($\lambda_{\text{OH}^*} = 307 \pm 5\text{nm}$). The velocity perturbations at the burner outlet u'_B can either be obtained from constant temperature anemometry (CTA) [6, 52, 66] or from dynamic pressure measurements by applying the MMM [11]. Their mean value \bar{u}_B is obtained from the mass flow through the burner outlet area. However, using OH*-chemiluminescence to infer on the heat release oscillations is restricted to perfectly premixed flames only as long as no measured light emissions from other species are acquired simultaneously [142, 143]. As a further optical measurement technique for determining the FTF, a laser-optical method based on the measurement of density fluctuations is given in [119]. A special feature of this method is that it can also be applied to flames with fluctuating equivalence ratio.

Alternatively, the FTF can be obtained from pure acoustic measurements by exploiting the relationship between the flame transfer matrix ($\underline{\mathbf{T}}_F$) and the FTF according to Equations (2.76) resp. (2.77) as derived in Section 2.5.2. In practice, the flame transfer matrix can not be determined separately since measurements with flame always incorporate the burner transfer matrix. However, this contribution can be eliminated in the evaluation pro-

cedure [140]. The basic idea is to use separately acquired transfer matrices for burner and flame ($\underline{\underline{\mathbf{T}}}_{\text{BF}}$) and burner without flame ($\underline{\underline{\mathbf{T}}}_{\text{B}}$) by applying the measurement procedure outlined in Section 3.1. In this context, note also the conversion rules between scattering matrices in fg -notation and transfer matrices in pu -notation, given by Equation (2.44) and Equation (2.41). The flame transfer matrix $\underline{\underline{\mathbf{T}}}_{\text{F}}$ can then be obtained by the following matrix operation:

$$\underline{\underline{\mathbf{T}}}_{\text{F}} = \underline{\underline{\mathbf{T}}}_{\text{BF}} \cdot \underline{\underline{\mathbf{T}}}_{\text{B}}^{-1}. \quad (3.8)$$

This operation relies on the assumption that the burner transfer matrix remains unchanged even in presence of the flame. The practicability of this assumption has been justified by several works in the past [6, 11, 140]. Finally, the purely acoustically determined FTF is obtained by the following relationship:

$$\text{FTF}_{ac}(\omega) = \frac{\text{TM}_{\text{F},22}(\omega)}{1 + T_h/T_c}, \quad (3.9)$$

where, $\text{TM}_{\text{F},22}$ represents the lower right element of the flame transfer matrix, T_c is the (cold) reactant temperature defined by the mixture preheat temperature T_{ph} , whereas T_h is the temperature of the (hot) burnt gas.

In this work, the purely acoustic method is applied to determine the FTF since it relies on the measurement of the scattering matrix. For the determination of the source term (see Section 3.2) and for numerical stability analyses scattering matrices are also required, as described later in Section 8.5.2. The temperatures T_h are estimated by a heat loss model of the combustor provided in [11]. The validity of this estimate is checked by means of comparing the resulting FTF_{ac} with the simultaneously measured FTF_{OH^*} .

3.4. Determination of Damping and Growth Rates

In this work, the influence of water injection on the thermoacoustic stability will be quantified by means of measured eigenfrequencies and damping rates. When operating the combustor without flame, external siren excitation is used for this purpose and allows for measuring the decay curve

after stopping the forcing abruptly. This method will be introduced first. Under reactive conditions the combustion noise of the turbulent flame is exploited to determine the thermoacoustic damping rate from the autocorrelation function of the acquired pressure signal. In addition, an extension of the latter method is presented, which provides for the separation of pure acoustic damping from the thermoacoustic damping rate. The aforementioned methods use time domain data to extract the damping rate using Bayesian statistics and require linear stable conditions, i.e. a positive net damping rate. Linearly unstable operating points can be considered by using a method to identify the linear growth rate, which will be described last.

3.4.1. Impulse Response Method

Using the impulse response method, the damping rate is extracted from a decaying acoustic signal in the combustor by using Bayesian parameter estimation (see Section 2.7.2). The method builds upon earlier work of Bodisco et al. [19] and Wagner et al. [159]. The application of the method to a practical combustor under reactive and non-reactive conditions was demonstrated by Stadlmair et al. [152]. In the scope of this work, this method is used to quantify the acoustic dissipation in the combustor under non-reactive conditions. The reason for this choice is that the noise excitation of the mean flow without flame is not sufficiently high to extract damping rates from its autocorrelation and thus external excitation is required. Practically, the method is based on externally exciting the combustion chamber at its resonance frequencies and then stopping the forcing abruptly. Subsequently, the oscillations decay exponentially over time with the decay rate ν and the frequency f . External forcing is provided monofrequently by a siren equipped with a valve to stop the externally supplied excited air flow almost instantaneously. The decay rate is considered to be constant and can be described by the temporal evolution of the acoustic energy in the system [51, 152]. In general, merely one dynamic pressure sensor is required to obtain the required pressure recordings. However, using multiple sensors at different locations increases the accuracy of the results [159]. The operational sequence of the measurement procedure is depicted in Figure 3.2.

Provided that the interruption of the forcing happens instantaneously and its moment is exactly known, the evolution of measured pressure fluctuations $p'(t)$ can be approximated by the following model equation:

$$p'(t) = e^{-\nu_n t} (A_{1,n} \sin(2\pi f_n t) + A_{2,n} \cos(2\pi f_n t)). \quad (3.10)$$

From this perspective, the decaying signal is treated as a superposition of longitudinal sinusoidal and cosinusoidal oscillations of frequency f , normally distributed around a time varying mean and scaled by their individual amplitudes $A_{1,n}$ and $A_{2,n}$. However, the achieved signal-to-noise ratio of the measured time traces is usually not sufficient for conventional fitting methods in a least-squares sense. This can be remedied by using Bayesian inference to obtain the desired unknown quantities from Equation (3.10), in particular the damping rate ν_n . More precisely, a Gibbs sampler is used for this purpose (see Section 2.7.5). With respect to the

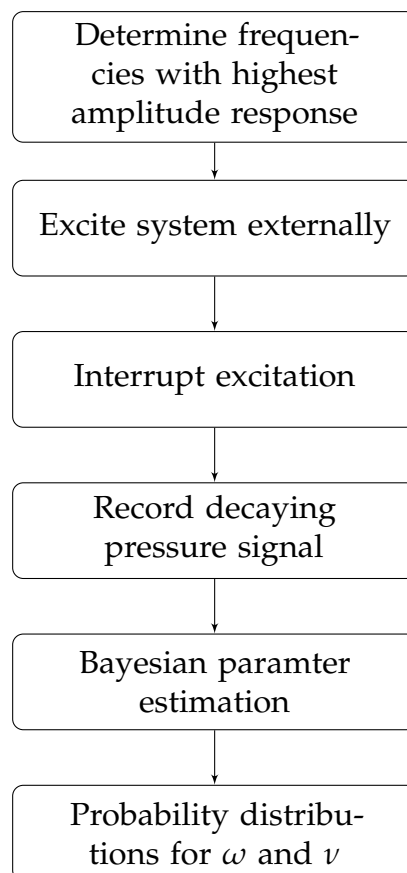


Figure 3.2.: Measurement procedure of the impulse response method to determine combustor damping.

parameter identification by Bayesian statistics, the time series of decaying pressure $p'(t)$ provides a series of conditional correlations between all known quantities. Model definition and performing the optimization procedure is carried out using the GNU licensed Gibbs Sampling tool JAGS [121] embedded in the MATLAB[®] environment for pre- and post-processing of the data. The results of the Gibbs sampling procedure finally returns probability distributions of eigenfrequencies and decay rates, from which the median values are used to reconstruct the decay curve (cf. Figure 3.3). The statistical properties can be evaluated for the purpose of error estimation.

In order to keep the error margin low, the sampling rate of the pressure recordings has to be chosen sufficiently high. Experience has shown that recording with 32 768 samples/s suffices in the considered frequency range. The damping rates under non-reactive conditions are calculated from the median values obtained from 10 independent measurements [152]. However, in the context of this work, the impulse response method is used under non-reactive operating conditions only. Under reactive conditions, the method presented hereinafter is much more convenient since it exploits the inherent, stochastic forcing of the flame.

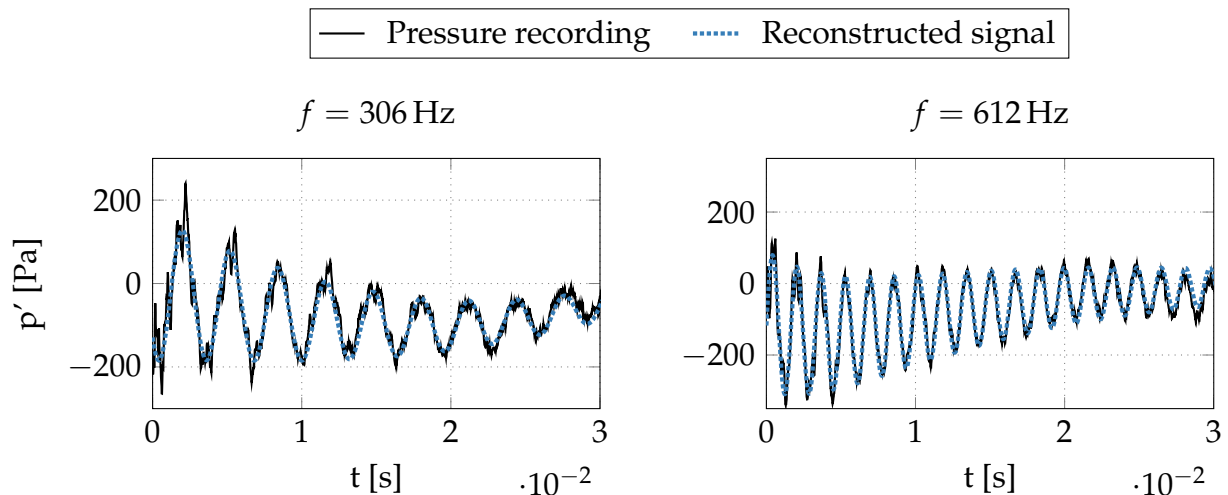


Figure 3.3.: Representative measured and reconstructed decaying pressure time series for two resonant frequencies of a combustor with mean flow.

3.4.2. Stochastic Forcing Method

The second method introduced here also relies on Bayesian inference to extract the eigenfrequencies and the damping rates from dynamic pressure data. In contrast to the impulse response method (see Section 3.4.1), no external forcing is required and instead the inherent combustion noise of the flame acting as a broadband thermoacoustic driver is evaluated by means of its autocorrelation function. This method was first introduced in [149] and has been validated by synthetically generated data with known frequencies and damping rates. The mathematical background and basic assumptions are provided in Section 2.6.2. A numerical validation study demonstrating robustness and accuracy of the method along with an error analysis can be found in Appendix B. Moreover, the method has already proved its applicability to premixed combustion chambers [149], to annular combustors [17] and to a premixed combustor with water injection [150]. In the context of this work, the stochastic forcing method is used to quantify the stability margin of the combustor with water injection for two resonant frequencies over a wide range of operating conditions by evaluating the thermoacoustic damping rates. Experimentally determined eigenfrequencies and damping rates are used to validate numerical predictions of the thermoacoustic stability, discussed later in Chapter 8.

The basis for this novel measuring method is provided by earlier work from Lieuwen [94]. He proposes that, in general, the damping coefficient of a combustion system can be obtained from the envelope of the autocorrelation function by assuming exponential decay according to $\exp(-\nu_n \tau)$. The autocorrelation $k_{\eta_n \eta_n}$ is obtained in advance from a bandpass filtered pressure signal. However, this method requires care in choosing an appropriate filter width so that neither energy from adjacent modes is captured nor the autocorrelation is solely dominated by the filter properties. Additionally, the envelope may only be considered over a certain range of oscillation periods to avoid over- or underestimation of the damping coefficient. In order to overcome these difficulties, Bayesian parameter estimation is used in the proposed approach to extract the damping rates and the eigenfrequencies directly from the autocorrelation function of an unfiltered pressure signal (see Equation (3.11)). As with the impulse response method, the parameter estimation is also carried out by a Gibbs Sampler (see Section 2.7.5) and

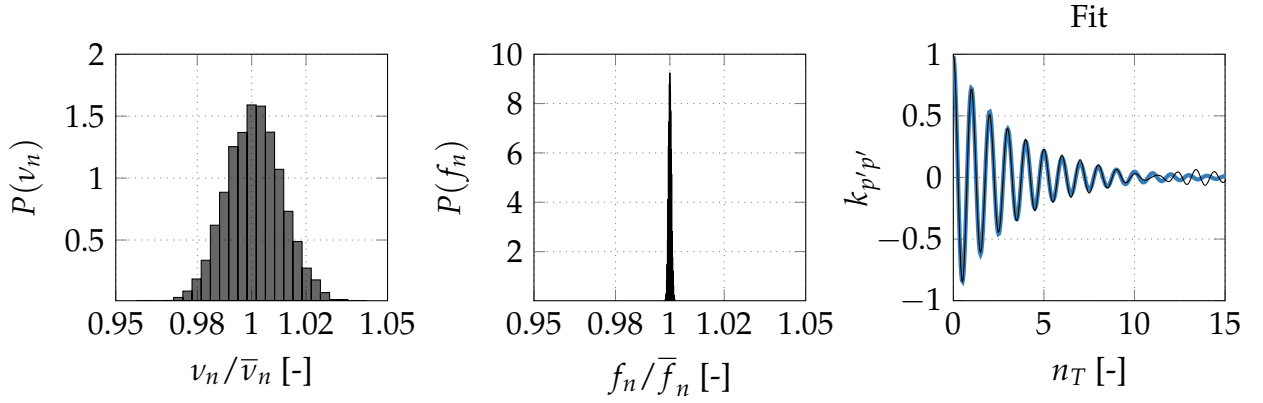


Figure 3.4.: Probability densities of the normalized damping rate and frequency and reconstructed autocorrelation function over the number of oscillation cycles for a representative pressure time series.

allows for a direct identification of the parameters ν_n and ω_n for each mode η_n . When using autocorrelation functions of an unfiltered pressure signal it was found to improve the robustness of the identification procedure by introducing the weighting coefficients A_n as additional fitting parameters. Thus, the full model equation for the autocorrelated raw pressure signal reads:

$$k_{p'p'} = \sum_{n=1}^N \exp(-\nu_n \tau) A_n \cos(\omega_n \tau). \quad (3.11)$$

The resulting curve fit according to Equation (3.11) is obtained using the median values of the statistical distributions. The goodness of the statistical fit is assessed by means of the standard deviation σ from the respective mean value, supplied by the PDFs (see Figure 3.4). The Gaussian distribution of the identified coefficients ν_n and $f_n = \omega_n/2\pi$ confirms the convergence of the Gibbs sampler.

In the implementation of the stochastic forcing method, requirements in terms of a minimum sample length of the measurement data sets are fairly moderate. In particular, an evaluation of the damping rates is even possible from time series of a length of the order of a few seconds. However, in order to ensure that the obtained damping rate represents a sufficient statistical average pressure time series recorded over a period of 60 s are taken into account. The sampling rate has been chosen to 32 768 samples/s. Experience has shown that considering a number of 15 oscillation periods n_T with a frequency resolution of approximately 30 points per period is

a reasonable choice to obtain robust results at low cost of computational time.

3.4.3. Determination of Acoustic Dissipation and Flame Gain

Evaluating the transfer function between heat release rate and pressure time traces allows for a direct extraction of the pure acoustic damping rate α_n [22,73]. The theoretical basis for this method is outlined in Section 2.6.2.1. Under reactive conditions, the acoustic dissipation α_n can be interpreted as the damping rate of the combustor with a passive flame. This work investigates how water injection affects the acoustic dissipation and the flame gain. The pure flame gain β_n can be retrieved by subtracting the thermoacoustic damping rate ν_n from the acoustic damping rate α_n , using the relationship given in Equation (2.96).

Experimentally, the transfer function between heat release oscillations and dynamic pressure H_{pq} (see Figure 3.5) can be obtained from simultaneously acquired time series of dynamic pressure and integral intensities of the OH^* -chemiluminescence. In this respect, the fluctuations of the integral OH^* -chemiluminescence intensity are assumed to be proportional to the

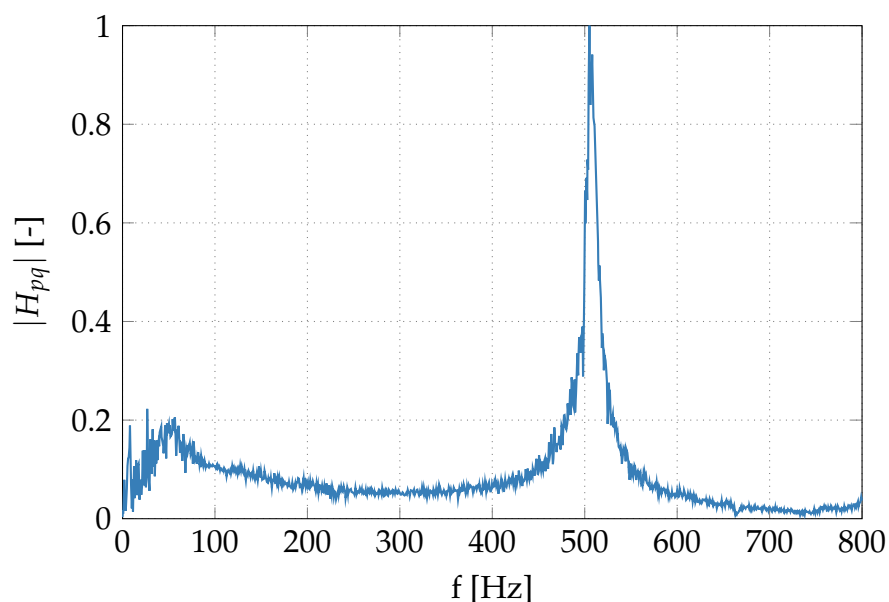


Figure 3.5.: Transfer function between integral OH^* -chemiluminescence as a marker for unsteady heat release and dynamic pressure.

heat release fluctuations $q'(t)$. In the measurement procedure, first the transfer function between heat release oscillations and dynamic pressure H_{pq} (see Equation (2.103)) is calculated. The parameters α_n and ω_n are subsequently identified from Bayesian parameter estimation by fitting them to the autocorrelation function $k_{\eta q}$ (see Equation (2.104)), as demonstrated in [73].

Both the measurement and post-processing procedures are analogous to those described in Section 3.4.2. The spatially integrated intensity of the OH^* -chemiluminescence is recorded in parallel by a UV-photomultiplier, which is equipped with a band-pass filter of the characteristic wavelength of $\lambda_{\text{OH}^*} = 307 \pm 5\text{nm}$.

3.4.4. Growth Rate Determination

Under linearly unstable operating conditions, neither the impulse response method nor the stochastic forcing method are applicable since they presume a linear correlation between flame response and acoustic pressure. In this case, the thermoacoustic damping rate of the overall system is negative, indicating a growth of the pressure pulsations until saturation occurs and the pressure oscillates in a limit cycle. In the context of this work, self-sustained limit cycle oscillations occur only for a small number of operating conditions. Nevertheless, their growth rates are of interest in order to make quantitative statements. To this end, the growth rate $\nu < 0$ is calculated by linearizing the limit cycle oscillations by means of their slowly varying amplitudes instead of the pressure oscillations itself. The method was originally introduced by Noiray and Schuermans [111], the underlying mathematical framework of this method is outlined in Section 2.6.2.2. Using dynamic pressure recordings from a limit cycle, the growth rate is obtained by fitting the right hand side of Equation (2.109) to the autocorrelation function calculated from the fluctuating, slowly varying amplitudes \mathcal{A}' . To obtain the \mathcal{A}' , a pressure time trace p' is first filtered around the frequency of interest f_n before the Hilbert transformation is calculated and the mean value $\bar{\mathcal{A}}$ is subtracted. In contrast to the autocorrelation function of the pressure signal itself, $k_{\mathcal{A}'\mathcal{A}'}$ exhibits a purely

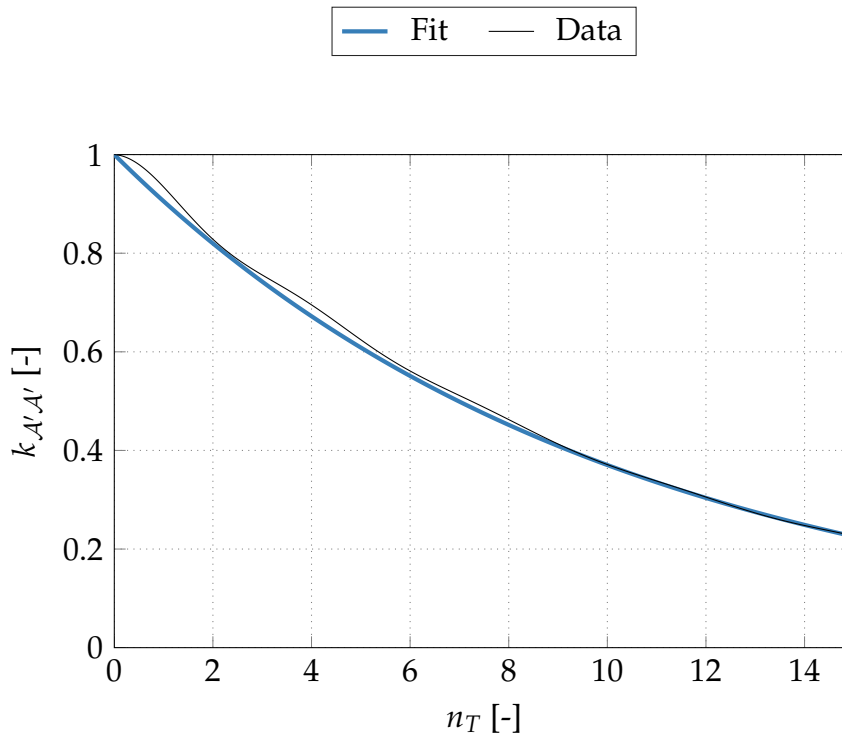


Figure 3.6.: Representative autocorrelation function of the slowly varying amplitude fluctuations for a limit-cycle oscillation.

exponential decay without any oscillatory component (see Figure 3.6). In this case, the growth rate is obtained by a simple least-squares fit.

3.5. Flame Imaging

Flame shape and position under steady operation as well information on intensity and location of the flame's oscillation activity are obtained from OH^* -chemiluminescence images. Analyzing the spatial distribution of the flame's chemiluminescence intensity has found wide application in combustion diagnostics [62] since it can often be interpreted as a marker for heat release [84]. In this work, the spatially resolved intensities of the OH^* -chemiluminescence are derived from images recorded by a PhotronTM SA-X high-speed camera in combination with a Hamamatsu C10880 image intensifier. Both are aligned perpendicular to the flow direction and are interconnected by an optical coupling element. The intensifier is equipped with a narrow band interference filter having a maximum transmission of

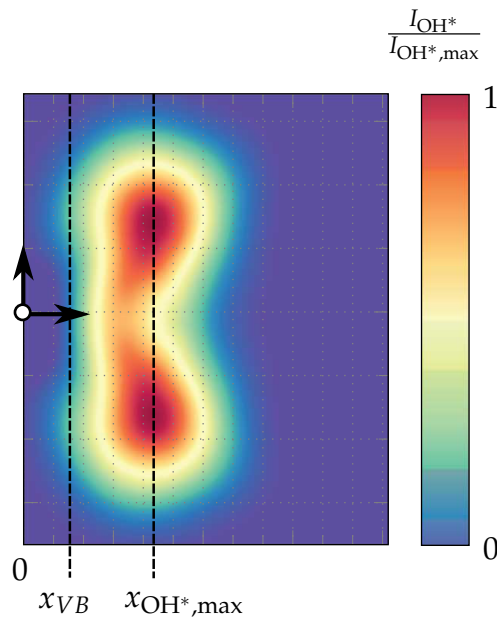


Figure 3.7.: Determination of the flame position from time-averaged OH*-chemiluminescence images.

16.17% and a bandwidth of 307 ± 5 nm corresponding to the characteristic wavelength of the OH*-radical is used.

3.5.1. Stationary Flame Images

Stationary flame images are acquired to obtain flame shapes and positions depending on the amount of water injected. For this purpose, line-of-sight integrated images are recorded at a rate of 1500 frames/s and are time-averaged over a set of 3000 images, respectively. Due to the high degree of rotational symmetry of the flame, Abel deconvolution is conducted using the Fourier method [126] which allows to calculate the OH*-intensity distribution in the centerplane of the combustor. In order to facilitate the comparability of the flame shapes and positions between the various operating conditions with and without water injection, the processed images are scaled to a color range from 0 (no intensity) to 1 (maximum intensity) by normalizing with the individual maximum OH*-chemiluminescence intensity of the respective set of images. The flame position is evaluated by means of the distance of the vortex breakdown from the burner exit (see Figure 3.7). This parameter will be termed axial stand-off distance of the

flame and is denoted as x_{VB} . Consistent with previous work by Bade [11], the axial position of the recirculation zone is defined at the position where

$$x_{VB} = x \left(I/I_{OH^*,\max} = 0.18 \right). \quad (3.12)$$

3.5.2. Phase-Resolved Flame Images

Phase-resolved flame images serve for the purpose of extracting local amplitude and phase information about the dynamic flame response. The results can be interpreted as a spatially resolved FTF associated with a certain oscillation frequency. Apart from illustrating intensity and motion of heat release waves in the flame, this technique is valuable for understanding the behavior of the global FTF. In contrast to conventional time averaging, the flame images are averaged for each phase angle to represent one oscillation period at a particular oscillation frequency. Phase-locked flame images can in general be recorded by using a time delayed reference signal (e.g. from a pressure sensor or the excitation unit) [114] as a trigger. This has the advantage that only very low image acquisition rates of the camera are required. However, when using a high-speed camera with a sufficiently high image acquisition rate - as available in the present setup - off-line phase averaging is a more flexible option. This method does not require an external trigger and allows to analyze multiple frequencies from one set of data at once [63]. In addition, the experimental effort is comparably low since the evaluation procedure is carried out apart from the experiment at a later stage. In addition, the method allows the analysis of images without external excitation by sorting the captured images according to any frequency content of interest. Thus, the latter method is used in this work. For this purpose, camera, image intensifier and interference filter are identical to the preceding method (see Section 3.5.1), whereas the image acquisition rate is chosen such that it is at least 12 times higher than the oscillation frequency to be investigated. Phase-averaging is performed over a set of in total 10916 images. Besides the image data itself, pressure data from a reference sensor as well as the recording trigger signal of the camera are required. The latter serves as a time stamp for each acquired image. The timing scheme of the recorded signals is depicted in Figure 3.8. Procedurally, the pressure signal obtained at a fixed reference location is

first band-pass filtered around the frequency of interest. Subsequently, a Hilbert Transformation is applied to extract the instantaneous phase angles from the pressure time traces. The individual images are then sorted according to their respective phase angle and are finally averaged over all oscillation cycles. By applying a fast Fourier transform (FFT) to each pixel, the resulting two-dimensional field is expressed by the complex valued Fourier coefficient, according to:

$$\mathcal{F} [\underline{I}(x, z)] = \frac{1}{N} \sum_{n=1}^N \underline{I}_n(x, z) \exp(i\varphi_n), \quad (3.13)$$

which represents a phase-locked ensemble average of the OH*-intensity fluctuations over one oscillation period. Therein, N denotes the total number of considered phase intervals φ_n and \underline{I}_n is the vector field containing the information of one individual image. From the resulting amplitude image, the regions of high intensity fluctuations can then be identified. The phase image represents the temporal relation of the intensity fluctuations with respect to the reference pressure sensor. In order to eliminate

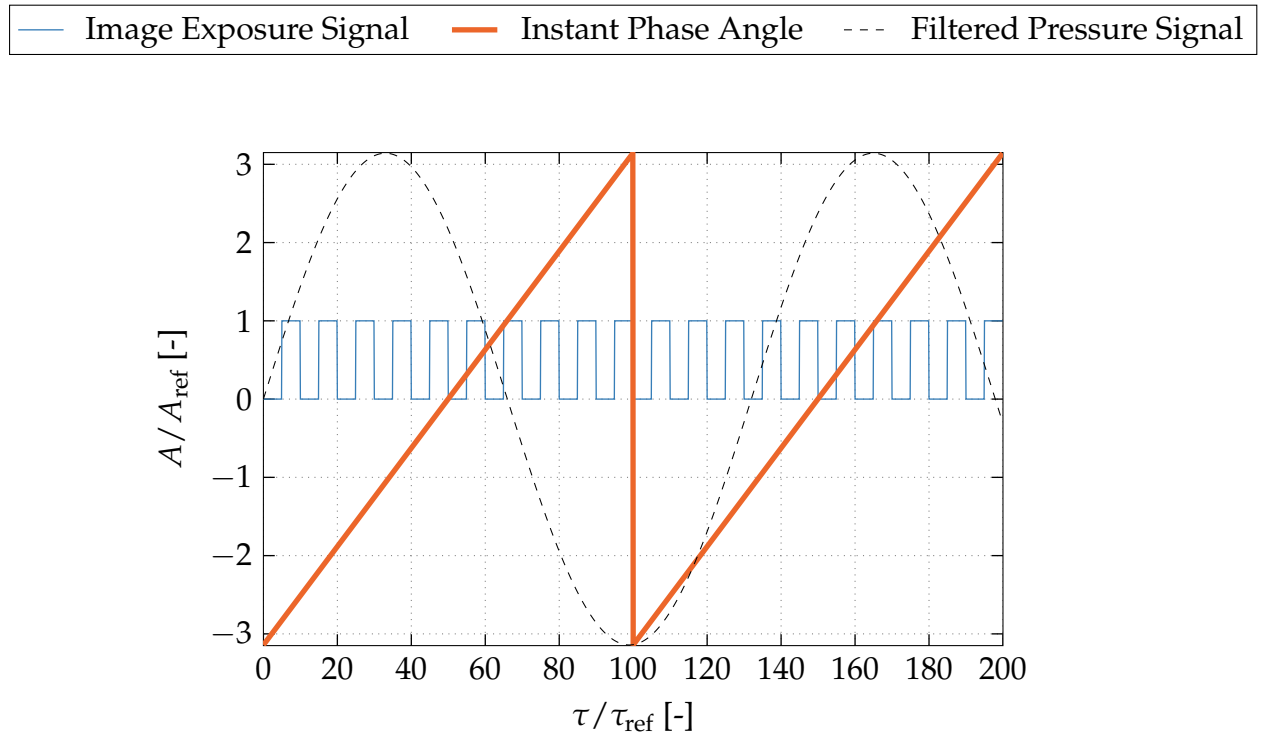


Figure 3.8.: Triggering scheme for offline phase averaging of OH*-chemiluminescence images.

unwanted distortions from the phase image from pixels with negligible amplitude, each individual phase value is weighted with its corresponding amplitude value. The amplitude is then expressed by the brightness and the phase by the color.

3.6. Spray Distribution and Droplet Sizes

In order to determine the qualitative distribution of the water spray in the flame and the mean droplet diameters, laser-optical methods are used. The spray distribution is derived from analyzing Mie-scattering intensities and the droplet diameters are determined using a Malvern Particle Sizer. Both techniques are briefly outlined in the following.

3.6.1. Mie-Scattering

Droplets scatter light when being illuminated, while steam does not. The higher the particle density is, the higher is the scattered light intensity and in the absence of interfering reflections, a scattering light intensity of zero indicates that no droplets exist in the field of view. Thus, it is possible to draw inferences on the spatial distribution of the water droplets in the flame by exposing the droplets to laser light and measuring the Mie-scattering intensity perpendicular to the line of sight [127].

To analyze the spatial distribution of the water spray in the combustor, a pulsed Nd:YLF high-speed PIV laser with a maximum pulsation frequency of 10 kHz is used. Employing a cylindrical lens with a focal length of -25 mm and a biconvex lens with a focal length of 500 mm, a laser sheet is generated parallel to the flow axis. The laser sheet is adjusted such that it covers the entire centerplane of the main combustion zone and has a thickness of approximately 0.5 mm. The spatially distributed Mie-scattering of the particles is recorded using a high-speed camera that is equipped with an optical bandpass filter with a width of 531 ± 10 nm at a recording rate of 2000 frames/s. Intensity images are averaged over a set of 5458 images and a background image is subtracted to eliminate disturbing reflections. From this, contours of light-intensity levels are evaluated which

qualitatively represent the spatial distribution of the water droplets in the flame.

3.6.2. Particle Sizing

Global droplet sizes are determined from laser diffraction. The used device consists of a transmitter and a receiver, whereas the transmitter emits a beam of Helium-Neon laser light of the wavelength 632 nm and a diameter of 10 mm. The receiver consists of an optical lens system combined with a ring-shaped photodiode array. The measurement principle works as follows: If no droplets exist between transmitter and receiver, the undisturbed laser light reaches the center of the diode array, otherwise the light is scattered by the particles. Small particles scatter the incoming laser light at large angles whereas for larger particles the scattering region narrows and results in a forward scattering at smaller angles. This causes the intensity of the scattered light to increase [161]. From the intensity distribution across the detector, the particle size distribution can be determined by using Mie theory [35]. Due to the line-of-sight integration in the beam direction, the method is only suitable for the determination of global droplet size distributions and cannot account for spatial deviations. In the present work, measurements of global droplet sizes are performed in an external spray test stand. Measurement data are acquired with a recording rate of 1 Hz over a time period of 60 sec to capture a statistically sufficient number of particles. As the measure for the droplet size, the Sauter mean diameter (SMD) is selected which is widely used for characterizing droplet properties in the field of combustion science [89] and thermoacoustics [29, 43]. The SMD, in the following denoted as d_{32} is a representative diameter of a droplet which has the same volume-to-surface ratio as the entire spray and is defined as:

$$d_{32} = \frac{\sum_{n=1}^N N_n d_n^3}{\sum_{n=1}^N N_n d_n^2}, \quad (3.14)$$

whereby d_n is the diameter of the n -th droplet in a control volume containing a number of N spherical droplets. Physically, the SMD represents the volume-to-surface ratio which dominates heat and mass transfer phenomena related to the spray [89, 161].

4 Experimental Setup

Experimental investigations presented in this thesis are carried out in a single burner test-rig under atmospheric conditions. Firstly, the components of the test-rig are described in detail. Special attention is given to the modular swirl burner which incorporates the injection system to investigate premixed turbulent natural gas flames with water injection. The test-rig provides the necessary prerequisites to apply the acoustical and optical measurement techniques which were described in Chapter 3.

4.1. Atmospheric Single Burner Test-Rig

The atmospheric single burner test-rig is schematically shown in Figure 4.1. The main combustion air is taken from the laboratory's compressed air supply at a pressure of 12 bar and is filtered and reduced to a pressure level of 10 bar. Before entering the test-rig section, air is pre-heated by an electric pre-heater ① to provide a constant combustor inlet temperature of $T_{ph} = 573$ K. Natural gas is supplied directly after the pre-heater in order to ensure a perfect mixture of air and fuel. Due to the long mixing distance between fuel supply and combustor, fluctuations of the equivalence ratio are avoided. Before entering the plenum section ③, the flow is split into two paths, one flows through the upstream siren and the other one is directly supplied to the plenum section through a bypass. The upstream siren unit ② consists of a disk with double sine shaped orifices to harmonically excite the mass flow. The unit is driven by an electric motor with a frequency converter to allow for controlling the rotational speed. More details on this siren unit can be found in [42]. A second siren ⑥, placed downstream of the combustor is supplied by pressurized air flowing through a fast-switching modulator valve. This valve allows to instantaneously interrupt the excitation source (see Figure 4.2). Using the siren arrangement in its standard configuration, two linearly independent

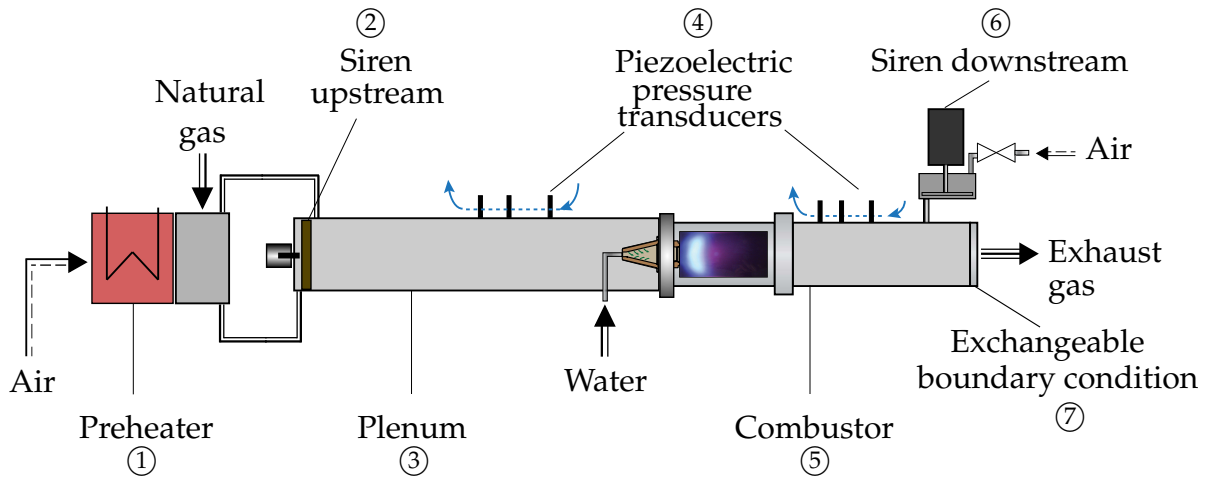


Figure 4.1.: Schematic of the atmospheric single burner test-rig.

excitation states can be created in order to apply the multi-microphone method (MMM). Additionally, the siren on the downstream side can be used for externally forced decay rate measurements using the impulse response method.

The plenum section ③ basically consists of insulated, cylindrical pipe elements with an inner diameter of $d_p = 124$ mm and a length of $l_p = 1365$ mm. The combustion chamber ⑤ has a rectangular cross-section with an area of $A_{CC} = 150 \times 150$ mm over a length of $l_{CC} = 730$ mm. Heat is removed from the combustor's external surfaces by impingement cooling. The available cooling system allows a maximum permissible thermal power of the flame of approximately $P_{th} = 65$ kW.

At the exit of the combustor, two different terminations ⑦ can be attached to provide varying acoustic boundary conditions. Low acoustic reflectivity is achieved by using a perforated disk e.g. when conducting externally excited measurements. Alternatively, a venturi nozzle is available which serves as an acoustically hard boundary condition. Using the nozzle termination, a reflection coefficient close to unity can be achieved over a wide range of frequencies. Both, the plenum and the combustor are equipped with three water-cooled PCB 106B piezo-electric pressure transducers ④. The probes are placed in non-equidistant intervals to each other. Pressure transducers located in the combustion chamber are additionally purged

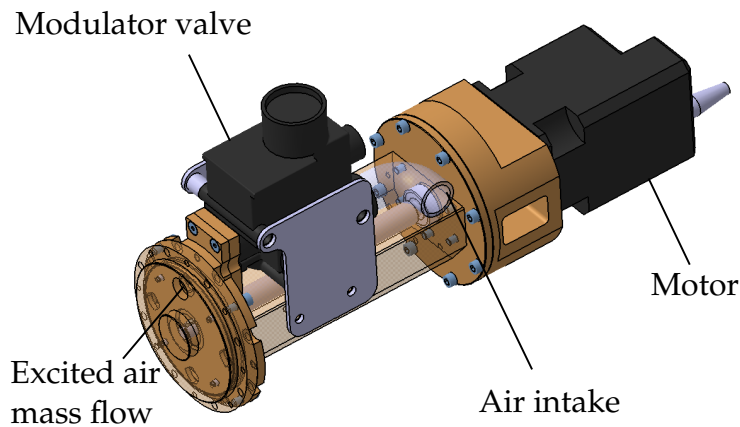


Figure 4.2.: Downstream siren for acoustic excitation with modulator valve for decay rate measurements using the impulse response method.

with air to avoid condensation of hot exhaust gas. Temperatures are acquired by means of several K type thermocouples.

4.2. Swirl-Burner with Water Injection

The used modular swirl burner system originates from Sangl [135] and is optimized for high flame flashback safety and low NO_x -emissions over a wide range of operating conditions. The burner consists of a divergent swirler with an attached converging mixing tube. The swirler has four tangential slots and an additional head air inlet at the tip of the cone. In general, the swirl number and the axial momentum can be adjusted by varying the slot width b_s or the free head air inlet ratio A_f . The burner configuration used in this work is a variant of the original swirl burner design, scaled down by a factor of 2.3 [134] with a fixed slot width but a variable head air inlet. The basic design has a fully open head air inlet corresponding to $A_f = 100\%$. The swirler is followed by a conical mixing tube which is available in various lengths l_{MT} . In the current setup, the longest mixing tube with a length of $l_{MT} = 1.875 d_B$ is used, where d_B is the diameter of the burner outlet. From a thermoacoustical viewpoint, the mixing tube produces a convective time delay between the fluctuations of swirl and axial velocity at the burner exit [87]. Vortex breakdown occurs

after a sudden change of the cross section between burner outlet and combustion chamber. This causes the flame to stabilize inside the core flow at the tip of a recirculation zone. The flame propagates through the inner shear layer whereas no reaction takes place in the outer shear layer due to heat loss and strain. This baseline configuration has already been extensively studied with regard to its thermoacoustic properties by Bade [11]. In the present work, this basic design of the swirl burner is used to create a modified version with an integrated water injection system. In order to operate the combustor with a lean-premixed, aerodynamically stabilized flame with water injection, the swirl burner is supplemented with a suitable injection system for liquid water. The present work will focus on measurements at very high injection ratios which are of particular technical interest for the highest possible load increase at constant flame temperature. At this point, the water-to-fuel ratio Ω is introduced, i.e.:

$$\Omega = \frac{\dot{m}_{\text{Water}}}{\dot{m}_{\text{Fuel}}}. \quad (4.1)$$

In the present configuration, water-to-fuel ratios of up to 2 are intended. In combination with the given burner and test-rig setup, this results in the following requirements for the design of the injection system:

1. A broad range of water-to-fuel ratios should be covered to reach at least $\Omega = 2.0$ for a given operating point.
2. Water must reach the combustion chamber in the liquid phase and evaporation should be completed before reaching the main reaction zone.
3. Even for the highest values of Ω , no impingement of water droplets should occur either within the mixing tube or at the combustor walls.
4. Steady atomization of the supplied water must be ensured at all times.
5. The water droplets should be distributed as homogeneously as possible over the burner exit plane.
6. The influence of the water injection system on the fluid-dynamic properties as well as on the acoustic scattering behavior of the burner should be low.

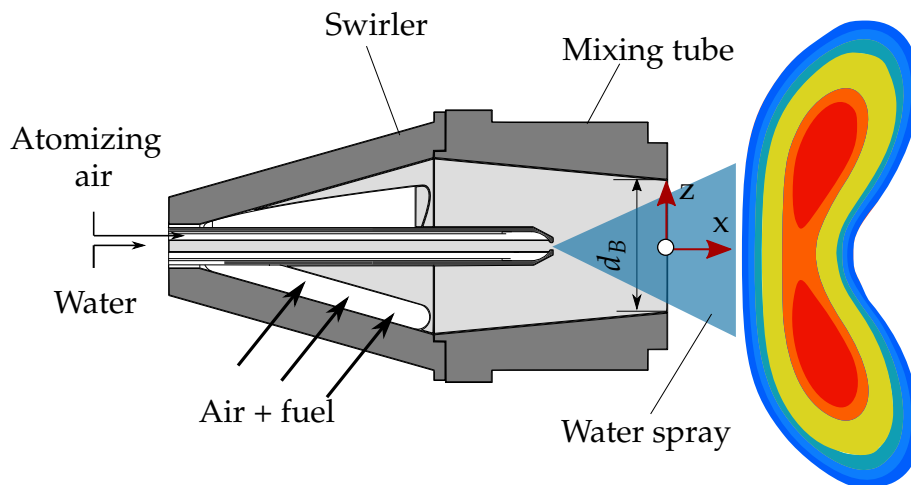


Figure 4.3.: Modular swirl burner with water injector.

In order to meet these requirements best and to reconcile the existing infrastructure as far as possible, a water injection lance is introduced through the head air inlet of the burner (see Figure 4.3). This leads to a reduction of the free axial head air to $A_f \approx 19\%$. The tip of the lance defining the point of injection is located at $0.125 l_{MT}$ upstream of the burner outlet. A twin-fluid nozzle, which is supplied by pressurized air is used for the atomization of water. The advantage of this system is that the water injection pressure is kept low and, in contrast to pressure atomizers, droplet size and water mass flow remain decoupled from each other [88]. The injector is equipped with an inner air swirler to enhance the atomization process. Its swirl direction is identical to the swirl direction of the main air flow through the burner. The water nozzle has a hole diameter of 0.5 mm. The flow rates are regulated by digital mass flow controllers. Water is filtered and deionized before entering the injector. The amount of the atomizing air is kept constant at all times. With this system an operating window of water mass flows $0.75 \leq \dot{m}_{\text{Water}} \leq 2.5 \text{g/s}$ can be covered. Depending on the fuel mass flow of the respective dry operating point this corresponds to $0.75 \leq \Omega \leq 2.0$. Mass flows below the lower limit lead to unsteady atomization and thus to non-stationary water supply to the flame. Operation above the upper limit results in the impingement of water droplets inside the mixing tube. Both conditions must be avoided under all circumstances.

5 Stationary Flame and Flow Properties

This chapter discusses the stationary properties of the given combustor with a lean premixed flame and water injection. After introducing the operating conditions, distributions of the heat release and the water droplets are presented as well as the characteristic droplet sizes. Measured OH^{*}-chemiluminescence is used as a marker for the heat release rate. Interaction between water spray and flame is visualized by considering OH^{*}-chemiluminescence in combination with Mie scattering images. Finally, measured droplet sizes are discussed which are used to derive the atomization quality of the water spray.

5.1. Operating Conditions

The operational parameters of the test-rig are outlined in the following. Besides introducing the notation of the different operating ranges and points used in this work, focus is placed on pointing out which parameters are varied and which are kept constant depending on the operation mode of the combustor. First of all, four operating points are selected which provide an aerodynamically stable flame under dry, perfectly premixed conditions. These operating points will be termed *baseline cases* and serve as the starting point from which water-injection is initiated. The chosen baseline operating conditions cover three levels of equivalence ratios, namely $\phi_0 = 0.625, 0.667$ and 0.714 and two levels of thermal load of $P_{th,0} = 50$ kW and 40 kW (see Table 5.1), respectively. The operating conditions with water injection are chosen based on the baseline operating conditions. Selection criteria are, above all, that steady atomization is ensured at all times, no accumulation of water occurs on the inner mixing tube walls and the maximum thermal load of the combustion chamber is not exceeded. In this work, two fundamentally different operating modes with water injection will be considered: Firstly, water injection at constant

Table 5.1.: Overview on the operating parameters of the dry baseline operating conditions.

Operating point	Water-to-fuel ratio	Adiabatic flame	Thermal Load	Equivalence
	Ω [-]	temperature $T_{ad,0}$ [K]	$P_{th,0}$ [kW]	ratio ϕ_0 [-]
Ⓐ	0.0	1923	40.0	0.625
Ⓑ	0.0	2070	50.0	0.714
Ⓒ	0.0	1986	50.0	0.667
Ⓓ	0.0	1923	50.0	0.625

equivalence ratio, denoted by $\phi = \text{const.}$ and secondly, water injection at constant adiabatic flame temperature, denoted by $T_{ad} = \text{const.}$ A complete list of the respective operating parameters can be found in Appendix C.

In the first case, water is injected at a certain water-to-fuel ratio while leaving the thermal power P_{th} and the equivalence ratio ϕ constant. An increase of Ω causes a dilution of the flame with water and leads to a drop of the adiabatic flame temperature. An overview on the operating parameters is given in Table C.1 in the Appendix. In operating range Ⓐ $|\phi$ the injector performance limits the lowest achievable water amount such that the starting point is $\Omega = 1.2$ at $\phi = 0.735$. For all remaining operating ranges i.e. Ⓑ $|\phi$, Ⓒ $|\phi$ and Ⓓ $|\phi$ water injection at constant equivalence ratio refers to the respective baseline operating point (cf. Tables C.2-C.4 in the Appendix). For instance, water injection which originates from baseline case Ⓑ at a water-to-fuel ratio of 1.0 at equivalence ratio is denoted by Ⓑ $|\phi^{\Omega=1.0}$. The second, technically more relevant operation mode is water injection at constant adiabatic flame temperature. In this case, the simultaneous increase of the fuel mass flow compensates the temperature drop caused by the addition of water. Consequently, the equivalence ratio increases and so the thermal load does. For example, water-injection originating from the baseline case Ⓐ at constant adiabatic flame temperature with a water-to-fuel ratio of 1.0 is labeled Ⓐ $|\phi^{\Omega=1.0}$. Starting at an initial thermal load of $P_{th,0} = 40$ kW and at an equivalence ratio of $\phi_0 = 0.625$ allows to exploit the maximum achievable thermal load increase with water injection. In this

case, this corresponds to around 41% compared to the baseline operating point at a water-to-fuel ratio to $\Omega = 2.0$. This maximum load increase is achieved for the operating range ① $|_{T_{ad}}$, which ensures sufficient injection performance at all times and prevents the maximum thermal load of the combustor from being exceeded. During operation, the equivalence ratio is always maintained below unity (cf. Table C.1). The minimum achievable water-to-fuel ratio for this operating range is $\Omega = 1.0$ due to poor atomizer performance at low water flow rates. Operation within ② $|_{T_{ad}}$, ③ $|_{T_{ad}}$ and ④ $|_{T_{ad}}$ allows to start with a lower water-to-fuel ratio of $\Omega = 0.75$. However, here the maximum permitted heat load of the combustion chamber limits the upper value to $\Omega = 1.5$ (cf. Tables C.2-C.4).

5.2. Flame Shape and Flame Length

It is known from literature that water injection into flames leads to a decrease of the burning velocity [36, 99, 100]. Consequently, water injection into a swirl-stabilized premixed flame is expected to influence the flame shape and position by changing the heat release distribution. Knowledge on the flame position is important for understanding the dynamic flame response since it has a major impact on the time delay between acoustic perturbations and unsteady heat release. For this purpose, time-averaged images of OH^* -chemiluminescence are analyzed. The operating conditions cover the entire range of flames with and without water injection. From these images, the flame position is finally determined.

Firstly, operating range ① $|_{T_{ad}}$ is selected as a representative example to discuss the impact of the water-to-fuel ratio on the flame shape. Water-to-fuel ratios are considered in the range of $0 \leq \Omega \leq 2.0$. The resulting time averaged, Abel-deconvoluted flame images are shown in Figure 5.1. Assuming rotational symmetry of the flame, the distribution of the intensities can be regarded as representative for the combustor center plane. Note that the values have been normalized with the maximum value of the respective mean image. For the case $\Omega = 0$, first, a compact flame is found which stabilizes at about $1 \cdot d_B$ downstream of the burner outlet. With water injection at a water-to-fuel ratio of 1.0 at constant flame temperature, both an axial displacement of the reaction zone and an increase of the

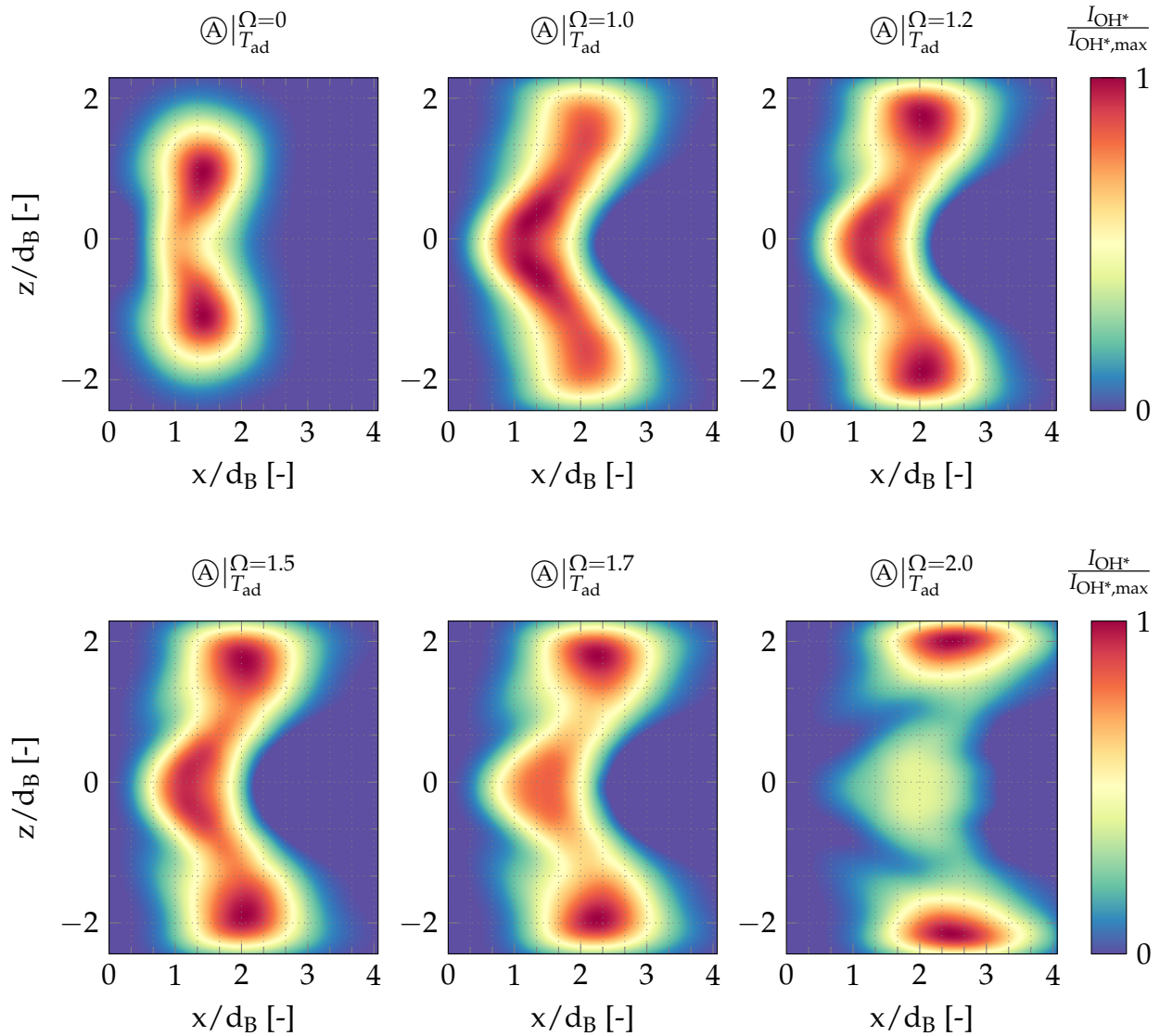


Figure 5.1.: Spatial distribution of the OH*-chemiluminescence intensity in the combustor centerplane with water injection at constant adiabatic flame temperature for operating range $\textcircled{A} |_{T_{\text{ad}}}$.

flame volume can be observed. The images exhibit increasing dispersion of the heat release zone with increasing water-to-fuel ratio. In addition, the outward, radial displacement of the zone of maximum heat release indicates that the flame approaches the combustor wall with increasing water content. At the same time, dilution of the reaction zone near the combustion chamber centerline is observed, which is most distinct in the case of $\textcircled{A} |_{T_{\text{ad}}}^{\Omega=2.0}$.

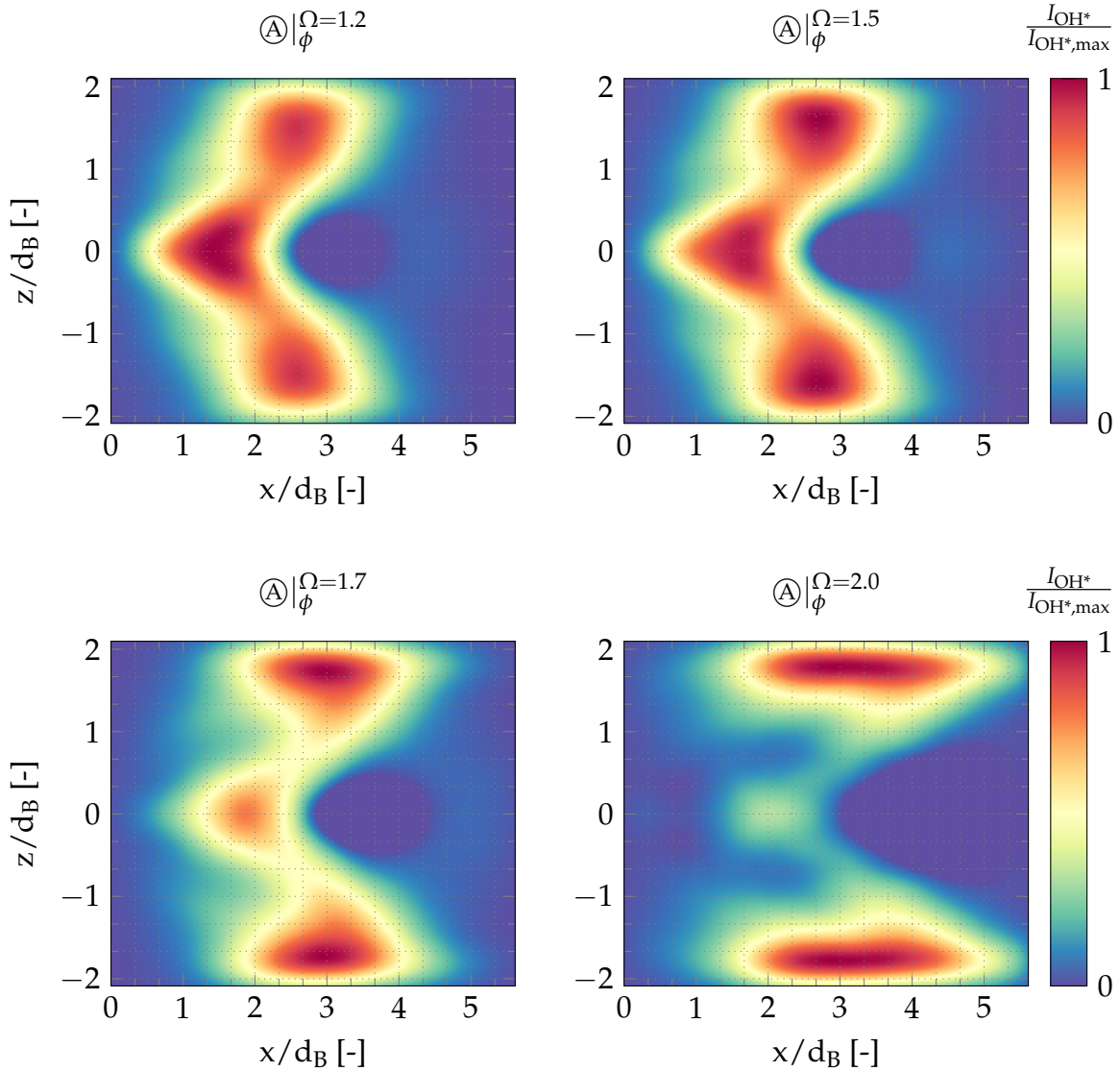


Figure 5.2.: Spatial distribution of the OH^* -chemiluminescence intensity in the combustor centerplane with water injection at constant equivalence ratio for operating range $\textcircled{A} |_{\phi}$.

It is known from previous work [7, 50, 66] that the interaction between the flame and the combustion chamber wall has also an impact on the flame transfer function (FTF). In the present case, the radial expansion of the flame with water injection leads to higher fluctuations of the vorticity. Therefore, a stronger flame response is expected in the lower frequency range. In addition, the observed axial dilution of the reaction zone increases the dispersion of the convective time scales with increasing water-to-fuel ratio. It is expected that this will lead to a weaker flame response with a longer time delay toward higher oscillation frequencies.

The results for water injection at constant equivalence ratio are displayed in Figure 5.2. It can be seen that the effect of an increase of Ω at constant ϕ is much stronger compared to the case of constant T_{ad} . This effect can be explained by the drop of flame temperature when water is injected at constant ϕ . Compared to water injection with the same water-to-fuel ratio at constant flame temperature, this additionally leads to a significant reduction of the burning velocity. Due to the dilution effect of water, similar effects are expected as with the reduction of the equivalence ratio for dry flames. In particular, a longer time delay between unsteady heat release and acoustic velocity is expected which causes a stronger low-pass behavior of the flame response. A comparison of the effects of water injection on heat-release and emissions at constant equivalence ratio and at constant flame temperature in a similar setup can be found in [90–92].

In the next step, the flame positions are derived from these time-averaged flame images. The characteristic flame length is represented by the axial stand-off distance of the recirculation zone x_{VB} . This quantity will be later used as a scaling parameter for the FTFs (see Section 6.3). The results are shown in Figure 5.3, wherein x_{VB} is plotted over the water-to-fuel ratio. The operating ranges introduced in Section 5.1 are considered at constant flame temperature and at constant equivalence ratio. Regarding the baseline operating points under dry conditions, the lowest value of x_{VB} is found for the richest operating point ②. The largest values occur for the leanest operating point with the lowest thermal power ①. Note that operating points ① and ④ only differ in their initial thermal load ($P_{th,0} = 40$ kW resp. 50 kW) but are equal in the equivalence ratio and thus have adiabatic flame temperatures. Both operating conditions are very similar regarding their flame positions which is consistent with findings from Bade [11]. Initiating water injection at constant flame temperature from each of these baseline operating conditions leads to a steady rise of x_{VB} with increasing water-to-fuel ratio. For operating range ② $|_{T_{ad}}$, however, this increase is much steeper compared to the remaining cases. The most moderate increase of the flame length is found for operating range ①.

However, water injection at constant equivalence ratio has a different influence on the axial position of the recirculation zone. Here, the initial increase of Ω first of all causes a much stronger rise of x_{VB} than at constant flame temperature. The measurements indicate that an increase of Ω be-

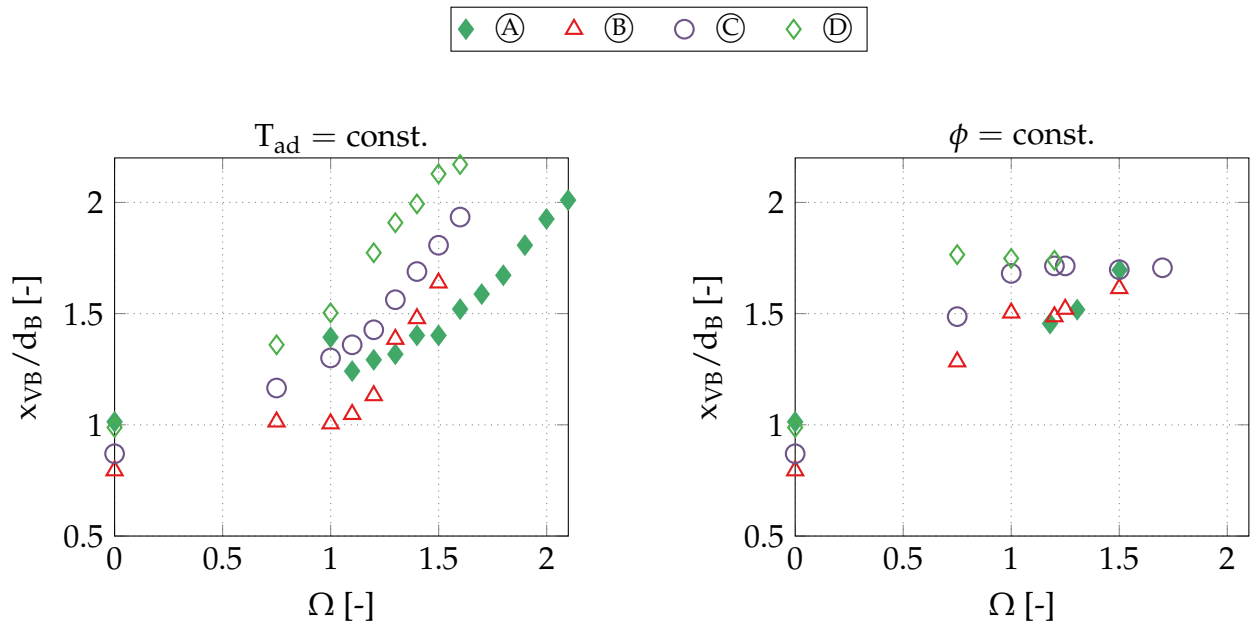


Figure 5.3.: Normalized axial stand-off distance of the vortex breakdown of the flame with water injection.

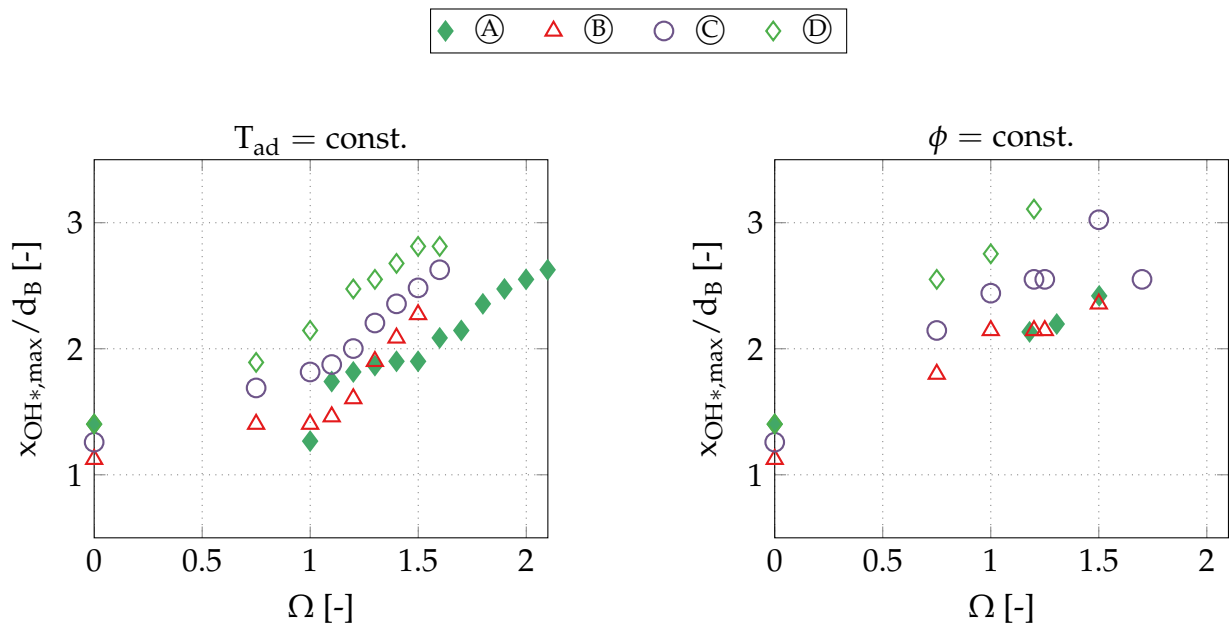


Figure 5.4.: Normalized axial position of maximum OH^* -chemiluminescence intensity in the flame with water injection.

yond a value of 1.0 causes no further significant axial displacement of the recirculation zone. This seems surprising at first since the axial location of the maximum OH^* -chemiluminescence (cf. Figure 5.4) indicates that especially the location of maximum heat release is disproportionately shifted downstream when adding water at constant equivalence ratio. Compared to identical values of Ω at constant adiabatic flame temperature, in most cases $x_{\text{OH}^*,\text{max}}$ is significantly higher for constant equivalence ratio.

5.3. Spray Distribution

In the following, Mie scattering images are presented to analyze the spatial distribution of the liquid water droplets in the combustor center plane. The underlying measuring principle is outlined in Section 3.6.1. Based on the results, it will be assessed whether the designed water injection system operates as intended. Experimental results are presented below for operating range $\textcircled{A} |_{T_{\text{ad}}}$ at water-to-fuel ratios of $\Omega = 1.0, 1.5$ and 2.0 .

To illustrate the spray distribution with respect to the mean heat release field in the flame, Mie scattering images are presented superimposed with

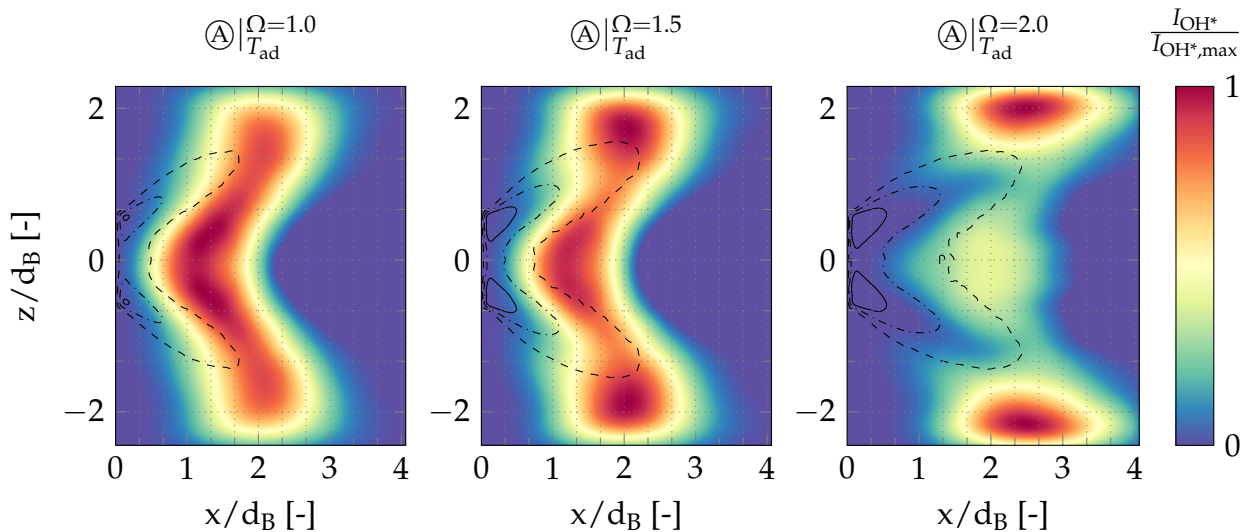


Figure 5.5.: Superposition of OH^* -chemiluminescence intensity and Mie scattering intensity in the combustor centerplane for operating range $\textcircled{A} |_{T_{\text{ad}}}$. Lines correspond to Mie scattering intensity levels of 40% (—), 10% (---) and 1% (· · ·) of the overall maximum intensity.

the mean intensities of OH^{*}-chemiluminescence. The latter were already discussed in Section 5.2. Results are shown in Figure 5.5. The local droplet densities are represented by isolines extracted from each averaged set of Mie scattering images. These correspond to constant values of 1%, 10% and 40% of the overall maximum scattering light intensity. Zones with high droplet densities occur in all cases very close to the burner outlet. Low droplet densities can be observed near the burner centerline, while the spray becomes denser with increasing radial distance. In all cases, the droplet density decreases with increasing axial distance to the burner outlet. In combination with the OH^{*}-images, it can be seen that areas of the flame with high heat release rarely coincide with zones of high droplet densities. This applies up to a water-to-fuel ratio of $\Omega = 2.0$ at constant flame temperature. Consequently, it is assumed that the injected water enters the combustion chamber in liquid form and the droplets are almost completely evaporated as soon as the main combustion zone is reached. Considering the evaporation process as a heat sink thus appears justifiable. An extensive study on the inference between heat release rate and droplet evaporation in a similar configuration is given in [90].

5.4. Droplet Properties

In the following, measured mean droplet sizes of the water spray will be discussed. First of all, this serves to determine the atomization quality of the spray over the entire operating window of injection flow rates. From the measured droplet diameters, conclusions are drawn on frequency ranges of possible interactions between the acoustic field in the combustor and the droplets.

The results presented below were obtained by laser diffraction (see Section 3.6.2) of the water droplets when operating the water injector in a quiescent environment using an external spray measurement rig. The axial distance between the injector outlet and the measuring volume is $2.5 d_B$. This value corresponds approximately to the distance between the water nozzle and the axial stand-off distance of the flame's recirculation zone (x_{VB}) in the combustion test-rig. In all experiments, the atomization air mass flow is $\dot{m}_{\text{air,at}} = 1 \text{ g/s}$. In Figure 5.6, the Sauter mean diameter (SMD)

is plotted over the droplet loading with respect to the atomization air flow. The water-to-fuel ratios for operating points of $\textcircled{A} |_{T_{\text{ad}}}$ are marked with vertical lines. These correspond, from the left to the right, to $\Omega = 1.0, 1.2, 1.5, 1.7$ and 2.0 , respectively. The measurements yield droplet diameters between 24 and $30 \mu\text{m}$ in the range of $1.0 \leq \Omega < 2.0$. This corresponds to an overall increase of the Sauter mean diameter by 25% when doubling the water-to-fuel ratio.

According to Chishti [29] droplets exhibit a second order response to acoustic fluctuations which results in oscillating droplet velocities and periodic displacement of the droplets. Sprays are particularly susceptible to oscillations at low frequencies. The associated cut-off frequency is determined by the relaxation time of the droplets, which correlates with the mean droplet size. More precisely, the spray reacts to acoustic disturbances when the time scales of the droplet lifetime correspond to those of an acoustic period. In addition, larger droplets are more susceptible to these fluctuations as secondary droplet breakdown may occur. In a further study by Chishti et al. [30], unsteady measurements of the droplet velocities of a water spray with a SMD of $d_{32} = 25 \mu\text{m}$ revealed a strong response to acoustic forcing for frequencies ranging between 80 and 100 Hz . The cut-off frequency of the spray response was determined by around 150 Hz .

Due to the present test-rig setup, measurement of droplet diameters were only feasible without acoustic excitation. Nevertheless, the results of

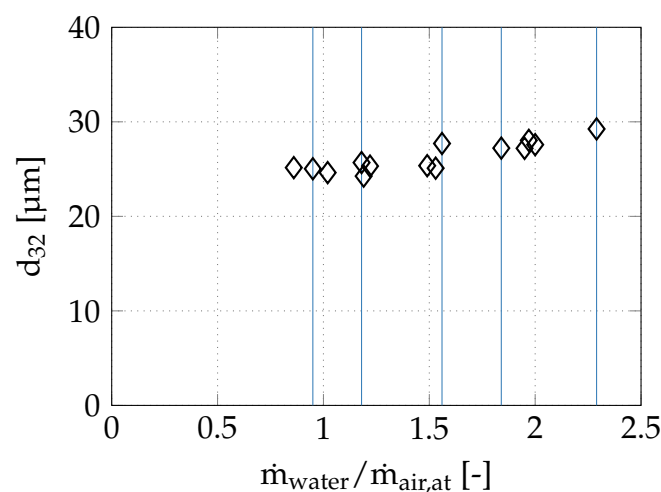


Figure 5.6.: Measured Sauter mean diameter (SMD) of water droplets for constant atomization air mass flow of 1 g s^{-1} .

Chishty et al. suggest that due to the similar droplet properties, some of the results can be transferred to the present configuration. According to this, an impact of water injection on the flame response can be expected for frequencies below 150 Hz, since oscillating droplet evaporation also influences the unsteady heat release of the flame. An increase of the water-to-fuel ratio results in a denser spray and larger droplets (cf. Figures 5.5 and 5.6). It is therefore assumed that the oscillation amplitudes at low frequencies will increase with increasing Ω . For higher frequencies, the flame response is less likely influenced by the droplet dynamics.

In the following chapters, both measured flame transfer functions and damping rates of the combustor will be discussed. Based on these data, the influence of the water-to-fuel ratio on the global flame response can be quantified over a wide frequency range.

6 Acoustic Properties and Flame Response

In this chapter, the dynamic response of the burner and the flame to external forcing will be discussed. Firstly, scattering matrices without flame are presented to characterize the acoustic properties of the swirl burner with water injector. Secondly, the influence of water injection on the sound generation in the flame is discussed on the basis of measured source terms. Subsequently, flame transfer functions (FTF) are presented for water-injection at constant equivalence ratio and at constant flame temperature. Special emphasis is placed on the scalability of the FTF with geometrical flame parameters. Finally, the influence of water injection on the local flame response is discussed on the basis of phase-resolved OH^{*}-chemiluminescence.

6.1. Scattering Matrices of the Burner

In the following, experimentally determined scattering matrices of the modified burner with water injector will be discussed and compared to those of the original burner. This serves to determine the influence of the water injector on burner acoustics. The burner with fully opened axial air inlet serves as the basis for comparison. Any other geometric parameters of the burner remain unchanged (see Section 4.2). The burner scattering matrices will be used to calculate the FTFs, which will be presented in Section 6.3. Furthermore, these results will be used to validate numerically calculated scattering matrices (see Section 8.3). Scattering matrices were measured in the single burner test-rig with a constant main air mass flow of $\dot{m}_{\text{air}} = 24 \text{ g s}^{-1}$ at a preheat temperature of $T_{\text{ph}} = 573 \text{ K}$. All experiments without flame were carried out without water injection.

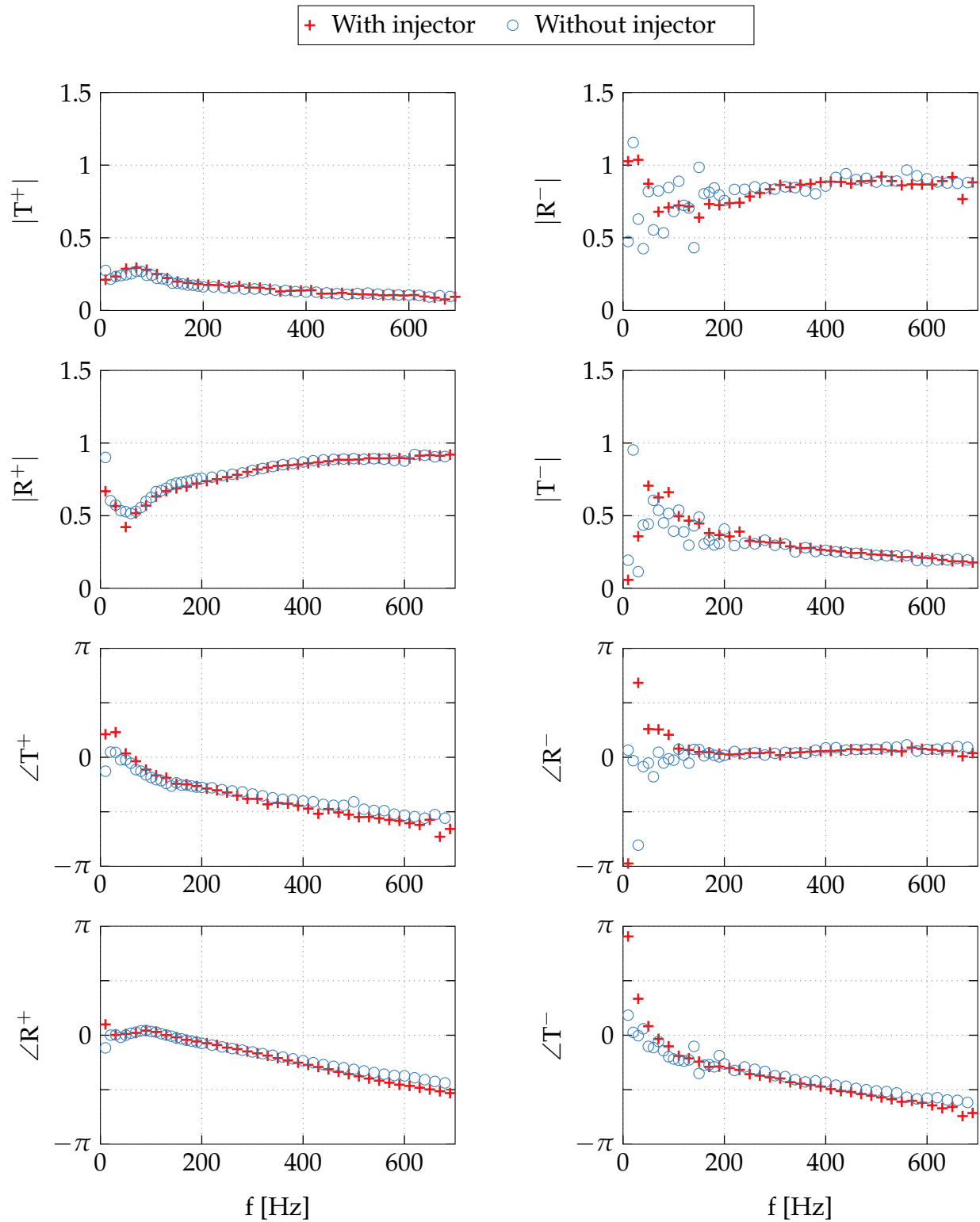


Figure 6.1.: Scattering matrices of the burner: Comparison between original burner and burner with water injector.

The measured scattering matrices are shown in Figure 6.1. It can be seen that the scattering matrices of the original burner and the burner with water injector differ only marginally. In both cases, the amplitudes of the transmission coefficients T^+ and T^- reach their maximum values at about 80 Hz. Towards higher frequencies their magnitudes approach zero. Their corresponding phases drop continuously towards higher frequencies. The amplitude response of the reflection coefficient R^+ reaches its minimum value of approximately 0.5 at a frequency of 80 Hz while subsequently approaching one with increasing frequency. The corresponding phases also decline continuously towards higher frequencies. The amplitude of R^- shows a similar behavior while its phase remains almost constant at zero. In general, the downstream scattering matrix elements show a wider scattering especially at low frequencies, which is attributed to the weaker acoustic forcing capabilities of the downstream siren. Based on these measurements, it is demonstrated that the acoustic scattering behavior of the burner is not significantly influenced by adding the water injection system. Thus, the design criterion with number 6 specified in Section 4.2 is fulfilled.

6.2. Noise Emission with Water Injection

The effect of water injection on the sound emission of the flame will be discussed in the following. For this purpose, measured source terms are evaluated. These were calculated from measured scattering matrices and an additional set of pressure data acquired without external forcing (see Section 3.2). Measurements were carried out based on operating range ④ for water-to-fuel ratios between $0 \leq \Omega \leq 2.0$ at constant flame temperature.

Figure 6.2 shows the measured source terms in the form of frequency-dependent amplitudes of the Riemann invariants f_s and g_s . Their phases are not shown here since noise source terms are not correlated with an external excitation signal and thus have a random phase. Note that frequencies above 250 Hz are not considered since noise generation in flames occurs predominantly at frequencies below [117, 140]. This fact is reflected in all cases shown in Figure 6.2 by amplitudes of the source term decreasing to zero for frequencies above approximately 200 Hz. Two specific frequencies

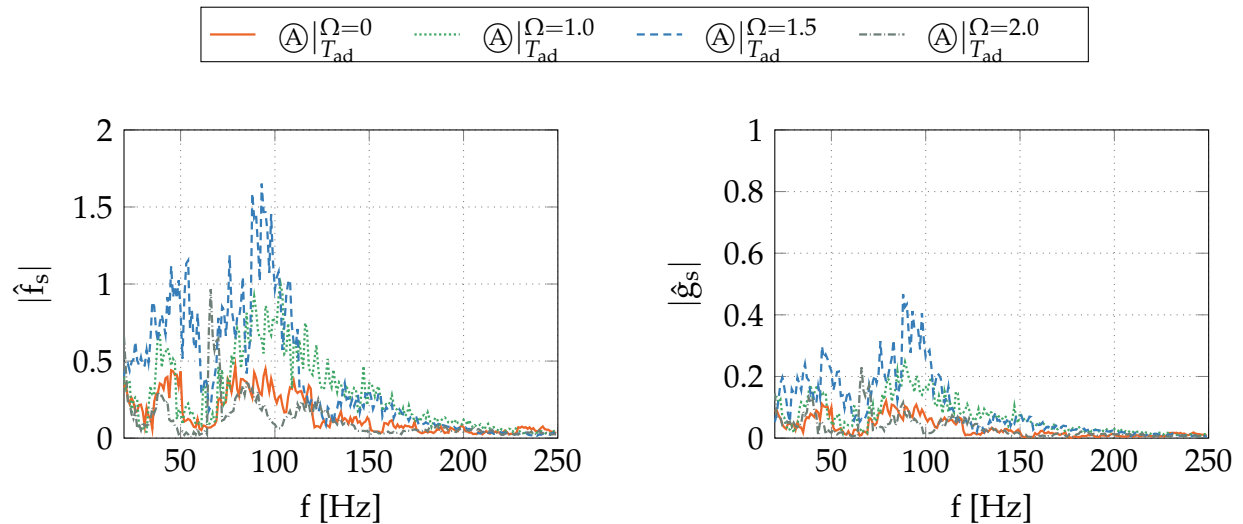


Figure 6.2.: Measured source terms for water injection at constant flame temperature of $T_{ad} = 1923$ K plotted over frequency.

with high noise emission can be determined from the amplitudes of the source terms: One is located at around 50 Hz and the other one at around 100 Hz. The lowest amplitudes of f_s and g_s occur under dry operation. With water injection, peak amplitudes are found to increase significantly. Especially at $\textcircled{A}|_{T_{ad}}^{\Omega=1.5}$ an increase of f_s and g_s by up to 300% is observed at a frequency of approximately 100 Hz. Below 150 Hz, the amplitudes of the upstream source term g_s are by approximately 25% lower than for f_s . Amplitudes of the source term reveal that water injection increases the permanent excitation of system acoustics by turbulent combustion noise at low frequencies. However, this excitation does not participate in the feedback loop, such as the flame transfer function. Note that for flames with water injection, the frequencies with high source term amplitudes correspond to the range in which interaction between combustor acoustics and droplet dynamics is possible (see Section 5.4). Excitation of the system acoustics by the droplet dynamics is therefore a possible cause for the strong increase of the flame's sound emission with water injection.

6.3. Flame Transfer Functions

In this section, the influence of water injection on the flame dynamics will be discussed based on measured flame transfer functions. Firstly, FTFs of

the four baseline operating conditions will be presented. On this basis, the focus is placed on the behavior of the FTF for water injection at constant equivalence ratio ($\phi = \text{const.}$), and subsequently, at constant adiabatic flame temperature ($T_{\text{ad}} = \text{const.}$). Apart from the frequency dependency of the flame response, scaling of the FTF with geometrical flame parameters will also be discussed. All flame transfer functions presented below were obtained from dynamic pressure measurements by applying the multi-microphone method (MMM), as described in Section 3.3.

6.3.1. Dry Operation

The amplitude and phase responses representing the FTFs of the four baseline operating points without water injection ①, ②, ③ and ④ are displayed in Figure 6.3. Firstly, the frequency dependent FTFs in the first

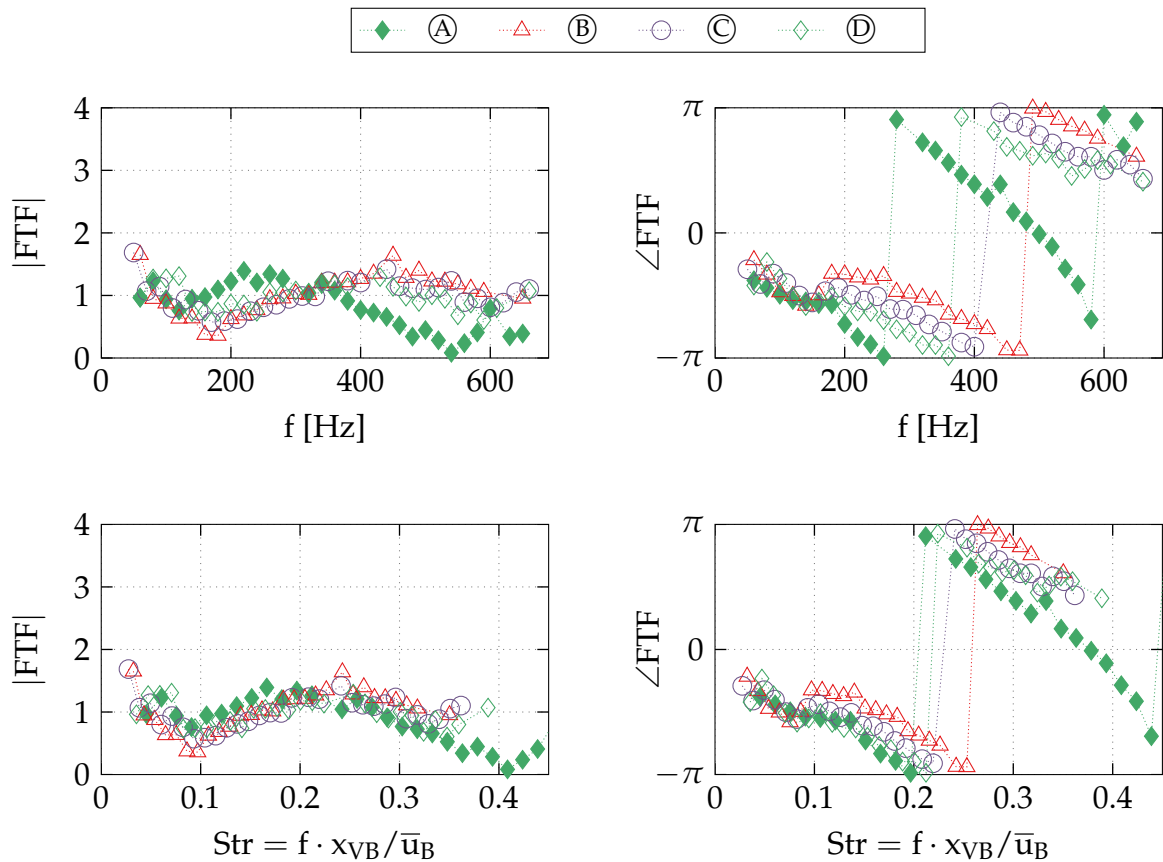


Figure 6.3.: Flame transfer functions of the four baseline operating conditions depending on frequency and Strouhal number.

row are considered. In all cases, the amplitudes of the FTF exhibit a minimum at low frequencies. This minimum is followed by a maximum and a subsequent continuous decrease with increasing frequency. The phases decline steadily with the forcing frequency. Note that operating points ②, ③ and ④ are equal in their thermal power but differ in the equivalence ratio, which decreases from ② to ④. Operating points ① and ④ have identical equivalence ratios while ① is the only operating point having a lower thermal load of $P_{th} = 40$ kW. The operating points ②, ③ and ④ which correspond to $P_{th} = 50$ kW exhibit larger amplitudes and flatter phase slopes than case ①. With decreasing thermal power, local minima and maxima are shifted towards lower frequencies. Across all three considered equivalence ratios, the amplitudes of the FTFs are very similar, while their phases differ considerably from each other. The phase responses indicate an increase of the time delay between acoustic velocity and unsteady heat release from operating point ② to ④. The shortest time delays are determined for operating point ①. In this context, this delay is significantly influenced by the mean flow velocity and the flame length. The flame lengths for the corresponding operating points have already been discussed in Section 5.2. The mean flow velocity, which is determined by the main air mass flow rate, decreases from case ① to ④.

For the scaling of the FTF across different operating conditions, the Strouhal number has found broad application in many previous publications [6, 11, 52, 133]. Mathematically, the Strouhal number is defined as follows:

$$\text{Str} = \frac{f x_{\text{VB}}}{\bar{u}_B}. \quad (6.1)$$

Therein, the flame position is represented by the axial stand-off distance of the vortex breakdown x_{VB} which is derived from stationary flame images (see Figure 5.3). The mean flow velocity at the burner outlet \bar{u}_B is calculated from the mass flow of the reactants through the burner exit plane. The scalability of the FTF has already been discussed in detail by Bade [11] on the basis of the original design of the swirl burner. The flame transfer functions for the swirl burner with water injector used in the present work are plotted over the Strouhal number in the lower row of Figure 6.3. In this representation, the diagrams show now very similar amplitudes of the FTFs across all four operating points without water injection. However,

the influence of the equivalence ratio is still visible by means of slight offsets between the phase slopes. In contrast, the scaled phases of the operating points \textcircled{A} and \textcircled{D} , which differ only in the thermal load and are equal in the equivalence ratio, are almost identical. The scalability of the FTF with the Strouhal number is thus demonstrated for the burner with water injector under dry operation. To what extent these findings can be applied to flames with water injection will be subject of the next sections.

6.3.2. Water Injection at Constant Equivalence Ratio

Flame transfer functions with water injection are discussed in the following. In particular, the influence of the water-to-fuel ratio is considered for water injection at constant equivalence ratio. The corresponding results for the operating ranges $\textcircled{A} |_{\phi}$ and $\textcircled{C} |_{\phi}$ are shown in Figure 6.4. First of all, with water injection a significant increase of the amplitudes is observed for very low frequencies when compared to the respective case at $\Omega = 0$. A

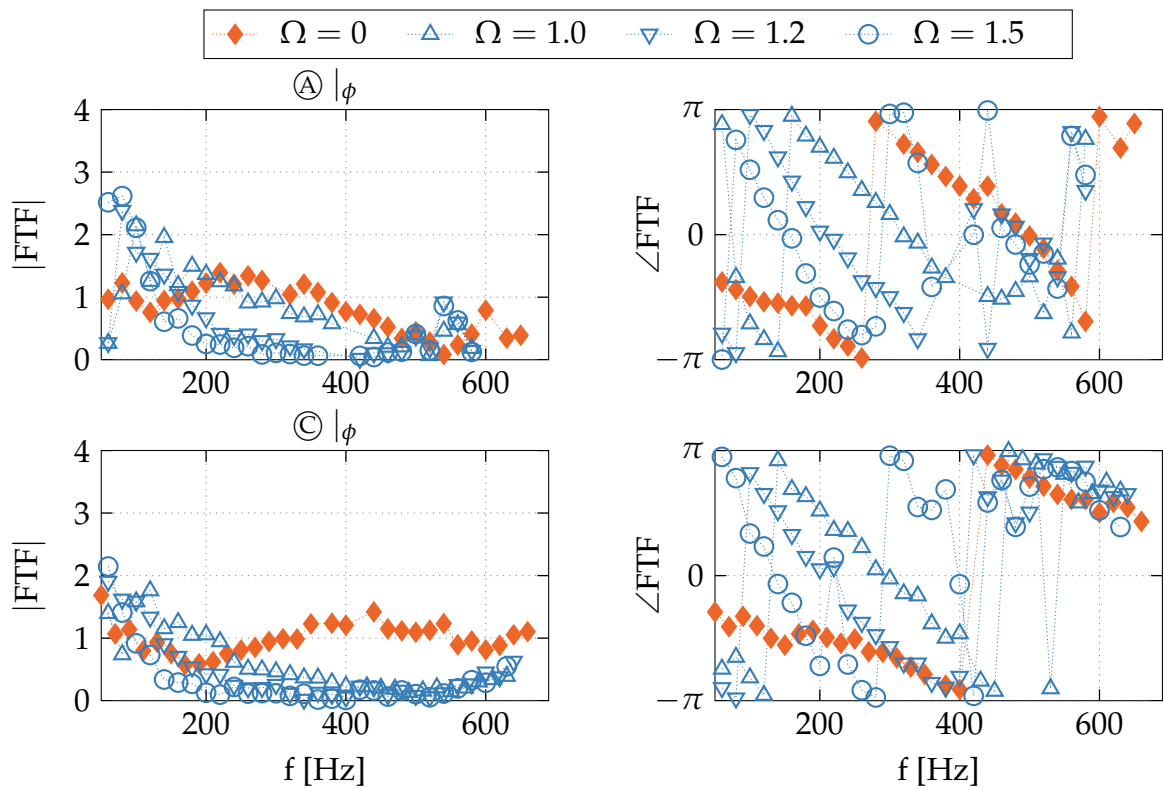


Figure 6.4.: Flame transfer functions with water injection at constant adiabatic flame temperature for varying operating conditions depending on frequency.

rise of the peak amplitudes is seen with increasing Ω . In contrast, the gains of the FTFs decrease with increasing water-to-fuel ratio for frequencies higher than 200 Hz. For water-to-fuel ratios of more than 1.0, amplitudes of close to zero occur at excitation frequencies of above approximately 250 Hz. Practically, this means that the flame no longer responds to acoustic disturbances. Water injection also leads to a steeper phase decline over the frequency. For both operating conditions, the largest phase shift is found between $\Omega = 0$ and $\Omega = 1.0$. The phase slope steepens as the water-to-fuel ratio increases. Scattered measuring points are found for frequencies at which the amplitude of the FTF is close to zero as in this case the phase angle is undefined. The measurement data therefore indicate that water injection increases the low-pass behavior of the FTF. The low-pass behavior is stronger for lower (\textcircled{C} $|\phi$) than for higher flame temperatures (\textcircled{A} $|\phi$) at identical water-to-fuel ratios. In addition, the time delay between unsteady heat release and velocity disturbances rises with increasing water-to-fuel ratio. This effect can be explained by the displacement of the flame and dilution of the reaction zone with increasing Ω , as discussed in Section 5.2. Consequently, dilution of the flame with water has similar effects on the FTF as a reduction of the equivalence ratio. This also causes higher dispersion of convective time scales between acoustic velocity and unsteady heat release. As a result, a weaker flame response towards higher frequencies is observed. The higher flame response due to water injection at low frequencies can be explained by the radial expansion of the flame, which causes an increase of the vorticity fluctuations.

Analogously to the FTFs for dry conditions, scaling with the Strouhal number is attempted also for water injection at constant equivalence ratio. Figure 6.5 shows the amplitude and phase responses of the FTFs scaled with the axial stand-off distance of the flame and the mean flow velocity, according to Equation (6.1). In contrast to dry operation, here neither the amplitudes nor the phases of the FTFs lie on top of each other. The influence of water injection on the FTF thus seems to be disproportionately high with decreasing flame temperature compared to the axial displacement of the flame. Within the given operating range, Strouhal scaling of the FTF for water injection at constant equivalence ratio is thus considered unsuitable.

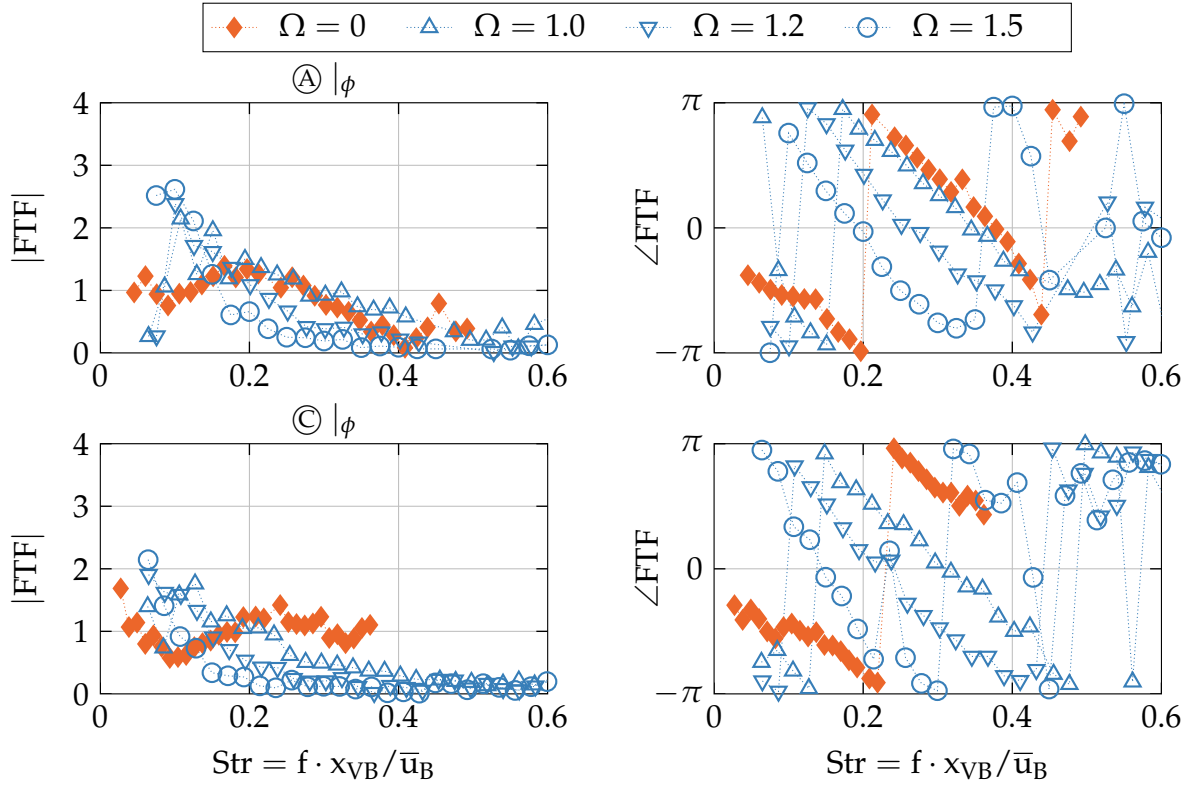


Figure 6.5.: Flame transfer functions with water injection at constant equivalence ratio for varying operating conditions depending on Strouhal number.

6.3.3. Water Injection at Constant Adiabatic Flame Temperature

The effect of water injection on the flame transfer functions at constant adiabatic flame temperature will be discussed below. From a technical point of view this operation mode with water injection allows to increase the thermal power of premixed flames at constant temperature level. In the present configuration a maximum thermal load increase of $P_{th,max}/P_{th,0} \approx 1.40$ is achieved for operating range (A) $|_{T_{ad}}$ at a water-to-fuel ratio of $\Omega = 2.0$.

Flame transfer functions are presented in Figure 6.6 for operating ranges (A) $|_{T_{ad}}$ –(D) $|_{T_{ad}}$. In case (A) $|_{T_{ad}}$ significantly higher amplitudes are observed for frequencies below 200 Hz when increasing Ω . With increasing water-to-fuel ratio the amplitudes are found to decline steeper towards higher frequencies. In contrast to water injection at constant equivalence ratio, the amplitude responses of the FTF at constant adiabatic flame temperature are more similar to the dry reference points. This applies not only to operating range (A) $|_{T_{ad}}$ but also to (B) $|_{T_{ad}}$, (C) $|_{T_{ad}}$ and (D) $|_{T_{ad}}$. The highest

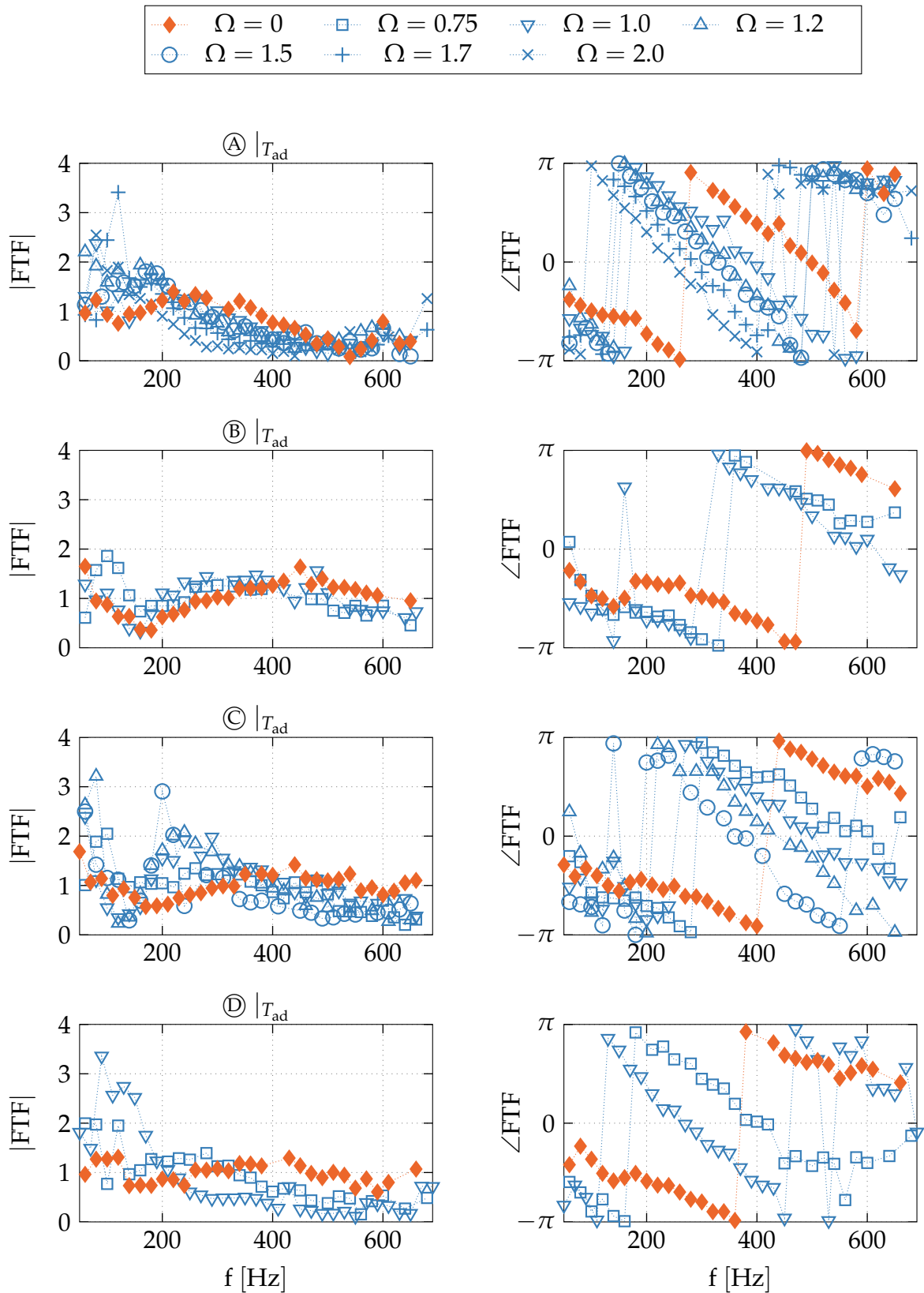


Figure 6.6.: Flame transfer functions for operating points with water injection at constant adiabatic flame temperature depending on frequency.

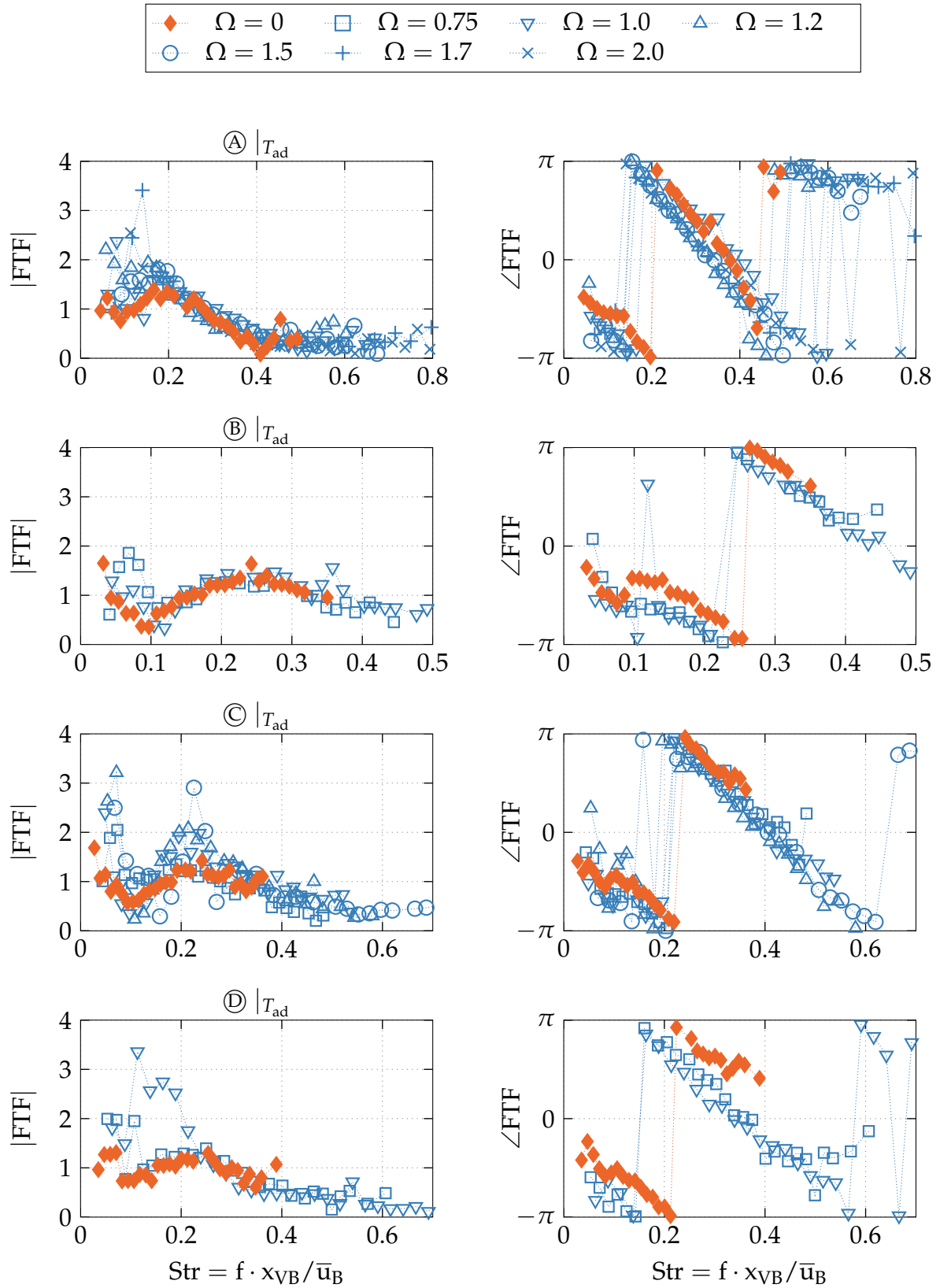


Figure 6.7.: Flame transfer functions for operating points with water injection at constant adiabatic flame temperature depending on Strouhal number.

peak amplitude occur in cases © $|_{T_{ad}}$ and ④ $|_{T_{ad}}$ at frequencies of below 100 Hz. However, these results should be interpreted with caution since the multi-microphone method is known to be less accurate at very low excitation frequencies [52, 140]. In addition, the measured source terms (see Section 6.2) indicate an excessive increase of uncorrelated combustion noise with water injection. Coherent noise which is not correlated to the excitation source causes a reduction of the signal-to-noise ratio during the measurements. This may explain the scattering of the data points at frequencies below 200 Hz. The phases of the FTFs decline more steeply when increasing the water-to-fuel ratio. Compared to water injection at constant equivalence ratio, however, the phase slopes are less steep at constant flame temperature (cf. Section 6.3.2). Across all considered operating conditions, the time delay between acoustic fluctuations and oscillating heat release rate thus increases also with increasing water-to-fuel ratios at constant flame temperature. For operating range ① $|_{T_{ad}}$ the phase slopes indicate that the time delay between $\Omega = 0$ and $\Omega = 1.0$ corresponds approximately to the time delay between $\Omega = 1.0$ and $\Omega = 2.0$. This indicates a steady rise of the time delay with increasing water-to-fuel ratio. Altogether, a weaker effect of Ω on the FTFs is observed than for constant equivalence ratio.

Figure 6.7 shows the FTFs plotted over the Strouhal number $\text{Str} = f \cdot x_{VB} / \bar{u}_B$. The diagrams show that the amplitudes for $\text{Str} > 0.2$ lie almost perfectly on top of each other. This applies to the range from $\Omega = 0$ to $\Omega = 2.0$ in case ① $|_{T_{ad}}$ and between $\Omega = 0.75$ and $\Omega = 1.5$ for the remaining three operating ranges. Slight deviations from this pattern are only seen in case © $|_{T_{ad}}$. When plotting the FTFs over the Strouhal number also the phases become almost identical across all investigated water-to-fuel ratios. This behavior is in contrast to the case of water injection at constant equivalence ratio. However, below the threshold of $\text{Str} \approx 0.2$ the FTF exhibits significantly larger amplitudes. In this range, Strouhal scaling with geometrical flame parameters seems unsuitable.

In summary, it emerges that flame temperature and flame position govern flame dynamics for $\text{Str} > 0.2$ when injecting liquid water at $T_{ad} = \text{const.}$ This behavior was found even for excessive water injection of up to $\Omega = 2.0$. With regard to the present setup, scaling of the FTF thus seems justifiable for Strouhal numbers of above 0.2.

6.4. Phase-Resolved Heat Release Oscillations

Results from the previous sections showed that water injection leads to a higher flame response at low frequencies and a weaker response towards higher frequencies. The latter effect has been ascribed to the displacement of the reaction zone with increasing Ω and applies for Strouhal numbers of above 0.2. Consequently, the mechanism governing the flame response with water injection appears to be different in the low-frequency range. Thus, the flame response is resolved locally to identify possible causes for this behavior. This will be demonstrated for two frequencies which are representative for $\text{Str} < 0.2$ and $\text{Str} > 0.2$, respectively. The former, lower frequency will be termed f_1 , the higher one f_2 . The aim is to identify, how water injection influences the oscillation mode of the flame in both frequency ranges. For this purpose, OH^* -chemiluminescence images were recorded under external forcing before being sorted by phase angle and averaged over one oscillation cycle. The respective measuring method is outlined in Section 3.5.2. The intensities are indicative for the heat release rate. Information on the local amplitude and phase distributions are extracted from the Fourier coefficient of each pixel. Based on operating conditions $\textcircled{A}|_{T_{\text{ad}}}^{\Omega=0}$ and $\textcircled{A}|_{T_{\text{ad}}}^{\Omega=1.0}$ the excitation frequencies are $f_1 = 111 \text{ Hz}$ and $f_2 = 540 \text{ Hz}$ for $\Omega = 0$ and $f_1 = 124 \text{ Hz}$ and $f_2 = 546 \text{ Hz}$ at $\Omega = 1.0$, respectively. The reason for choosing slightly differing excitation frequencies for $\Omega = 0$ and $\Omega = 1.0$ is due to the frequency shift observed in the spectrum between dry and water injected operation. To obtain comparable phase resolutions between both frequency regimes, images were recorded with different recording rates (see Table 6.1).

Table 6.1.: Overview on operating parameters used to record phase-resolved OH^* -chemiluminescence images.

Water-to-fuel ratio	Forcing frequency	Recording frequency	Phase intervals
Ω [-]	f [Hz]	f_R [Hz]	N [-]
0	111	1500	12
0	540	6000	10
1.0	124	1500	12
1.0	546	6000	10

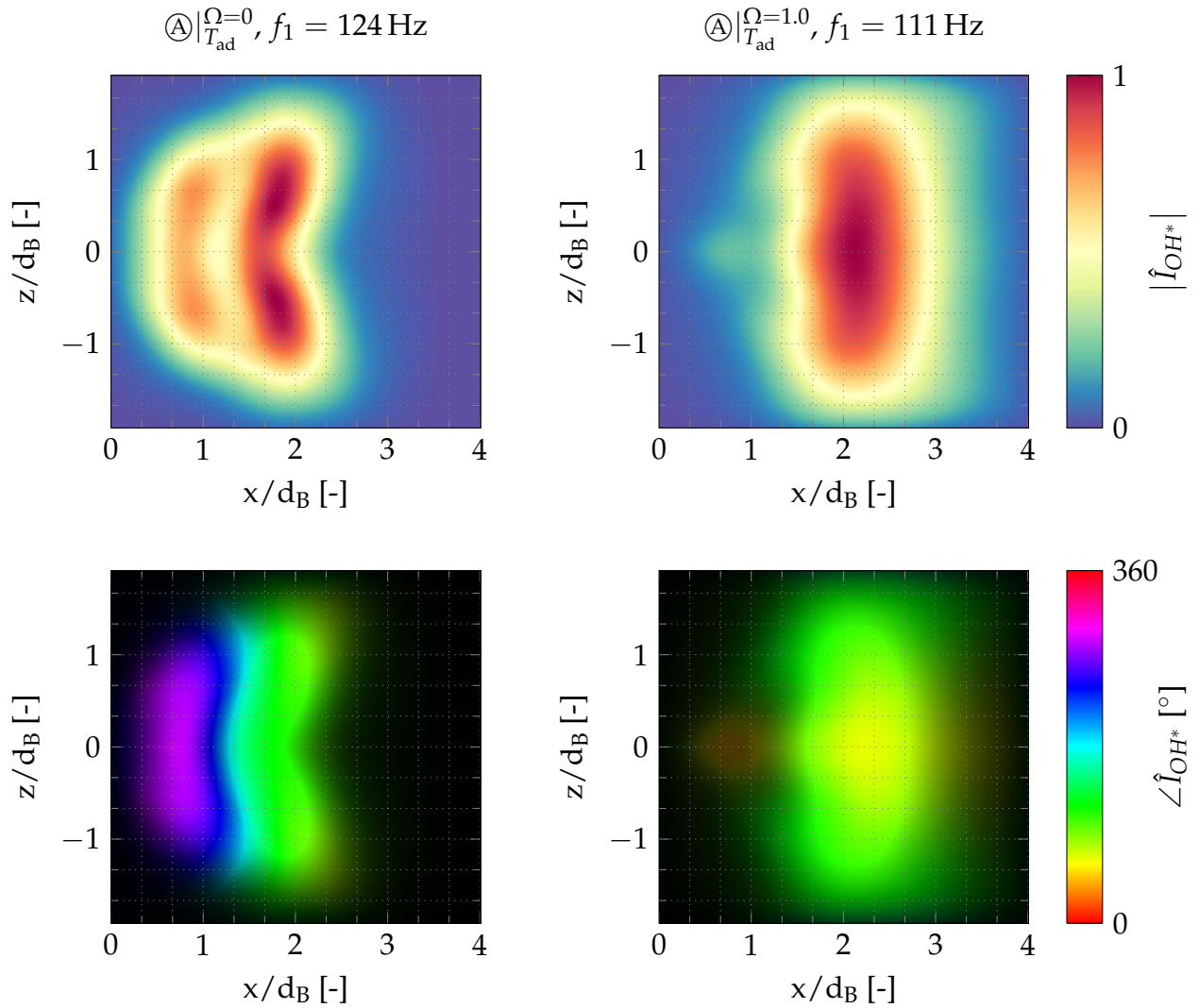


Figure 6.8.: Fourier amplitude and phase images from phase-resolved OH^* -chemiluminescence images at excitation frequency f_1 .

Amplitude and phase images obtained for f_1 are shown in Figure 6.8. At dry operation, the amplitude image exhibits two distinct zones of high oscillation activity. Both zones oscillate with opposite phases relative to each other. This indicates that the flame response is almost completely cancelled, resulting in a FTF amplitude of approximately 1 (see Figure 6.6) at this frequency. Surprisingly, this is fundamentally different for $\Omega = 1.0$. In this case, merely one predominant oscillation region with a nearly constant phase angle is observed. Altogether, it can be assumed that for $\Omega = 0$ the oscillation mode of the flame is governed by a convective process with two opposing zones of heat release overshoot and deficit.

This may be the reason for the observed low amplitudes of the flame transfer functions in the low frequency range without water injection. In contrast, the phase distribution of $\Omega = 1.0$ indicates that the entire flame periodically expands and contracts. In comparison to dry operation, the oscillating water droplets may act as a further driving mechanism, since interaction between water droplets and the acoustic field is likely in this frequency range. Depending on the phase relationship, this may explain the significant gain of the flame's heat release oscillations in the low-frequency range.

A different behavior is observed at the higher excitation frequency (cf. Figure 6.9 for f_2). For $\Omega = 0$, the respective amplitude image exhibits only one compact zone of high oscillation activity in the axial direction. In this region, the phase angle between excitation signal and heat release oscillations is almost constant. With water injection the increasing flame volume leads to a displacement of the location of the maximum oscillation amplitude. Due to the dilution of the flame with water, the oscillating heat release is distributed over a wider range of the combustion chamber than without water injection. The displacement and dilution of the heat release zone can also be seen in the phase distribution: The phases corresponding to the zones of maximum heat release oscillations deviate from those measured for dry conditions. Generally, the determined phase angles are spread over a wider range across the flame. This explains the significant phase shift of the FTF between dry operation and operation with water injection (cf. Figure 6.6). Contrary to f_1 , no obvious switching of the flame's oscillation mode is observed when comparing $\Omega = 0$ and $\Omega = 1.0$ at the frequency f_2 . For both dry operation and water injection, the amplitudes of the FTF at f_2 are below 1 and differ only slightly from each other. From this it is concluded that water injection mainly leads to a dispersion of convective times at the frequency f_2 , which explains the phase shift and the very similar amplitudes of the FTF compared to $\Omega = 0$.

The results obtained from phase-resolved OH^* -chemiluminescence provide a possible explanation for the global behavior of the FTF with water injection for two representative frequency ranges. However, to identify the underlying mechanisms leading to the observed distribution of the heat release fluctuations with water injection, droplet dynamics must be included in the analysis. In particular, phase-resolved measurements of

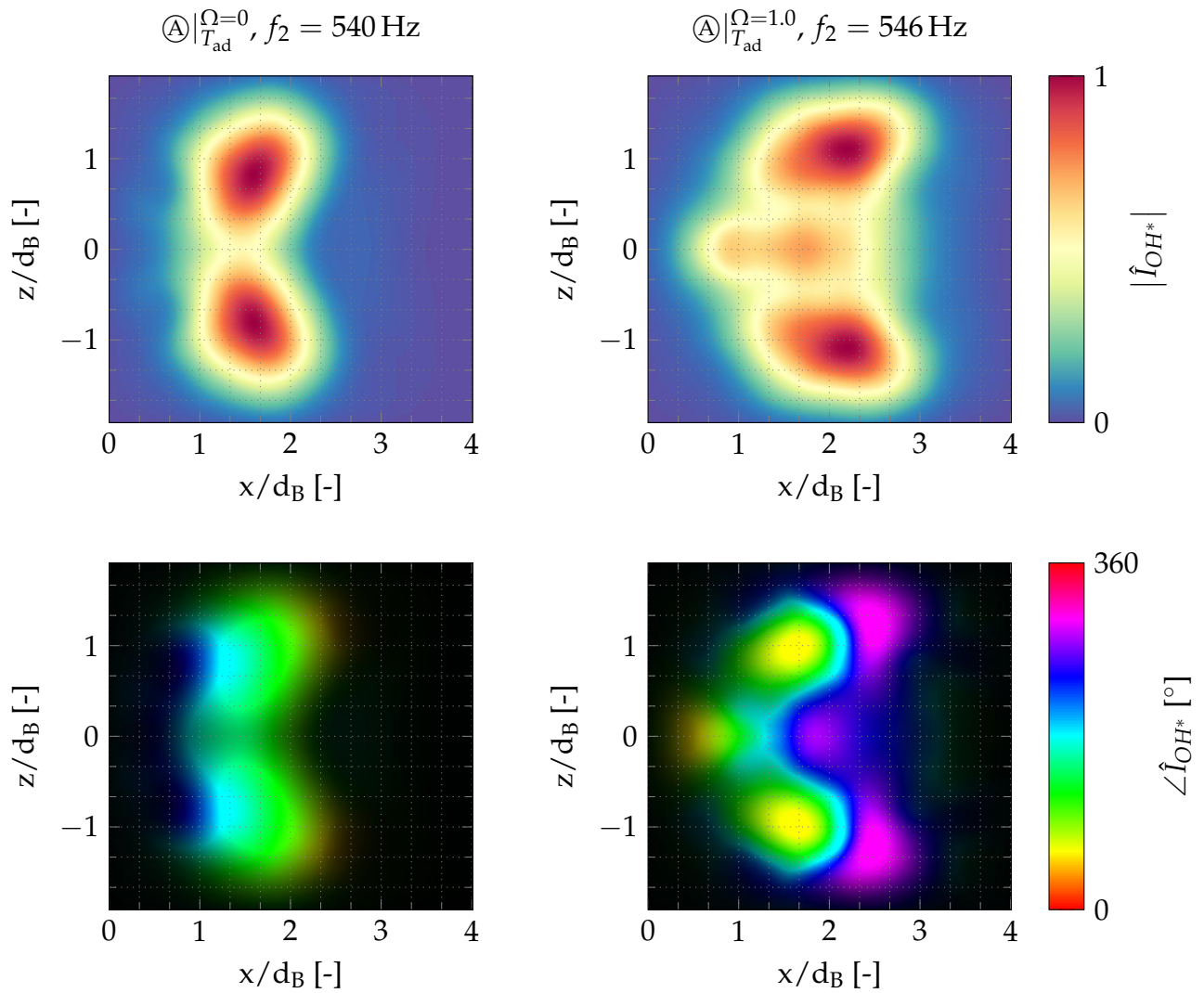


Figure 6.9.: Fourier amplitude and phase images from phase-resolved OH^* -chemiluminescence images at excitation frequency f_2 .

spray distribution, droplet velocities and diameters would be beneficial to determine the convective times between droplet dynamics and heat release oscillations. This may allow to understand under which conditions the spray interacts with the acoustic field in the combustor and to what extent distribution, intensity and phase of the flame's heat release oscillations are influenced.

7 Thermoacoustic Modes with Water Injection

This chapter discusses the influence of water injection on the eigenfrequencies of the combustor and their damping rates. Experimental results presented in this chapter were obtained in the given single burner test-rig. Firstly, the boundary conditions and aeroacoustic damping of the combustor will be discussed. In the next step, eigenfrequencies and thermoacoustic damping rates are presented for dry reference conditions as well as for water injection at constant equivalence ratio and adiabatic flame temperature. In this context, also the influence of the water-to-fuel ratio on the acoustic dissipation in the combustor and the flame driving will be pointed out. Finally, water injection will be compared with other methods for increasing the thermal load of the combustor with regard to thermoacoustic damping. The results presented in this chapter provide the experimental dataset for a quantitative validation of numerical stability predictions in Chapter 8.

7.1. Aeroacoustic Damping Properties of the Combustor

Acoustic damping of the combustor under non-reactive conditions will be discussed below. The damping rates were obtained with the impulse response method (see Section 3.4.1). Eigenfrequencies and damping rates are extracted from time series of the decaying pressure signal after stopping the mono-frequent forcing abruptly. The outlet of the present combustion chamber can be equipped with either a nozzle or a perforated plate. The majority of the presented results with flame were obtained with the nozzle, which allows to create thermoacoustically stable as well as unstable conditions. However, some of the experiments with flame were also conducted with a perforated plate mounted at the combustor exit. For this reason, the acoustic damping of the combustion chamber without flame is determined

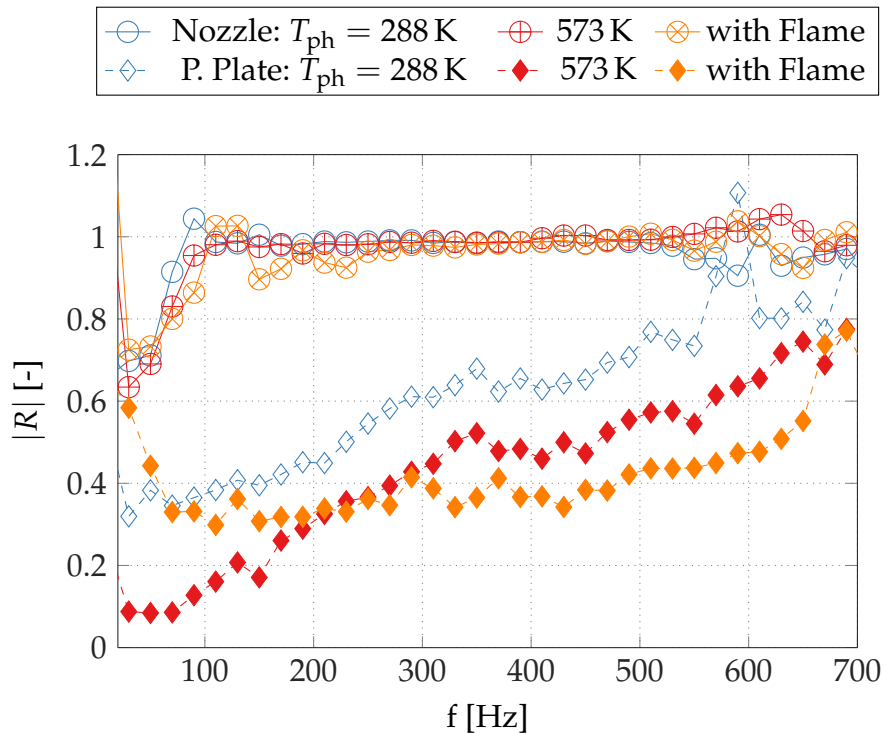


Figure 7.1.: Reflection coefficients with nozzle and perforated plate for three different temperature levels.

for both configurations. The use of either the nozzle or the plate allows to impose different acoustic boundary conditions at the combustor outlet. These are characterized by their respective reflection coefficients, which are shown in Figure 7.1. The nozzle provides an almost constant reflection coefficient of 1 for frequencies above 100 Hz. This applies to both cold and preheated main air flow and with combustion. In contrast, the reflection coefficient of the perforated plate depends strongly on frequency as well as on temperature. Damping measurements without flame are presented for cold ($T_{\text{ph}} = 288 \text{ K}$) and preheated main air flow ($T_{\text{ph}} = 573 \text{ K}$).

The resulting damping rates are displayed in Figure 7.2 for both boundary conditions. The plots show results for two temperature levels and cover each two longitudinal eigenfrequencies. Note that these results correspond to the eigenfrequencies which occur without flame at a significantly lower combustor mean temperature. Thus, both the eigenfrequencies of a half-wave as well as of a full wave in the combustor occur in the investigated frequency range. The error bars correspond to the standard error of the probability densities and represent a number of 10 independent measure-

ments. In general, significantly lower damping rates are determined when using the venturi nozzle. This is an expected result, since the reflection coefficient of the perforated plate is lower than for the nozzle, in particular at low frequencies. It is furthermore noted that the error margin of the damping rate is quite large for the first eigenfrequency when using the perforated plate. This effect is ascribed to the high losses of acoustic energy to the surrounding which reduces the signal-to-noise ratio of the forcing such that even the Bayesian parameter estimation yields imprecise results. In both cases, the measured eigenfrequencies and decay rates clearly depend on temperature. However, for both configurations and modes, the mean damping rates vary by less than 25 rad s^{-1} when considering a temperature difference of 284 K. If the perforated plate is used, the mean acoustic damping rate of the first mode is approximately 100 rad s^{-1} higher than with the nozzle. For the second mode, this difference amounts to approximately 80 rad s^{-1} . These experimental results serve to validate the numerically calculated eigenfrequencies and damping rates for the configuration with the venturi nozzle, which will be discussed in Chapter 8.

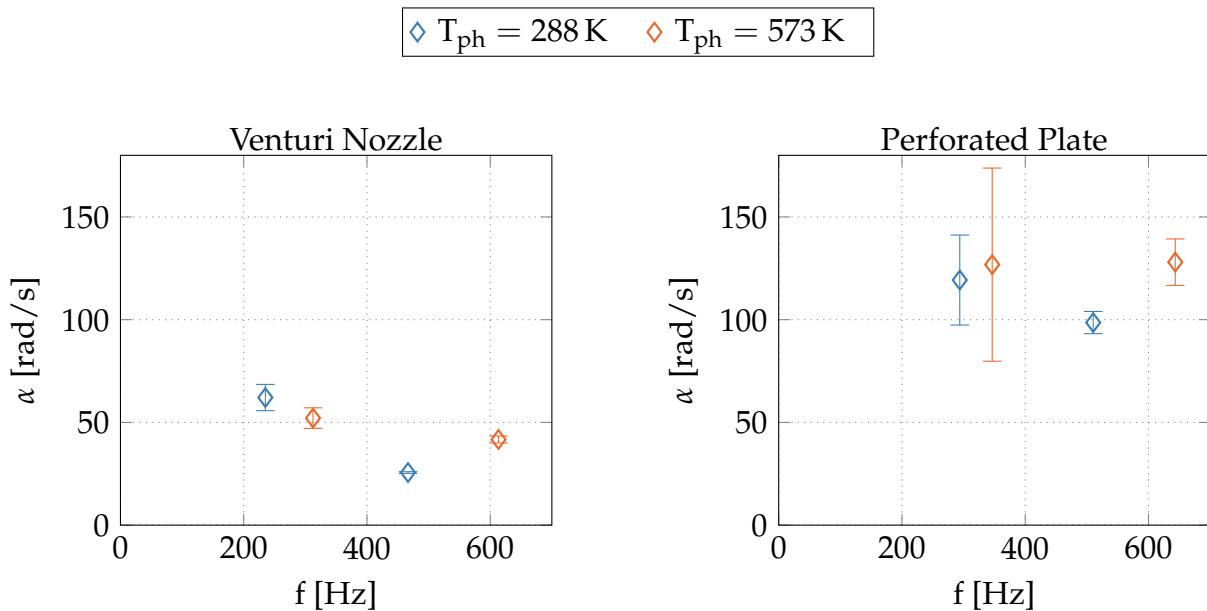


Figure 7.2.: Experimentally determined acoustic damping rates for two modes without combustion.

7.2. Combustor Damping under Dry Operation

In the following, thermoacoustic modes that occur in the combustion chamber under dry conditions will be discussed. To this end, the four baseline cases ①, ②, ③ and ④ are initially subdivided into stable and unstable operating points. Subsequently, their eigenfrequencies and damping resp. growth rates are analyzed. All results presented in this section were obtained in the single burner test-rig with a dry, lean premixed flame and using the venturi nozzle attached to the outlet of the combustor. The preheat temperature is $T_{\text{ph}} = 573 \text{ K}$.

Figure 7.3 shows statistical distributions, power density spectra and the corresponding autocorrelation functions obtained from the respective dynamic pressure recordings. For operating points ①, ③ and ④ the distribution of the pressure time series is Gaussian. This confirms that the combustor operates in the linearly stable regime [96]. The autocorrelation functions $k_{p'p'}$ associated with operating points ①, ③ and ④ decay exponentially over time. Note that in all cases $k_{p'p'}$ has been calculated from unfiltered pressure time series. Therefore, the envelopes of the autocorrelation functions do not exactly reflect exponential decay since the signal contains components at multiple frequencies. In contrast, ② shows a bimodal pressure distribution and very high peak amplitudes, which are clear indications that the system is linearly unstable and oscillates in a limit cycle. In this case, the envelope of the autocorrelation function exhibits no exponential decay. All operating points show a distinct peak at approximately 500 Hz in the pressure spectrum. For ② this peak is more than one order of magnitude higher than for the remaining three operating points. The peaks located in the vicinity of 500 Hz correspond to a half-wave mode in the combustor which is hereinafter denoted by η_2 . A more detailed discussion of the mode shape will be given in Section 8.4.

For operating points ① and ④ a second, less sharp peak is visible at approximately 100 Hz. This frequency is significantly lower than the resonance frequency of the first standing half-wave mode of the combustor. Moreover, it was observed that the dynamic pressure at this frequency is almost uniformly distributed in the axial direction and oscillates with constant phase. Section 8.4 will discuss the mode shapes in more detail in

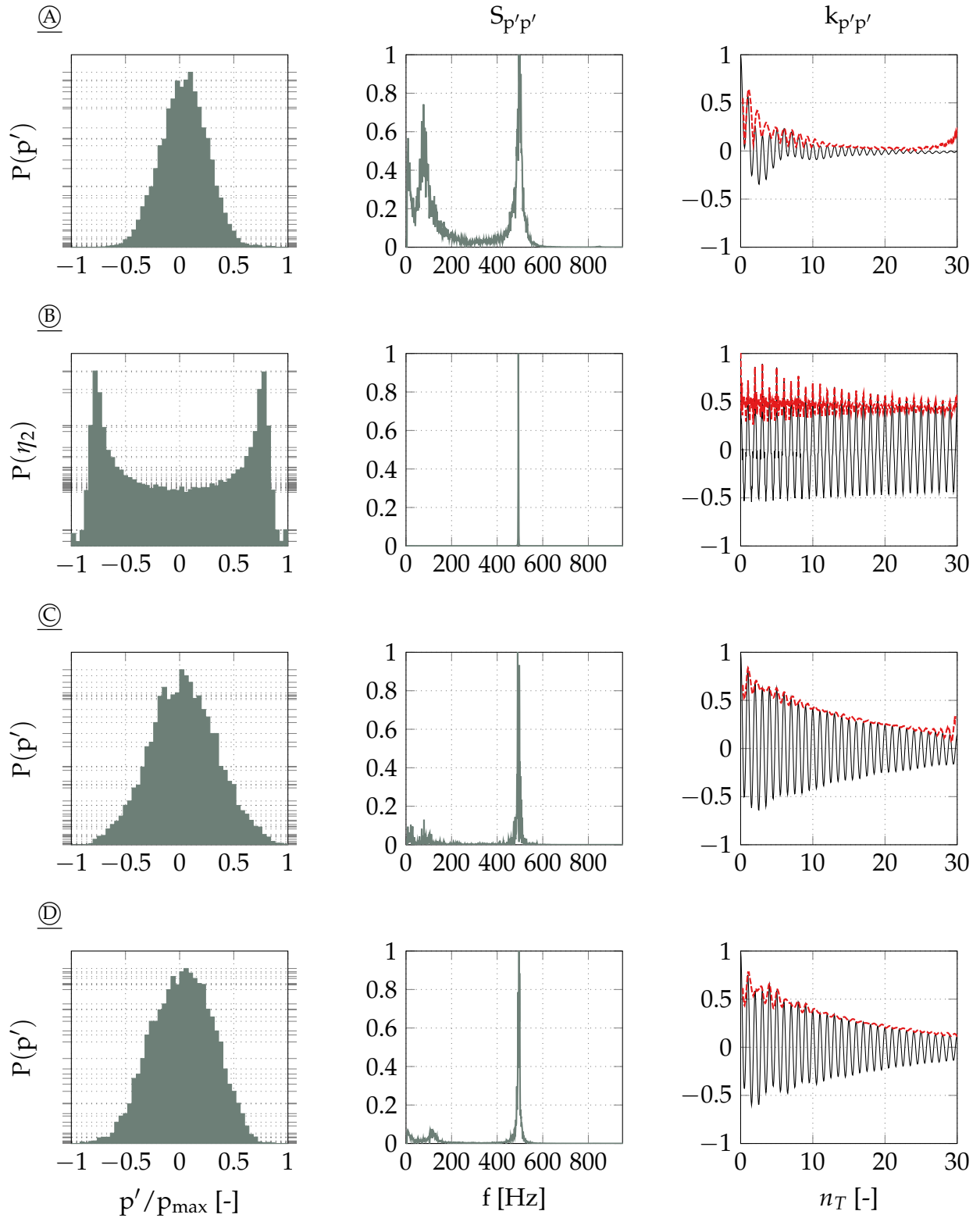


Figure 7.3.: Distribution of the pressure amplitudes, power spectral density and autocorrelation functions with envelope (----) under dry operation.

combination with numerical calculations of the pressure field. It is therefore concluded that the pressure peak at this frequency corresponds to a Helmholtz mode. The Helmholtz mode is hereinafter denoted by η_1 . Note that in the present configuration, η_1 only occurs at equivalence ratios of $\phi = 0.625$. The pressure spectra corresponding to operating points ② and ③ do not indicate the existence of a Helmholtz Mode.

In the next step, the thermoacoustic stability margin is quantified by measured damping rates at their respective eigenfrequencies. For the linearly stable cases, both parameters are identified using the stochastic forcing method introduced in Section 3.4.2. The required autocorrelation functions are calculated from time traces recorded over a time interval of 60 s. Again, this procedure can only handle linearly stable operating points with a positive thermoacoustic damping rate. Since this does not apply for case ②, the corresponding net growth rate is extracted by linearizing the limit cycle oscillations as outlined in Section 3.4.4. Figure 7.4 shows the eigenfrequencies and the damping rates obtained for operating conditions ①–④. The

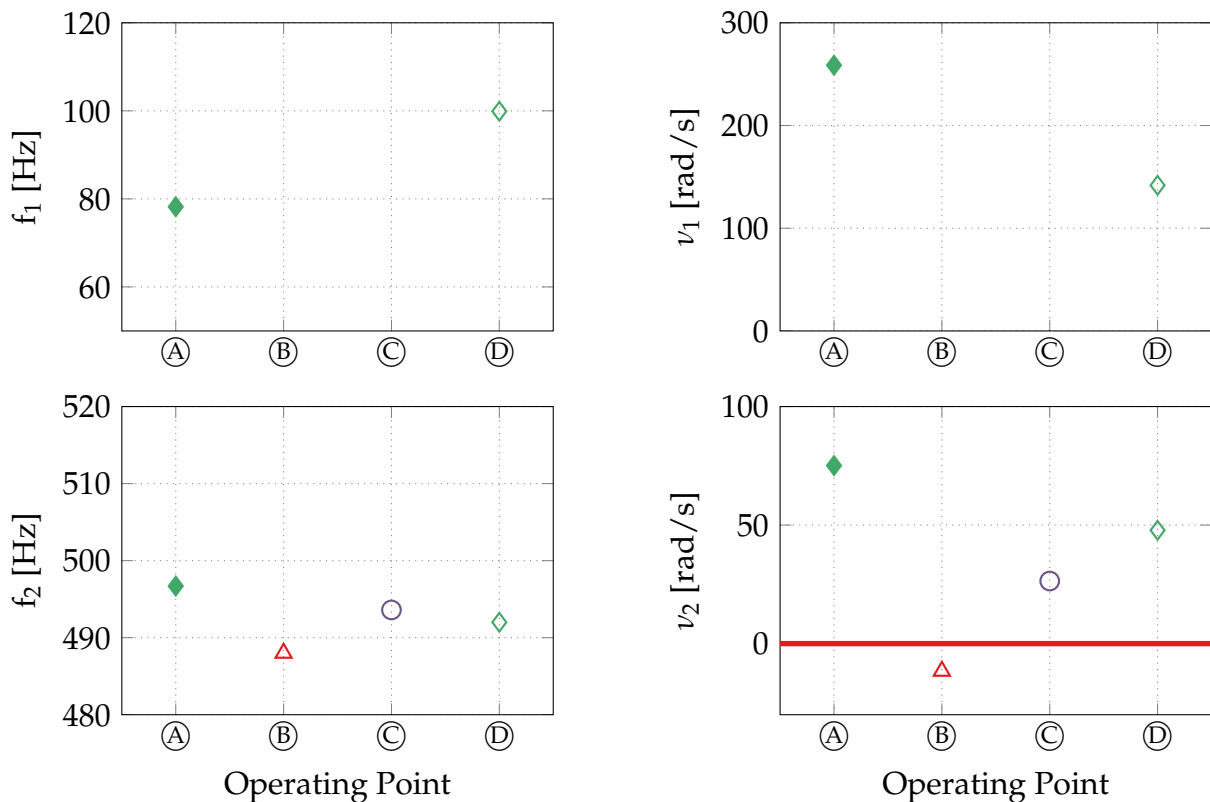


Figure 7.4.: Experimentally determined eigenfrequencies and thermoacoustic damping rates under dry operation.

frequencies f_1 denote the eigenfrequency and ν_1 is the net damping rate of mode η_1 . Furthermore, f_2 and ν_2 correspond to mode η_2 . The Helmholtz mode η_1 is found to occur only at operating points ① and ④. For both cases, however, η_1 appears to be strongly damped. This is indicated by damping rates of 260 rad s^{-1} and 140 rad s^{-1} , respectively. In contrast to the Helmholtz mode, the longitudinal half-wave mode η_2 occurs at all considered dry operating conditions. Their associated eigenfrequencies range between 488 and 497 Hz. For all linearly stable operating points, i.e. ①, ③ and ④, it is observed that a decrease of the equivalence ratio leads to an increase of the net damping rate ν_2 . Note that case ② is linearly unstable and thus the damping rate has a negative sign. Case ① has the highest damping rate determined in this measurement series. The equivalence ratio of this operating point is identical to ④, while the thermal power is by 20% lower. In this special case, a reduction of the thermal load thus leads to a greater stability margin. With regard to both thermoacoustic modes, operating point ① is found to be most stable.

7.3. Combustor Damping with Water Injection

The influence of water injection on the eigenfrequencies and on thermoacoustic damping is discussed in the following section. At first, the focus will be placed on water injection at constant equivalence ratio before water injection at constant flame temperature is considered. Experimentally determined eigenfrequencies and damping rates will be presented for the Helmholtz mode as well as for the longitudinal half-wave mode.

7.3.1. Water Injection at Constant Equivalence Ratio

Firstly, the influence of water injection on the stability margin is considered for water-injection at constant equivalence ratio. All operating parameters other than the water-to-fuel ratio remain unchanged. This means that an increase of Ω always results in a decrease of the adiabatic flame temperature (cf. Section 5.1).

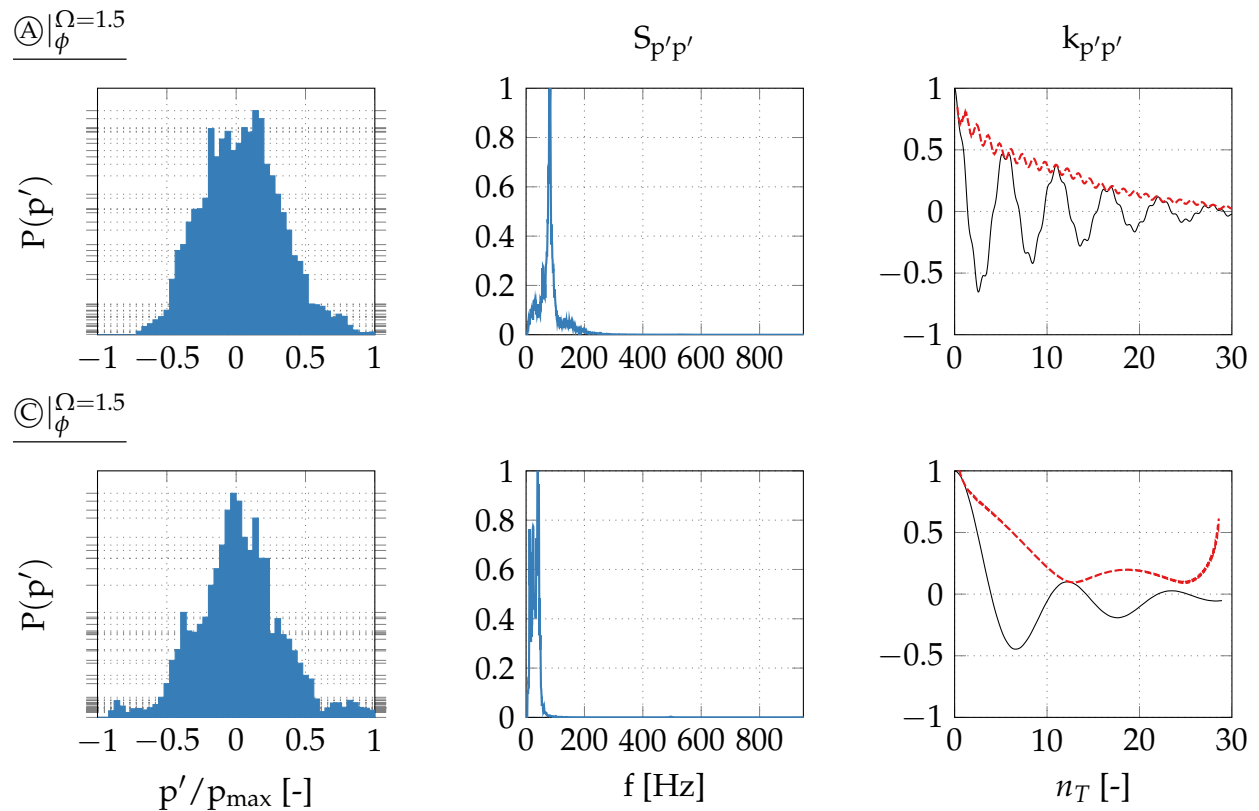


Figure 7.5.: Distribution of the pressure amplitudes, power spectral density and autocorrelation functions with envelope (----) for water injection at constant equivalence ratio.

Statistical distributions, power density spectra and the corresponding autocorrelation functions obtained from the dynamic pressure recordings are displayed in Figure 7.5. Two representative operating ranges, i.e. (A) $|\phi$ and (C) $|\phi$, were selected for this purpose. In contrast to dry operation, both pressure spectra obtained with water injection at constant equivalence ratio show sharp peaks only for mode η_1 . For (A) $|\phi^{\Omega=1.5}$ this pressure peak is located at 89 Hz. In case (C) $|\phi^{\Omega=1.5}$ the corresponding frequency is considerably lower with a value of 33 Hz. In the latter case, a loss of the aerodynamic stabilization of the flame is occasionally observed. However, additional pressure peaks in the vicinity of 500 Hz are hardly visible here. With respect to (A) $|\phi^{\Omega=1.5}$, the PDFs of the pressure amplitudes indicate linear stable operation. For operating point (C) $|\phi^{\Omega=1.5}$ a slight tendency to a bimodal distribution is seen. In both cases, the autocorrelation function is found to decay over time while the contribution of f_1 clearly dominates.

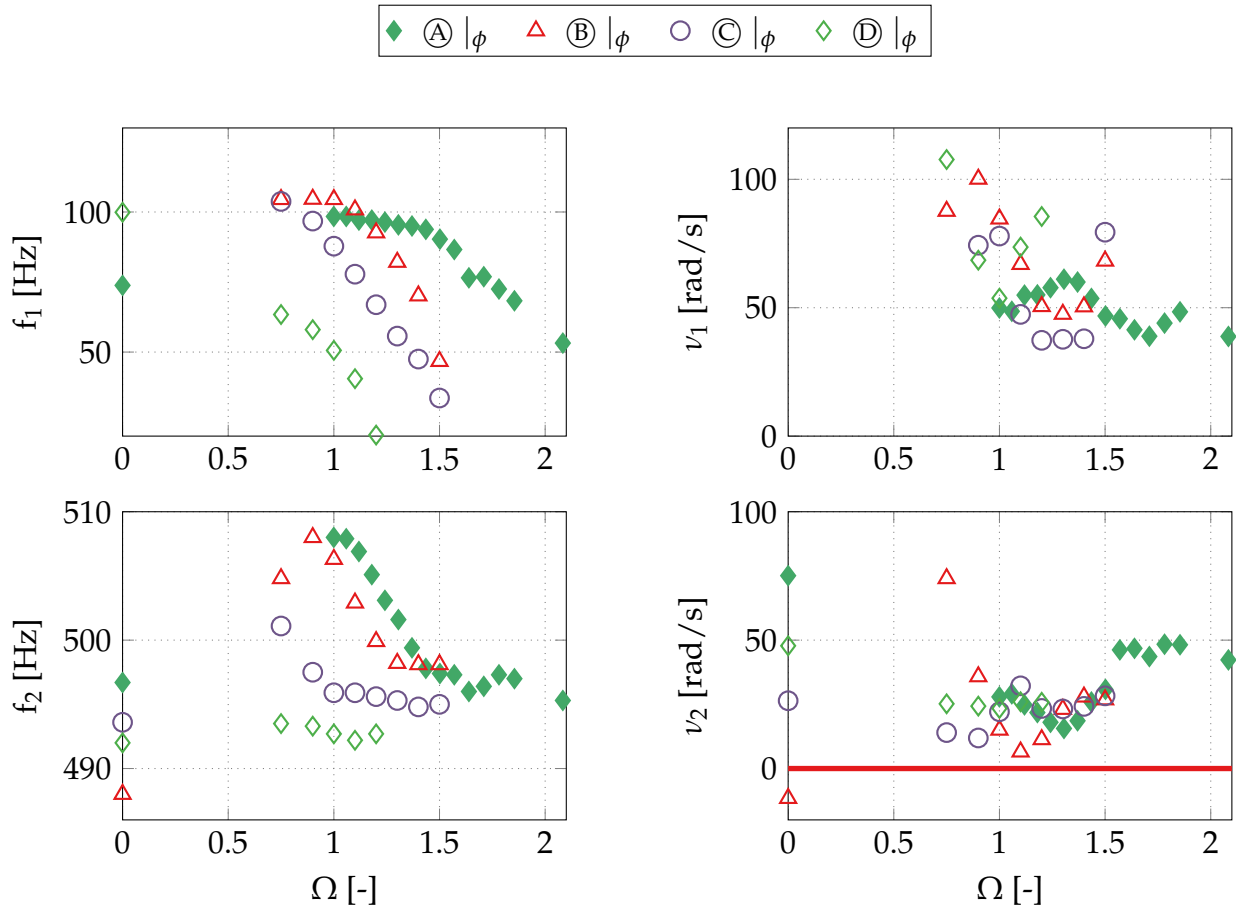


Figure 7.6.: Experimentally determined eigenfrequencies and thermoacoustic damping rates for water injection at constant equivalence ratio.

However, for operating range (A) $|\phi$ a second, superimposed oscillation mode is still visible in the autocorrelation function. From the respective autocorrelation functions, eigenfrequencies and damping rates are calculated for two modes. The results obtained for water injection at constant equivalence ratio are shown in Figure 7.6. With regard to the Helmholtz mode the eigenfrequencies f_1 are found to decrease steadily with Ω . This applies to all investigated operating ranges, with the curve decline for (A) $|\phi$ being the smallest. In general, it is found that Helmholtz modes η_1 are significantly weaker damped with water injection when compared to dry operating conditions. In contrast to dry operation, Helmholtz modes now also occur for operating ranges (B) $|\phi$ and (C) $|\phi$. All operating ranges have in common that their damping rates ν_1 initially decrease when increasing the water amount. Interestingly, the damping rates tend to increase again once the respective eigenfrequency falls below 50 Hz.

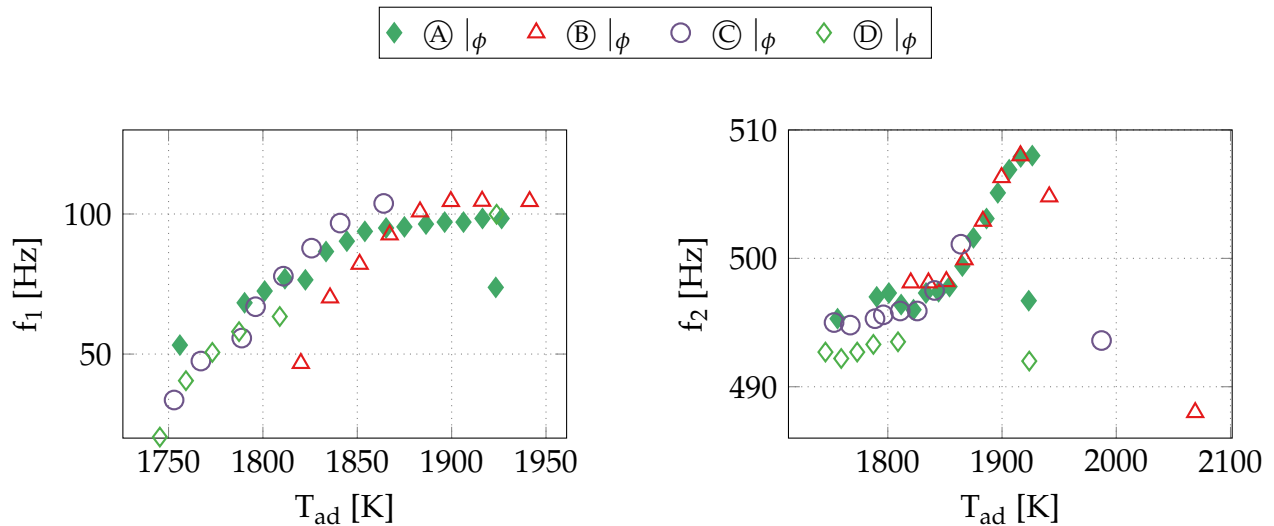


Figure 7.7.: Experimentally determined eigenfrequencies for water injection at constant equivalence ratio depending on the adiabatic flame temperature.

For the second mode η_2 , the damping rates ν_2 range in a limited band between 10 rad s^{-1} and 40 rad s^{-1} for most of the operating points with water injection. For $\textcircled{A} | \phi$, the damping rate ν_2 appears to reach a plateau at $\nu_2 \approx 50 \text{ rad s}^{-1}$ at all water-to-fuel ratios of above $\Omega = 1.5$. In case $\textcircled{B} | \phi$ it is remarkable that water injection causes the combustor to return to stable operation with a positive damping rate. In addition, it is found that the eigenfrequencies correlate with the adiabatic flame temperature rather than with the water-to-fuel ratio. This is clearly shown in Figure 7.7, as the curves of f_1 and f_2 plotted over the adiabatic flame temperature lie almost perfectly on top of each other across all operating points.

7.3.2. Water Injection at Constant Adiabatic Flame Temperature

The following section discusses the influence of thermal load increase on thermoacoustic damping of the combustor when injecting water at constant adiabatic flame temperature. The results will be discussed on the basis of the four known baseline operating points \textcircled{A} – \textcircled{D} . This allows to discuss the results for three different flame temperature levels. Thermoacoustic stability is quantified using eigenfrequencies and damping rates which were measured for water-to-fuel ratios of up to 2.

Figure 7.8 displays statistical distributions, pressure spectra and autocorrelation functions for the four selected operating points in the range given by $\textcircled{A} |_{T_{\text{ad}}}$. For $1.0 \leq \Omega \leq 1.7$ the pressure spectrum exhibits two sharp resonance peaks. Again, the respective peaks at the lower frequencies correspond to the Helmholtz mode, while peaks at higher frequencies result from the first half-wave mode in the combustor. At identical Ω the frequencies of the Helmholtz modes are found to be higher than those for water injection at constant equivalence ratio (cf. Figure 7.5). With increasing water-to-fuel ratio, the frequency of the Helmholtz mode shifts to lower values. Pressure peaks associated with mode η_2 are still visible for water-to-fuel ratios of up to $\Omega = 1.7$. Linearly stable operation is indicated by the Gaussian shape of the distribution of the pressure time traces for $1.0 \leq \Omega \leq 1.7$. In this range, also the shape of the autocorrelation functions suggest the coincidence of two superimposed oscillation modes. At $\Omega = 2.0$, the Helmholtz mode η_1 is most dominant. In this case, the pulsation amplitudes exhibit a bimodal shape which indicates that the pressure oscillates in a limit-cycle. During operation unsteady lifting and reattaching of the flame base location was observed, while the flame remained detached in more than 90% of the recording time. The PDF shown for $\textcircled{A} |_{T_{\text{ad}}}^{\Omega=2.0}$ in Figure 7.8 represents only those states in which the flame was detached. Note that in this case the pressure signal has been bandpass-filtered around the dominant pulsation frequency of 50 Hz.

In the next step, the influence of Ω on eigenfrequencies and damping rates will be considered for water injection at constant flame temperature. As for water injection at constant equivalence ratio (cf. Section 7.3.1), results are discussed for modes η_1 and η_2 . Figure 7.9 shows the determined eigenfrequencies and damping rates for all four operating ranges plotted over the water-to-fuel ratio. When considering the cases $\textcircled{A} |_{T_{\text{ad}}}$ and $\textcircled{D} |_{T_{\text{ad}}}$ water injection is found to increase the eigenfrequency of the Helmholtz mode by approximately 20% compared to dry operation. In case $\textcircled{A} |_{T_{\text{ad}}}$ an increase of Ω beyond 0.9 causes f_1 to remain almost constant at a value of approximately 100 Hz. A decrease of the frequency is only observed for water-to-fuel ratios of larger than 1.5. At water-to-fuel ratios of more than 1.9 the eigenfrequency of the Helmholtz mode f_1 suddenly drops by approximately 50% and keeps decreasing with increasing water-to-fuel ratio. Finally, at $\Omega \approx 2.0$ the Helmholtz mode becomes linearly unstable.

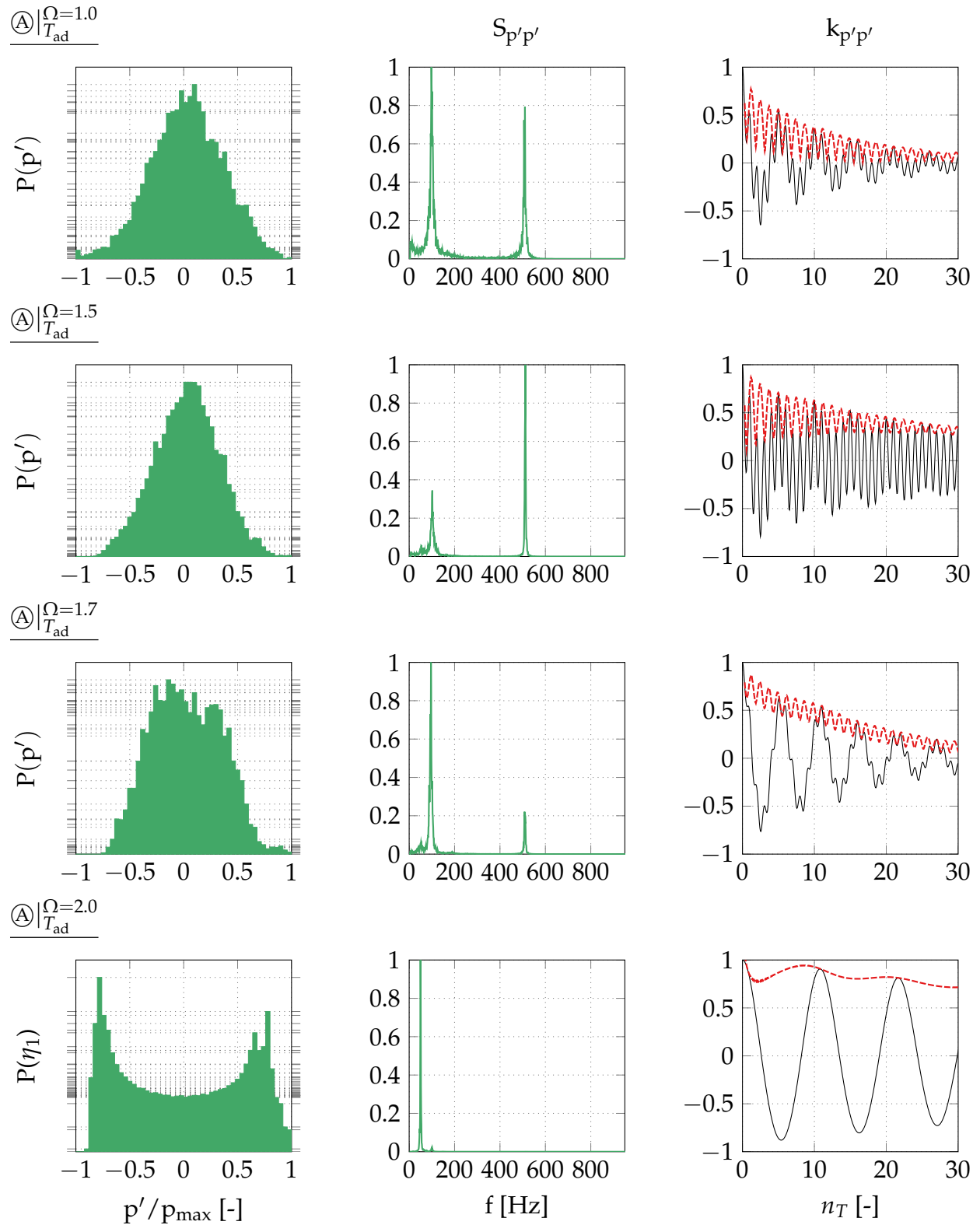


Figure 7.8.: Distribution of the pressure amplitudes, power spectral density and autocorrelation functions with envelope (---) for water injection at constant adiabatic flame temperature for operating range $\textcircled{A} |_{T_{ad}}$.

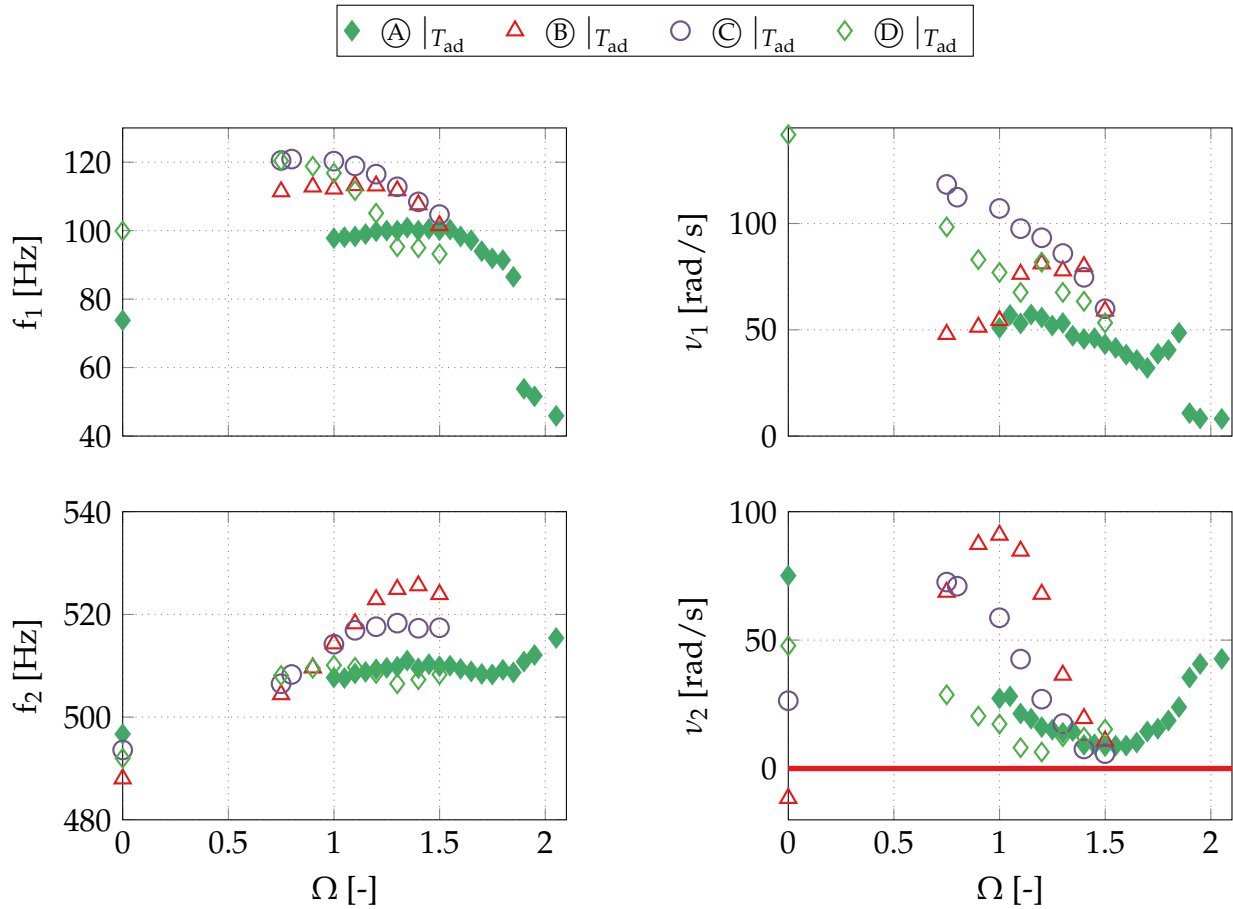


Figure 7.9.: Experimentally determined eigenfrequencies and thermoacoustic damping rates for water injection at constant adiabatic flame temperature.

For all other cases similar trends are seen, while the onset of the frequency drop shifts towards lower values of Ω . With only a few exceptions all damping rates ν_1 with water injection are below 100 rad s^{-1} . In particular for operating range $\textcircled{A} |_{T_{\text{ad}}}$ between $\Omega = 0.9$ and 1.3 the values fluctuate around 50 rad s^{-1} . A further increase of Ω leads to a continuous drop of the damping rate associated with the Helmholtz mode. This applies to the cases $\textcircled{C} |_{T_{\text{ad}}}$ and $\textcircled{D} |_{T_{\text{ad}}}$ for water-to-fuel ratios of up to $\Omega = 1.5$. Case $\textcircled{B} |_{T_{\text{ad}}}$ does not exhibit a clear trend.

In all investigated cases water injection causes a frequency shift of mode η_2 . Compared to dry operation this difference is in the order of $+10 \text{ Hz}$. Beyond water-to-fuel ratios of 1.0 , a further increase of Ω in operating ranges $\textcircled{A} |_{T_{\text{ad}}}$ and $\textcircled{B} |_{T_{\text{ad}}}$ has only minor impact on the eigenfrequency f_2 . Note that the mean temperature in the combustion chamber actually rises when

increasing Ω at constant adiabatic flame temperature. This is due to the fact that the flame's net heat release increases by simultaneously adding more fuel and leaving the external cooling of the combustor unchanged. As a result, the average speed of sound also increases, which in turn leads to an increase of the resonance frequency of the first half-wave mode η_2 . As already observed for water injection at constant equivalence ratio, the linearly unstable mode η_2 at operating point ② returns to a thermoacoustically stable state also when injecting water at constant adiabatic flame temperature. This already occurs at the minimum possible water-to-fuel ratio of $\Omega = 0.75$. Quantitatively, this corresponds to an increase of the damping rate ν_2 by more than 80 rad s^{-1} . For the case ③ $|_{T_{ad}}$, which is stable at $\Omega = 0$, water injection leads to an increase of ν_2 by approximately 25 rad s^{-1} at $\Omega = 0.75$. When further increasing the water-to-fuel ratio, the damping rate keeps decreasing again. Operating ranges ① $|_{T_{ad}}$ and ④ $|_{T_{ad}}$ exhibit the highest damping rates under dry operation when compared to the remaining two cases ② $|_{T_{ad}}$ and ③ $|_{T_{ad}}$. Moreover, both cases show a similar dependency of the thermoacoustic damping rate on Ω . In contrast to ② $|_{T_{ad}}$ and ③ $|_{T_{ad}}$, water injection at constant adiabatic flame temperature leads initially to a gradual decrease of ν_2 with increasing water content. This applies within $0 < \Omega \leq 1.5$. In case ① $|_{T_{ad}}$, after passing its minimum damping rate determined at approximately $\Omega = 1.5$, a subsequent steady rise of ν_2 is seen until $\Omega = 2.0$. Interestingly, at approximately $\Omega = 1.5$ all the investigated operating conditions exhibit a minimum distance to the stability border. Noted that ν_2 remains positive for all investigated operating conditions with water injection. Linear stability of mode η_2 is additionally verified by the normal distribution of the respective pressure signals.

7.3.3. Influence of the Downstream Boundary Condition on Thermoacoustic Damping

The thermoacoustic damping ν can be considered as the net damping rate of the combustion chamber, which combines flame driving and pure acoustic damping (cf. Equation (2.96)). By changing the combustor termination from the nozzle to a perforated plate, modification of the eigenfrequencies is achieved and the acoustic damping increases (cf. Section 7.1). This be-

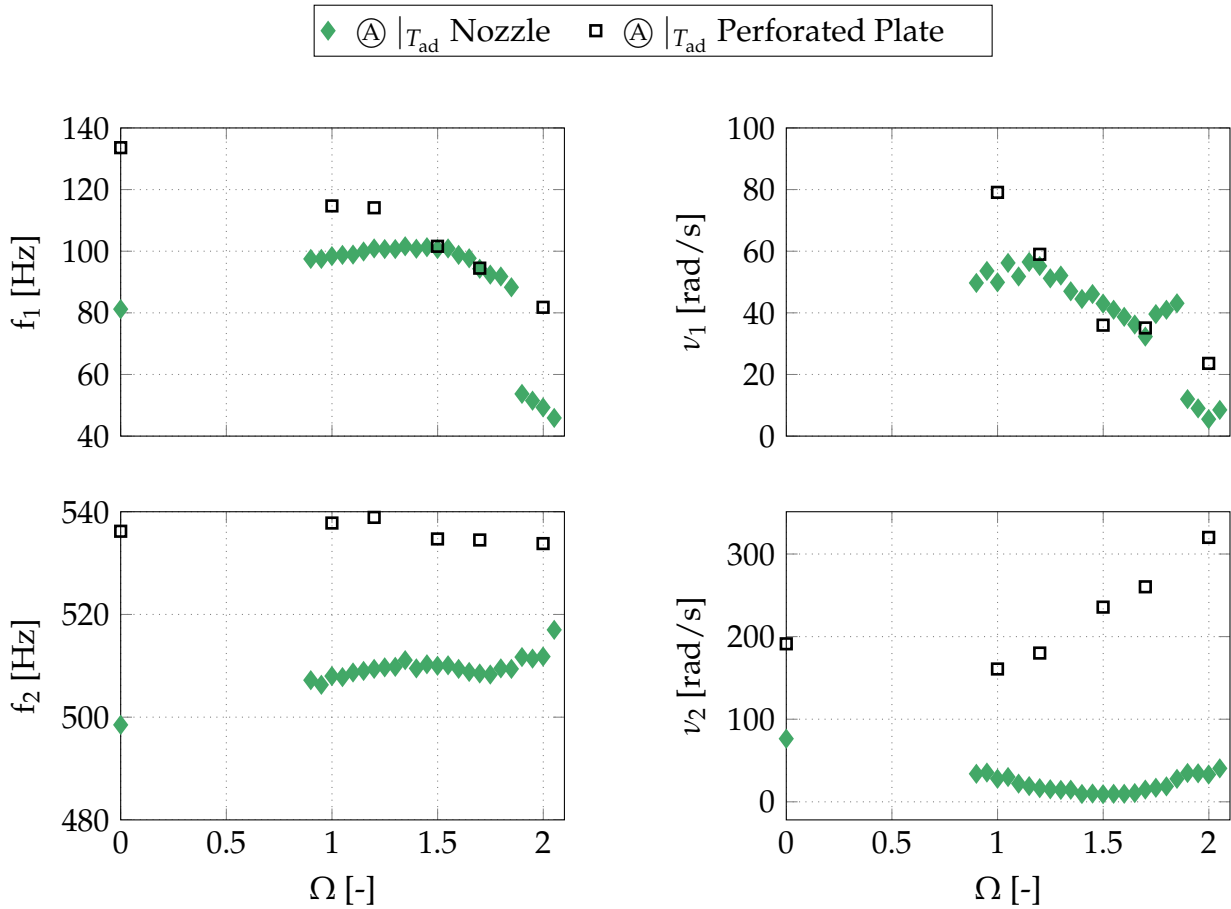


Figure 7.10.: Experimentally determined eigenfrequencies and thermoacoustic damping rates for operating range $\textcircled{A} |_{T_{\text{ad}}}$ using different boundary conditions at the combustor exit.

havior is mainly due to the different reflection coefficients of nozzle and perforated plate (cf. Figure 7.1). The aim of the following section is to examine to what extent the modes η_1 and η_2 depend on the acoustic impedance at the combustion chamber outlet. This is of particular interest for mode η_1 , which predominates with water injection. Results will be discussed by means of measured eigenfrequencies and damping rates depending on the water-to-fuel ratio. Focus is on water injection at constant flame temperature. Results are discussed on the basis of operating range $\textcircled{A} |_{T_{\text{ad}}}$ for water-to-fuel ratios between 0 and 2.

A comparison between eigenfrequencies and damping rates obtained with the nozzle and the perforated plate is shown in Figure 7.10. At first, it is observed that the oscillation frequency of the Helmholtz mode under dry

operation is by approximately 50 Hz higher when using the perforated plate. An increase of Ω leads to a gradual decrease of the eigenfrequencies in both configurations. Interestingly, in the range $1.5 \leq \Omega \leq 1.7$ the frequencies associated with mode η_1 appear to be almost independent on the acoustic boundary condition. The frequency then decreases continuously with increasing Ω . However, discontinuities between $1.7 \leq \Omega \leq 2.0$ as seen for operation with the nozzle are not observed when using the perforated plate instead. Regarding the damping rates, similar trends are discovered. Under dry operating conditions, mode η_1 is strongly damped with a damping rate of 260 rad s^{-1} in case of the nozzle and 300 rad s^{-1} with the perforated plate, respectively. Note that both values are not displayed in Figure 7.10 since they exceed the damping rates measured for $\Omega > 0$ by far. Considering the first point with water injection at $\Omega = 1.0$, the damping rate ν_1 is about 200 rad s^{-1} lower than under dry operating conditions. This applies to operation with the nozzle and with the perforated plate as well. Interestingly, a further increase of Ω leads to almost identical damping rates in the range $1.2 \leq \Omega \leq 1.7$ for both configurations. This result is remarkable since the imposed boundary conditions differ in their reflection coefficient on average by approximately 0.61 when considering a frequency range of $80 < f < 140 \text{ Hz}$. In contrast to operation with the nozzle, the Helmholtz mode remains linearly stable at all times when using the perforated plate. This is expressed by positive damping rates.

A different picture is seen for mode η_2 . In this case, the eigenfrequencies obtained with the perforated plate exceed the values for the nozzle on average by approximately 25 Hz. Their associated damping rates are found to be higher and show a different trend as for the Helmholtz mode. For $\Omega = 0$, the damping rate obtained with the perforated plate is by approximately 120 rad s^{-1} higher and increases gradually with increasing water-to-fuel ratio. Its maximum of approximately 300 rad s^{-1} is determined for $\Omega = 2.0$. Altogether, the damping rates of mode η_2 are up to one order of magnitude higher when using the perforated plate instead of the nozzle. Qualitatively, these results meet the expectations from the respective reflection coefficient of nozzle and perforated plate.

It can thus be concluded that the thermoacoustic damping rate of mode η_2 strongly depends on the reflection coefficient at the exit of the combus-

tor. In contrast, the damping of the Helmholtz indicates a much weaker dependency on the impedance at the combustor outlet.

7.3.4. Acoustic Dissipation and Flame Gain

So far, the influence of water injection on the stability margin of the combustion chamber has been investigated on the basis of the thermoacoustic net damping rates ν associated with the eigenfrequencies f . The aim of the following investigation is to determine the influence of water injection on the acoustic dissipation α and the flame driving β separately. For this purpose, the present combustion system with flame feedback will be compared to a hypothetical system without feedback. Flame feedback can be eliminated by using the measurement technique described in Section 3.4.3 to determine pure acoustic eigenfrequencies and damping rates by analyzing integral OH^* -intensity and pressure signal in parallel. Firstly, a system with passive flame will be considered to discuss the influence of Ω on the acoustic damping. In the next step, flame gains will be analyzed for the entire range of operating conditions with and without water injection to discuss the influence of flame dynamics.

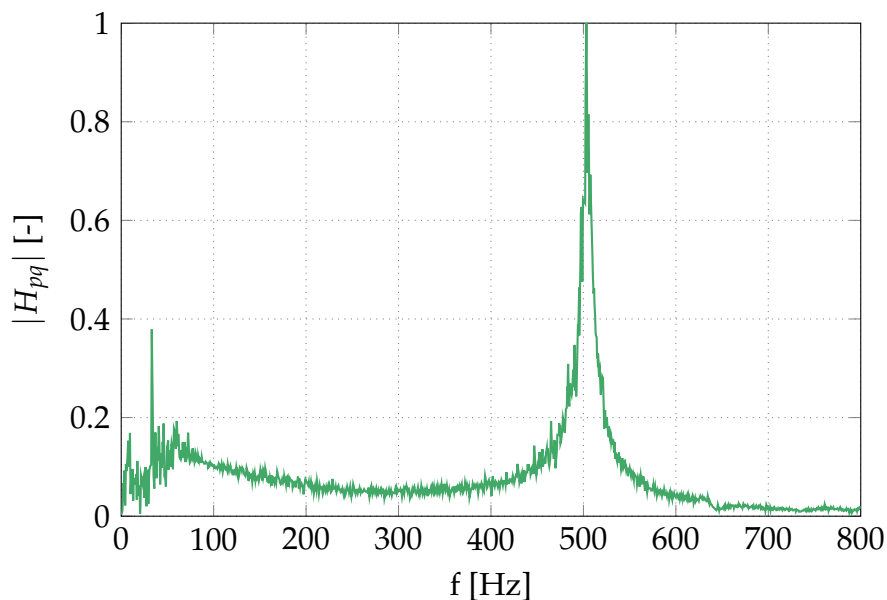


Figure 7.11.: Transfer function between integral OH^* -chemiluminescence as a marker for unsteady heat release and dynamic pressure for operating point $\textcircled{A}|_{T_{\text{ad}}^{\Omega=1.0}}$.

The required acoustic damping rates of the passive system are identified from the autocorrelation function k_{pq} associated with the transfer function H_{pq} between acoustic pressure and unsteady heat release. The transfer functions are calculated for each operating condition separately. One example is presented in Figure 7.11, which is representative for operating point $\textcircled{A} \big|_{T_{\text{ad}}^{\Omega=1.0}}$. The plot shows a sharp resonance peak in the vicinity of $f = 500$ Hz. This peak corresponds to the characteristic eigenfrequency of mode η_2 . However, in none of the cases peaks were detected in the low frequency range where the Helmholtz mode occurs. Measured pure acoustic damping rates are therefore only available for η_2 . Consequently, results will be discussed in the following on the basis of the first standing half-wave mode in the combustion chamber.

The influence of water injection at constant equivalence ratio on the acoustic dissipation will be considered first. Figure 7.12 shows acoustic eigenfrequencies $f_{2,\text{ac}}$ and acoustic damping rates α_2 of mode η_2 of the combustor with a passive flame. It is evident from the figure that, in contrast to the thermoacoustic eigenfrequencies f_2 (cf. Figure 7.6), the acoustic eigenfrequencies tend to decrease steadily as the water-to-fuel ratio increases. The acoustic damping rates, however, remain almost constant over a wide range of operating conditions. Only for operating range $\textcircled{A} \big|_{T_{\text{ad}}}$ damping rates are found to increase slightly with Ω . The largest shift of the damping

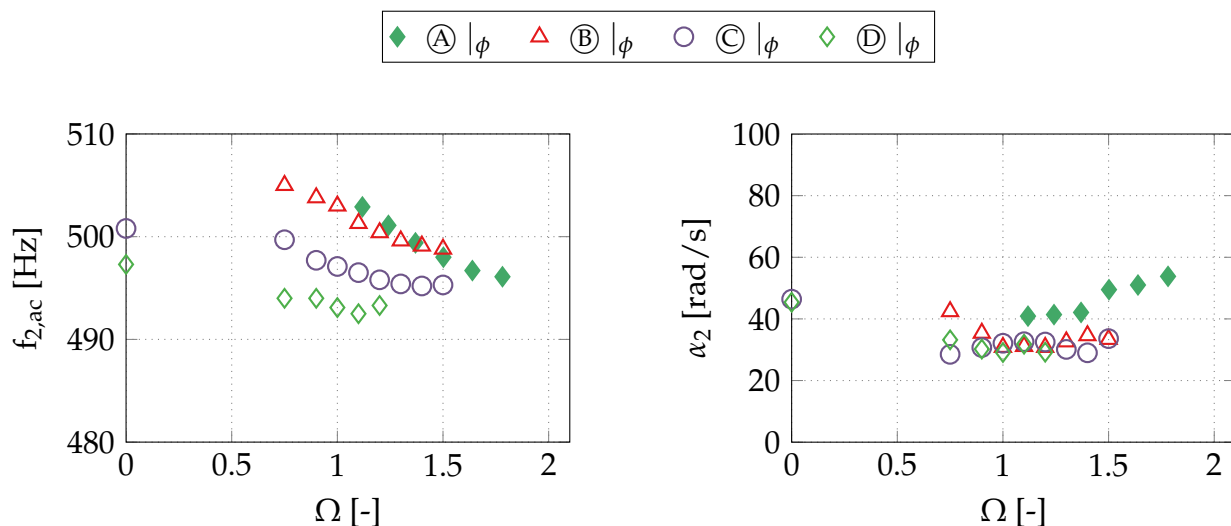


Figure 7.12.: Experimentally determined acoustic eigenfrequencies and damping rates for water injection at constant equivalence ratio.

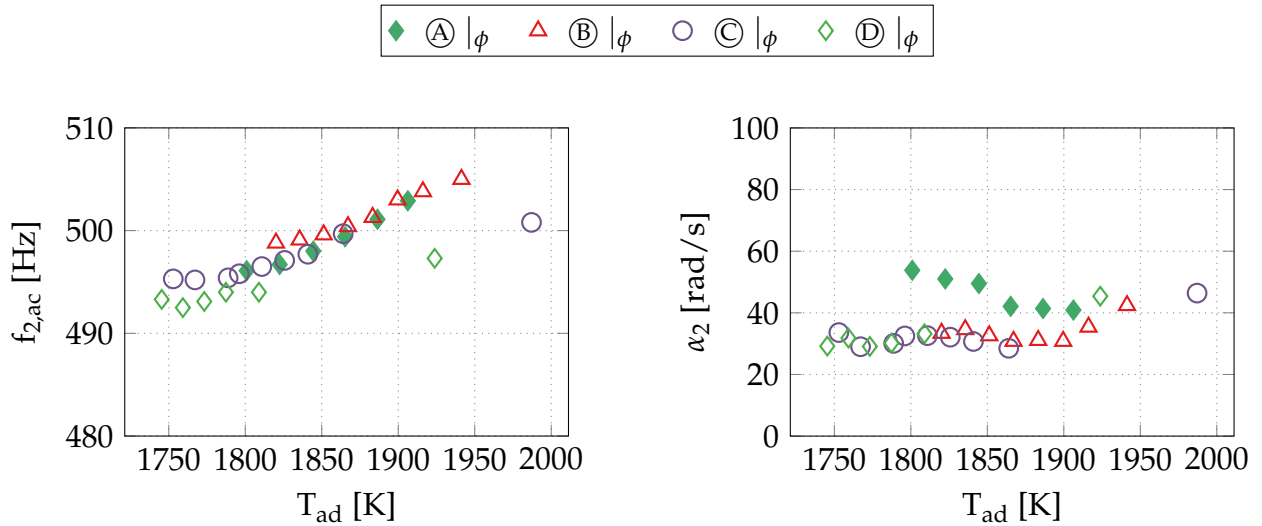


Figure 7.13.: Experimentally determined acoustic eigenfrequencies and damping rates for water injection at constant equivalence ratio depending on the adiabatic flame temperature.

rates is determined between $\Omega = 0$ and the respective minimal achievable water-to-fuel ratio. This applies to all investigated operating ranges. These results for water injection are also in line with the results of the authors introducing the measurement method [22]. Therein, the authors also observed almost constant pure acoustic damping rates α when varying the equivalence ratio of a premixed flame, while the thermoacoustic damping rates ν were more sensitive to varying operating conditions. The nearly constant acoustic dissipation was explained by the weak effect of the varying operating parameters on temperature field and flow conditions in the combustor. In the present case with water injection at constant equivalence ratio, the determined acoustic eigenfrequencies $f_{2,ac}$ indicate a decrease of the speed of sound of the hot gas in the combustor with increasing Ω . This is attributed to the reduction of the exhaust gas temperature caused by the drop of the flame temperature. The correlation between $f_{2,ac}$ and the flame temperature is clearly illustrated in Figure 7.13. It can be seen that, except for a few outliers, the frequency increases steadily with T_{ad} in the given temperature range for all operating conditions examined. Note that under adiabatic conditions, water addition would in fact increase the speed of sound since the water content in the hot gas rises with the water-to-fuel ratio.

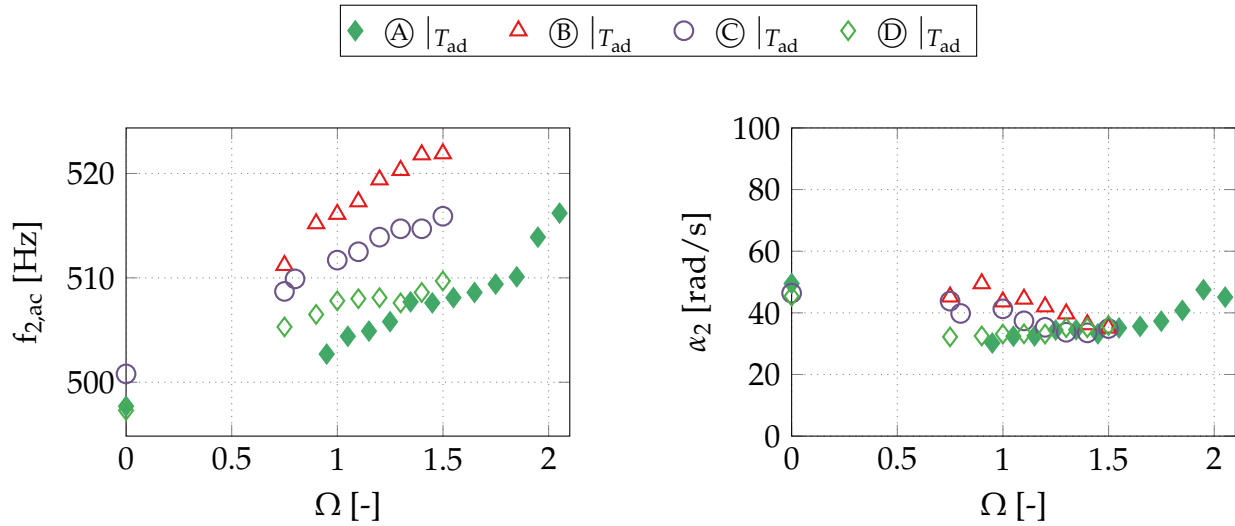


Figure 7.14.: Experimentally determined acoustic eigenfrequencies and damping rates for water injection at constant adiabatic flame temperature.

In the next step, water injection at constant adiabatic flame temperature will be analyzed. For this purpose, acoustic eigenfrequencies $f_{2,ac}$ and acoustic damping rates α_2 are shown in Figure 7.14 for increasing water-to-fuel ratio. In contrast to water injection at constant equivalence ratio, the measurements indicate a steady rise of the acoustic eigenfrequency with increasing Ω . From this, an increase of the speed of sound with rising water-to-fuel ratio can be concluded. This increase can be explained both by the higher water content in the exhaust gas and the rising mean temperature in the combustor due to the increase of the overall thermal load. As for water injection at constant equivalence ratio, acoustic damping rates α_2 are found to vary only slightly with the water-to-fuel ratio under all operating conditions. It is therefore concluded that water injection in a combustor with passive flame primarily affects the acoustic eigenfrequency $f_{2,ac}$ rather than the acoustic dissipation α_2 . If the equivalence ratio is kept constant, $f_{2,ac}$ decreases with increasing water-to-fuel ratio. In contrast, water injection at constant adiabatic flame temperature leads to an increase of the acoustic eigenfrequency $f_{2,ac}$. This allows to infer on the average speed of sound in the combustor, which is explained in more detail in Section 8.2.2.

After determining the eigenfrequencies and damping rates with water injection for the active and the passive system, the contribution of flame

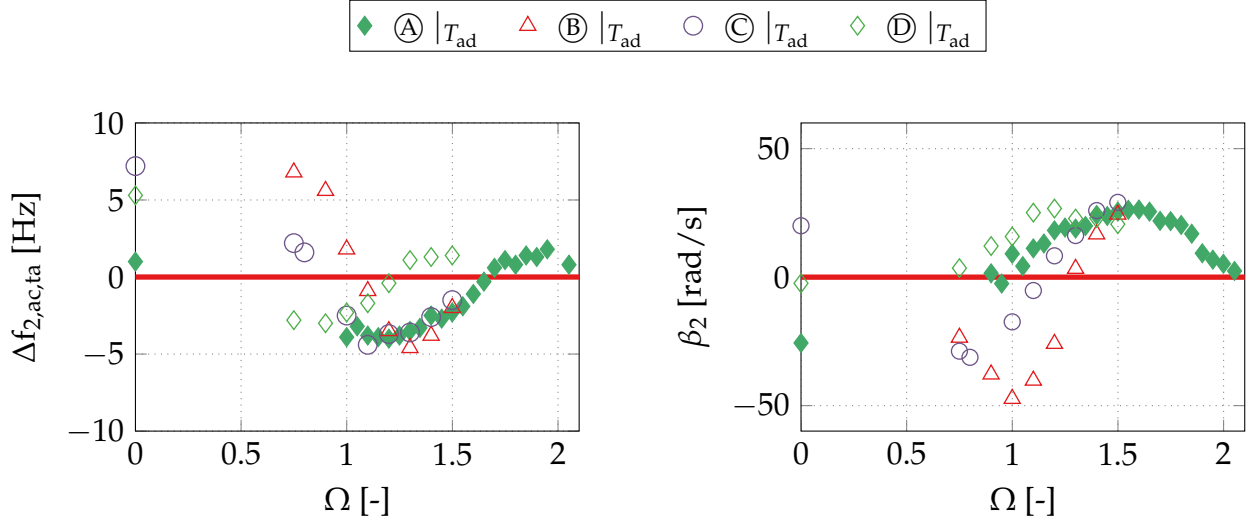


Figure 7.15.: Experimentally determined frequency shifts and flame gains for water injection at constant adiabatic flame temperature.

feedback can be obtained. This will be expressed by the frequency shift between passive (purely acoustic) and active (thermoacoustic) system, denoted by $\Delta f_{2,ac,ta}$ and the flame gain β_2 . The flame gain β_2 is calculated by adapting Equation (2.96) to yield $\beta_2 = \alpha_2 - \nu_2$. The frequency shift between passive and active system is obtained by $\Delta f_{2,ac,ta} = f_{2,ac} - f_2$. The results are shown in Figure 7.15. It can be seen from the figure that the flame gain under dry operation is negative in case (A). A gradual increase of the water-to-fuel ratio initially leads to an increase of β_2 . After exceeding $\Omega \approx 0.9$, the flame gain changes its sign from negative to positive. The maximum flame gain is reached at approximately $\Omega = 1.5$. A further increase of Ω ultimately leads to a decrease of β_2 . With respect to the three remaining operating ranges, the trends appear to be similar. However, depending on the operating range the curves of $\Delta f_{2,ac,ta}$ and β_2 are shifted along the Ω axis. Note that for operating ranges (B) $|T_{ad}$, (C) $|T_{ad}$ and (D) $|T_{ad}$ data are only provided for water-to-fuel ratios of up to 1.5.

While the pure acoustic damping of the combustor depends on passive factors such as temperature, flow field and acoustic boundary conditions the flame gain is a result of the flame's response to acoustic perturbations. The flame response is commonly described by the flame transfer function. It was concluded from Section 6.3 that the FTFs of flames with water injection at constant adiabatic flame temperature scale for Strouhal numbers

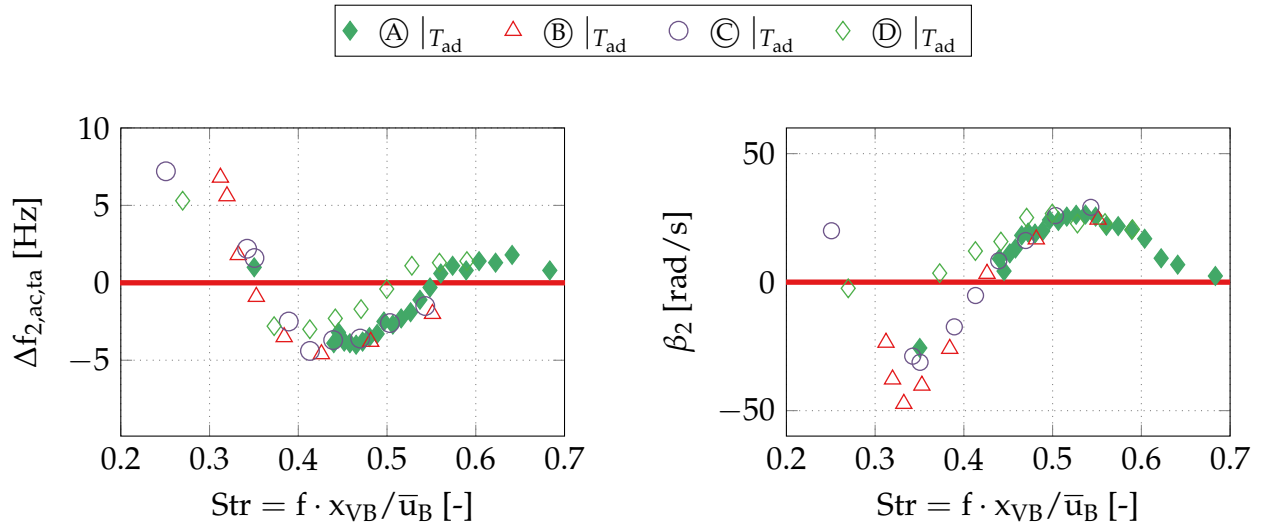


Figure 7.16.: Experimentally determined frequency shifts and flame gains for water injection at constant adiabatic flame temperature depending on the Strouhal number.

above 0.2 with the flame length. Figure 7.16 shows that this behavior is also seen for the frequency shifts $\Delta f_{2,ac,ta}$ between the passive (from $f_{2,ac}$) and the active system (from f_2) as well as for the flame gains β_2 . Both curves lie almost perfectly on top of each other when they are plotted over the Strouhal number instead of Ω . The lowest flame driving is observed at approximately $\text{Str} = 0.38$. In this case, flame dynamics increases the net damping of the system ν_2 (cf. Figure 7.9). In contrast, at approximately $\text{Str} = 0.5$ the driving force of the flame is at its maximum, which results in the lowest measured thermoacoustic damping ν_2 since the acoustic dissipation α_2 (cf. Figure 7.14) remains approximately constant. Note that β_2 is always lower than α_2 such that mode η_2 remains thermoacoustically stable under all operating conditions with water injection. At both extrema of β_2 , the frequency shift between active and passive system is approximately zero. In contrast, at approximately $\text{Str} \approx 0.68$ flame driving is close to zero. Note that case (D) $|T_{ad}$ deviates slightly from the other cases, as the point $\beta_2 = 0$ is shifted towards lower Strouhal numbers. At this point, flame dynamics has no influence on the thermoacoustic damping ν_2 , but induces a frequency shift of approximately 5 Hz. At $\text{Str} \approx 0.66$, β_2 is close to zero. The same applies to the frequency shift between active passive system.

The fact that not only the FTF, but also β_2 and $\Delta f_{2,ac,ta}$ exhibit a clear scalability with the Strouhal number indicates that the main effect of water injection at constant flame temperature on flame dynamics is the induced phase shift due to the axial displacement of the flame with increasing Ω . This has been shown for Strouhal numbers ranging between approximately 0.25 and 0.68. A detailed comparison of the results for $\Delta f_{2,ac,ta}$ and β_2 with the FTF can be found in Appendix D demonstrating consistency between both measurement approaches. It is therefore assumed that thermoacoustic stability of the combustor with water injection at constant flame temperature can be predicted by using the FTF to account for flame dynamics. Furthermore, Strouhal scaling may be exploited to calculate thermoacoustic stability at water-to-fuel ratios for which no measured FTFs are available. Note that this only applies for sufficiently high frequencies at which no interaction between acoustics and spray response occurs.

7.4. Benchmark of Different Methods for Thermal Power Increase

Previously, damping of thermoacoustic modes with water injection has been discussed based on the water-to-fuel ratio. With technical applications in mind, water injection into premixed flames is used to increase the thermal output of the combustor at constant flame temperature. The impact of the load increase by water injection on the stability margin is therefore of particular interest. This last section of the chapter discusses the relationship between the achievable thermal load increase and the stability margin of the given combustor in more detail. In this context, water injection will be compared with two other methods to increase the thermal load without adding water.

The results are discussed based on operating point (A), from which a gradual increase of the thermal power is initiated. In practice, the thermal load of the combustor is controlled by adjusting the fuel mass flow rate. In this framework, three cases will be considered: Firstly, power augmentation by increasing the fuel mass flow only (F). In this case, the increase of the ther-

Table 7.1.: Control parameters for three methods to increase the thermal load of the combustor.

Notation	Control Parameter	\dot{m}_{Fuel}	\dot{m}_{Air}	ϕ	T_{ad}	P_{th}
(F)	Fuel	↑	→	↑	↑	↑
(F+A)	Fuel + Air	↑	↑	→	→	↑
(F+W)	Fuel + Water	↑	→	↑	→	↑

mal load is achieved by increasing the equivalence ratio. Consequently, the adiabatic flame temperature also rises. In the second case, fuel and main air mass flow rate (F+A) are increased at the same time to maintain the equivalence ratio constant. In turn, this means that the adiabatic flame temperature is held constant with increasing thermal load. The relationships between the parameters fuel mass flow, air mass flow, equivalence ratio, adiabatic flame temperature and thermal power are given in Table 7.1.

As discussed in Section 7.2, the Helmholtz mode has found to be strongly damped under all dry operating conditions ①–④. This also applies to all investigated operating points within (F) and (F+A). Therefore, this section discusses the results on the basis of thermoacoustic damping rates for the first longitudinal half-wave mode in the combustion chamber (η_2). Measurements were taken during a step-by-step increase of the thermal load by using the three aforementioned methods (F), (F+A) and (F+W). The obtained results are displayed in Figure 7.17. Compared to methods (F) and (F+A), a significant shift of the frequency f_2 is noticed when increasing the thermal power with water injection (F+W). The largest frequency shift is observed between 40 kW and 46 kW. The eigenfrequencies f_2 of case (F+W) are by up to 20 Hz higher than those measured for cases (F) and (F+A). This behavior is mainly attributed to the increased speed of sound in the combustion chamber caused by water injection. In case (F), the eigenfrequency of mode η_2 tends to drop with increasing P_{th} , whereas in case (F+A) the frequency gradually increases with the thermal load. In operating mode (F), the stability margin drops steeply with increasing P_{th} after reaching the peak value of 95 rad s⁻¹. Using this method, the stability limit is already reached when increasing the thermal load by approximately 10%. In contrast, the decrease of the stability margin with P_{th} is

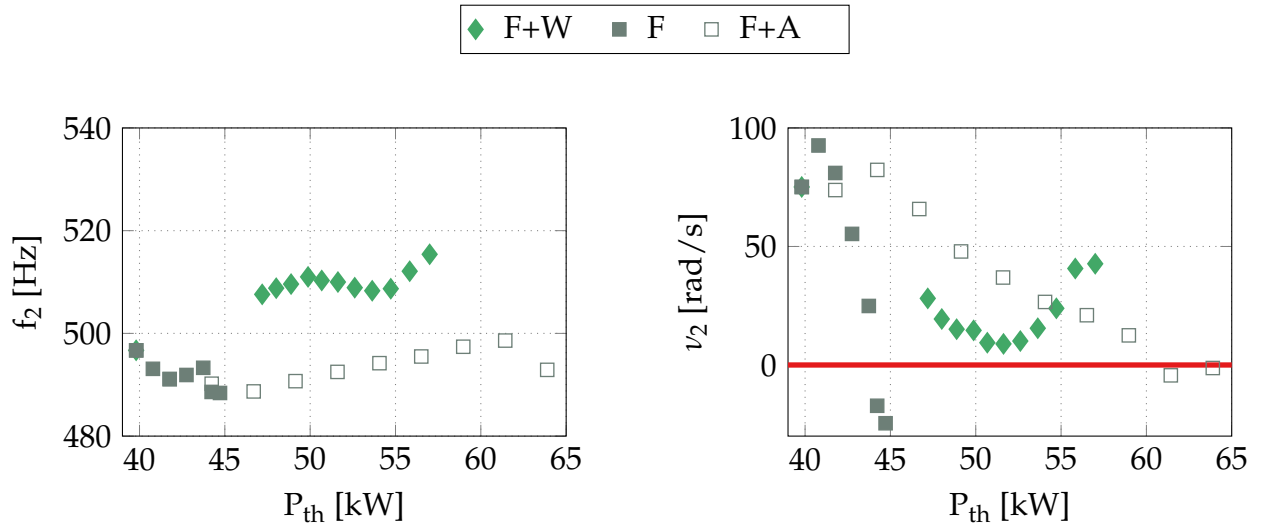


Figure 7.17.: Eigenfrequencies and thermoacoustic damping rates when increasing the thermal load of the combustor.

found to be less steep when increasing thermal power by simultaneously increasing fuel and air mass flow rate (F+A). This means that P_{th} may be raised by more than 60% before the combustor reaches the stability border. In general, (F) and (F+A) have in common that their thermoacoustic damping rates decrease steadily with increasing P_{th} after passing its first maximum value. A different picture is seen for operation mode (F+W). At first, the damping rate gradually decreases with increasing thermal load until approximately 53 kW. Initially, ν_2 drops less steep than in case (F), but steeper than in case (F+A). After passing a minimum, the damping rate ν_2 increases again with P_{th} . Note that up from $\Omega \approx 2.0$ low-frequency pressure pulsations start to grow (see Section 7.3.2). In this case, the onset of Helmholtz instability poses the upper stability limit in terms of thermal power. Given this limit, water injection allows to increase the thermal power of the at present combustor by up to 40% compared to the thermal load of (A) while preserving thermoacoustically stable operation.

8 Numerical Simulation and Stability Analysis

After presenting and discussing experimental results in Chapters 5–7, this chapter deals first, with the numerical determination of the acoustic scattering matrices of the burner and second, with the prediction of thermoacoustic modes with water injection. For this purpose, two simulation models are deployed. At first, details on the modeling approach as well as the numerical setup are presented. Subsequently, numerically calculated scattering matrices will be discussed. Finally, acoustic damping and thermoacoustic stability is predicted based on both modeled and experimentally determined scattering matrices.

8.1. Modeling Approach and Numerical Setup

First, a modeling strategy to calculate the acoustic scattering matrices of the burner will be introduced. The chosen approach is based on combining stationary simulations of the flow field from computational fluid dynamics (CFD) and a subsequent calculation of the acoustic quantities by using computational aero-acoustics (CAA) to solve the linearized Euler equations (LEE). Subsequently, the framework for conducting global stability analyses of the entire combustion system is introduced. This involves the solution of an eigenvalue problem. Scattering matrices are employed to include acoustic losses across the burner and the dynamic flame response with water injection. Both types of simulations rely on the finite element method (FEM) and are implemented in the commercially available software package COMSOL Multiphysics [33].

8.1.1. Acoustic Scattering Behavior: CFD/CAA Approach

The basic idea of hybrid CFD/CAA approaches for determining the acoustic scattering behavior of components such as swirl burners is to separate

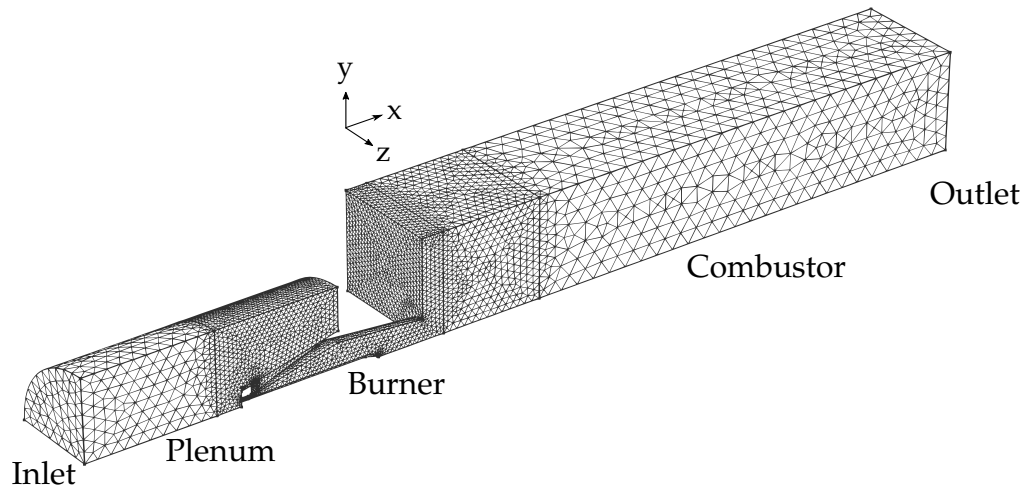


Figure 8.1.: Computational grid used for the CAA simulation: Representation of one quarter of the burner and injector geometry ($\approx 420\,000$ elements).

the calculation procedure into two steps. Initially, the mean flow quantities describing the stationary flow field are obtained from Reynolds averaged Navier Stokes (RANS) CFD simulations by using a turbulence model. Afterwards, the fluctuating fields which describe acoustic wave propagation [48, 108] are computed by solving the linearized Euler equations (LEE) using a stabilized Galerkin/least-squares (GLS) approach, as introduced in Section 2.4. The CFD solution provides the linearization point and allows to account for acoustic losses due to mean flow. This approach is based on the assumption that the acoustic quantities $\hat{\Phi}$ (see Section 2.1.1) are influenced by the mean flow field but not vice versa. Within the last few years, this methodology has gained increasingly in importance and has found various applications (see e.g. [57, 58, 75, 81, 163]).

A discretized FEM representation of the burner including the water injector is provided by a computational grid consisting of approximately 420 000 tetrahedral elements, as depicted in Figure 8.1. Exploiting the symmetry of the used swirl burner (see Section 4.2) allows to constrain the mesh to one quarter of the full geometry. The regions encompassing the burner itself and the shear layers evolving downstream of the burner outlet are represented by a distinctly finer grid resolution. The grid resolution decreases with increasing distance from the burner outlet. Periodic boundary conditions are imposed at the symmetry planes. The remaining walls are represented by slip conditions. Acoustic boundary layer effects near the wall are neglected. External forcing is achieved by implementing a veloc-

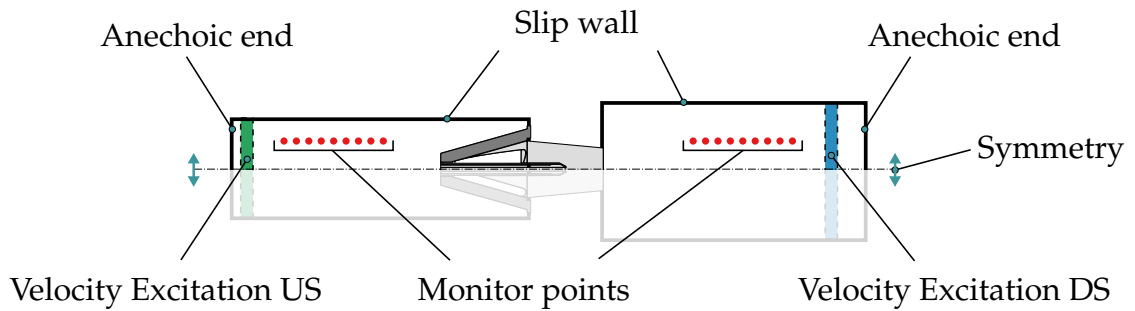


Figure 8.2.: FEM-Model with boundary conditions used for the determination of the burner scattering matrix using CAA.

ity excitation term imposed over the entire cross-section at locations far upstream (US) and downstream (DS) of the burner. To prevent reflection of acoustic waves at the in- and outlets of the model, anechoic boundary conditions are used. A schematic of the numerical setup is given in Figure 8.2. On the basis of this model, the LEEs are solved in frequency space (Equation (2.48)). The stabilization parameter is chosen to $\alpha_\tau = 0.1$ in accordance with [70, 128] (see Section 2.4). Using velocity forcing from up- and downstream and sweeping over a certain frequency range yields in a field solution at each discrete frequency f . Note that the acoustic fields obtained from the LEEs still incorporate vorticity disturbances associated with the vortex shedding in the shear layers (see e.g. [157]). According to their definition (see Equation (2.43)), acoustic scattering matrices describe solely the transmission and reflection of acoustic waves. For this purpose, the contribution of acoustic waves have to be separated from each of the modal LEE solutions before calculating the scattering matrix. Similarly to the handling of experimental data, this is achieved by applying the multi-microphone method (MMM) to determine the Riemann variants (cf. Equation (3.1)) at fixed locations, as outlined in Section 3.1. In the present case, extraction of the required complex valued modal pressures \hat{p} is implemented for 10 equally spaced monitor points up- and downstream of the burner geometry. Thus, acoustic losses originating e.g. from vortex shedding in the shear layers can be lumped into the acoustic scattering matrix. One of the major advantages over the use of conventional network models to describe the acoustic scattering behavior of swirl burners (see e.g. [13]) is that the CFD/CAA approach does not rely on additional experimental

data. Specifically, effective lengths or pressure losses to account for the transfer of acoustic energy into other forms of energy are not required. In conventional network models these parameters are incorporated by fitting constants to experimental data (see e.g. [11, 52, 115]).

8.1.2. Thermoacoustic Stability: Eigenvalue Analysis

The FEM based numerical setup presented in the following provides the framework for conducting eigenvalue studies in order to calculate the acoustic damping and the stability margin of the combustor with water injection. The basic idea is to subdivide the given test-rig configuration into two separate zones while providing coupling conditions and boundary conditions from external sources. A schematic of the computational domain and the imposed boundary conditions is displayed in Figure 8.3. In particular, the model consists of two geometrically independent domains: Firstly, the cylindrical plenum and secondly, the rectangular combustion chamber. Their dimensions are chosen identically to those in the experimental setup. Boundary conditions at the plenum inlet (R_{in}) and the combustor outlet (R_{out}) are specified by prescribing measured reflection coefficients. The transmission and reflection of acoustic waves between the plenum and the combustor is achieved by imposing a frequency dependent scattering matrix.

Acoustic quantities in the domain are calculated by solving the Helmholtz Equations (2.27) in frequency space¹. In all cases discussed below, the source term on the right hand side is set to zero. Using this simplified set of conservation equations is justifiable since all potential sources of acoustic loss and gain are included in the scattering matrix $\underline{\underline{S}}$ and the boundary conditions R_{in} and R_{out} . Circumventing the detailed resolution of complex geometries and considering only longitudinal wave propagation allows for the use of a substantially coarser computational grid than required for the LEEs. The respective equations are discretized by a standard finite element method (FEM) using linear shape functions requiring no additional stabilization techniques (see Section 2.4). In this specific

¹Solving the LEEs instead to calculate the acoustic eigenmodes would lead to erroneous results since hydrodynamical effects like vorticity are still included. For a discussion on this, see [74].

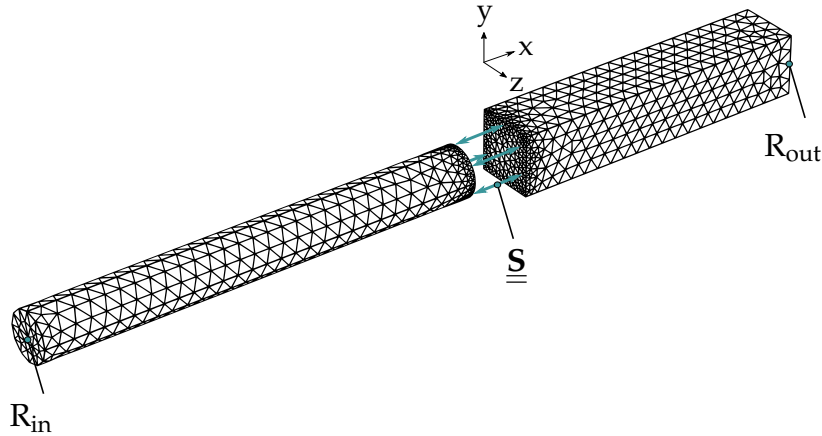


Figure 8.3.: Computational Grid for FEM-Model of the single-burner test-rig with experimentally determined boundary conditions and coupling between plenum and combustor via scattering matrix (≈ 4000 elements) used for stability analysis.

case, a computational grid consisting of approximately 4000 tetrahedrons is used, as displayed in Figure 8.3. Due to the comparably coarse grid size, exploitation of any geometrical symmetry is not necessary and the domain can be discretized in all three spatial directions at a low cost of computational power. A grid study was conducted beforehand to ensure that its resolution is still high enough to resolve the spatial distributions of the acoustic modes and to obtain grid-independent results. Applications of similar procedures can be found in several previous works in the context of gas turbine combustors [25, 26, 164] and rocket engines [147]. Using the proposed approach, a Helmholtz type of eigenvalue problem is established which can be solved numerically to obtain the eigenmodal solutions for the acoustic quantities $\hat{\Phi}$ of the entire system. These occur at specific eigenvalues ω_n which are calculated by solving the system matrix through direct LU factorization with a so-called multifrontal massively parallel sparse direct solver (MUMPS) [8] implemented in COMSOL Multiphysics [33]. More background information on the working principle of this solver and its application to thermoacoustic problems can be found in [56]. The real part $\text{Re}(\omega_n)$ of calculated eigenfrequency ω_n corresponds to the oscillation frequency and the imaginary part $\text{Im}(\omega_n)$ represents the (linear) damping rate of the n -th mode. In general, solution algorithms such as MUMPS require that the eigenvalue itself is not part of the solution. However, the scattering matrices of the burner and the flame e.g. from experiments depend on the oscillation frequency (see Chapter 6). Their complex valued coefficients are usually represented by polynomial fits

depending on $\text{Re}(\omega)$. To allow for frequency-dependent scattering matrices in combination with this solver, an outer iteration routine is used for determining the eigenfrequencies of the system. This methodology was originally proposed by Nicoud et al. [107] and has also found application in other works [145, 147]. Basic idea of this strategy is that the frequency-dependent scattering matrix coefficients and reflection coefficients are initially prescribed for a fixed frequency before running the eigenvalue solver. In the first step this frequency corresponds, for example, to an analytically estimated value, which is replaced in the next step by the calculated eigenvalue obtained from the MUMPS solver. This ensures that frequency dependent boundary conditions are always provided to the inner solution algorithm by fixed values. As long as the scattering matrices and reflection coefficients are smooth functions in the considered frequency range, this method usually leads to a convergent solution after a few iteration steps. Real and imaginary parts of the obtained eigenvalues can be validated with experimentally determined eigenfrequencies and damping rates. This allows for a quantitative validation of the numerical results.

For the present test-rig configuration, experimentally determined scattering matrices of the burner are available as well as of the burner with flame under varying operating conditions. Using scattering matrices of the burner only allows to predict the pure acoustic damping of the present combustor. Based on measured scattering matrices with flame the influence of the water-to-fuel ratio on the stability margin can be studied numerically. The tool also allows to use either purely experimentally obtained scattering matrices or to couple numerically simulated burner scattering matrices with flame transfer functions e.g. from analytical models. Due to the FEM discretization of the Helmholtz equations, also temperature gradients in the combustor can be taken into account. For each eigenmodal solution, the mode shapes are provided which can be compared with the experimental observations.

8.2. Determination of Stationary Flow- and Temperature Fields

Using linearized Euler equations (LEE) to determine the scattering matrix of the burner ($\underline{\underline{S}}_B$) requires a spatial solution of the mean velocity field. This is obtained from a stationary simulation of the flow field and will be discussed first. To predict the acoustic dissipation and the thermoacoustic stability margin such that their results can be compared quantitatively with experimental results, the temperature field in the combustion chamber is required. For this purpose, stationary simulations of the combustion processes are used in combination with measured acoustic eigenfrequencies to obtain the temperature field in the combustor. The particular procedure is explained in Section 8.2.2.

8.2.1. Stationary Flow Field

In the present configuration, a three-dimensional model of the burner with included water-injector is used. The geometry is discretized on a structured computational grid consisting of approximately 1.5 million elements using the *Cut-Cell* algorithm. Simulations of the flow field are carried out using the commercially available software package ANSYS Fluent [10]. The solver uses the finite volume method (FVM) for discretizing the Navier-Stokes Equations (2.1-2.2). Turbulence modeling is achieved with the k - ϵ turbulence model. Under non-reactive conditions, isothermal conditions and incompressibility of the medium are assumed.

The resulting field representing the velocity magnitudes $|\underline{\bar{u}}| = \sqrt{u^2 + v^2 + w^2}$ in the burner centerplane is displayed in Figure 8.4. Note that u , v and w denote the velocity components in the x , y and z direction, respectively. The velocity field clearly shows a strong axial acceleration of the flow in the burner, which is caused by the reorientation of the flow tangentially through the swirl slits. This is accompanied by an increase of the tangential velocity in the direction of the burner exit and adjacent to the rotational axis. In combination with the subsequent sudden area increase, this leads to the formation of an internal and an external recirculation zone and causes the flow to stabilize downstream of the burner exit. This

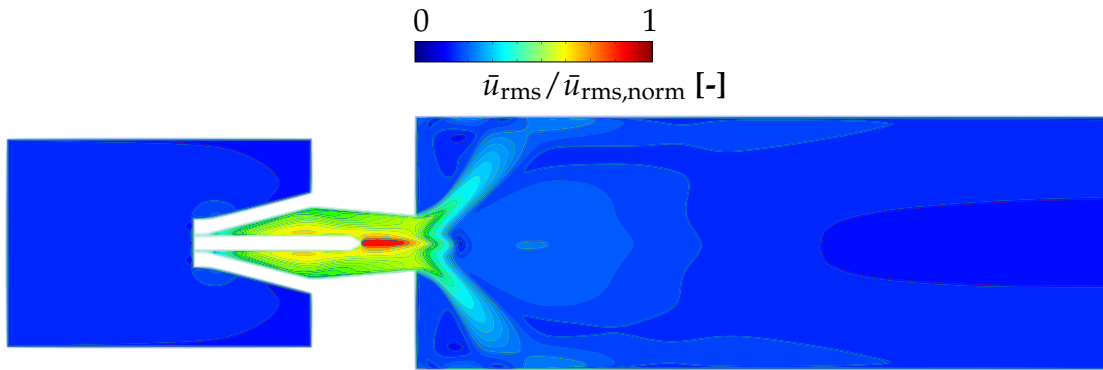


Figure 8.4.: Normalized root mean square (RMS) values of the flow velocity in the burner centerplane obtained from non-reactive CFD simulations of the flow field.

effect is found to be well reproduced by the simulated velocity field. The influence of the secondary air injection through the water lance is evident from the high axial flow velocity on the burner axis.

8.2.2. Determination of the Local Speed of Sound

In the present test-rig, strong external cooling of the outer combustor surfaces is used to remove the heat released from the combustion process. This leads to steep temperature gradients in the hot gas inside the combustor. Previously, analytical estimates of the heat losses have been used for the determination of the temperature in order to calculate the speed of sound under reactive conditions [11]. Satisfactory results have been obtained when employing these estimates in low-order network models for qualitative stability analyses. However, to predict the thermoacoustic stability of the present combustor quantitatively accurate, a precise and robust calculation of the eigenfrequencies is essential. For this purpose, it is necessary to account for temperature gradients occurring in the single-burner test-rig. Eigenvalue studies based on a FEM discretized solution of the Helmholtz equations allow, for example, to account for spatially non-uniform temperature or speed of sound.

The approach chosen here is to extract the temperature profile from a CFD simulation of the combustor under reactive conditions which allows to calculate the spatial distribution of the speed of sound in the combustor. Since simulations of the reaction processes are computationally expensive, only one single simulation is used to obtain a normalized field for the

speed of sound in the combustor. Subsequently, this solution is scaled to the respective operating point by using an experimentally determined average value for the speed of sound.

Specifically, the proposed approach deploys an extended flamelet generated manifold (FGM) model which is embedded in a RANS-CFD simulation to calculate the combustion processes while accounting for flame stretch and heat loss [82,83]. For a detailed discussion of the underlying theory and concepts of the extended FGM models and a description of the numerical setup the reader is referred to [82,83]. In the present case, a numerical simulation of the combustion processes is carried out for one representative operating condition under fully premixed, dry operation at $\phi = 0.625$ and $P_{\text{th}} = 46 \text{ kW}$. Due to the lack of a suitable model for premixed flames with water injection simulations for each individual operating point are not feasible. The selected equivalence ratio corresponds to the baseline operating point \textcircled{A} . The thermal power is chosen according to its average value in the operating range $\textcircled{A} |_{T_{\text{ad}}}$ between $\Omega = 0$ and $\Omega = 2.0$. The inflow conditions at the burner outlet are provided from the stationary RANS solution under non-reactive conditions (see Section 8.2.1). Thus, the simulation domain under reactive conditions can be restricted to the combustion chamber. Heat losses caused by impingement cooling of the test-rig are lumped in a heat transfer coefficient applied to the combustor walls. The required combustion chamber wall temperature is approximated according to the temper color at the surface. The heat transfer coefficient is then adapted to yield the estimated wall temperature [83].

The resulting temperature field in the combustor centerplane is shown in Figure 8.5. The figure clearly illustrates the temperature gradients occurring in the combustion chamber. The assumption of a compact flame allows to consider only plane wave propagation in the flow direction. For the purpose of simplification, the resulting three-dimensional temperature field is thus averaged over the combustor cross-section A_{cc} in the xz -plane. The one-dimensional temperature gradient depending on the x -coordinate only is thus obtained by applying the following integration:

$$T(x) = \frac{1}{A_{\text{cc}}} \iint T(x, y, z) \, dy \, dz. \quad (8.1)$$

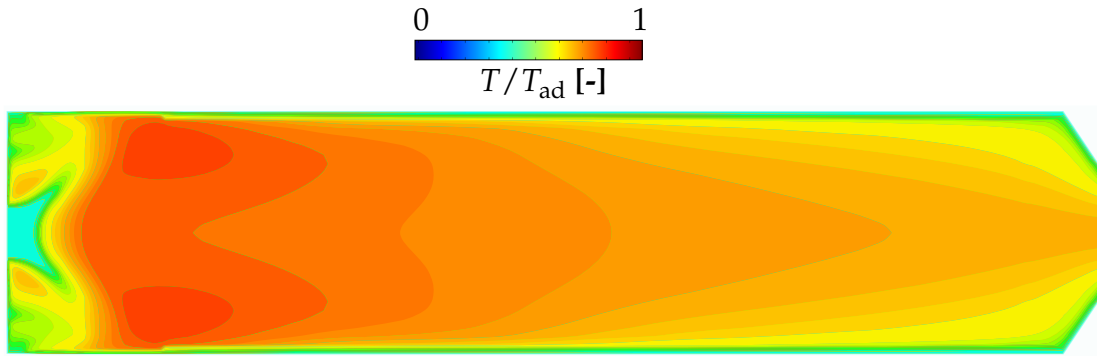


Figure 8.5.: Normalized temperature field along the combustor centerplane obtained from reactive CFD simulation.

The injection of liquid water not only changes the hot gas temperature, but also the gas composition of the combustion products. For this purpose, the axially varying speed of sound $c(x)$ is calculated from the temperature gradient $T(x)$ without water injection. In order to scale $c(x)$ to the respective operating points with water injection, the experimentally determined acoustic resonance frequency (see Section 7.3.4) is used to provide the mean speed of sound at the operating point of interest. The measured mean speed of sound \bar{c}_{cc} allows to consider both the temperature effect and the changed exhaust gas composition with water injection. For this purpose, it is assumed that the determined acoustic resonance frequency always corresponds to the first half-wave mode in the combustor. This assumption has been confirmed by checking the mode shape for all operating conditions by means of dynamic pressure measurements at different axial locations in the combustor. By rearranging the analytical relationship for the first longitudinal half-wave frequency in a closed channel, i.e. $f = c/2l$ the mean speed of sound in the combustor can be calculated by:

$$\bar{c}_{cc} = 2l_{cc}f_{2,ac}. \quad (8.2)$$

Therein, f is replaced by the experimentally determined acoustic eigenfrequency $f_{2,ac}$ for mode η_2 and l_{cc} corresponds to the length of the combustor. Note again that $f_{2,ac}$ represents the acoustic eigenfrequency of the passive system rather than the thermoacoustic eigenfrequency including flame feedback (compare e.g. Figure 7.9 against Figure 7.14). To cover all operating points in the range $\textcircled{A} |_{T_{ad}}$, the respective values of $f_{2,ac}$ are inserted into Equation (8.2). The resulting dependency of the mean speed of sound on the water-to-fuel ratio is illustrated in Figure 8.6. The figure shows

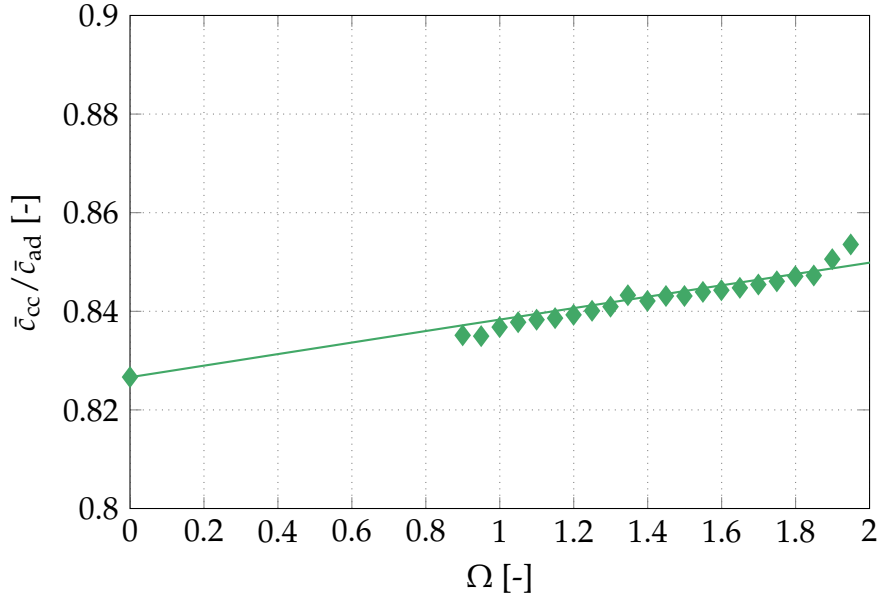


Figure 8.6.: Mean speed of sound obtained from acoustic eigenfrequency for operating range $\textcircled{A} |_{T_{ad}}$.

an increase of \bar{c}_{cc} with increasing water-to-fuel ratio at constant adiabatic flame temperature. For the given operating range, a relationship between the mean speed of sound \bar{c}_{cc} and the water-fuel ratio Ω can be approximated by a linear interpolation function. Note that all values have been normalized by the mean speed of sound \bar{c}_{ad} for $\Omega = 0$ under adiabatic conditions. In the specified range, the linear function also allows to determine the mean speed of sound in the combustor at water-to-fuel ratios for which measurements were not possible. In the next step, the numerically obtained axial gradient of the speed of sound $c(x)$ is scaled such that its spatial average $\bar{c}_{cc, \text{scaled}}$ equals the experimentally determined mean speed of sound \bar{c}_{cc} . The resulting scaled profile of $c(x)$ is shown in Figure 8.7 for operating point $\textcircled{A} |_{T_{ad}}^{\Omega=1.0}$ as an example. With the proposed method, the spatially varying speed of sound can be individually calculated for each operating point with water injection. For numerical stability analyses, the speed of sound in the combustor can then be specified either in the form of a constant mean value \bar{c}_{cc} or an axial gradient $c(x)$.

8.3. Acoustic Scattering Behavior of the Burner

This section presents the results of the numerically calculated scattering matrices of the burner. Numerical results will be validated with experi-

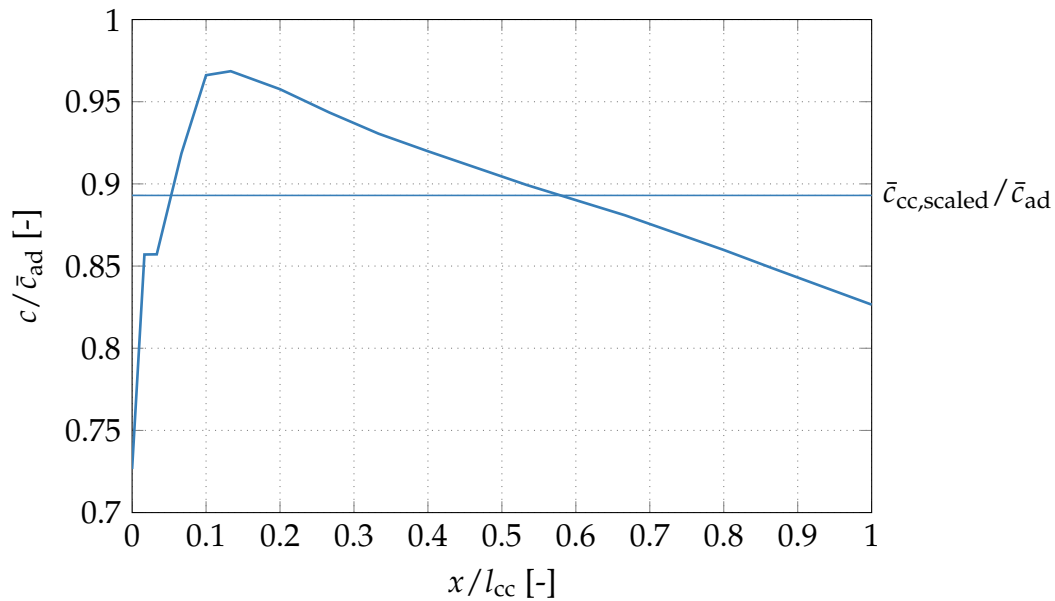


Figure 8.7.: Axial gradient of the speed of sound from reactive CFD simulations and scaled to acoustically determined speed of sound at operating point $\textcircled{A}|_{T_{\text{ad}}^{\Omega=1.0}}$.

mental data. The objective of this is to demonstrate the suitability of the CFD/CAA approach to simulate the acoustic properties of the modified swirl burner with water injector lance. The resulting scattering matrices will be deployed later for calculating the acoustic damping of the combustor. Simulations based on the LEEs are carried out for frequencies ranging from 20 to 700 Hz with a frequency resolution of $\Delta f = 20$ Hz. Two separate simulations were performed by using velocity forcing from the upstream and downstream side of the domain, respectively. Both LEE simulations yield field solutions of the acoustic quantities $\hat{\underline{\Phi}}$ for each forcing condition (see Section 3.1) and frequency. By reconstructing the acoustic field before and after the burner section using the multi-microphone method (MMM), the influence of vorticity is eliminated. This allows to calculate the acoustic scattering matrices, analogously to the experimental procedure (see Section 3.1). The four complex valued scattering matrix coefficients T^+ , R^- , R^+ and T^- are depicted in Figure 8.8 over the forcing frequency. The LEE results ($\underline{\underline{\mathbf{S}}}_{\text{B,LEE}}$) are compared with the measured scattering matrices ($\underline{\underline{\mathbf{S}}}_{\text{B,exp}}$) discussed in Section 6.1. Regarding the amplitudes, very good agreement between measurement and LEE simulations is found for frequencies above 200 Hz. Deviations are merely observed in the amplitudes of the T^- and the R^- element at lower frequencies. These deviations may

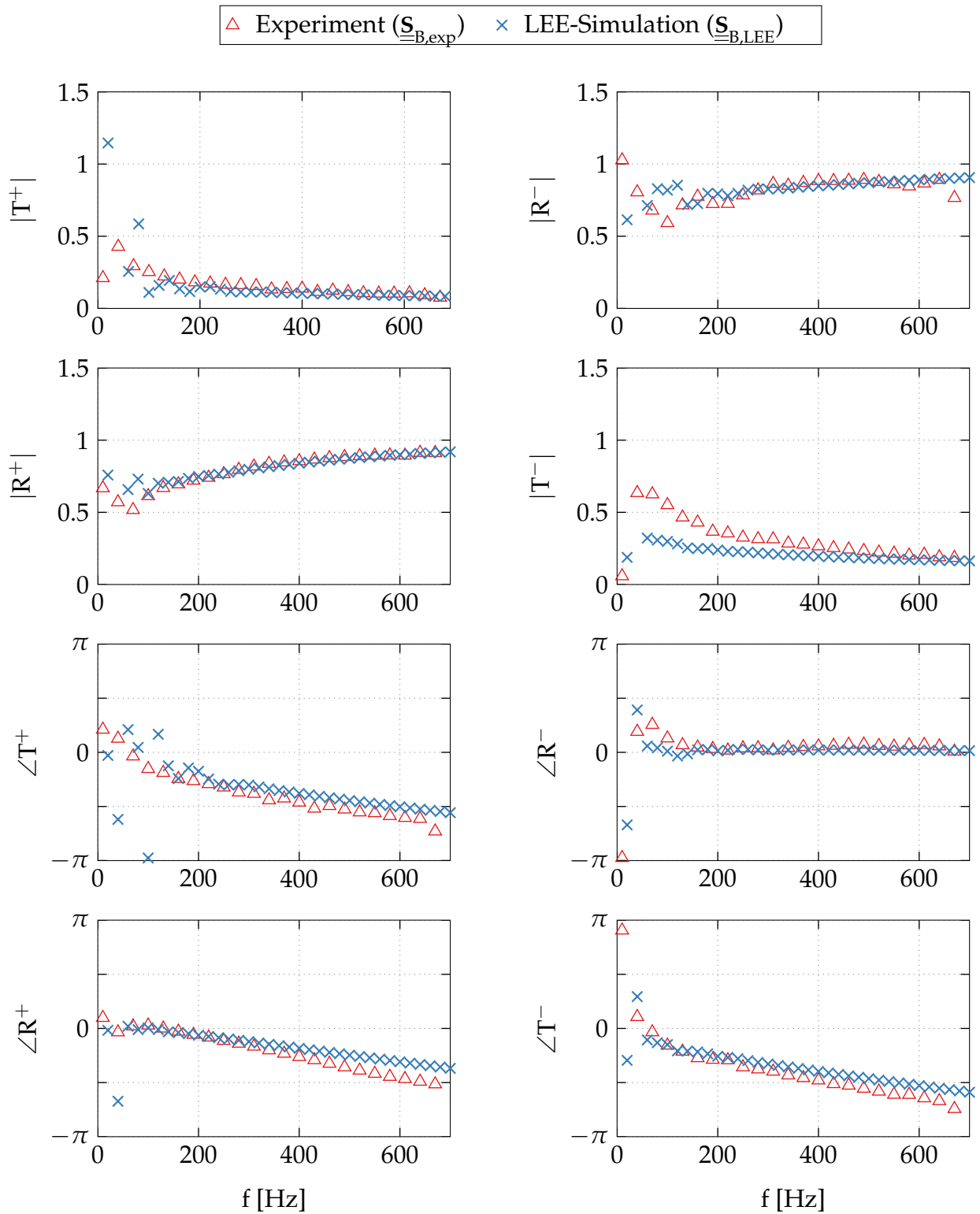


Figure 8.8.: Scattering matrices of burner with water injector: Comparison between numerical results and experiment.

originate from strong interaction between acoustics and flow due to high amplitudes of the vorticity modes, which makes filtering of the purely acoustic components by the MMM more difficult. For a detailed discussion on the influence of vorticity on numerically determined scattering matrices, see [58]. However, for the remaining elements T^+ and R^+ simulated and measured amplitudes coincide almost perfectly over the entire frequency range. Regardless of the excitation frequency, the simulated phases of all elements are almost identical to the experimentally determined values.

After validation with experimental data the simulated scattering matrix $\underline{\mathbf{S}}_{\text{B,LEE}}$ is considered suitable for being deployed in eigenvalue studies. This allows to account for acoustic losses across the burner due to mean flow from simulation results alone. Note that these acoustic scattering matrices describe only propagation of plane, longitudinal waves. Furthermore, caution is advised when interpreting results for frequencies of below 200 Hz.

8.4. Qualitative Analysis of Occurring Modes

Before quantitative comparisons between numerical simulations and experiments are drawn, it must be ensured that the eigenmodes calculated by the eigenvalue solver are physical solutions and coincide with the experimental observations. For this purpose, eigenvalue studies are discussed in the following for one representative case using the numerical setup described in Section 8.1.2. Note that this involves the solution of an eigenvalue problem based on the Helmholtz Equations (2.27) which are discretized on a FEM basis. This applies for this and all subsequent sections in this chapter. In the following, the experimentally determined scattering matrices $\underline{\mathbf{S}}_{\text{BF,exp}}$ are used to represent the burner and the flame dynamics. The speed of sound of the hot gas in the combustor is determined in accordance with the method outlined in Section 8.2.2. As a representative example, operating point $\textcircled{\text{A}}|_{T_{\text{ad}}^{\Omega=1.0}}$ has been selected. According to the experiment, this operating point exhibits two linearly stable thermoacoustic modes in the investigated frequency range, denoted by η_1 and η_2 . The former is the Helmholtz mode and the latter is the first half-wave mode in the combustor (see Section 7.3.2).

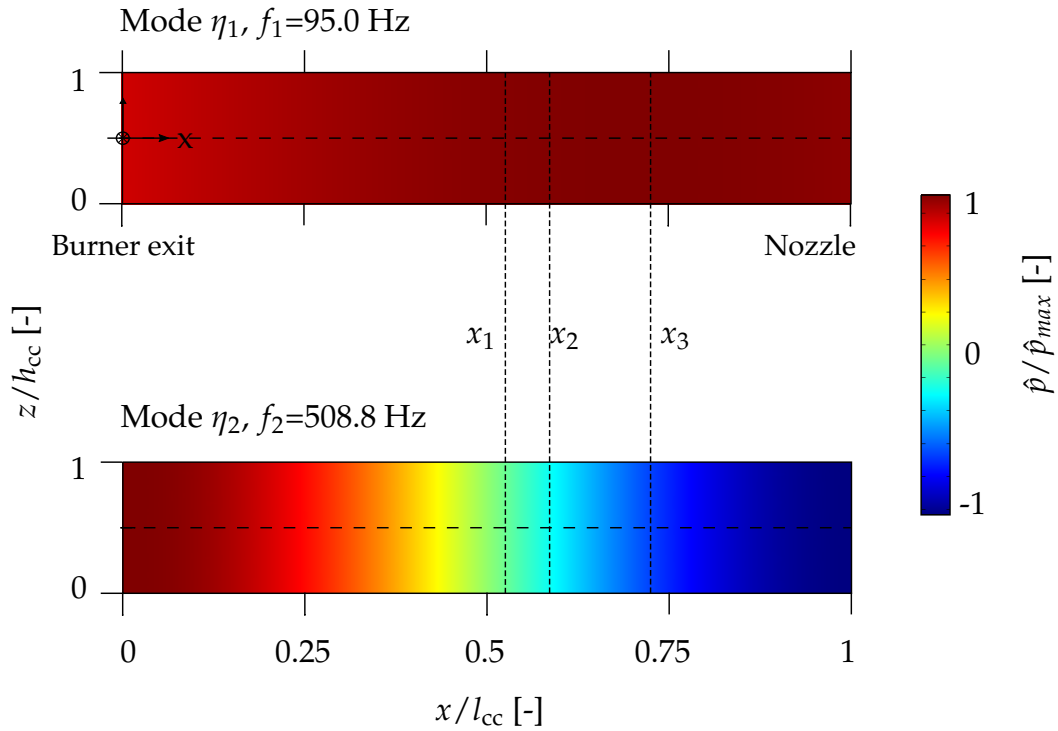


Figure 8.9.: Calculated mode shapes with water injection at operating point $\textcircled{A}|_{T_{\text{ad}}^{\Omega}=1.0}$.

As a result, numerical eigenvalue studies showed that both modes can in general be clearly identified. Their calculated mode shapes are shown in Figure 8.9. The locations x_1 - x_3 denote the axial positions where dynamic pressure probes are mounted in the test-rig. First, it can be seen that the dynamic pressure field corresponding to η_1 exhibits a nearly uniform pressure distribution in the xy -plane. As stated by several authors [28, 34, 155] characteristics of a Helmholtz mode are, firstly, the acoustic pressure fluctuates only in time and is approximately uniformly distributed in space. This directly leads to $u' \approx 0$ in the combustor. Secondly, the pressure in the combustor oscillates in phase over the whole axial length. Both applies here. The pressure distribution of η_2 exhibits a node at $0.5 l_{\text{cc}}$ and antinodes at $x = 0$ and $x = l_{\text{cc}}$. Simulations confirm that η_2 corresponds to the first half-wave mode in the combustor. A comparison between numerical simulation and experimentally determined modal pressure amplitudes and phases at the reference locations x_1 - x_3 is given in Figure 8.10. Note that all pressure amplitudes and phases are normalized by the respective value at sensor location x_3 . This confirms, that both the Helmholtz mode and the

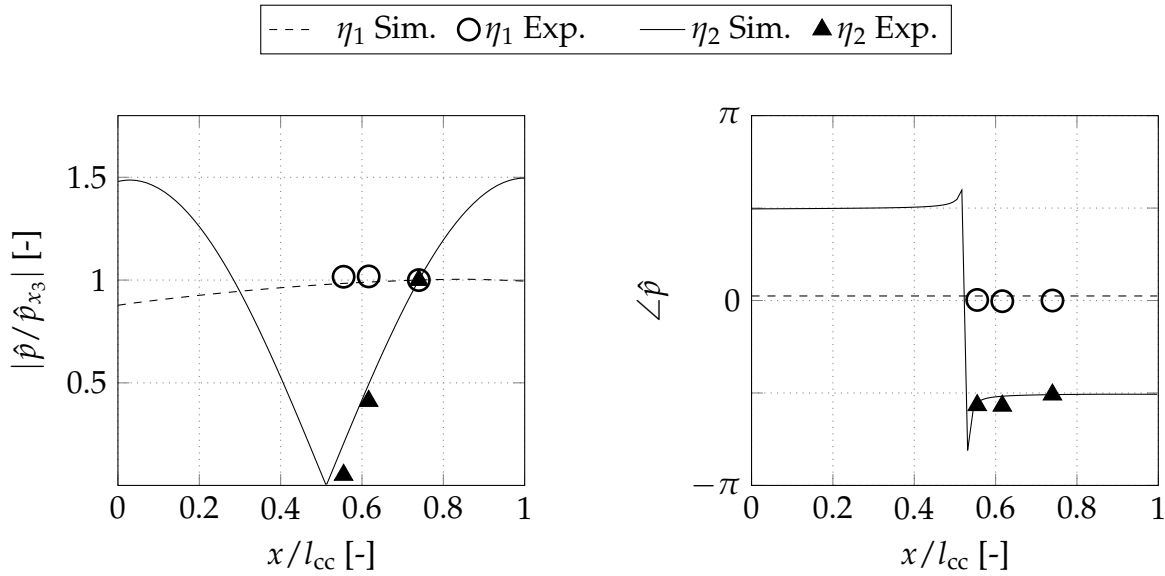


Figure 8.10.: Amplitude and phase of pressure oscillations in the combustor: Comparison between experiment and numerical simulations based on experimentally determined scattering matrices.

first longitudinal mode η_2 coincide qualitatively well with the experiment. This qualitative check is carried out each time before comparing simulated eigenfrequencies and damping rates with experimental data to avoid misinterpretation of unphysical solutions provided by the eigenvalue solver.

Due to the strong scattering of the experimentally determined scattering matrices in the low-frequency range, it was not possible to achieve a quantitatively robust prediction of the eigenfrequencies and the damping rates of the Helmholtz mode. In general, the prediction of Helmholtz oscillations in combustion chambers is considered difficult because of the very low frequencies involved. Reasons for this are that low frequency oscillations often interfere with the combustion process itself, which is expressed for example through local flame extinction [9, 34]. In particular, combustion oscillations at very low frequencies are often observed in liquid fueled combustors [28, 30, 43]. Furthermore, also rocket engines operating at low pressures are reported to suffer from these oscillations [34]. Recently, some analytical approaches have been published aiming to assess Helmholtz modes in a simple model combustor [28, 166]. However, these methods are not yet capable of providing quantitatively robust results in terms of damping rates. Other groups suspect Helmholtz mode oscillations as a re-

sult of intrinsic modes occurring alongside with acoustic modes [45,46,69]. According to the authors their prediction involves the use of state-space modeling approaches and the consideration of non-linear mechanisms [47]. Modeling of intrinsic modes is, however, the subject of current research and it is therefore classified as not (yet) applicable to the present lean-premixed turbulent combustor with water injection. In the present scenario, it is thus assumed that the linear scattering matrix representation is not sufficient to account for low-frequency oscillations of the flame with water injection. Therefore, quantitative assessment of calculated eigenfrequencies and damping rates associated with the Helmholtz mode is not carried out.

8.5. Quantitative Stability Analysis

In the following, calculations of the thermoacoustic stability of the combustor with water injection will be presented. The simulation framework has been introduced in Section 8.1.2. As stated in the previous section, the proposed modeling approach is not fully robust for mode η_1 . Thus, numerical results will be validated with respect to the first half-wave mode of the combustor η_2 . This ensures that the calculated eigenfrequencies are not within the concerned frequency range. Experimentally determined eigenfrequencies and damping rates presented in Chapter 7 are used as a benchmark to validate the results. By deploying the scattering matrices of the burner only ($\underline{\mathbf{S}}_{\text{B}}$) the acoustic damping of the combustor is calculated. Thermoacoustic stability with water injection is predicted by accounting for the flame response using scattering matrices of the burner and the flame ($\underline{\mathbf{S}}_{\text{BF}}$). Results will be discussed based on four cases, namely ①, ②, ③ and ④. The origin of the respective scattering matrices used for the individual simulation cases is illustrated schematically in Figure 8.11. A distinction is made between scattering matrices which were determined experimentally (index exp) and scattering matrices which originate from LEE simulations (index LEE). At first, the acoustic dissipation of the combustor will be calculated. This is achieved by using either the measured scattering matrix of the burner ($\underline{\mathbf{S}}_{\text{B,exp}}$) or its simulated counterpart ($\underline{\mathbf{S}}_{\text{B,LEE}}$). The former is referred to as case ① and the latter as ③. Measurements of the pure acoustic damping rate are used to validate the results of the eigenvalue studies in a quantitative manner. Secondly, cases ② and ④

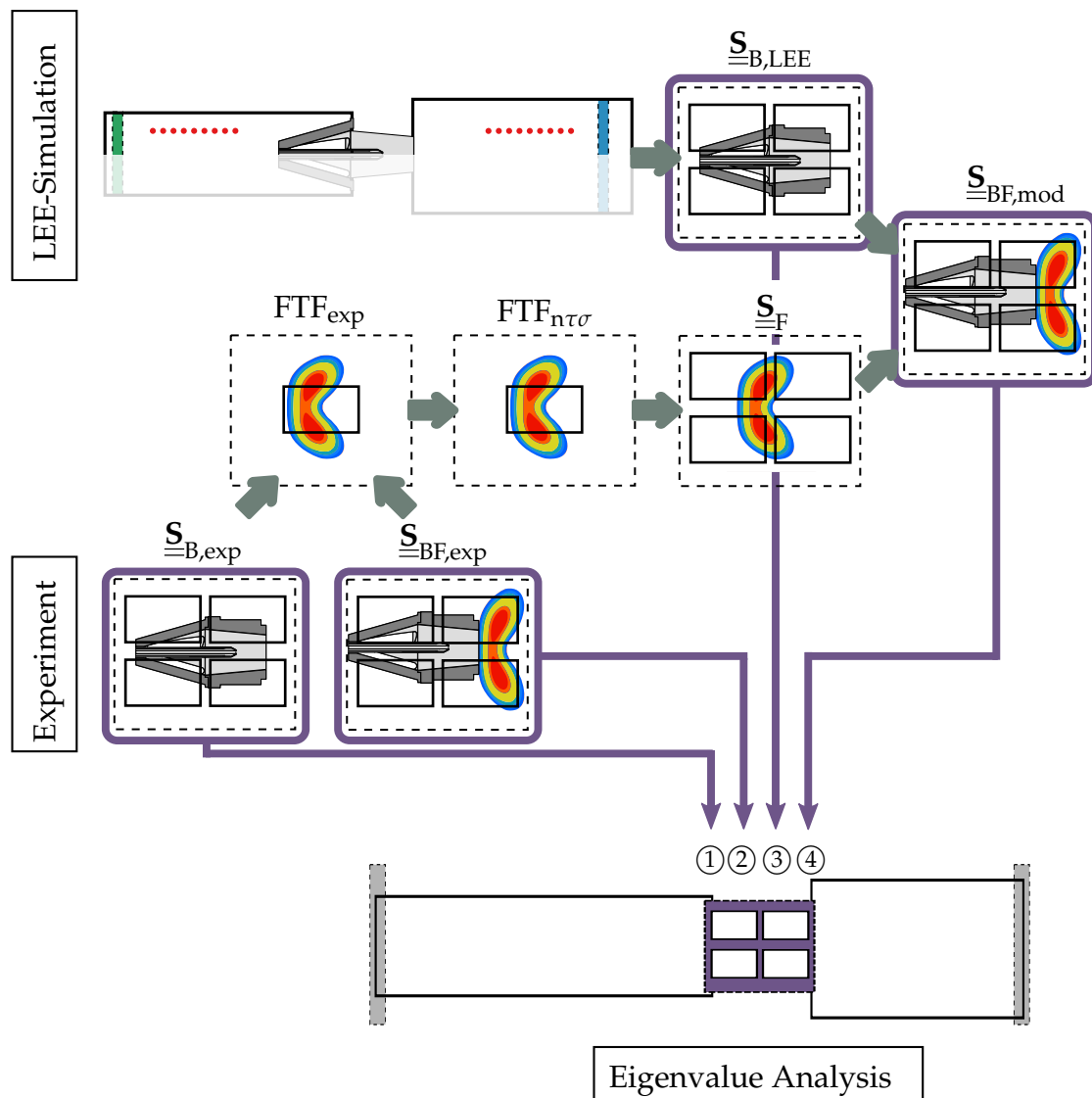


Figure 8.11.: Schematic representation of the simulation cases for eigenvalue studies based on scattering matrices.

seek to quantify thermoacoustic damping over a wide range of operating conditions with water injection. This additionally requires consideration of the dynamic flame response at the respective operating points. For this purpose, either measured scattering matrices of burner and flame ($\underline{S}_{BF,exp}$) are used in case ②. Alternatively, case ④ combines the numerically calculated burner scattering matrix $\underline{S}_{B,LEE}$ with an analytical representation of the flame transfer function ($FTF_{nt\sigma}$) by including a sensitive time lag model of the flame. The advantage of this representation lies in the provision of a smooth fitting function that eliminates discontinuities in the measurement

data and thus facilitates interpolation across different operating points. This allows to predict the stability margin even for operating points for which no measured FTFs are available. To this end, the resulting flame scattering matrix $\underline{\underline{S}}_F$ is combined with the scattering matrix of the burner $\underline{\underline{S}}_{B,LEE}$ to obtain the scattering matrix for burner and flame ($\underline{\underline{S}}_{BF,mod}$).

8.5.1. Acoustic Damping

This section aims at presenting and discussing the numerical calculations of the pure acoustic damping rates for the present combustor. Two different operating conditions will be addressed: First, the combustor is considered with preheated mean-flow only. Subsequently, pure acoustic damping rates with combustion but without flame feedback are discussed. The acoustic damping rate will be later used to calculate the flame gain with water injection. Results are validated with measured acoustic damping rates. For both non-reactive and reactive conditions, acoustic coupling between the plenum and the combustor is achieved by implementing the scattering matrices of the burner $\underline{\underline{S}}_B$.

8.5.1.1. Acoustic Damping under Non-reactive Conditions

At first, the combustor is considered with preheated mean flow only. In this case, the mean temperature in the plenum is fixed to $T_{ph} = 573$ K. In accordance with thermocouple measurements acquired in the test-rig, the mean combustor temperature to calculate the speed of sound is $\bar{T}_{cc} = 513$ K. Eigenvalue studies are conducted on the basis of experimentally determined $\underline{\underline{S}}_{B,exp}$ and numerically calculated scattering matrices of the burner $\underline{\underline{S}}_{B,LEE}$ (see Section 8.3). Referring to the illustration given in Figure 8.11, the first case corresponds to method ① and the latter to method ③, respectively.

Figure 8.12 displays simulated acoustic damping rates which are plotted over their corresponding eigenfrequencies. Taking the experimentally determined values as reference, both frequencies are accurately captured by the eigenvalue analysis with less than 2% deviation. The lower frequency corresponds to the first standing half-wave mode in the combustor (η_2)

and the higher frequency corresponds to one full wavelength. Note that for simulation results based on ($\underline{\mathbf{S}}_{\underline{\mathbf{B}},\text{exp}}$) the predicted value of α_2 is slightly below the experimentally determined values. Instead, when using the numerically simulated scattering matrix for the calculation of the eigenvalues, the predicted damping rate tends to be marginally higher than its experimental benchmark. It is assumed that this discrepancy results from the minor offset obtained between $\underline{\mathbf{S}}_{\underline{\mathbf{B}},\text{LEE}}$ and $\underline{\mathbf{S}}_{\underline{\mathbf{B}},\text{exp}}$ (cf. Figure 8.8). Towards higher frequencies, a generally lower deviation between the two simulations is found with regard to mode η_3 . These results highlight accuracy and robustness of the eigenvalue calculations with respect to the frequency for quasi-isothermal conditions in the combustor. The accuracy of the predicted acoustic damping rate tends to increase with increasing frequency.

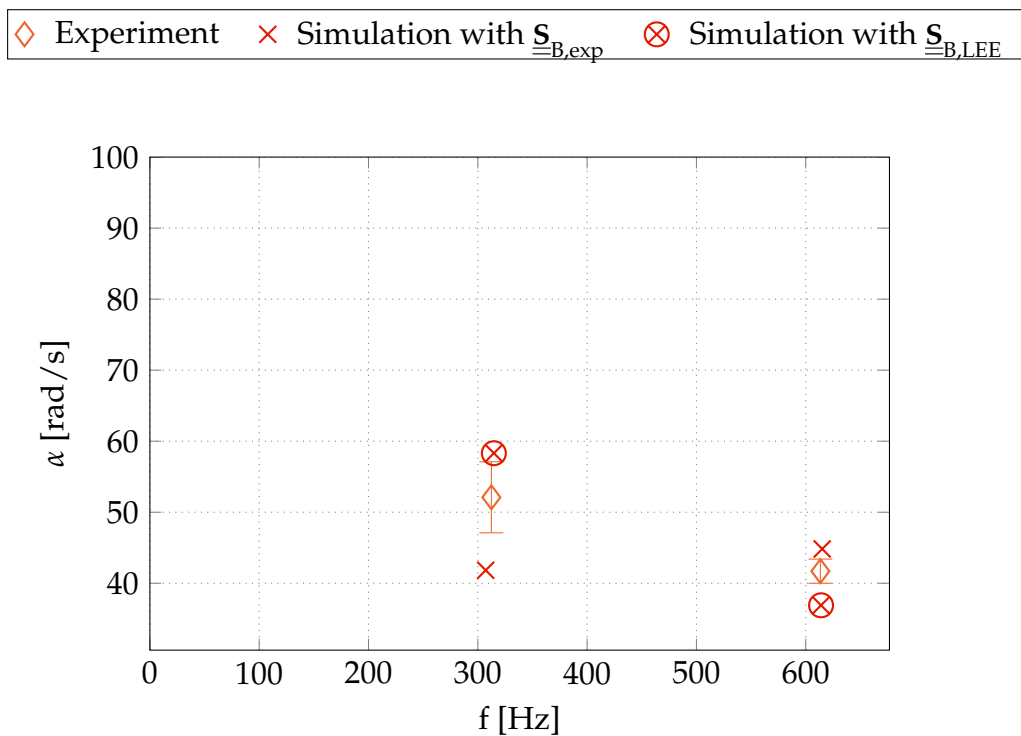


Figure 8.12.: Acoustic eigenfrequencies and damping rates under non-reactive conditions: Comparison between experiment and numerical results for two modes.

8.5.1.2. Acoustic Damping under Reactive Conditions

In the previous section, the predicted pure acoustic damping rates of the combustor have been discussed for operating conditions with preheated mean flow and in the absence of temperature gradients. Main objective of the subsequent analyses is to assess the capabilities of the model to predict pure acoustic damping rates under reactive conditions. This means that flame feedback remains deactivated for the time being. The results of the calculated acoustic dissipation in the combustor are discussed and compared with the experimental results presented in Section 7.3.4. The axial distribution of the speed of sound in the combustor is determined individually for each operating point in operating range $\textcircled{A} |_{T_{ad}}$, as described in Section 8.2.2. The plenum and the combustor are coupled by using the scattering matrix of the burner. As in the previous section, either the experimentally determined (method $\textcircled{1}$) or the numerically determined scattering matrices (method $\textcircled{3}$) are used.

The resulting acoustic eigenfrequencies and damping rates are shown in Figure 8.13 with the experimental results, already discussed in Section 7.3.4. When comparing experiment and simulation, almost perfect match is achieved when simulations are based on $\underline{\mathbf{S}}_{\text{B,LEE}}$. A slight frequency offset is observed when comparing the simulated frequencies for $\underline{\mathbf{S}}_{\text{B,exp}}$

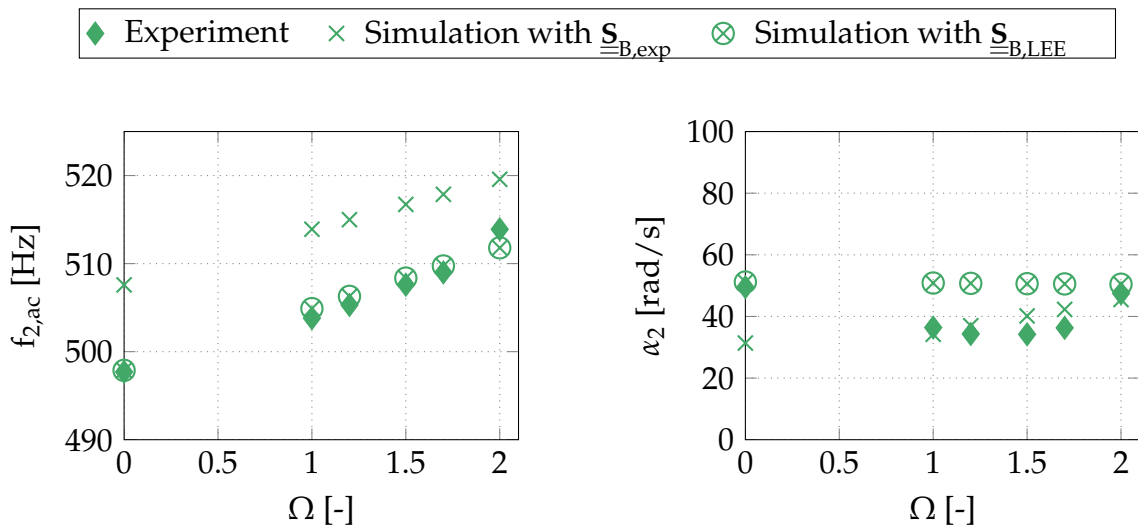


Figure 8.13.: Acoustic eigenfrequencies and damping rates for operating range $\textcircled{A} |_{T_{ad}}$: Comparison between experiments and numerical results.

instead. However, the largest observed deviation between experimentally determined and simulated frequencies is less than 2%. In turn, it is recognized that there is only a minor offset between the measured acoustic damping rates and the simulation results, when using $\underline{\mathbf{S}}_{\equiv B, \text{exp}}$. On average, simulations based on $\underline{\mathbf{S}}_{\equiv B, \text{LEE}}$ tend to over-predict the damping rate by approximately 11 rad s^{-1} . A similar tendency has also been observed for the acoustic damping rate with mean-flow only (cf. Section 8.5.1.1).

8.5.2. Thermoacoustic Damping with Water Injection

In the following, the calculated thermoacoustic damping rates with a lean-premixed, turbulent flame and water injection will be discussed. In contrast to the setup used in Section 8.5.1, flame feedback is now included in the respective scattering matrices. At first, experimentally determined scattering matrices of burner and flame ($\underline{\mathbf{S}}_{\equiv BF, \text{exp}}$) are used. This corresponds to method ② in Figure 8.11. The respective scattering matrices can be found in Appendix E. In a second step, calculations based on method ④ utilize simulated scattering matrices of the burner and FTFs obtained from a fitted and scaled time lag model. The underlying FTFs were discussed in Section 6.3.3. The simulation results are validated on the basis of operating range ① $|_{T_{\text{ad}}}$. The thermoacoustic damping rates as well as the acoustic dissipation and the flame gain are validated with experiments already discussed in Section 7.3.

8.5.2.1. Experimental Scattering Matrices of Burner and Flame

Eigenvalue studies based on experimentally determined scattering matrices of the burner and the flame are considered first (method ②). At first, a constant speed of sound is assumed which is calculated separately for each operating point in ① $|_{T_{\text{ad}}}$ according to Equation (8.2). Figure 8.14 shows the comparison between experimentally and numerically determined eigenfrequencies f_2 and thermoacoustic damping rates ν_2 for operating range ① $|_{T_{\text{ad}}}$ associated with mode η_2 . With regard to the eigenfrequencies, good agreement between calculated and experimentally determined eigenfrequencies is found. Especially for water-to-fuel ratios of $\Omega = 0, 1$ and 1.5 experiment and simulation are in perfect agreement. A slight deviation

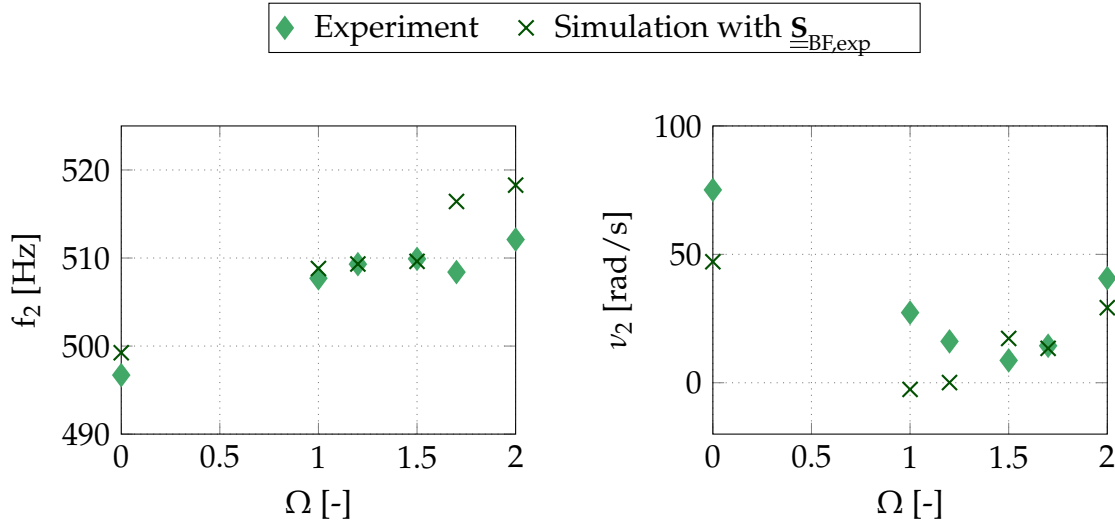


Figure 8.14.: Eigenfrequencies and thermoacoustic damping rates for operating range
 (A) $|_{T_{ad}}$: Comparison between experiment and numerical results based on experimentally determined scattering matrices.

of approximately 1% is seen for the remaining two cases at water-to-fuel ratios of 1.7 and 2.0. With regard to the thermoacoustic damping rates, both the calculated and the experimentally determined values show the same trend. In particular, the initial drop of ν_2 between $\Omega = 0$ and $\Omega = 1.5$ and the subsequent increase towards higher water-to-fuel ratios are well predicted by the simulation. From $\Omega = 1.5$ to $\Omega = 2.0$ excellent agreement between experiment and numerical calculations is achieved. Regarding ν_2 corresponding to $\Omega = 0$ and $\Omega = 1$ it is found that the model tends to underpredict the stability margin compared to the experimental benchmark. Considering frequencies and damping rates in combination, it can be seen that exact prediction of the frequency does not necessarily mean that the damping rate is predicted with similar accuracy and vice versa. One possible source of errors when calculating eigenvalues are discontinuities in the underlying experimental scattering matrices. Measuring points are only available for discrete frequencies, while linear interpolation between two adjacent points is used to determine the desired value of the frequency-dependent coefficients. Scattered measurement data as well as measurement uncertainties should be noted as possible sources of error in eigenvalue studies based on experimentally determined scattering matrices.

In summary, it can be concluded that measured scattering matrices of burner and flame allow for a quantitative prediction of the thermoacoustic

stability with water injection. This results from the validation with experimental data. Regarding the eigenfrequencies, very good agreement with the experiment was found. The calculated and measured thermoacoustic damping agree satisfactory for low water-to-fuel ratios and very well for high water-to-fuel ratios.

8.5.2.2. Simulated Burner Scattering Matrix and Analytical Flame Transfer Function

In the following analysis, the experimentally determined scattering matrices of the burner and the flame ($\underline{\mathbf{S}}_{\text{BF,exp}}$) are replaced by modeled scattering matrices ($\underline{\mathbf{S}}_{\text{BF,mod}}$). More specifically, the simulated scattering matrix of the burner ($\underline{\mathbf{S}}_{\text{B,LEE}}$) is used to represent the burner acoustics. The frequency dependent flame response is described by an analytical time-lag model ($\text{FTF}_{n\tau\sigma}(\omega)$) which is fitted to the experimentally determined FTF. This corresponds to simulation method ④ as illustrated in Figure 8.11. The simulated scattering matrix of the burner $\underline{\mathbf{S}}_{\text{B,LEE}}$ has already proved its suitability for predicting the acoustic losses across the burner (see Section 8.5.1). The analytical FTF and the burner scattering matrix $\underline{\mathbf{S}}_{\text{B,LEE}}$ are merged into the scattering matrix ($\underline{\mathbf{S}}_{\text{BF,mod}}$). In the following, eigenvalue studies based on $\underline{\mathbf{S}}_{\text{BF,mod}}$ will be discussed regarding their capability to predict thermoacoustic stability quantitatively accurate. First, this will be assessed by using an analytical representation of the FTF, wherein the coefficients are fitted for each experimentally determined FTF separately. The function is therefore primarily used for smoothing the measurement data. In the next step, one single analytical FTF is used as a starting point to obtain the FTF for all other operating points. In particular, Strouhal similarity will be exploited to scale the FTF from dry operating conditions to water-injected conditions at constant flame temperature.

The analytical representation of the FTF used in the present work was originally introduced by Freitag [53] and further developed by Hauser [66]. Adaptation of the model to the present swirl burner was achieved by Bade [11]. The mathematical representation of the FTF is given by the following relationship:

$$\text{FTF}_{n\tau\sigma}(\omega) = \frac{e^{-i\omega\tau_1^*}}{1 + \alpha_1^*i\omega + (\alpha_2^*i\omega)^2} + n^*(e^{-i\omega\tau_2^* - \frac{\omega^2}{2}\sigma_2^{*2}} - e^{-i\omega\tau_3^* - \frac{\omega^2}{2}\sigma_3^{*2}}). \quad (8.3)$$

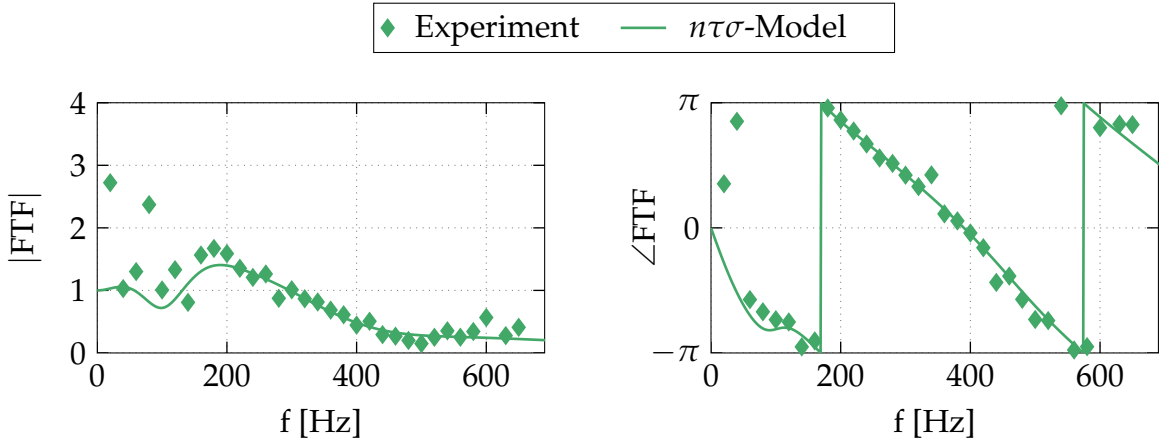


Figure 8.15.: Experimentally determined flame transfer functions for operating point $\textcircled{A}|_{T_{\text{ad}}}^{\Omega=1.0}$ and fitted analytical representation.

In the present case, the unknowns n^* , τ_1^* , τ_2^* , τ_3^* , α_1^* , α_2^* , σ_2^* and σ_3^* are determined by Bayesian parameter estimation (see Section 2.7.2), which is a very robust method for fitting parameters to measurement data. In principle, conventional optimization routines may also be suitable for this purpose. However, these generally require greater efforts in selecting starting values and constraints to achieve robust results. Thus, the Bayesian fitting is preferred here. A comparison between the experimentally determined data points and the fitted FTF is depicted in Figure 8.15 for operating point $\textcircled{A}|_{T_{\text{ad}}}^{\Omega=1.0}$. It is shown that discontinuities can be effectively eliminated when representing the FTF as a continuous function. This also facilitates Strouhal scaling and interpolation between operating points for which measured FTFs are not available. For more details on modeling of FTFs of premixed swirl flames the reader is referred to [11]. The scattering matrices of the flame $\underline{\underline{\mathbf{S}}}_{\text{F}}$ are determined for each operating point separately by fitting the parameters in Equation (8.3) to experimentally determined FTFs for operating range $\textcircled{A}|_{T_{\text{ad}}}$ (cf. Figure 6.6) and inserting the results into Equation (2.78). The resulting scattering matrix $\underline{\underline{\mathbf{S}}}_{\text{BF,mod}}$ is then obtained by combining $\underline{\underline{\mathbf{S}}}_{\text{F}}$ with the scattering matrix of the burner $\underline{\underline{\mathbf{S}}}_{\text{B,LEE}}$ (cf. Figure 8.8). In accordance with the procedure outlined in Section 8.2.2, the axial gradient of the speed of sound $c(x)$ is calculated for each operating point and water-to-fuel ratio individually.

The results of the eigenfrequencies and damping rates computed for mode η_2 are presented in Figure 8.16 with the experimental data. It is shown

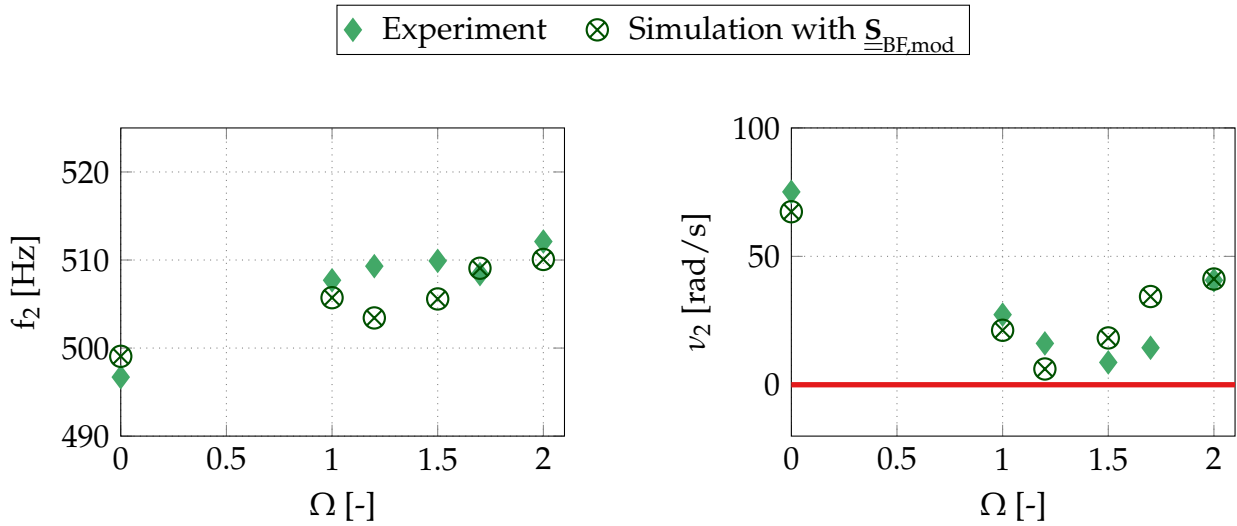


Figure 8.16.: Eigenfrequencies and thermoacoustic damping rates for operating range $\textcircled{A} |_{T_{\text{ad}}}$: Comparison between experiment and numerical results based on modeled scattering matrices.

that the calculated eigenfrequencies agree well with the experimental data. Deviations of less than 1% between simulation and experiment are observed. Higher thermoacoustic damping rates are obtained for mode η_2 when the eigenvalue studies are based on modeled scattering matrices. On the one hand, higher calculated damping rates when using $\mathbf{S}_{\text{BF,mod}}$ instead of $\mathbf{S}_{\text{BF,exp}}$ were already expected from the results discussed in Section 8.5.1.2. The reason for this expectation is the higher calculated acoustic damping under non-reactive conditions when using simulated scattering matrices. On the other hand, the higher predicted thermoacoustic damping rates can not be explained quantitatively by the overestimated acoustic damping alone. This is illustrated by means of the results at $\Omega = 0$. In this case, there is a deviation between experiment and simulation of the pure acoustic damping rate α_2 of less than 2 rad s^{-1} between method $\textcircled{1}$ and $\textcircled{3}$. In contrast, the corresponding thermoacoustic damping rates differ by more than 20 rad s^{-1} when comparing the results for simulation methods $\textcircled{2}$ and $\textcircled{4}$ with each other. Compared to method $\textcircled{2}$, the results obtained here show a clear improvement in the prediction accuracy when using experimental data as benchmark.

From the calculated acoustic and thermoacoustic damping rates for mode η_2 also the flame gains β_2 can be determined numerically. Flame gains are

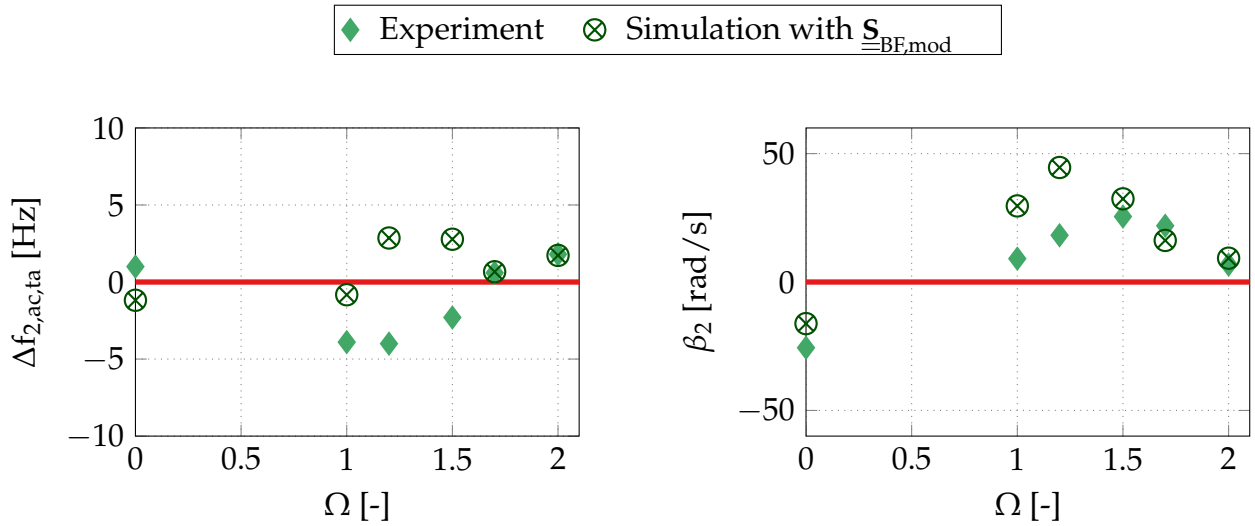


Figure 8.17.: Frequency shifts and flame gains for operating range $\textcircled{A} |_{T_{ad}}$: Comparison between experiment and numerical results based on modeled scattering matrices.

thus obtained for operating points with water-injection at constant flame temperature in the range $\textcircled{A} |_{T_{ad}}$. For this purpose, separately calculated eigenvalues of the combustor with thermoacoustic flame feedback (delivers f_2 and ν_2 , cf. Figure 8.16) and without feedback (delivers $f_{2,ac}$ and α_2 , cf. Figure 8.13) and exploiting the relationship $\beta_2 = \alpha_2 - \nu_2$, as defined by Equation (2.96) are used. The results are shown in Figure 8.17 and represent the flame gain β_2 as well as the frequency shift between the eigenfrequency with and without flame feedback ($\Delta f_{2,ac,ta}$). When comparing the frequency shifts, it is evident that the simulated values are very close to the experimentally determined values with a deviation of approximately ± 5 Hz. Based on an average eigenfrequency of mode η_2 of approximately 500 Hz, this shift corresponds to around 1%. However, sign and absolute values of $\Delta f_{2,ac,ta}$ are not always consistent with the experiments. From a qualitative point of view, the flame gain closely reflects the trends seen in the experiments. The significant increase of the flame gain at low water-to-fuel ratios is reproduced properly by the calculation. Also the subsequent decrease with further increasing Ω is captured well. Quantitatively, simulated and experimentally determined values for water-to-fuel ratios of 0, 1.5, 1.7 and 2 lie almost perfectly on top of each other. Offsets in the order of up to approximately 20 rad s^{-1} are observed for points $\Omega = 1.0$ and $\Omega = 1.2$.

8.5.2.3. Simulated Burner Scattering Matrix and Scaled Flame Transfer Function

The purpose of the analysis presented below is to assess the performance of the model for predicting thermoacoustic stability and flame gain by using modeled scattering matrices of the burner and scaled flame transfer functions. Specifically, the performance of the simulation results is evaluated when only FTFs for dry operating points are available. Strouhal scaling is used in this respect to obtain the FTF for water injection at water-to-fuel ratios of up to 2 at constant flame temperature. In the present configuration, scaled FTFs allow for assessing thermoacoustic stability for water-to-fuel ratios in the range $0 < \Omega < 1$ for which no measurements were technically feasible. As discussed in Section 6.3.3, the FTF of the present flame with water injection exhibits scalability with the flame length for Strouhal numbers of $\text{Str} > 0.2$. This property was observed for water-to-fuel ratios of up to $\Omega = 2.0$ at constant adiabatic flame temperature. As further discussed in Section 7.3.4, the flame gain for mode η_2 also indicates scalability with the Strouhal number. Results will be discussed based on thermoacoustic damping rates and flame gains associated with the first half-wave mode of the combustor η_2 . Experimental validation data used in the following have already been introduced in Section 7.3.4. Scaled FTFs used for these analyses are calculated based on the dry reference case (A). Interpolation of the FTF with respect to the Strouhal number requires a smooth function for the characteristic flame position. This is function is obtained by applying a higher order polynomial fit to the experimentally determined values which represent the axial stand-off of the flame's recirculation zone x_{VB} (see Figure 5.3). This allows to express x_{VB} as a function of the water-to-fuel ratio Ω . Note that it is assumed that the flame length increases steadily with increasing water-to-fuel ratio. Furthermore, a linear fit to the experimentally determined mean speed of sound \bar{c}_{cc} is used to obtain the required axial profile $c(x)$ at the respective operating conditions (see Figure 8.6). For this purpose, FTFs and $c(x)$ are scaled to water-to-fuel ratios in the range $0 \leq \Omega \leq 2.0$.

The resulting eigenfrequencies and thermoacoustic damping rates are displayed with the experimental data in Figure 8.18. The numerical results cover the range $0 \leq \Omega \leq 2$ with a resolution of $\Delta\Omega = 0.1$ thus closing the gap between $\Omega = 0$ and $\Omega = 1.0$ for which no experimental data are available. With regard to the eigenfrequencies, remarkably good agreement

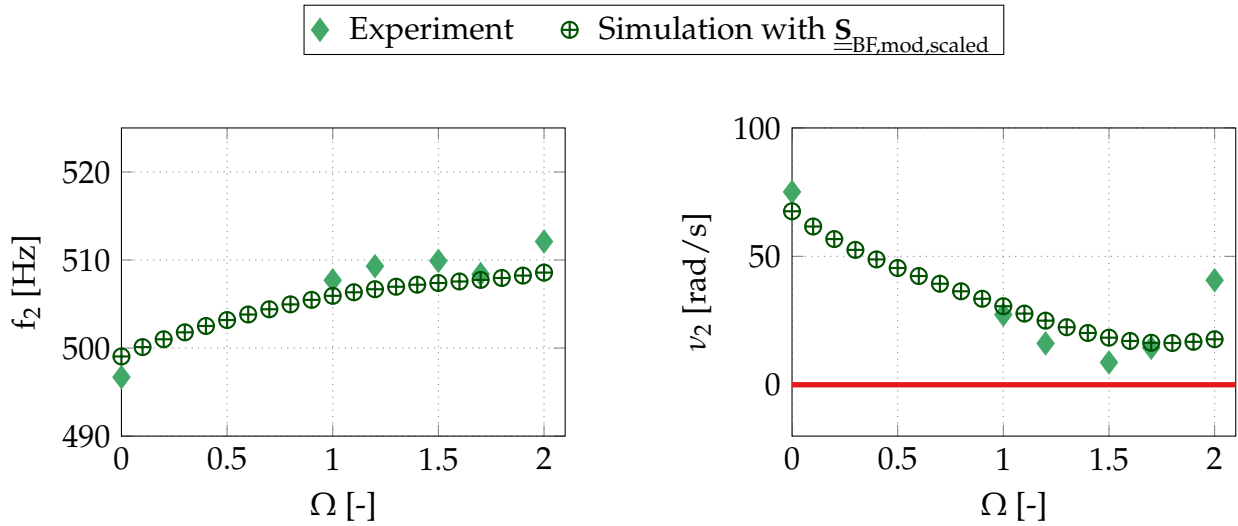


Figure 8.18.: Eigenfrequencies and thermoacoustic damping rates for operating range $\textcircled{A} |_{T_{\text{ad}}}$: Comparison between experiment and numerical results based on modeled and scaled scattering matrices.

is found between experimental results and numerical calculations. The simulation predicts a steady increase of the eigenfrequency with increasing Ω at constant adiabatic flame temperature. This appears conclusively since a steady increase of the water-to-fuel ratio at constant adiabatic flame temperature leads also to an increase of the speed of sound (see Section 8.2.2). With respect to the thermoacoustic damping rates ν_2 the trend predicted by the simulation is only well captured up to $\Omega = 1.5$. Originating from an almost perfectly predicted damping rate for $\Omega = 0$, ν_2 decreases smoothly when raising the water-to-fuel ratios gradually from 0 to 1. However, with increasing Ω the deviation between measured and calculated thermoacoustic damping rates increases. In particular, the minimum observed in the experiments at $\Omega = 1.5$ is not reproduced correctly. Note that the predicted qualitative stability state (i.e. stable or unstable) is consistent with the experiment across all considered operating conditions.

Finally, simulation results for the flame gain β_2 will be discussed for eigenvalue studies based on scaled FTFs. As in the previous section, the flame gain is obtained from subtracting the thermoacoustic damping rate ν_2 from the acoustic damping rate α_2 . Both simulations were carried out separately. The calculated frequency shifts between thermoacoustic and acoustic eigenfrequency $\Delta f_{2,\text{ac,ta}}$ and their associated flame gains are shown

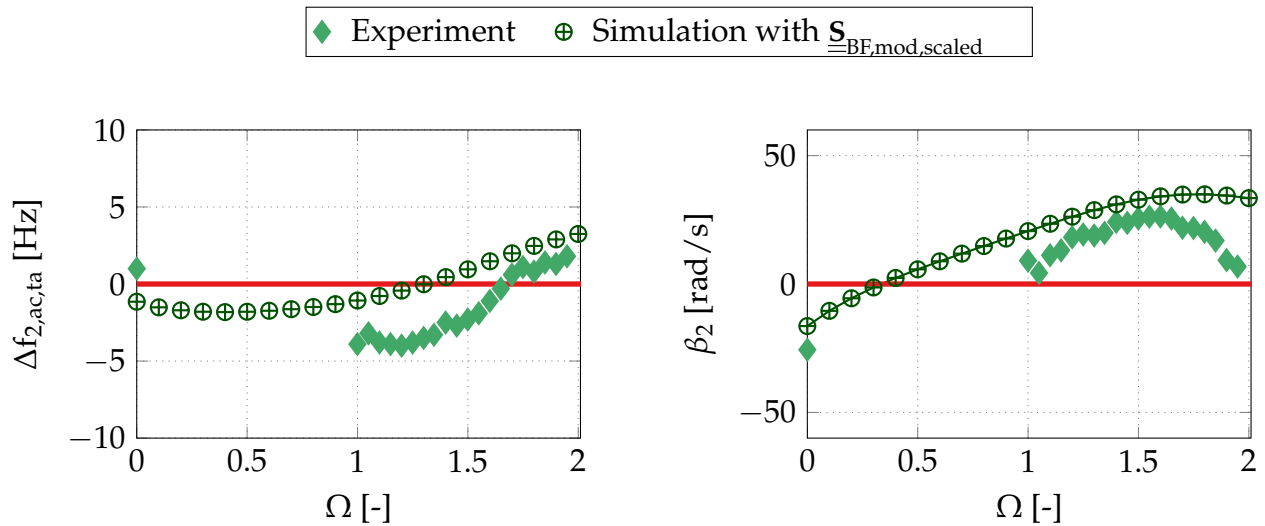


Figure 8.19.: Frequency shifts and flame gains for operating range $\textcircled{A} |_{T_{ad}}$: Comparison between experiment and numerical results based on modeled and scaled scattering matrices.

in Figure 8.19. Both results are compared with experimental data. It is shown that computational results and experiments agree reasonably in the range of $1.0 \leq \Omega \leq 1.7$. A gradual increase of the flame gain is predicted for water-to-fuel ratios in the range of $0 < \Omega \leq 1.0$. The calculated water-to-fuel ratio at which the flame gain changes from negative to positive is predicted between $\Omega = 0.3$ and $\Omega = 0.4$. Compared to the experiment, β_2 becomes positive already at lower water-fuel ratios. The maximum calculated flame gain is 35.0 rad s^{-1} at $\Omega = 1.7$. In the experiment a maximum of 26.3 rad s^{-1} is obtained at $\Omega = 1.6$. Beyond $\Omega = 1.7$, the simulation predicts a considerably flatter plateau and fails to predict the dropping flame gains towards $\Omega = 2.0$ correctly. In general, the flame driving with water injection is found to be slightly overpredicted with respect to the experiment.

In summary it is found that numerical stability analyses show limitations in predicting thermoacoustic stability and flame gains accurately when using scaled FTFs to represent the flame response with water injection. Results become increasingly inaccurate in particular towards high water-to-fuel ratios. In the given operating range, however, stability analyses based on scaled FTFs are a reasonable approach for estimating the stability margin if no measurements of the flame dynamics with water injection are available.

9 Summary and Conclusion

In this work, the influence of water injection on the combustion dynamics of lean premixed, turbulent natural gas flames was studied. Special emphasis was placed on water injection to increase the thermal load at constant flame temperature level by using water-to-fuel ratios of up to 2. Both experimental and numerical studies were performed, while measurements were used to validate the simulation results.

Experiments were carried out in an atmospheric single burner test-rig using a modular swirl burner with an integrated water injection system. At first, the practicability of the designed water injection system was demonstrated by using optical diagnostic techniques. The occurring flame shapes and geometrical flame parameters have been characterized for varying equivalence ratios, thermal loads and water-to-fuel ratios by using OH^* -chemiluminescence. Additionally, the spray distribution as well as the associated droplet diameters were obtained using laser-optical measurement techniques. The essential findings are summarized as follows:

- With increasing water content, a downstream axial displacement of the recirculation zone and a dispersion of the reaction zone is observed. This is most evident for water injection at constant equivalence ratio but less intensive at constant adiabatic flame temperature.
- Mie scattering images indicated for water-to-fuel ratios of up to 2 that the droplets in the combustor are homogeneously distributed and evaporation is complete upstream of the main reaction zone.

The thermoacoustic properties of burner and flame were then characterized for longitudinal wave propagation. Firstly, these analyses encompassed the characterization of the acoustic scattering behavior of the modified burner configuration in the absence of a flame. Secondly, flame transfer functions were presented for various operating conditions with water injection. Measured source terms which provided information on the noise gener-

ation of the flame with water injection were discussed. Local deviations in the flame response were illustrated on the basis of phase-locked OH*-chemiluminescence. The key findings emerging from these investigations can be summarized as follows:

- Modifications of the scattering behavior of the burner due to introducing the water injection device were identified to be small.
- A significant increase of the flame's sound emission was observed for flames with water injection. This was manifested by increasing amplitudes of the noise source term at frequencies of below 150 Hz.
- Water injection in general caused higher peak amplitudes of the flame transfer functions for very low frequencies while lower amplitudes occurred at higher frequencies. With increasing water-to-fuel ratio, steeper phase drops were observed over the entire frequency range examined.
- Measured flame transfer functions with water injection at constant adiabatic flame temperature indicated frequency scaling with geometrical flame parameters when considering Strouhal numbers of larger than 0.2.

In the scope of this work, a new method was developed which provided robust identification of the combustor stability margin from dynamic pressure data only. This method relies on identifying the eigenfrequencies and the damping rates from the autocorrelation function. By applying this measuring method, the influence of water injection on thermoacoustic damping, acoustic dissipation and flame driving were quantified for the present combustor. These results led to the following key findings:

- Water injection considerably amplified low pressure oscillations, indicated by decreasing thermoacoustic damping rates with increasing water-to-fuel ratio.
- Low-frequency oscillations corresponded to the Helmholtz mode and resulted in a self-excited thermoacoustic instability after exceeding a water-to-fuel ratio of approximately 2 at constant adiabatic flame temperature.

-
- Even for water-to-fuel ratios of up to 2, water injection hardly changed the acoustic dissipation associated with the first half-wave mode of the combustor. The observed shift of the eigenfrequencies was mainly attributed to the change of the speed of sound due to water injection.
 - Both the frequency shift between acoustic and thermoacoustic eigenfrequency as well as the flame gain scaled with geometrical flame parameters rather than being directly linked to the water-to-fuel ratio. This finding was consistent with the results from measured flame transfer functions.

Numerical simulations were carried out based on a three-dimensional model of the combustor using the finite element method (FEM). These involved two separate approaches: Firstly, a hybrid approach using computational fluid dynamics (CFD) and computational aero-acoustics (CAA) was used to calculate the acoustic scattering matrices of the modified burner configuration by solving the linearized Euler equations (LEE). Secondly, thermoacoustic modes and damping rates with water injection were calculated by conducting eigenvalue studies using the Helmholtz equations. This model incorporated acoustic scattering matrices to account for acoustic losses and flame dynamics. The dynamic flame response was provided by measured flame transfer functions. Obtained results were validated quantitatively by using experimentally determined acoustic and thermoacoustic eigenfrequencies, their associated damping rates as well as flame gains. The most important findings can be summarized as follows:

- The scattering matrices of the present swirl burner with water injector can be accurately reproduced by the proposed CFD/CAA procedure based on the LEEs. This was concluded from validating the results with experimentally determined scattering matrices.
- Qualitative prediction of the low frequency modes with water injection was achieved. This was manifested by comparing the computed mode shapes with dynamic pressure measurements.
- The ability of FEM-based eigenvalue studies to calculate the eigenfrequencies and the acoustic dissipation of the combustion chamber was shown for non-reactive and reactive conditions by using measured as well as numerically obtained scattering matrices of the burner.

- Quantitatively accurate prediction of eigenfrequencies and damping rates with water injection was achieved for the first longitudinal half-wave mode. This was demonstrated by validating the thermoacoustic damping rates and the flame gain with experiments. Accounting for the axial temperature gradient in the combustor, representing the measured FTFs by a time-lag model and using the numerically calculated scattering matrices of the burner yielded the best match with the experimental data.
- Flame transfer functions were scaled due to their dependency on geometrical flame parameters from dry operating conditions to water-to-fuel ratios of up to 2 and were successfully deployed for quantitative stability analyses. This yielded calculated damping rates for water-to-fuel ratios between 0 and 1 for which no measurements were feasible.
- It was demonstrated that it is possible to predict the thermoacoustic stability margin of the first half-wave mode of the combustor with water injection even if no measured FTFs with water injection are available.

While the stability analyses yielded accurate results for the quantitative prediction of the longitudinal acoustic modes in the combustor, there were still difficulties with calculating low-frequency oscillations. Experimentally, amplification of low-frequency oscillations was concluded from decreasing damping rates of the Helmholtz mode with increasing water-to-fuel ratio. Future work on thermoacoustics of combustors with water injection should therefore focus on low-frequency oscillations. In particular, creating a better understanding on the underlying interactions between oscillating droplets, heat release and pressure would provide added value to develop enhanced modeling strategies. For this purpose, phase-resolved measurements of the droplet diameters and velocities in combination with the oscillating heat release field would be beneficial.

A Matrix-Vector Notation of the LEEs

The matrix-vector notation of the Linearized Euler Equations (LEE) was introduced by the following equation:

$$\underline{\mathcal{L}}(\underline{\hat{\Phi}}) = i\omega\underline{\hat{\Phi}} + \underline{\underline{\mathbf{A}}}_i \frac{\partial \underline{\hat{\Phi}}}{\partial x_i} + \underline{\underline{\mathbf{C}}}\underline{\hat{\Phi}} - \underline{\hat{f}}_s = 0. \quad (2.48 \text{ revisited})$$

Herein, the vector containing the primary acoustic variables $\underline{\hat{\Phi}}$ and the source term vector $\underline{\hat{f}}_s$ are defined as follows:

$$\underline{\hat{\Phi}} = [\hat{\rho} \ \hat{u} \ \hat{v} \ \hat{w} \ \hat{p}]^T, \quad \underline{\hat{f}}_s = [0 \ \hat{f}_x \ \hat{f}_y \ \hat{f}_z \ (\gamma - 1)\hat{q}_v]^T. \quad (A.1)$$

The coefficient matrices $\underline{\underline{\mathbf{A}}}_i$ and $\underline{\underline{\mathbf{C}}}$ are given by:

$$\underline{\underline{\mathbf{A}}}_x = \begin{bmatrix} \bar{u} & \bar{\rho} & 0 & 0 & 0 \\ 0 & \bar{u} & 0 & 0 & \frac{1}{\bar{\rho}} \\ 0 & 0 & \bar{u} & 0 & 0 \\ 0 & 0 & 0 & \bar{u} & 0 \\ 0 & \gamma\bar{p} & 0 & 0 & \bar{u} \end{bmatrix}, \quad \underline{\underline{\mathbf{A}}}_y = \begin{bmatrix} \bar{v} & 0 & \bar{\rho} & 0 & 0 \\ 0 & \bar{v} & 0 & 0 & 0 \\ 0 & 0 & \bar{v} & 0 & \frac{1}{\bar{\rho}} \\ 0 & 0 & 0 & \bar{v} & 0 \\ 0 & 0 & \gamma\bar{p} & 0 & \bar{v} \end{bmatrix}, \quad \underline{\underline{\mathbf{A}}}_z = \begin{bmatrix} \bar{w} & 0 & 0 & \bar{\rho} & 0 \\ 0 & \bar{w} & 0 & 0 & 0 \\ 0 & 0 & \bar{w} & 0 & 0 \\ 0 & 0 & 0 & \bar{w} & \frac{1}{\bar{\rho}} \\ 0 & 0 & 0 & \gamma\bar{p} & \bar{w} \end{bmatrix} \quad (A.2)$$

$$\underline{\underline{\mathbf{C}}} = \begin{bmatrix} \frac{\partial \bar{u}_i}{\partial x_i} & \frac{\partial \bar{p}}{\partial x} & \frac{\partial \bar{p}}{\partial y} & \frac{\partial \bar{p}}{\partial z} & 0 \\ -\frac{1}{\bar{\rho}^2} \frac{\partial \bar{p}}{\partial x} & \frac{\partial \bar{u}}{\partial x} & \frac{\partial \bar{u}}{\partial y} & \frac{\partial \bar{u}}{\partial z} & 0 \\ -\frac{1}{\bar{\rho}^2} \frac{\partial \bar{p}}{\partial y} & \frac{\partial \bar{v}}{\partial x} & \frac{\partial \bar{v}}{\partial y} & \frac{\partial \bar{v}}{\partial z} & 0 \\ -\frac{1}{\bar{\rho}^2} \frac{\partial \bar{p}}{\partial z} & \frac{\partial \bar{w}}{\partial x} & \frac{\partial \bar{w}}{\partial y} & \frac{\partial \bar{w}}{\partial z} & 0 \\ 0 & \frac{\partial \bar{p}}{\partial x} & \frac{\partial \bar{p}}{\partial y} & \frac{\partial \bar{p}}{\partial z} & \gamma \frac{\partial \bar{u}_i}{\partial x_i} \end{bmatrix}. \quad (A.3)$$

B Validation of the Stochastic Forcing Method

In the following, a numerical validation study is presented to demonstrate the accuracy and robustness of the newly developed method for the identification of damping rates. This is carried out by using a stochastically forced van-der-Pol oscillator which is set up in the MATLAB Simulink[®] environment. The model of the system is shown in Figure B.1 and basically represents Equation (2.97) in the form of a block diagram.

$$\ddot{\eta}_n + 2\nu_n\dot{\eta}_n + \omega_n^2\eta_n = \xi(t) \quad (2.97 \text{ revisited})$$

Therein, $\eta(t)$ denotes a synthetically generated time series of a damped, second order oscillator system. Similar approaches have already proven their effectiveness in previous studies [109,111] to provide benchmark data for system identification techniques.

The damping rate is identified by Bayesian parameter estimation from the analytical representation of the autocorrelation function, according to:

$$k_{p'p'} = \sum_{n=1}^N \exp(-\nu_n \tau) A_n \cos(\omega_n \tau). \quad (3.11 \text{ revisited})$$

At first, the applicability of the method is demonstrated for a system with only one oscillation mode η before systems with two modes are examined.

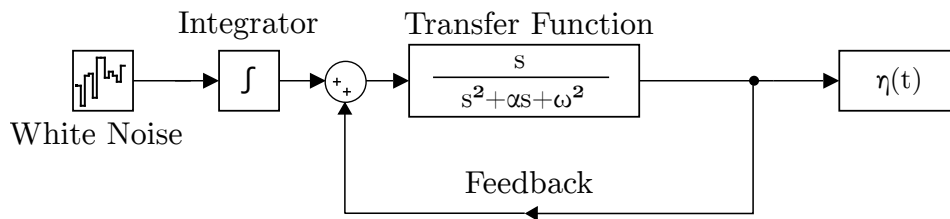
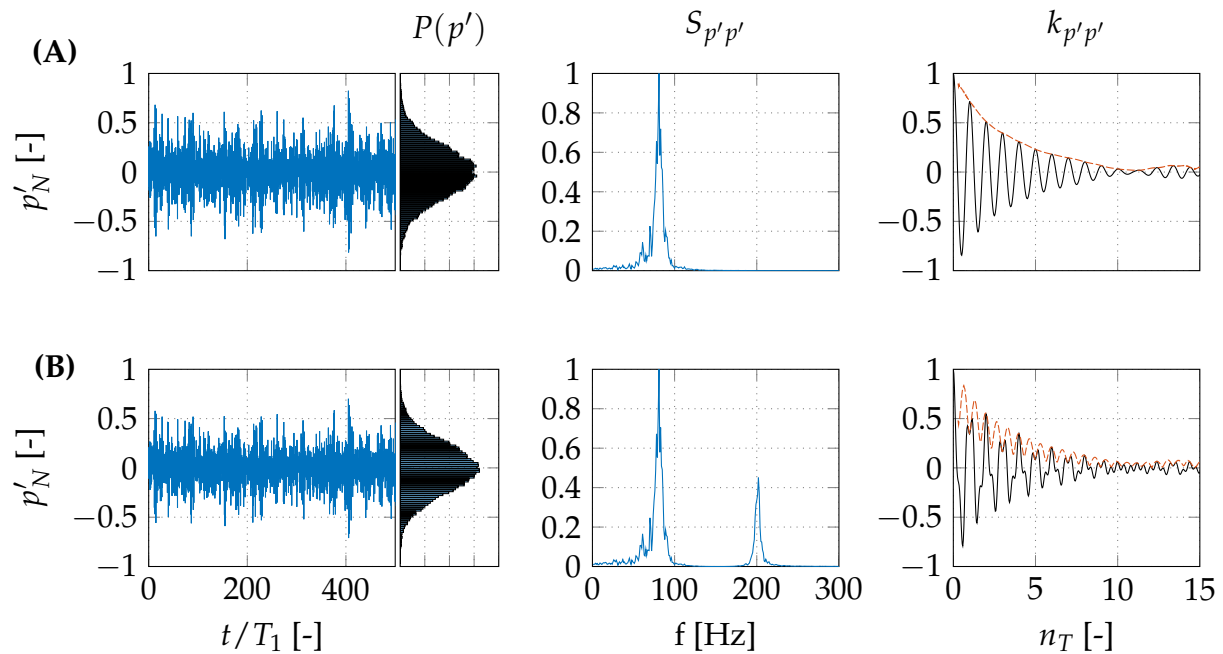


Figure B.1.: Block diagram of the second order oscillator system to generate synthetic time series.

Table B.1.: Overview of numerical validation cases for the statistical identification of damping rates from the autocorrelation function.

Case	\underline{f} [Hz]	$\underline{\beta}$ [-]	$\underline{\nu}$ [-]	Δt [s]	τ_{sim} [s]
A	80	0	25	$1 \cdot 10^{-4}$	10
B	80 200	0	25 12.5	$1 \cdot 10^{-4}$	10

An overview on the simulation parameters used for the benchmarking test cases is shown in Table B.1. Note that f and ν are displayed in vector notation when multiple modes are involved. The characteristics of both conducted simulations A and B are depicted in Figure B.2 by means of time series, power spectral density $S_{p'p'}$ and the autocorrelation function $k_{p'p'}$. Linear stability of the cases is confirmed by a Gaussian distribution of the simulated pressure time signal [96] which is concluded from the PDF of the time series ($P(p')$).


Figure B.2.: Numerical validation test cases for a single mode system (A) and multi-mode system (B): Time series of raw signal, probability density of pressure signal p' , normalized power spectral density of p' , autocorrelation functions with envelope (----).

B.1. Single Mode Case

First, a van-der-Pol oscillator composed of only mode is simulated. Mathematically, this means that $p' = \eta_1 + \zeta(t)$. The simulated oscillation frequency for case A is set to 80 Hz with an effective damping rate of $\nu = 25$ rad/s. The results obtained from the statistical fitting procedure for case A are displayed in Figure B.3 and reveal the PDFs of the identified parameters ν and $f = \omega/2\pi$. The resulting curve fit according to Equation (3.11) is obtained using the median values of the statistical distributions. Since the coefficients ν and f are both Gaussian distributed it is confirmed that the MCMC algorithm has converged to its target distribution. The goodness of the statistical fit is assessed by means of the standard deviation σ from the respective mean value. It is seen from the results that the parameters identified by the outlined procedure agree excellently with the benchmark values prescribed in the simulation model. Considering the frequency, the relative error to the simulation parameter is less than 1% and 2.7% for the damping rate. The accuracy of the identified parameters is confirmed by comparing the original autocorrelation function and the fitted solution. The computational time required for the calculation is about 20 s when using one single processor of a personal computer.

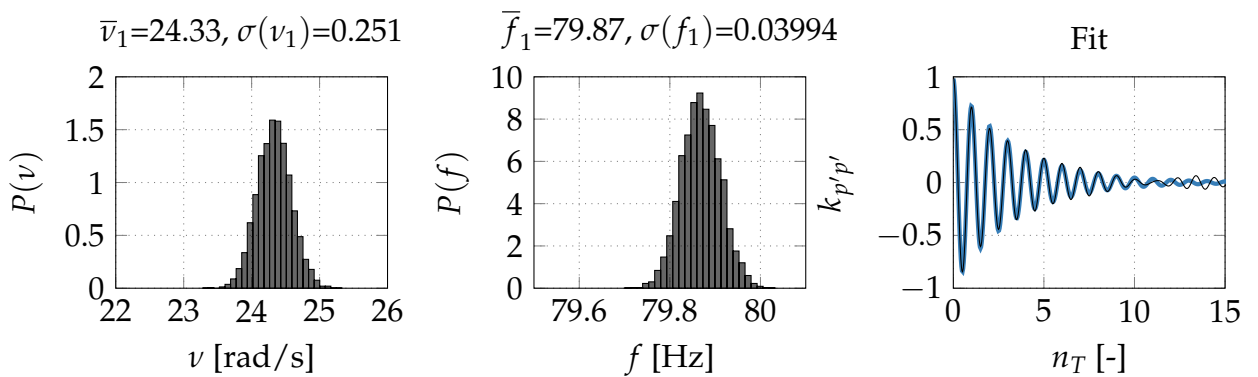


Figure B.3.: Numerical validation test case A: Probability densities of the fitting parameters ν_1 and f and their corresponding standard deviations $\sigma(\dots)$ and autocorrelation functions.

B.2. Multi-Mode Case

In a second step, a simulation test case featuring two distinct modes with different oscillation frequencies and damping rates is used to assess the performance of the proposed identification method. Following Table B.1, this refers to case B. The damping rate is identified for each of the occurring modes by solving the fitting problem according to Equation (3.11) for $N = 2$ modes. For case B the damping rate ν_1 is identified by using the same model equation as taken for the single mode case ($N = 1$). That is, the contribution of the second mode is not captured by the underlying model. Subsequently, the model equation (3.11) is expanded to $N = 2$ to calculate the damping rates for both modes η_1 and η_2 from the same dataset. All other parameters and settings remain unchanged compared to case A. This case is in the following denoted as $B|_{N=2}$. The results of the different test cases are summarized in Figure B.4 in the form of curve fits calculated from median values of the identified parameters. To allow for a better comparison, obtained PDFs of the damping rates are represented as boxplots. Presentation of the identified frequencies will be omitted due to their very low relative standard deviations of below 1% in all cases. When considering case $B|_{N=1}$ first, it is seen that $\nu_{1,calc}$ still agrees well with the benchmark value from the simulation model. The median value only differs by approximately 1% when compared to case A. However, it is noticed from the obtained distributions that the standard deviation of ν_1 has increased but still remains in the single-digit

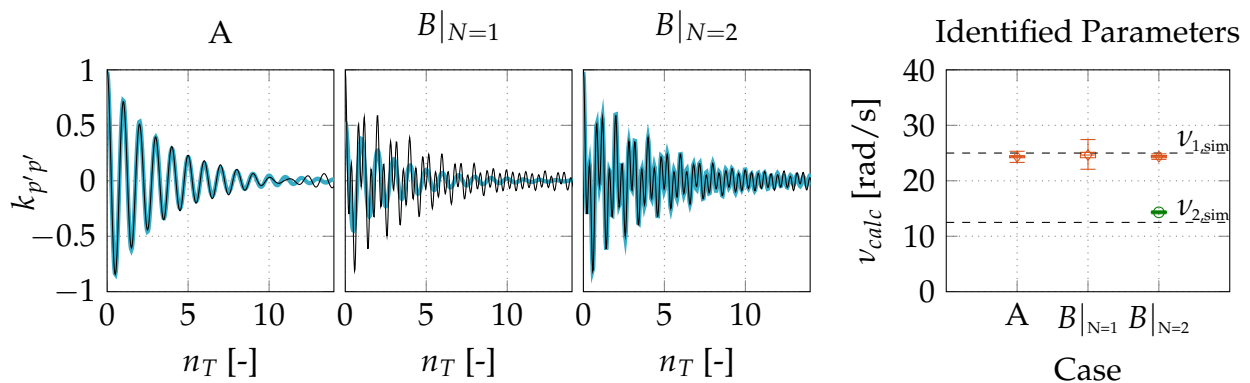


Figure B.4.: Comparison of different simulation test cases A and B: Autocorrelation of the signal (—), fitted autocorrelation (—), identified parameters ν_1 (\diamond), ν_2 (\circ) and simulation parameters (---).

percentage range. The reconstructed curve consequently contains only the contribution of mode η_1 when compared to the autocorrelation function for case $B|_{N=1}$. Regarding case $B|_{N=2}$, the damping rate ν_1 reveals a similar level of accuracy as found for case A whereas the deviation between ν_2 and the simulation parameter is in the order of 10%. Beyond that, it is remarked that for case $B|_{N=2}$ the number of degrees of freedom has increased by a factor of two compared to A and $B|_{N=1}$, and so the computational effort does. In summary, it is found that when considering a system with multi-modal content, the damping rate of one mode can in principle be identified even when the other mode is not considered in the underlying model equation. To what extent this is possible will be clarified in the next section.

B.3. Error Analysis

The following parameter study quantifies how the result quality is affected when a second mode is present but is deliberately disregarded in the underlying model equation. This is achieved by analyzing the PDFs of the identified damping rates ν_1 . The aim is to derive a general rule according to which modes being not of particular interest should be accounted for in the fitting equation or may be neglected. Based on test case B, a set of van-der-Pol oscillators is simulated by fixing ν_2 to 12.5 rad/sec while varying the damping rate ν_1 gradually between 5 and 70 rad/sec. That is, two modes are included in the synthetic time series. The parameters ν_1 and ν_2 are then, first, calculated separately by fitting the autocorrelation function to Equation (3.11) for $N = 1$ and thus the other mode is disregarded, respectively. Secondly, both damping rates ν_1 and ν_2 are determined simultaneously using Equation (3.11) for $N = 2$. The latter procedure is analogously to the previous presented test case $B|_{N=2}$. The results obtained from these analyses are shown in Figure B.5. Considering the situation for $N = 1$, both standard error and deviation of ν_2 from the simulation parameter remain virtually unaffected when increasing ν_1 in the simulation. However, the situation is different for mode η_1 where the simulated damping rate is varied. In this particular case, a standard deviation $\sigma(\nu_1)$ of less than 15% can only be obtained unless ν_1 does not exceed approximately twice the value of ν_2 . From this point, the deviation to the simulated values

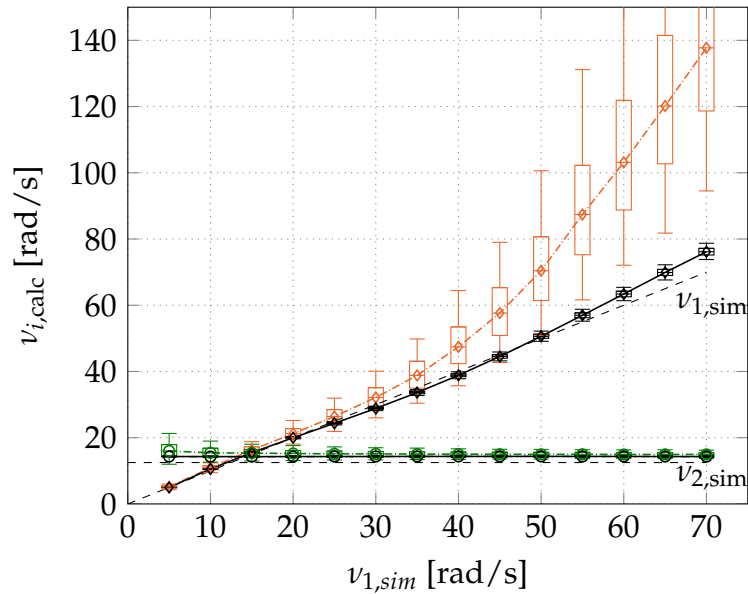


Figure B.5.: Evolution of the error for the damping rate when identifying one mode $N = 1$: (v_1 \blacklozenge , v_2 \blacklozenge) and two modes $N = 2$: (v_1 \blacklozenge , v_2 \blacklozenge) while varying $v_{1,sim}$. Simulation Parameters (---).

grows disproportionately with increasing v_1 when mode η_2 is omitted. The large uncertainty is additionally indicated by the widely spread error bars. Nevertheless, if two (or more) modes with similar damping rates occur in a system, most accurate results are obtained by accounting for both modes in the fit equation. The results shown in Figure B.5 indicate that even for the largest investigated damping rate of η_1 the discrepancies between simulated and identified damping rate remain in the single-digit percentage range.

C Operating Parameters of the Test-Rig

A complete list of the operating parameters used in this work is given in Tables C.1-C.4. The tables are divided into three parts: The first row defines the respective baseline case under dry operation ($\Omega = 0$). The following two table sections contain the corresponding operating parameters for water injection at constant equivalence ratio ($\phi = \text{const.}$) and constant adiabatic flame temperature ($T_{\text{ad}} = \text{const.}$), respectively.

Table C.1.: Overview on the operating conditions with water injection on the basis of operating point \textcircled{A} .

Operating point	Water-to-fuel ratio	Adiabatic flame	Thermal load	Equivalence
	Ω [-]	temperature T_{ad} [K]	P_{th} [kW]	ratio ϕ [-]
\textcircled{A}	0.0	1923	40.0	0.625
$\textcircled{A} _{\phi}^{\Omega=1.2}$	1.2	1896	46.8	0.735
$\textcircled{A} _{\phi}^{\Omega=1.5}$	1.5	1844	46.8	0.735
$\textcircled{A} _{\phi}^{\Omega=1.7}$	1.7	1812	46.8	0.735
$\textcircled{A} _{\phi}^{\Omega=2.0}$	2.0	1766	46.8	0.735
$\textcircled{A} _{T_{\text{ad}}}^{\Omega=1.0}$	1.0	1923	46.8	0.735
$\textcircled{A} _{T_{\text{ad}}}^{\Omega=1.2}$	1.2	1923	48.4	0.758
$\textcircled{A} _{T_{\text{ad}}}^{\Omega=1.5}$	1.5	1923	51.1	0.800
$\textcircled{A} _{T_{\text{ad}}}^{\Omega=1.7}$	1.7	1923	53.1	0.833
$\textcircled{A} _{T_{\text{ad}}}^{\Omega=2.0}$	2.0	1923	56.4	0.885

Table C.2.: Overview on the operating conditions with water injection on the basis of operating point ②.

Operating point	Water-to-fuel ratio Ω [-]	Adiabatic flame temperature		Thermal load P_{th} [kW]	Equivalence ratio ϕ [-]
		T_{ad} [K]			
②	0.0	2070		50.0	0.714
② $\Omega=0.75$ ϕ	0.75	1941		50.0	0.714
② $\Omega=1.0$ ϕ	1.0	1900		50.0	0.714
② $\Omega=1.2$ ϕ	1.2	1867		50.0	0.714
② $\Omega=1.5$ ϕ	1.5	1820		50.0	0.714
② $\Omega=0.75$ T_{ad}	0.75	2070		56.7	0.813
② $\Omega=1.0$ T_{ad}	1.0	2070		59.4	0.847
② $\Omega=1.2$ T_{ad}	1.2	2070		61.7	0.885
② $\Omega=1.5$ T_{ad}	1.5	2070		65.6	0.935

Table C.3.: Overview on the operating conditions with water injection on the basis of operating point ③.

Operating point	Water-to-fuel ratio Ω [-]	Adiabatic flame temperature		Thermal load P_{th} [kW]	Equivalence ratio ϕ [-]
		T_{ad} [K]			
③	0.0	1986		50.0	0.667
③ $\Omega=0.75$ ϕ	0.75	1864		50.0	0.667
③ $\Omega=1.0$ ϕ	1.0	1826		50.0	0.667
③ $\Omega=1.2$ ϕ	1.2	1796		50.0	0.667
③ $\Omega=1.5$ ϕ	1.5	1753		50.0	0.667
③ $\Omega=0.75$ T_{ad}	0.75	1986		56.4	0.746
③ $\Omega=1.0$ T_{ad}	1.0	1986		58.9	0.781
③ $\Omega=1.2$ T_{ad}	1.2	1986		61.0	0.806
③ $\Omega=1.5$ T_{ad}	1.5	1986		64.6	0.855

Table C.4.: Overview on the operating conditions with water injection on the basis of operating point ①.

Operating point	Water-to-fuel ratio Ω [-]	Adiabatic flame	Thermal load P_{th} [kW]	Equivalence ratio ϕ [-]
		temperature T_{ad} [K]		
①	0.0	1923	50.0	0.625
① $\Omega=0.75$ ϕ	0.75	1809	50.0	0.625
① $\Omega=1.0$ ϕ	1.0	1773	50.0	0.625
① $\Omega=1.2$ ϕ	1.2	1745	50.0	0.625
① $\Omega=1.5$ ϕ	1.5	1705	50.0	0.625
① $\Omega=0.75$ T_{ad}	0.75	1923	56.1	0.704
① $\Omega=1.0$ T_{ad}	1.0	1923	58.5	0.730
① $\Omega=1.2$ T_{ad}	1.2	1923	60.5	0.758
① $\Omega=1.5$ T_{ad}	1.5	1922	63.9	0.800

D Comparison Between Flame Driving and FTF

As demonstrated in Section 6.3, the measured flame transfer functions with water injection at constant adiabatic flame temperature scale with the flame position when considering Strouhal numbers of larger than 0.2. As further discussed in Section 7.3.4, similar behavior was also observed for the shift of the eigenfrequencies between passive and active flame ($\Delta f_{2,ac,ta}$) as well as for the flame gain β_2 . It will be shown in the following that the behavior of $\Delta f_{2,ac,ta}$ and β_2 can be explained on the basis of measured FTFs. For this purpose, the results already discussed in Section 7.3.4 are compared with experimentally determined FTFs presented in Section 6.3. Specifically, one representative FTF corresponding to operating point $\textcircled{A}|_{T_{ad}^{\Omega=1.0}}$ is chosen as benchmark. Procedurally, the FTF is determined for a fixed operating point by sweeping over a certain frequency range and measuring the flame response to external forcing (see Section 3.3). This means, that mean flow velocity at the burner exit \bar{u}_B and characteristic flame position x_{VB} are kept constant while varying the forcing frequency f . In contrast, no external forcing is used when determining $\Delta f_{2,ac,ta}$ and β_2 . In this case, variation of the Strouhal number is achieved by varying the operating conditions. More precisely, the water-to-fuel ratio is varied at constant flame temperature which determines x_{VB} and \bar{u}_B , while the frequency f changes only marginally. Based on the premise that in case of strong resonance results obtained from the transfer function H_{pq} (cf. Section 3.4.3) can be linked to the flame transfer function [22], $\Delta f_{2,ac,ta}$, β_2 and measured FTFs will be compared in the range $0.25 \leq \text{Str} < 0.68$.

The results are presented in Figure D.1. Note that the FTF is expressed in the form of its real ($\text{Re}(\text{FTF})$) and imaginary part ($\text{Im}(\text{FTF})$) and is represented by a smooth fitting function provided by the time lag model defined in Equation (8.3). In addition, the phase ($\angle \text{FTF}$) is also included in the figure. Positions of relevant phase angles are marked by numbers $\textcircled{1}$ – $\textcircled{7}$.

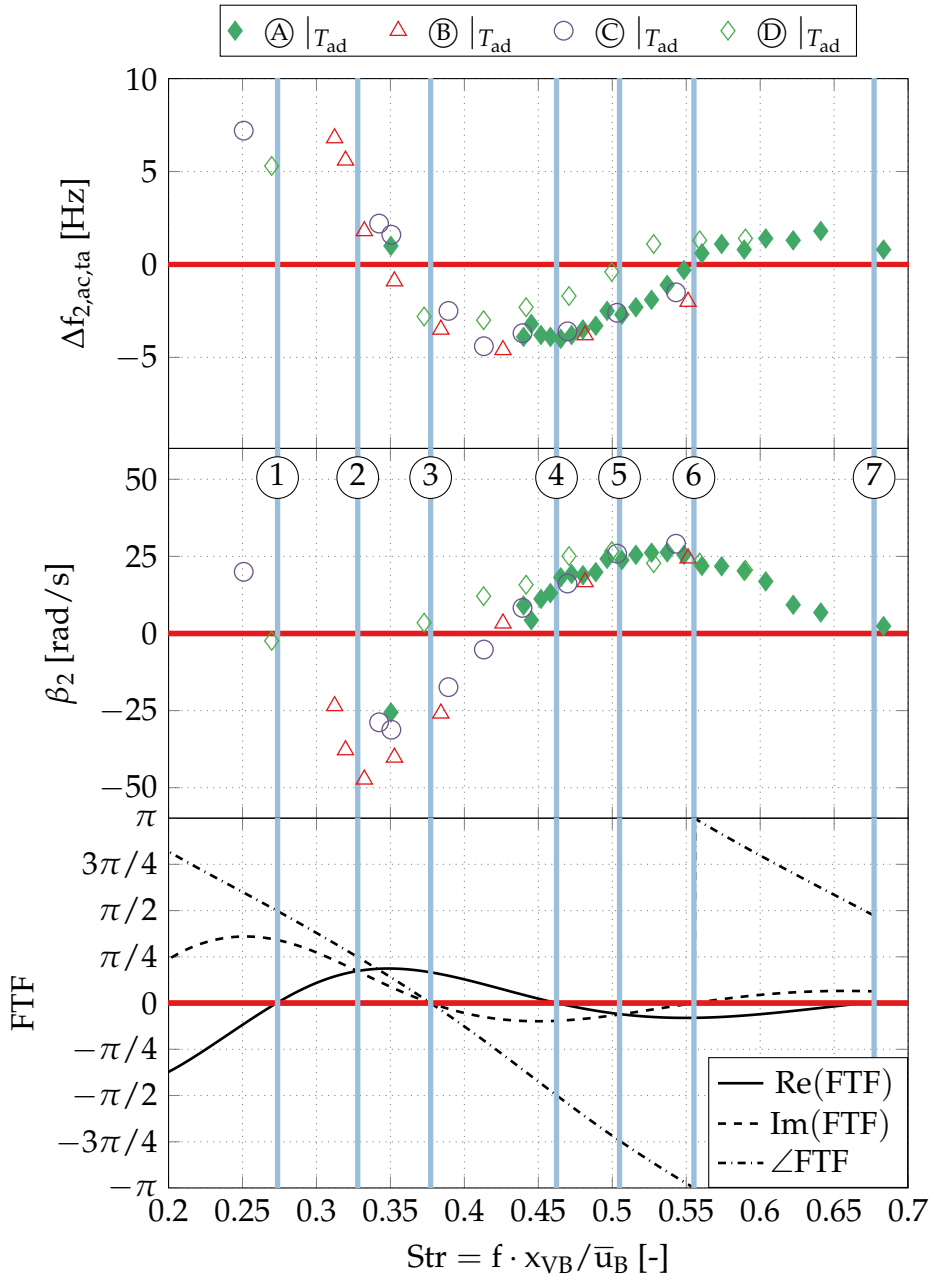


Figure D.1.: Comparison between frequency shifts, flame gain and flame transfer function for water injection at constant flame temperature.

At first, points ① and ⑦ are considered: In both cases, the phase of the FTF is $+\pi/2$ while the real part of the FTF is zero and the imaginary part is non-zero. In parallel, the measured flame gain β_2 is approximately zero and a clear frequency shift between active and passive system is determined by $\Delta f_{2,ac,ta}$. The frequency shift associated with case ① is larger than for case ⑦. This can be explained by the larger imaginary part of the FTF at ① than in case ⑦. At points ② and ⑤ the phase of the FTF is $\pi/4$ and $-3\pi/4$,

respectively. In both cases, the real and the imaginary part are identical, while the absolute value is larger in case ② than case ⑤. In case ② the flame gain is negative and has a local minimum. In contrast, the flame gain at point ⑤ is positive and has a local maximum. The finding that the absolute value of β_2 is larger at point ② than at point ⑤ can be explained by the fact that the amplitude of the FTF at point ② is also higher than at point ⑤. When assuming constant acoustic dissipation in the combustor with $\alpha_2 > \beta_2$, most stable operation would be obtained at point ②, while the combustor is least stable at point ⑤. Note that the phase shift of the FTF is $-\pi$ between ② and ⑤. In both cases, flame feedback also induces a frequency shift, which is expressed by $\Delta f_{2,ac,ta} \neq 0$. At points ③ and ⑥, the phase of the FTF is equal to zero and $\pm\pi$ respectively, while in both cases $\text{Im}(\text{FTF}) = 0$ and $\text{Re}(\text{FTF}) \neq 0$ is evident. Accordingly, a frequency shift $\Delta f_{2,ac,ta}$ of zero and a flame gain β_2 unequal to zero are expected. This is consistent with measured values of $\Delta f_{2,ac,ta} \approx 0$ and $\beta_2 \neq 0$ at point ⑥ and $\beta_2 \neq 0$ at point ③. For all operating points ①_{| T_{ad}} –④_{| T_{ad}} , the experimentally determined frequency shift is at least close to zero at point ③. Regarding point ④, the phase of the FTF is $-\pi/2$, while its real part is zero and the imaginary part is non-zero. The latter is reflected by the measured frequency shift of $\Delta f_{2,ac,ta} \neq 0$. According to the vanishing real part of the FTF, β_2 at point ④ would be expected to be zero. However, the experimentally determined point where $\beta_2 = 0$ is slightly shifted towards lower Strouhal numbers.

In summary, it is demonstrated that experimental results of the damping measurements and the flame transfer functions are consistent for the majority of the considered operating points with water injection at constant flame temperature. Note that the comparison is based on the assumption that the analyzed systems are identical for both measurement methods. In reality, this is not exactly true since flame transfer functions were measured under external forcing and using a perforated plate attached to the combustor. On the contrary, measurements of the damping parameters were conducted with a venturi nozzle without external forcing. Due to the different boundary conditions, slight deviations e.g. in flame shapes are possible, which may lead to discrepancies between the results.

E Scattering Matrices of Burner and Flame

Scattering matrices of the burner with flame are presented in the following. The scattering matrix of burner and flame is used for calculating the FTF as well as to represent the burner and flame in numerical eigenvalue studies. Amplitudes and phase angles of the $\underline{\underline{\mathbf{S}}}_{\text{BF}}$ are depicted in Figures E.1-E.2 for operating range $\textcircled{\text{A}}|_{T_{\text{ad}}}$. With increasing Ω , markedly larger gains are observed for frequencies below 200 Hz for the scattering matrix coefficients T^+ , T^- and R^- along with a major drop in R^+ at around 100 Hz. Furthermore, operational points with water injection reveal a distinct phase shift when comparing them to the reference case $\Omega = 0$ which is most noticeable in the T^+ -element. The phase delay increases clearly with increasing water-to-fuel ratio. It should also be noted that the data points exhibit a much wider scattering in the very low frequency range. One reason for this is the strong disruption of the excitation signal due to turbulent combustion noise which results in a weak signal-to-noise ratio. This leads to higher measurement uncertainties in the very low frequency range.

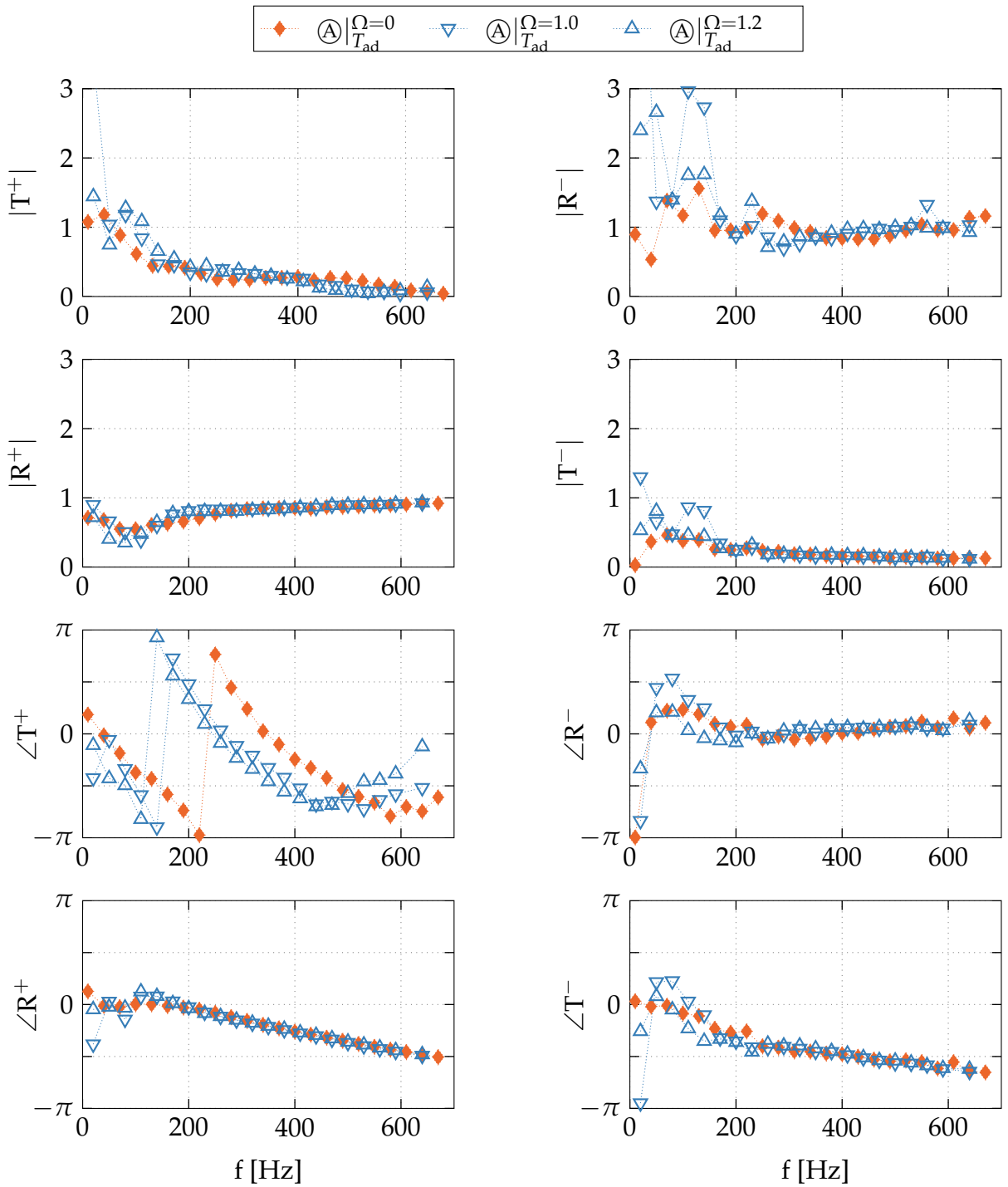


Figure E.1.: Scattering matrices of burner and flame for operating range $\textcircled{A} |_{T_{ad}}$, for $\Omega = 0$, 1.0 and 1.2 at constant adiabatic flame temperature.

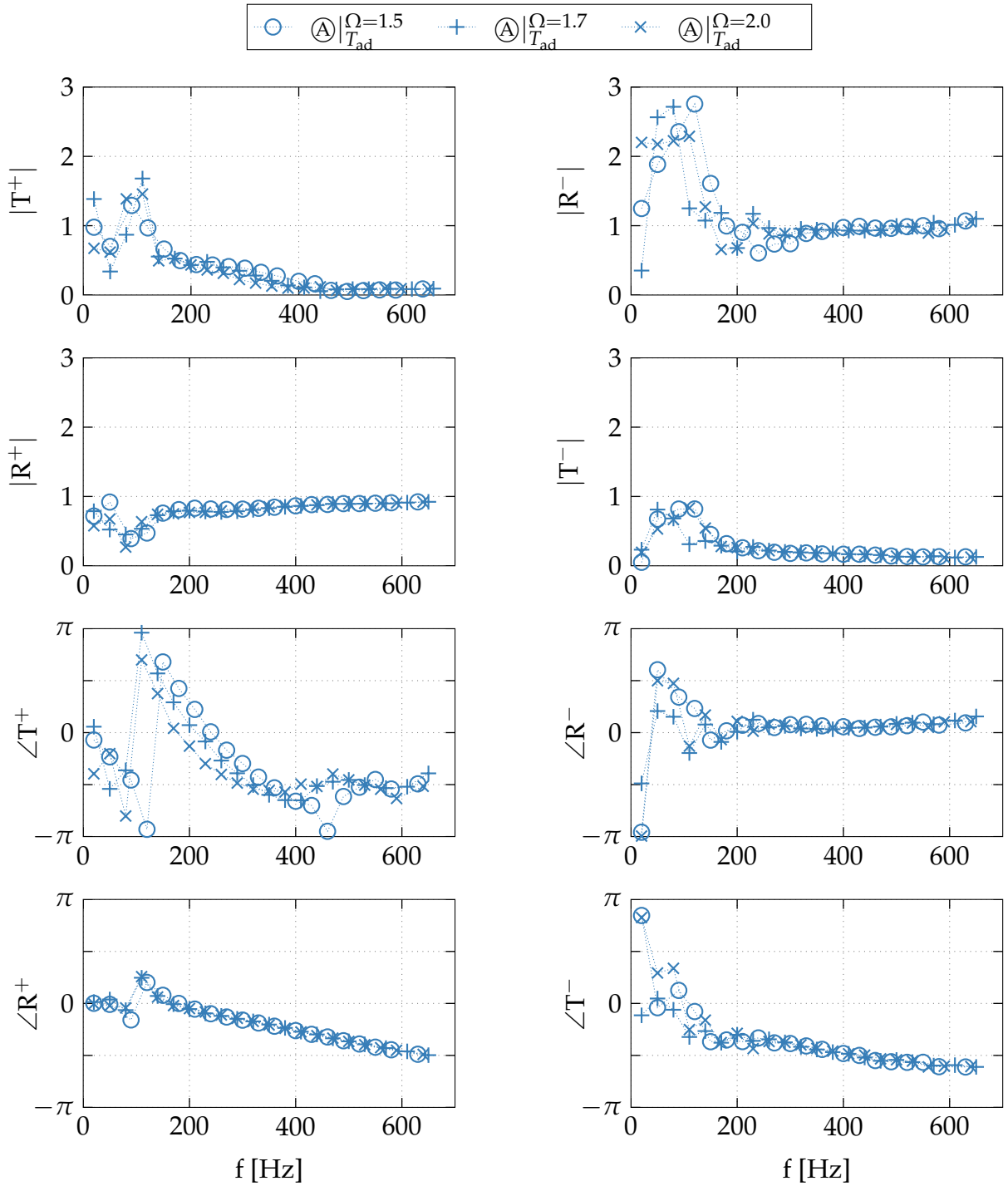


Figure E.2.: Scattering matrices of burner and flame for operating range $\textcircled{A} |_{T_{ad}}$, for $\Omega = 1.5, 1.7$ and 2.0 at constant adiabatic flame temperature.

Supervised Student Theses

Im Rahmen dieser Dissertation entstanden am Lehrstuhl für Thermodynamik, Technische Universität München in den Jahren 2013 bis 2016 unter wesentlicher wissenschaftlicher, fachlicher und inhaltlicher Anleitung des Autors die im Folgenden aufgeführten studentischen Arbeiten. Ergebnisse aus diesen Arbeiten können in Teilen in das vorliegende Dokument eingeflossen sein. Der Autor dankt hiermit explizit allen ehemals betreuten Studenten für ihr Engagement bei der Unterstützung des hier behandelten Forschungsprojekts.

Associated with this Ph.D. thesis, a number of student theses were supervised by the author of the present work. These theses were prepared at the Lehrstuhl für Thermodynamik, Technische Universität München in the years 2013 to 2016 under the close supervision of the present author. Parts of these supervised theses may be incorporated into the present thesis. The author would like to express his sincere gratitude to all formerly supervised students for their commitment and support of this research project.

Name	Title, thesis type, submission date
Florian Königbauer	Erstellung und Validierung eines akustischen Brennkammermodells, Bachelor's thesis, filed 30.09.2014
Ferdinand Wöhr	Dämpfungsmessungen an einer Einzelbrennkammer, Bachelor's thesis, filed 15.11.2014
Fabian Dawo	Konstruktion einer Vorrichtung zur Wasserinjektion in einen Einzelbrennerprüfstand, Bachelor's thesis, filed 01.12.2014
Pejman Mir	Thermoacoustic Analysis of a Lean Premixed Swirl Flame with Water Injection by OH*-Chemiluminescence, Semester thesis, filed 29.09.2015
Kilian-Josep Andres Escayola	Numerische Simulation des Strömungsfeldes eines Skalierten A2EV-Drallbrenners in einem Einzelbrennerprüfstand, Bachelor's thesis, filed 05.12.2015
Payam Mohammadzadeh Keleshtery	Hybrid Modeling Approach for Thermoacoustic Characterization of Lean-Premixed, Swirl-Stabilized Combustors with Water Injection, Master's thesis, filed 04.05.2016

Previous Publications

Wesentliche Teile dieser Dissertation wurden vom Autor bereits standardmäßig vorab als Konferenz- und Zeitschriftenbeiträge veröffentlicht [17, 73, 120, 149–152]. Alle Vorveröffentlichungen sind entsprechend der gültigen Promotionsordnung ordnungsgemäß gemeldet. Sie sind deshalb nicht zwangsläufig im Detail einzeln referenziert. Vielmehr wurde bei der Referenzierung eigener Vorveröffentlichungen Wert auf Verständlichkeit und inhaltlichen Bezug gelegt.

Significant parts of this thesis have already been published by the author in conference proceedings and journal papers [17, 73, 120, 149–152]. All relevant publications are registered according to the valid doctoral regulations. However, not all of them are quoted explicitly everywhere. Whether these personal prior printed publications were referenced depends on maintaining comprehensibility and providing all necessary context.

Stadlmair, N. V., Wagner, M., Hirsch, C., and Sattelmayer, T., 2015. "Experimentally Determining the Acoustic Damping Rates of a Combustor with a Swirl Stabilized Lean Premixed Flame". In Proceedings of ASME Turbo Expo 2015, no. GT2015-42683.

Peterleithner, J., Stadlmair, N. V., Woisetschlager, J., and Sattelmayer, T., 2015. "Analysis of Measured Flame Transfer Functions With Locally Resolved Density Fluctuation and OH-Chemiluminescence Data". *Journal of Engineering for Gas Turbines and Power*, 138(3), p. 31504.

Stadlmair, N. V., and Sattelmayer, T., 2016. "Measurement and Analysis of Flame Transfer Functions in a Lean-Premixed, Swirl-Stabilized Combustor with Water Injection". In AIAA Science and Technology Forum and Exposition (SciTech 2016).

Stadlmair, N. V., Hummel, T., and Sattelmayer, T., 2017. "Thermoacoustic Damping Rate Determination from Combustion Noise using Bayesian Statistics". *Journal of Engineering for Gas Turbines and Power* (in press).

Stadlmair, N. V., Mohammadzadeh Keleshtery, P., Zahn, M., and Sattelmayer, T., 2017. "Impact of Water Injection on Thermoacoustic Modes in a Lean Premixed Combustor under Atmospheric Conditions". In Proceedings of ASME Turbo Expo 2017, no. GT2017-63342.

Betz, M., Zahn, M., Wagner, M., Stadlmair, N. V., Schulze, M., Hirsch, C., and Sattelmayer, T., 2017. "Impact of Damper Parameters on the Stability Margin of an Annular Combustor Test Rig". In Proceedings of ASME Turbo Expo 2017, no. GT2017-64239.

Hummel, T., Berger, F. M., Stadlmair, N. V., Schuermans, B., and Sattelmayer, T., 2017. "Extraction of Linear Growth and Damping Rates of High-Frequency Thermoacoustic Oscillations from Time Domain Data". In Proceedings of ASME Turbo Expo 2017, no. GT2017-64233.

Bibliography

- [1] Åbom, M., 1991. "Measurement of the Scattering-Matrix of Acoustical Two-Ports". *Mechanical Systems and Signal Processing*, 5(2), pp. 89–104.
- [2] Åbom, M., 1992. "A Note on the Experimental Determination of Acoustical Two-Port Matrices". *Journal of Sound and Vibration*, 155(1), pp. 185–188.
- [3] Åbom, M., and Bodén, H., 1988. "Error Analysis of Two-Microphone Measurements in Ducts With Flow". *The Journal of the Acoustical Society of America*, 83(6), pp. 2429–2438.
- [4] Agarwal, A., Morris, P. J., and Mani, R., 2004. "The Calculation of Sound Propagation in Nonuniform Flows: Suppression of Instability Waves". *AIAA Journal*, 42(1), pp. 80–88.
- [5] Ahlfors, L. V., 1966. *Complex Analysis: An Introduction to the Theory of Analytic Functions of One Complex Variable*. McGraw-Hill.
- [6] Alemela, P. R., 2009. "Measurement and Scaling of Acoustic Transfer Matrices of Premixed Swirl Flames". PhD thesis, Technische Universität München.
- [7] Alemela, P. R., Fanaca, D., Ettner, F., Hirsch, C., Sattelmayer, T., and Schuermans, B., 2008. "Flame Transfer Matrices of a Premixed Flame and a Global Check with Modelling and Experiments". In *Proceedings of ASME Turbo Expo 2008*, no. GT2008-50111.
- [8] Amestoy, P. R., Duff, I. S., L'Excellent, J.-Y., and Koster, J., 2001. "A Fully Asynchronous Multifrontal Solver Using Distributed Dynamic Scheduling". *SIAM Journal on Matrix Analysis and Applications*, 23(1), pp. 15–41.

-
- [9] Anderson, F. A., Strehlow, R. A., and Strand, L. D., 1963. “Low Pressure Rocket Extinction”. *AIAA Journal*, **1**(11), pp. 2669–2671.
- [10] Ansys Inc., 2017. *ANSYS Fluent, Release 18.0*.
- [11] Bade, S., 2014. “Messung und Modellierung der thermoakustischen Eigenschaften eines modularen Brennersystems für vorgemischte Drallflammen”. PhD thesis, Technische Universität München.
- [12] Bade, S., Wagner, M., Hirsch, C., and Sattelmayer, T., 2014. “Influence of Fuel-Air Mixing on Flame Dynamics of Premixed Swirl Burners”. In Proceedings of ASME Turbo Expo 2014, no. GT2014-2538.
- [13] Bade, S., Wagner, M., Hirsch, C., Sattelmayer, T., and Schuermans, B., 2013. “Design for Thermo-Acoustic Stability: Modeling of Burner and Flame Dynamics”. *Journal of Engineering for Gas Turbines and Power*, **135**(11), p. 111502.
- [14] Bade, S., Wagner, M., Hirsch, C., Sattelmayer, T., and Schuermans, B., 2013. “Design for Thermo-Acoustic Stability: Procedure and Database”. *Journal of Engineering for Gas Turbines and Power*, **135**(12), p. 121507.
- [15] Bayes, T., and Price, R., 1763. “An Essay Towards Solving a Problem in the Doctrine of Chances. By the Late Rev. Mr. Bayes, F. R. S. Communicated by Mr. Price, in a Letter to John Canton, M. A. and F. R. S”. *Philosophical Transactions of the Royal Society of London*, **53**(1), pp. 370–418.
- [16] Berger, F. M., Hummel, T., Hertweck, M., Kaufmann, J., Schuermans, B., and Sattelmayer, T., 2017. “High-Frequency Thermoacoustic Modulation Mechanisms in Swirl-Stabilized Gas Turbine Combustors—Part I: Experimental Investigation of Local Flame Response”. *Journal of Engineering for Gas Turbines and Power*, **139**(7), p. 71501.
- [17] Betz, M., Zahn, M., Wagner, M., Stadlmair, N. V., Schulze, M., Hirsch, C., and Sattelmayer, T., 2017. “Impact of Damper Parameters on the Stability Margin of an Annular Combustor Test Rig”. In Proceedings of ASME Turbo Expo 2017, no. GT2017-64239.
- [18] Bhargava, A., Colket, M., Sowa, W., Casleton, K., and Maloney, D.,

2000. "An experimental and modeling study of humid air premixed flames". *Journal of Engineering for Gas Turbines and Power-Transactions of the ASME*, **122**(3), pp. 405–411.
- [19] Bodisco, T., Reeves, R., Situ, R., and Brown, R., 2012. "Bayesian Models for the Determination of Resonant Frequencies in a DI Diesel Engine". *Mechanical Systems and Signal Processing*, **26**, pp. 305–314.
- [20] Bonciolini, G., Boujo, E., and Noiray, N., 2016. "Effects of Turbulence-Induced Colored Noise on Thermoacoustic Instabilities in Combustion Chambers". In *Proceedings of the International Symposium on Thermoacoustic Instabilities: Industry meets Academia*, no. GTRE-050.
- [21] Bothien, M. R., 2008. "Impedance Tuning: A Method for Active Control of the Acoustic Boundary Conditions of Combustion Test Rigs". PhD thesis, Technische Universität Berlin.
- [22] Boujo, E., Denisov, A., Schuermans, B., and Noiray, N., 2016. "Quantifying Acoustic Damping Using Flame Chemiluminescence". *Journal of Fluid Mechanics*, **808**, pp. 245–257.
- [23] Boujo, E., and Noiray, N., 2016. "Robust Identification of Harmonic Oscillator Parameters Using The Adjoint Fokker-Planck Equation". *Proceedings of the Royal Society A*, **473**(2200).
- [24] Brooks, S. P., 1998. "Markov Chain Monte Carlo Method and its Application". *The Statistician*, **47**(1), pp. 69–100.
- [25] Campa, G., and Camporeale, S. M., 2012. "Eigenmode Analysis of the Thermoacoustic Combustion Instabilities Using a Hybrid Technique Based on the Finite Element Method and the Transfer Matrix Method". *Advances in Applied Acoustics*, **1**(1), pp. 1–14.
- [26] Camporeale, S. M., Fortunato, B., and Campa, G., 2010. "A Finite Element Method for Three-Dimensional Analysis of Thermo-acoustic Combustion Instability". *Journal of Engineering for Gas Turbines and Power*, **133**(1), p. 11506.
- [27] Candel, S., 2002. "Combustion Dynamics and Control: Progress and Challenges". *Proceedings of the Combustion Institute*, **29**(1), pp. 1–28.

-
- [28] Chen, Y., and Driscoll, J. F., 2016. "A Multi-Chamber Model of Combustion Instabilities and its Assessment Using Kilohertz Laser Diagnostics in a Gas Turbine Model Combustor". *Combustion and Flame*, **174**, pp. 120–137.
- [29] Chishty, W. A., 2005. "Effects of Thermoacoustic Oscillations on Spray Combustion Dynamics with Implications for Lean Direct Injection Systems". PhD thesis, Virginia Polytechnic Institute and State University.
- [30] Chishty, W. A., and Vandsburger, U., 2016. "Interaction Between Thermoacoustic Oscillations and Liquid Fuel Sprays". In *Thermoacoustic Instabilities in Gas Turbines and Rocket Engines: Industry Meets Academia*, no. GTRE-045.
- [31] Chong, L.-T. W., Komarek, T., Kaess, R., Foller, S., and Polifke, W., 2010. "Identification of Flame Transfer Functions from LES of a Premixed Swirl Burner". *Proceedings of ASME Turbo Expo 2010*(GT2010-22769).
- [32] Chu, B.-T., 1953. "On the Generation of Pressure Waves at a Plane Flame Front". In *Symposium (International) on Combustion*, Vol. 4, Elsevier, pp. 603–612.
- [33] COMSOL Inc., 2014. *COMSOL Multiphysics, Version 5.0*.
- [34] Culick, F. E., 2006. *Unsteady Motions in Combustion Chambers for Propulsion Systems*. Tech. Rep. AG-AVT-039, North Atlantic Treaty Organisation (NATO).
- [35] de Boer, G. B. J., de Weerd, C., Thoenes, D., and Goossens, H. W. J., 1987. "Laser Diffraction Spectrometry: Fraunhofer Diffraction Versus Mie Scattering". *Particle & Particle Systems Characterization*, **4**(1-4), pp. 14–19.
- [36] Dlugogorski, B. Z., Hichens, R. K., Kennedy, E. M., and Bozzelli, J. W., 1998. "Propagation of Laminar Flames in Wet Premixed Natural Gas-Air Mixtures". *Process Safety and Environmental Protection*, **76**(2), pp. 81–89.
- [37] Donea, J., and Huerta, A., 2003. *Finite Element Methods for Flow*

- Problems*. John Wiley & Sons.
- [38] Dowling, A. P., 1995. "The Calculation of Thermoacoustic Oscillations". *Journal of Sound and Vibration*, **180**(4), pp. 557–581.
- [39] Draper, N. R., and Smith, H., 1998. *Applied Regression Analysis*.
- [40] Dryer, F. L., 1977. "Water Addition to Practical Combustion Systems". *Symposium (International) on Combustion*, **16**(1), pp. 279–295.
- [41] Ducruix, S., Schuller, T., Durox, D., and Candel, S., 2003. "Combustion Dynamics and Instabilities: Elementary Coupling and Driving Mechanisms". *Journal of Propulsion and Power*, **19**(5), pp. 722–734.
- [42] Eckstein, J., 2004. "On the Mechanisms of Combustion Driven Low-Frequency Oscillations in Aero-Engines". PhD thesis, Technische Universität München.
- [43] Eckstein, J., and Sattelmayer, T., 2006. "Combustion Instabilities in Aeroengines". *Journal of Propulsion and Power*, **22**(2), pp. 425–432.
- [44] Elster, C., and Wübbeler, G., 2016. "Bayesian Regression versus Application of Least Squares - an Example". *Metrologia*, **53**(1), pp. 10–16.
- [45] Emmert, T., Bomberg, S., Jaensch, S., and Polifke, W., 2015. "Acoustic and Intrinsic Thermoacoustic Modes of a Premixed Combustor". *Proceedings of the Combustion Institute*, **36**(3), pp. 3835–3842.
- [46] Emmert, T., Bomberg, S., and Polifke, W., 2015. "Intrinsic Thermoacoustic Instability of Premixed Flames". *Combustion and Flame*, **162**(1), pp. 75–85.
- [47] Emmert, T. M., 2016. "State Space Modeling of Thermoacoustic Systems with Application to Intrinsic Feedback". PhD thesis, Technische Universität München.
- [48] Ewert, R., and Schröder, W., 2003. "Acoustic Perturbation Equations Based on Flow Decomposition via Source Filtering". *Journal of Computational Physics*, **188**(2), pp. 365–398.
- [49] Fanaca, D., 2010. "Influence of Burner-Burner Interactions on the

Flame Dynamics in an Annular Combustor". PhD thesis, Technische Universität München.

- [50] Fanaca, D., Alemela, P. R., Ettner, F., Hirsch, C., Sattelmayer, T., and Schuermans, B., 2008. "Determination and Comparison of the Dynamic Characteristics of a Perfectly Premixed Flame in both Single and Annular Combustion Chambers". In Proceedings of ASME Turbo Expo 2008, no. GT2008-50781.
- [51] Fiala, T., Kathan, R., and Sattelmayer, T., 2011. "Effective Stability Analysis of Liquid Rocket Combustion Chambers: Experimental Investigation of Damped Admittances". In IAC, no. 11.C4.3.11.
- [52] Fischer, A., 2004. "Hybride, thermoakustische Charakterisierung von Drallbrennern". PhD thesis, Technische Universität München.
- [53] Freitag, E., 2009. "On the Measurement and Modelling of Flame Transfer Functions at Elevated Pressure". PhD thesis, Technische Universität München.
- [54] Gardiner, C., 2009. *Stochastic Methods*. Springer, Berlin.
- [55] Geman, S., and Geman, D., 1984. "Stochastic Relaxation, Gibbs Distributions, and the Bayesian Restoration of Images". *IEEE Transactions on Pattern Analysis and Machine Intelligence*(6), pp. 721–741.
- [56] Gikadi, J., 2013. "Prediction of Acoustic Modes in Combustors using Linearized Navier-Stokes Equations in Frequency Space". PhD thesis, Technische Universität München.
- [57] Gikadi, J., Schulze, M., Schwing, J., Foeller, S., and Sattelmayer, T., 2012. "Linearized Navier-Stokes and Euler Equations for the Determination of the Acoustic Scattering Behaviour of an Area Expansion". In 18th AIAA/CEAS Aeroacoustics Conference, American Institute of Aeronautics and Astronautics.
- [58] Gikadi, J., Ullrich, W. C., Sattelmayer, T., and Turrini, F., 2013. "Prediction of the Acoustic Losses of a Swirl Atomizer Nozzle Under Non-Reactive Conditions". In Proceedings of ASME Turbo Expo 2013, no. GT2013-95449.

- [59] Gill, P. E., Murray, W., Saunders, M. A., and Wright, M. H., 1981. "Aspects of Mathematical Modelling Related to Optimization". *Applied Mathematical Modelling*, 5(2), pp. 71–83.
- [60] Göke, S., 2012. "Ultra-Wet Combustion: An Experimental and Numerical Study". PhD thesis, Technische Universität Berlin.
- [61] Göke, S., Füre, M., Bourque, G., Bobusch, B., Göckeler, K., Krüger, O., Schimek, S., Terhaar, S., and Paschereit, C. O., 2013. "Influence of Steam Dilution on the Combustion of Natural Gas and Hydrogen in Premixed and Rich-Quench-Lean Combustors". *Fuel Processing Technology*, 107(C), pp. 14–22.
- [62] Guethe, F., Guyot, D., Singla, G., Noiray, N., and Schuermans, B., 2012. "Chemiluminescence as Diagnostic Tool in the Development of Gas Turbines". *Applied Physics B: Lasers and Optics*, 107(3), pp. 619–636.
- [63] Guethe, F., and Schuermans, B., 2007. "Phase-locking in Post-Processing for Pulsating Flames". *Measurement Science and Technology*, 18, pp. 1–7.
- [64] Hake, J. F., Fischer, W., Venghaus, S., and Weckenbrock, C., 2015. "The German Energiewende - History and Status Quo". *Energy*, 92, pp. 532–546.
- [65] Hastings, W. K., 1970. "Monte Carlo Sampling Methods Using Markov Chains and Their Applications". *Biometrika*, 57(1), p. 97.
- [66] Hauser, M., 2014. "Zum Einfluss transversaler akustischer Anregung auf die Dynamik turbulenter vorgemischter Drallflammen". PhD thesis, Technische Universität München.
- [67] Hermann, F., Klingmann, J., and Gabrielsson, R., 2003. "Computational and Experimental Investigation of Emissions in a Highly Humidified Premixed Flame". In Proceedings of ASME Turbo Expo 2003, no. GT2003-38337.
- [68] Hirsch, C., Fanaca, D., Reddy, P., Polifke, W., and Sattelmayer, T., 2005. "Influence of the Swirler Design on the Flame Transfer Function of Premixed Flames". In Proceedings of ASME Turbo Expo 2005,

no. GT2005-68195.

- [69] Hoeijmakers, M., Kornilov, V., Lopez Arteaga, I., de Goey, P., and Nijmeijer, H., 2014. "Intrinsic instability of flame-acoustic coupling". *Combustion and Flame*, **161**(11), pp. 2860–2867.
- [70] Hughes, T. J. R., Franca, L. P., and Balestra, M., 1986. "A New Finite Element Formulation for Computational Fluid Dynamics: V. Circumventing the Babuska-Brezzi Condition: A Stable Petrov-Galerkin Formulation of the Stokes Problem Accommodating Equal-order Interpolations". *Computer Methods in Applied Mechanics and Engineering*, **59**(1), pp. 85–99.
- [71] Hughes, T. J. R., Franca, L. P., and Hulbert, G. M., 1989. "A new finite element formulation for computational fluid dynamics: VIII. The galerkin/least-squares method for advective-diffusive equations". *Computer Methods in Applied Mechanics and Engineering*, **73**(2), pp. 173–189.
- [72] Hummel, T., Berger, F., Hertweck, M., Schuermans, B., and Sattelmayer, T., 2017. "High-Frequency Thermoacoustic Modulation Mechanisms in Swirl-Stabilized Gas Turbine Combustors—Part II: Modeling and Analysis". *Journal of Engineering for Gas Turbines and Power*, **139**(7), p. 71502.
- [73] Hummel, T., Berger, F. M., Stadlmair, N. V., Schuermans, B., and Sattelmayer, T., 2017. "Extraction of Linear Growth and Damping Rates of High-Frequency Thermoacoustic Oscillations from Time Domain Data". In *Proceedings of ASME Turbo Expo 2017*, no. GT2017-64233.
- [74] Hummel, T., Hofmeister, T., Schuermans, B., and Sattelmayer, T., 2017. "Modeling and Quantification of Acoustic Damping Induced by Vortex Shedding in Non-Compact Thermoacoustic Systems". In *24th International Congress on Sound and Vibration (ICSV)*.
- [75] Hummel, T., Temmler, C., Schuermans, B., and Sattelmayer, T., 2015. "Reduced Order Modeling of Aeroacoustic Systems for Stability Analyses of Thermoacoustically Non-Compact Gas Turbine Combustors". In *Proceedings of ASME Turbo Expo 2015*, no. GT2015-43338.

- [76] Hummel, T., Temmler, C., Schuermans, B., and Sattelmayer, T., 2016. "Reduced-Order Modeling of Aeroacoustic Systems for Stability Analyses of Thermoacoustically Noncompact Gas Turbine Combustors". *Journal of Engineering for Gas Turbines and Power*, **138**(5), p. 51502.
- [77] Institutional Organization for Standardization (ISO), 1998. DIN ISO 10534-2 Acoustics, Determination of Sound Absorption Coefficient and Impedance in Impedance Tubes.
- [78] Jonsson, M., and Yan, J., 2005. "Humidified Gas Turbines - A Review of Proposed and Implemented Cycles". *Energy*, **30**(7), pp. 1013–1078.
- [79] Kaess, R., Poinso, T., and Polifke, W., 2009. "Determination of the Stability Map of a Premix Burner Based on Flame Transfer Functions Computed with Transient CFD". *4th European Combustion Meeting. The Combustion Institute, Vienna, Austria*.
- [80] Keller, J. J., 1995. "Thermoacoustic Oscillations in Combustion Chambers of Gas Turbines". *AIAA Journal*, **33**(12), pp. 2280–2287.
- [81] Kierkegaard, A., Boij, S., and Efraimsson, G., 2010. "A Frequency Domain Linearized Navier-Stokes Equations Approach to Acoustic Propagation in Flow Ducts with Sharp Edges". *The Journal of the Acoustical Society of America*, **127**(2).
- [82] Klarman, N., Sattelmayer, T., Geng, W., and Magni, F., 2016. "Flamelet Generated Manifolds for Partially-Premixed, Highly-Stretched and Non-Adiabatic Combustion in Gas Turbines". In AIAA Science and Technology Forum and Exposition (SciTech 2016).
- [83] Klarman, N., Sattelmayer, T., Weiqing, G., and Magni, F., 2016. "Impact of Flame Stretch and Heat Loss on Heat Release Distributions in Gas Turbine Combustors: Model Comparison and Validation". In Proceedings of ASME Turbo Expo 2016, no. GT2016-57625.
- [84] Lauer, M. R. W., 2011. "Determination of the Heat Release Distribution in Turbulent Flames by Chemiluminescence Imaging". PhD thesis, Technische Universität München.
- [85] Lawson, C. L., and Hanson, R. J., 1974. "Solving Least Squares Problems". *Journal of Chemical Information and Modeling*, **53**(9), pp. 1689–

1699.

- [86] Le Cong, T., and Dagaut, P., 2008. "Effect of Water Vapor on the Kinetics of Combustion of Hydrogen and Natural Gas: Experimental and Detailed Modeling Study".
- [87] Lechner, C., and Seume, J., 2010. *Stationäre Gasturbinen*. Springer, Berlin, Heidelberg.
- [88] Lefebvre, A., 1988. *Atomization and Sprays*. CRC press.
- [89] Lefebvre, A. H., and Ballal, D. R., 2010. *Gas Turbine Combustion*. CRC Press, Boca Raton.
- [90] Lellek, S., Barfuß, C., and Sattelmayer, T., 2017. "Experimental Study of the Interaction of Water Sprays With Swirling Premixed Natural Gas Flames". *Journal of Engineering for Gas Turbines and Power*, **139**(2), p. 21506.
- [91] Lellek, S., and Sattelmayer, T., 2015. "Influence of Water Injection on Heat Release Distribution, Lean Blowout and Emissions of a Premixed Swirl Flame in a Tubular Combustor". In Proceedings of ASME Turbo Expo 2015, no. GT2015-42602.
- [92] Lellek, S., and Sattelmayer, T., 2017. "NO_x-Formation and CO-Burnout in Water Injected, Premixed Natural Gas Flames at Typical Gas Turbine Combustor Residence Times". In Proceedings of ASME Turbo Expo 2017, no. GT2017-63128.
- [93] Lieuwen, T., 2002. "Experimental Investigation of Limit-Cycle Oscillations in an Unstable Gas Turbine Combustor". *Journal of Propulsion and Power*, **18**(1), pp. 61–67.
- [94] Lieuwen, T., 2005. "Online Combustor Stability Margin Assessment Using Dynamic Pressure Data". *Journal of Engineering for Gas Turbines and Power*, **127**(3), pp. 478–482.
- [95] Lieuwen, T., and Zinn, B. T., 1998. "The Role of Equivalence Ratio Oscillations in Driving Combustion Instabilities in Low-NO_x Gas Turbines". *International Symposium on Combustion*.

- [96] Lieuwen, T. C., 2003. "Statistical Characteristics of Pressure Oscillations in a Premixed Combustor". *Journal of Sound and Vibration*, **260**, pp. 3–17.
- [97] Lieuwen, T. C., 2012. *Unsteady Combustor Physics*. Cambridge University Press.
- [98] Lira, I., and Wöger, W., 2006. "Comparison Between the Conventional and Bayesian Approaches to Evaluate Measurement Data". *Metrologia*, **43**, pp. 249–259.
- [99] Mazas, A., Lacoste, D., Fiorina, B., and Schuller, T., 2009. "Effects of Water Vapor Addition on the Laminar Burning Velocity of Methane Oxygen-Enhanced Flames at Atmospheric Pressure". In Proceedings of the European Combustion Meeting.
- [100] Mazas, A. N., Fiorina, B., Lacoste, D. A., and Schuller, T., 2011. "Effects of Water Vapor Addition on the Laminar Burning Velocity of Oxygen-Enriched Methane Flames". *Combustion and Flame*, **158**(12), pp. 2428–2440.
- [101] Meacock, A. J., and White, A. J., 2006. "The Effect of Water Injection on Multispool Gas Turbine Behavior". *Journal of Engineering for Gas Turbines and Power*, **128**(1), pp. 97–102.
- [102] Metropolis, N., Rosenbluth, A. W., Rosenbluth, M. N., Teller, A. H., and Teller, E., 1953. "Equation of State Calculations by Fast Computing Machines". *The Journal of Chemical Physics*, **21**(6), pp. 1087–1092.
- [103] Moore, M. J., 1997. "NO_x Emission Control in Gas Turbines for Combined Cycle Gas Turbine Plant". *Proceedings of the Institution of Mechanical Engineers, Part A: Journal of Power and Energy*, **211**(43).
- [104] Mordechai, S., 2011. *Applications of Monte Carlo Method in Science and Engineering*. InTech, Rijeka.
- [105] Munjal, M. L., 1987. *Acoustics of Ducts and Mufflers*. John Wiley & Sons.
- [106] Munjal, M. L., and Doige, A. G., 1990. "Theory of a two Source-Location Method for Direct Experimental Evaluation of the Four-

Pole Parameters of an Aeroacoustic Element". *Journal of Sound and Vibration*, **141**(2), pp. 323–333.

- [107] Nicoud, F., Benoit, L., Sensiau, C., and Poinsot, T., 2007. "Acoustic Modes in Combustors with Complex Impedances and Multidimensional Active Flames". *AIAA Journal*, **45**(2), pp. 426–441.
- [108] Nicoud, F., and Wieczorek, K., 2009. "About the zero Mach number assumption in the calculation of thermoacoustic instabilities". *International Journal of Spray and Combustion Dynamics*, **1**(1), pp. 67–111.
- [109] Noiray, N., 2017. "Linear Growth Rate Estimation from Dynamics and Statistics of Acoustic Signal Envelope in Turbulent Combustors". *Journal of Engineering for Gas Turbines and Power*, **139**(4), p. 41503.
- [110] Noiray, N., Bothien, M., and Schuermans, B., 2011. "Investigation of Azimuthal Staging Concepts in Annular Gas Turbines". *Combustion Theory and Modelling*, **15**(5), pp. 585–606.
- [111] Noiray, N., and Schuermans, B., 2013. "Deterministic Quantities Characterizing Noise Driven Hopf Bifurcations in Gas Turbine Combustors". *International Journal of Non-Linear Mechanics*, **50**, pp. 152–163.
- [112] Noiray, N., and Schuermans, B. A., 2013. "On the Dynamic Nature of Azimuthal Thermoacoustic Modes in Annular Gas Turbine Combustion Chambers". *Proceedings of the Royal Society A*, **469**.
- [113] O'Connor, J., Acharya, V., and Lieuwen, T., 2015. "Transverse Combustion Instabilities: Acoustic, Fluid Mechanic, and Flame Processes". *Progress in Energy and Combustion Science*, **49**, pp. 1–39.
- [114] Paschereit, C., Gutmark, E., and Weisenstein, W., 1999. "Coherent Structures in Swirling Flows and their Role in Acoustic Combustion Control". *Physics of Fluids*, **11**(9), p. 2667.
- [115] Paschereit, C. O., Gutmark, E., and Weisenstein, W., 1998. "Structure and Control of Thermoacoustic Instabilities in a Gas-Turbine Combustor". In 36th AIAA Aerospace Sciences Meeting and Exhibit, no. 98-1067.

- [116] Paschereit, C. O., and Polifke, W., 1998. "Investigation of the Thermoacoustic Characteristics of a Lean Premixed Gas Turbine Burner". In *Proceedings of International Gas Turbine & Aeroengine Congress & Exhibition*, no. 98-GT-582.
- [117] Paschereit, C. O., Schuermans, B., Polifke, W., and Mattson, O., 2002. "Measurement of Transfer Matrices and Source Terms of Premixed Flames". *Journal of Engineering for Gas Turbines and Power*, **124**(2), p. 239.
- [118] Pavri, R., and Moore, G. D., 2001. GER 4211 - Gas Turbine Emissions and Control. Tech. rep., GE Energy Systems, Atlanta, GA.
- [119] Peterleithner, J., Basso, R., Heitmeir, F., Woisetschläger, J., Schlüßler, R., and Czarske, J., 2016. "Comparison of Flame Transfer Functions Acquired by Chemiluminescence and Density Fluctuation". In *Proceedings of ASME Turbo Expo 2016*, no. GT2016-57485.
- [120] Peterleithner, J., Stadlmair, N. V., Woisetschläger, J., and Sattelmayer, T., 2015. "Analysis of Measured Flame Transfer Functions With Locally Resolved Density Fluctuation and OH-Chemiluminescence Data". *Journal of Engineering for Gas Turbines and Power*, **138**(3), p. 31504.
- [121] Plummer, M., 2003. "JAGS: A Program for Analysis of Bayesian Graphical Models Using Gibbs Sampling". *3rd International Workshop on Distributed Statistical Computing*.
- [122] Polifke, W., Hoek, J., and Verhaar, B., 1997. Everything you always Wanted to Know about f and g. Tech. rep., ABB Corporate Research, Baden, CH.
- [123] Polifke, W., and Lawn, C., 2007. "On the Low-Frequency Limit of Flame Transfer Functions". *Combustion and Flame*, **151**(3), pp. 437–451.
- [124] Polifke, W., Paschereit, C. O., and Döbbeling, K., 2001. "Constructive and Destructive Interference of Acoustic and Entropy Waves in a Premixed Combustor with a Choked Exit". *Journal of Acoustics and Vibration*, **6**(3), pp. 135–146.

-
- [125] Prax, C., Golanski, F., and Nadal, L., 2008. "Control of the Vorticity Mode in the Linearized Euler Equations for Hybrid Aeroacoustic Prediction". *Journal of Computational Physics*, **227**(12), pp. 6044–6057.
- [126] Pretzler, G., Jäger, H., Neger, T., Philipp, H., and Woisetschläger, J., 1992. "Comparison of Different Methods of Abel Inversion Using Computer Simulated and Experimental Side-On-Data". *Journal of Physical Sciences*, **47**(9), pp. 955–970.
- [127] Raffel, M., Willert, C. E., Wereley, S. T., and Kompenhans, J., 2007. *Particle Image Velocimetry: A Practical Guide*, Vol. 2. Springer, Berlin, Heidelberg.
- [128] Rao, P. P., and Morris, P. J., 2006. "Use of Finite Element Methods in Frequency Domain Aeroacoustics". *AIAA Journal*, **44**(7).
- [129] Rayleigh, 1878. "The Explanation of Certain Acoustical Phenomena". *Nature*, **18**(4), pp. 319–321.
- [130] Rienstra, S., and Hirschberg, A., 2004. *An Introduction to Acoustics*. Eindhoven University of Technology, Netherlands.
- [131] Robert, C. P., and Casella, G., 2004. *Monte Carlo Statistical Methods*, Vol. 95. Springer, Berlin, Heidelberg.
- [132] Rubinstein, R. Y., and Kroese, D. P., 2011. *Simulation and the Monte Carlo Method*. John Wiley & Sons.
- [133] Russ, M., Meyer, A., and Büchner, H., 2007. "Scaling Thermo-Acoustic Characteristics of LP and LPP Swirl Flames". In Proceedings of ASME Turbo Expo 2007, no. GT2007-27775.
- [134] Sangl, J., 2012. "Erhöhung der Brennstoffflexibilität von Vormischbrennern durch Beeinflussung der Wirbeldynamik". PhD thesis, Technische Universität München.
- [135] Sangl, J., Mayer, C., and Sattelmayer, T., 2011. "Dynamic adaptation of aerodynamic flame stabilization of a premix swirl burner to fuel reactivity using fuel momentum". *Journal of Engineering for Gas Turbines and Power*, **133**(7), p. 71501.

- [136] Sattelmayer, T., and Polifke, W., 2003. "A Novel Method for the Computation of the Linear Stability of Combustors". *Combustion Science and Technology*, **175**, pp. 477–497.
- [137] Sattelmayer, T., and Polifke, W., 2003. "Assessment of Methods for the Computation of the Linear Stability of Combustors". *Combustion Science and Technology*, **175**(3), pp. 453–476.
- [138] Schimek, S., Göke, S., Schrödinger, C., and Paschereit, C. O., 2012. "Analysis of Flame Transfer Functions for Blends of CH₄ and H₂ at Different Humidity Levels". In 50th AIAA Aerospace Sciences Meeting including the New Horizons Forum and Aerospace Exposition.
- [139] Schimek, S., Göke, S., Schrödinger, C., and Paschereit, C. O., 2012. "Flame Transfer Function Measurements With CH₄ and H₂ Fuel Mixtures at Ultra Wet Conditions in a Swirl Stabilized Premixed Combustor". In Proceedings of ASME Turbo Expo 2012, no. GT2012-69788.
- [140] Schuermans, B., 2003. "Modeling and Control of Thermoacoustic Instabilities". PhD thesis, École Polytechnique Fédérale de Lausanne.
- [141] Schuermans, B., Bellucci, V., Guethe, F., Meili, F., Flohr, P., and Paschereit, C. O., 2004. "A Detailed Analysis of Thermoacoustic Interaction Mechanisms in a Turbulent Premixed Flame". In Proceedings of ASME Turbo Expo 2004, no. GT2004-53831.
- [142] Schuermans, B., Guethe, F., and Mohr, W., 2008. "Optical Transfer Function Measurements for Technically Premixed Flames". *Journal of Engineering for Gas Turbines and Power*, **132**, pp. 1121–1131.
- [143] Schuermans, B., Guethe, F., Pennell, D., Guyot, D., and Paschereit, C. O., 2010. "Thermoacoustic Modeling of a Gas Turbine Using Transfer Functions Measured Under Full Engine Pressure". *Journal of Engineering for Gas Turbines and Power*, **132**(11), p. 111503.
- [144] Schuermans, B., Polifke, W., and Paschereit, C. O., 1999. "Modeling Transfer Matrices of Premixed Flames and Comparison with Experimental Results". In Proceedings of International Gas Turbine & Engine Congress & Exhibition, no. 99-GT-132.

-
- [145] Schulze, M., 2016. "Linear Stability Assessment of Cryogenic Rocket Engines". Phd thesis, Technische Universität München.
- [146] Schulze, M., Hummel, T., Klarmann, N., Berger, F., Schuermans, B., and Sattelmayer, T., 2016. "Linearized Euler Equations for the Prediction of Linear High-Frequency Instability in Gas Turbine Combustors". In Proceedings of ASME Turbo Expo 2016, no. GT2016-57818.
- [147] Schulze, M., and Sattelmayer, T., 2015. "A Comparison of Time and Frequency Domain Descriptions of High Frequency Acoustics in Rocket Engines with Focus on Dome Coupling". *Aerospace Science and Technology*, **45**, pp. 165–173.
- [148] Schwing, J., Grimm, F., and Sattelmayer, T., 2012. "A Model for the Thermo-Acoustic Feedback of Transverse Acoustic Modes and Periodic Oscillations in Flame Position in Cylindrical Flame Tubes". In Proceedings of ASME Turbo Expo 2012, no. GT2012-68775.
- [149] Stadlmair, N. V., Hummel, T., and Sattelmayer, T., 2017. "Thermoacoustic Damping Rate Determination from Combustion Noise using Bayesian Statistics". *Journal of Engineering for Gas Turbines and Power*(in press).
- [150] Stadlmair, N. V., Mohammadzadeh Keleshtery, P., Zahn, M., and Sattelmayer, T., 2017. "Impact of Water Injection on Thermoacoustic Modes in a Lean Premixed Combustor under Atmospheric Conditions". In Proceedings of ASME Turbo Expo 2017, no. GT2017-63342.
- [151] Stadlmair, N. V., and Sattelmayer, T., 2016. "Measurement and Analysis of Flame Transfer Functions in a Lean-Premixed, Swirl-Stabilized Combustor with Water Injection". In AIAA Science and Technology Forum and Exposition (SciTech 2016).
- [152] Stadlmair, N. V., Wagner, M., Hirsch, C., and Sattelmayer, T., 2015. "Experimentally Determining the Acoustic Damping Rates of a Combustor with a Swirl Stabilized Lean Premixed Flame". In Proceedings of ASME Turbo Expo 2015, no. GT2015-42683.
- [153] Tay-Wo-Chong, L., Bomberg, S., Ulhaq, A., Komarek, T., and Polifke, W., 2012. "Comparative Validation Study on Identification of

- Premixed Flame Transfer Function". *Journal of Engineering for Gas Turbines and Power*, **134**(2), p. 021502.
- [154] Temme, J. E., Allison, P. M., and Driscoll, J. F., 2012. "Low Frequency Combustion Instabilities Imaged in a Gas Turbine Combustor Flame Tube". In 50th AIAA Aerospace Sciences Meeting, no. AIAA 2012-0542, pp. 1–6.
- [155] Temme, J. E., Allison, P. M., and Driscoll, J. F., 2014. "Combustion Instability of a Lean Premixed Prevaporized Gas Turbine Combustor Studied Using Phase-Averaged PIV". *Combustion and Flame*, **161**(4), pp. 958–970.
- [156] Ullrich, W., and Sattelmayer, T., 2015. "Transfer Functions of Acoustic, Entropy and Vorticity Waves in an Annular Model Combustor and Nozzle for the Prediction of the Ratio Between Indirect and Direct Combustion Noise". *21st AIAA CEAS Aeroacoustics Conference*(June), pp. 1–19.
- [157] Ullrich, W. C., Gikadi, J., Jörg, C., and Sattelmayer, T., 2014. "Acoustic-Entropy Coupling Behavior and Acoustic Scattering Properties of a Laval Nozzle". In 20th AIAA/CEAS Aeroacoustics Conference.
- [158] Versteeg, H. K., and Malalasekera, W., 2007. *An Introduction to Computational Fluid Dynamics: The Finite Volume Method*. Pearson Education.
- [159] Wagner, M., Jörg, C., and Sattelmayer, T., 2013. "Comparison of the Accuracy of Time-Domain Measurement Methods for Combustor Damping". In Proceedings of ASME Turbo Expo 2013, no. GT2013-94844.
- [160] Wilcox, E. C., and Trout, A. M., 1951. Analysis of Thrust Augmentation of Turbojet Engines by Water Injection at Compressor Inlet Including Charts for Calculating Compression Processes With Water Injection. Tech. Rep. 1006, NACA.
- [161] Wozniak, G., 2013. *Zerstäubungstechnik: Prinzipien, Verfahren, Geräte*. Springer, Berlin, Heidelberg.
- [162] Zahn, M., Betz, M., Schulze, M., Hirsch, C., and Sattelmayer, T., 2017. "Predicting the Influence of Damping Devices on the Stability Margin

-
- of an Annular Combustor". In Proceedings of ASME Turbo Expo 2017, no. GT2017-64238.
- [163] Zahn, M., Schulze, M., Hirsch, C., Betz, M., and Sattelmayer, T., 2015. "Frequency Domain Predictions of Acoustic Wave Propagation and Losses in a Swirl Burner With Linearized Navier-Stokes Equations". In ASME Turbo Expo 2015: Turbine Technical Conference and Exposition.
- [164] Zahn, M., Schulze, M., Hirsch, C., and Sattelmayer, T., 2016. "Impact of Quarter Wave Tube Arrangement on Damping of Azimuthal Modes". In Proceedings of ASME Turbo Expo 2016, no. GT2016-56450.
- [165] Zellhuber, M., Schwing, J., Schuermans, B., Sattelmayer, T., and Polifke, W., 2014. "Experimental and Numerical Investigation of Thermoacoustic Sources Related to High-Frequency Instabilities". *International Journal of Spray and Combustion Dynamics*, 6(1), pp. 1–34.
- [166] Zhang, M., Lin, Y., and Tao, W., 2017. "Analytical Study of Low-Frequency Helmholtz Mode Oscillation in a Model Combustor". In Proceedings of ASME Turbo Expo 2017, no. GT2017-64130.